受理 60.12.19

DOCTORAL DISSERTATION

ON

PULSE ENERGIZATION IN ELECTROSTATIC PRECIPITATOR

電気集塵におけるパルス荷電の研究

SHUNSUKE HOSOKAWA

Department of Electrical Engineering

Under the guidance of

Prof. Dr. SENICHI MASUDA

電気工学科　８５６７

細川俊介

指導教官

増田閃一教授

21th December 1985

Department of Electrical Engineering

Faculty of Engineering

UNIVERSITY OF TOKYO

TABLE OF CONTENTS

CHAPTER 1. INTRODUCTION

1-1. Present Status of Pulse Energization in Electrostatic Precipitator

One of the urgent problems in electrostatic precipitators is to cope with the high resistivity dust causing the back corona troubles [1]. Back corona is a phenomena of breakdown of a dust layer on a collection electrode to provide positive ions to the collection field which reduces the particle charging drastically resulting in a collection performance degradation. Back corona takes place when the following criterion is satisfied [2,3]:

$$E_d = i_d \times r_d > E_{ds} \qquad \text{-----(1.1)}$$

where E_d : electric field in dust layer

i_d : current density in dust layer

r_d : dust layer resistivity

E_{ds} : breakdown field strength of dust layer

In order to prevent back corona, whether i_d or r_d should be lowered.

Hot side electrostatic precipitators [1,3] and gas conditioning [1,4-8] are aimed to lower r_d. These are already used in many practical plants. However, they are not always effective and occasionally cause the unexpected troubles. Moreover the installation cost and the running cost are another problem.

On the other hand, pulse energization is a method of lowering the ionic current density, i_d, with keeping uniformity of its distribution in the entire collection electrode. A pulse voltage with a very high peak

voltage can produce very uniform corona in the entire corona electrode without causing a spark due to its very short duration time. The current density is controlled by its repetition frequency, F_p. It also enhances peak field strength between the corona and the collection electrodes and particle charging. Pulse energization is purely an electrical means so that its counter effect to the total system such as relocation of a precipitator, a harmful chemical product, increase of a pressure loss, and so on becomes smallest. Moreover, the control capability increases.

However, its applications to the practical plants are not many. This is probably because its evaluation is not certain, and its initial cost is not competitive yet. Pulse energization is still an introduction stage.

1-2. Classification of Pulse Energization Systems

The use of pulse energization for enhancing the collection performance of electrostatic precipitator was firstly proposed by H. White in 1952 [9]. Although his work was brought to full scale field tests with a prototype pulser, the lack of reliable pulser elements prevented a further commercial development.

Since 1970's, intensive works have been made to develop the pulse energization systems to the practical application [10-33]. In Table 1.1 is shown the classification of the pulse energization systems proposed so far.

The first type shown in Table 1.1 is a semi-pulse concept by controlling the primary current of the high voltage transformer to energize intermittently, resulting a milisecond pulse like voltage wave form. The power consumption is reduced in proportion to decrease in duty ration. This acts more like a conventional dc energization and its effect to correct back corona is small. However, it is now widely used and becomes almost standard because of the very small retrofitting of the controller of the primary current and the energy saving effect.

A shorter pulse with less than several hundreds microseconds duration time is produced by switching to deliver charge stored in a pulse forming condenser to the precipitator load. There are many pulse energization systems proposed which are classified by the following three categories:

- pulse voltage coupling means, (use of separate dc power supply or not)
- corona electrode configuration, (twin-electrode or tri-electrode; and conventional corona electrode or elongated corona electrode)
- high voltage switch, (thyristor or spark gap)

In order to superpose a pulse voltage on a dc bias voltage, a coupling means is necessary where a pulse voltage and a dc voltage are supplied from the separate power supplies. In this case, a coupling condenser is usually used and a pulse transformer with insulation capacity of a dc bias voltage is also usable. The concept of the direct coupling by supplying a dc components from the pulser is shown to be also applicable to the practical precipitators.

In the electrostatic precipitator, the electrode configuration is usually a twin-electrode type in which corona wires supported by the frame are placed at the middle of the parallel duct. The load characteristic of this standard type of a precipitator in the case of the pulse energization is a lumped constant circuit of a large capacity with a parallel resistor due to corona loss. If the corona wires are connected in series to form a long corona line and a very short pulse voltage is applied, the load characteristic becomes a distributed constant circuit with a surge impedance determined by the corona wire and the parallel duct.

In the case of tri-electrode system, the third electrode is placed close to the corona electrode. The pulse voltage is applied between these two electrodes to produce coronas resulting a smaller pulse voltage necessary and its direct coupling possible by placing the pulser on the dc bias potential. However, the electrode configuration becomes very complicated.

As for the switching element, a thyristor or a spark gap is usable for this purpose. A thyristor has advantage in controllablity and a spark gap in the cost. A spark gap can produce a very fast rising pulse with less than 1 μs of the rise time but a thyristor in the present stage more than 10 μs.

Table 1.1 Classification of Pulse Energization Systems of Electrostatic Precipitator

	Coupling	Switch	Electrode Configuration	Pulse Width
Pulse Energization (Pulse-Forming Condenser + High Voltage Switch)	Direct	Spark Gap	Conventional	Submicrosecond
		Thyristor	Conventional	Microsecond
	Condenser Coupling (Pulse Trans-former)	Spark Gap	Conventional	Submicrosecond
			Twin-Electrode Long Corona Line	
			Tri-Electrode Long Corona Line	
		Thyristor	Conventional	Microsecond
			Tri-Electrode Lumped Constant	
Semi-Pulse Energization (Primary Current Contral)	Direct	Thyristor	Conventional	Milisecond

1-3. Outline of Author's Work

The author realizes the supriority of a spark gap in producing a fast rising pulse and simplicity of its arrangement and has been made an intensive work to build the pulse energization system using a spark gap. The uniformity of corona and the threshold of a sparking voltage is related to the pulse rising time and the duration time. The shorter of the pulse rise time, the better in uniformity and in increase of the threshold. As a result the fast rising pulse is expected to give the upmost play of pulse energization. Considering these conditions and its practical applications, a submicrosecond rise time is preferable but at least it should be less than 2 - 3 μs. Such a fast pulse rise time with a very high peak current can not be produced by a thyristor. Moreover, the cost of a spark gap becomes smaller than a thyristor switch because many thyristors should be assembled in series to make a switch for the pulse energization system.

The tri-electrode system of the corona electrode has many advantages. However, the electrode system is so complicated that its application to the practical plants is difficult. The author made a fundamental research on the tri-electrode system but the reason above prevented the further research.

The developmental work treated in this thesis is concerning novel pulse energization systems of the combination of the twin-corona-electrode and a pulser using a spark gap as shown in Table 1.1. The contents of the following chapters are:

Chapter 2 : Four pulse energization systems are developed in the laboratory using a clean electrode system with full scale dimensions The experimental data on their corona characteristics are shown. The most elegant system in these is the condenser coupled traveling wave pulse energization which uses a traveling corona

on an elongated corona transmission line. However, as the demand of the use of the conventional construction of the corona electrode is very large, the pulse energization which can be applied to the conventional systems are developed. The direct-coupled pulse energization the author finally arrived is the simplest system and has the potential of the smallest initial cost in all the pulse energization systems.

Chapter 3 : The collection performance of the direct-coupled pulse energization is tested in two series of tests in the laboratory. The effectiveness for back corona correction and the enhancement of collection efficiency is confirmed.

Chapter 4 : The pulser module to be installed in the practical plants is developed based on the direct-coupled pulse energization concept. It is designed to be inserted between the existing dc power supply and the electrostatic precipitator. The designing process and the test results by the simulated load are shown.

Chapter 5 : Two series of field tests of the direct-coupled pulse energization are made. Its effect on back corona correction in the practical plant is confirmed. However, its limit in coping with a space charge trouble and an extremely high resistivity dust is also obtained. These valuable data obtained in these series of fields tests are shown with their analysis.

Chapter 6 : Conclusions

CHAPTER 2. CORONA CHARACTERISTICS OF PULSE ENERGIZATION

2-1. Introduction

Most of existing electrostatic precipitators are the twin-electrode type comprizing of parallel collection ducts and corona wires placed at the middle of ducts. Corona wires are attached on the rigid frame supported by high voltage insulators and negative high voltage is applied to produce corona as an ion source and to form electric field between the duct and the wire as a charging and collection field. As the result, load characteristics of electrostatic precipitators are expressed by the lumped constant circuit of capacity, C_{EP}, and a non-liner corona resistance, R_c, in parallel in both cases of conventional dc energization and pulse-energization.

If the corona electrode is replaced to form a long corona line and a very short-circuited pulse voltage is used, the load characteristics can be changed to the distributed constant circuit of the surge impedance, Z_0. In this case, the pulse voltage propagate in a form of a traveling wave and an effective conversion into corona discharge of the pulse energy, concentrated in a traveling wave packet and not distributed along the total length of the wire in a form of capacitive energy, is possible. As a result, the capacity of the pulse generator can be minimized. This type of pulse energization ("Condenser-Coupled Traveling-Pulse Energization") is treated in the paragraph 2-2.

Traveling pulse energization can not be used for the existing electrostatic precipitators and the demand for the retrofitting application is very large. The use of pulse forming resistor placed in parallel to the electrostatic precipitator is one method to apply a pulse voltage to the

capacitive load. But the most of the pulse energy is wasted in this resistor and the cost-effective pulse energization can not be expected. The use of pulse forming feeder line placed between the pulse generator and the electrostatic precipitator is a better method. In this case the voltage wave reflection at the end terminal of the feeder line (capacitive short terminal) which is the inlet terminal of the precipitator is used ("Condenser-Coupled Feeder-Formed Pulse Energization"). Here again a sub-microsend pulse can be applied. Another method is the use of LC oscillation between the capacity of the pulse generator and the load capacity of the precipitator ("Condenser-Coupled LC-oscillatry Pulse Energization"). The first cycle of the oscillation acts as a submicro-second pulse. These two methods are treated in the paragraph 2-3.

In these three types, the dc bias voltage is supplied by another power supply and the pulse voltage is applied through the coupling condenser. The use of two power supply and the coupling condenser results in a higher initial cost, although both the ionic current density and the field intensity can be controlled. The author finally comes to the most simple method of "Direct-Coupled Pulse Energization" where the coupling condenser is took off and the pulse generator is directly connected to the electro-static precipitator. Here again the most cheapest pulse forming method of LC oscillation is used. The distributed charge on the inter-electrode capacity of the precipitator from the pulser condenser plays a role of a dc component. As the result, one power supply operation becomes possible. This is treated in the paragraph 2-4.

In this chapter, test results of corona characteristics of each pulse energization in the clean electrode system of a full-scale duct is treated. Corona characteristics are very important factor of precipitator operation and back corona correction. The parametric study gives the information of the pulser design.

2-2. Condenser-Coupled Traveling Pulse Energization

2-2-1. Introduction

An extremely short pulse high voltage with several hundreds nanoseconds duration time proceeds in a form of a traveling wave along a corona transmission line consisting of an elongated corona wire and conventional grounded duct of collecting electrodes and produces streamer coronas as a plasma ion source uniformly distributed on the line. A rough criterion of a pulse voltage to behave as a traveling wave is given by:

$$L > 0.3 \times T_h \qquad \text{-----(2.1)}$$

where

L : length of corona electrode or corona transmission line

T_h : pulse duration time in nanosecond

0.3 m/ns : pulse voltage propagation velocity assumed

The pulse energy supplied from its source is localized in a traveling wave packet occupying only a fraction of the line, and is used only for producing of electron avalanche in a form of negative streamer coronas. Streamer coronas cause wave form modification in its leading edge in a predictable fashion. The subsequent energy required for separation of monopolar ions from the streamer plasmas and driving these towards the collection electrodes is supplied from the cheaper dc power source. This wave-mode injection of pulse energy from the source to the line enables the use of a much smaller pulse forming condenser in the pulse power supply. Moreover, the injection of power from the ac main into the pulse forming condenser of the pulse power supply with an energy-efficient ac charging mode becomes possible with a combination of rectifier and a phase-selective

synchronous rotating spark switch where the switching is made in the blocking period of the rectifier for avoiding rush current. All these factors make the construction and operation of the nanosecond-pulse power supply very cost-effective and energy-efficient.

In this paragraph are treated the results of investigations on the fundamental characteristics of the corona transmission line in the electrostatic precipitator including its corona current distribution, effects of pulse parameters on corona production, pulse voltage wave form modification, pulse peaking technology for the regeneration of pulse voltage after corona-induced erosion.

2-2-2. Experimental apparatus

A small experimental set-up illustrated in Fig. 2.1 is used for a detailed test of corona characteristics produced by an extremely short pulse voltage. Its electrode configuration is essentially the same as that of a large scale set-up shown in Fig. 2.2. The length of a corona wire in Fig. 2.1 is L = 40 cm but its dust spacing, p = 250 mm, is the same as in the second series of experiments made with the large test set-up (Case II). The lower plate has 15 probe electrodes, each with a 20 x 150 mm dimension, for measuring the distribution of corona current density in the direction perpendicular to the corona wire.

Fig. 2.2 shows the large scale set-up of a wire-to-duct type corona transmission line representing a single duct of an electrostatic precipitator with full scale dimensions. The corona wire consists of many stainless steel wire units, zig-zag arranged and series connected, each having a square cross-section (4 mm x 4 mm) and 8 m length, supported by a rigid frame at its both ends by insulators. Two series of experiments are performed with different total length of the corona wire, L : one with L =

106.4 m at a wire-to-wire spacing g = 200 mm using 13 wires (Case I) and another with L = 202.4 m using 25 wires at g = 100 mm (Case II). A dc base voltage is applied to the frame supported by the insulators, and a pulse voltage is applied on top of this dc voltage to the inlet end of the corona wire at the bottom. A duct spacing of p = 400 mm is used in the Case I, and p = 250 mm in the Case II so as to get a satisfactory pulse-induced corona discharge within the available range of dc and pulse voltages. In front of each wire unit three rectangular probe with 200 x 100 mm are attached on a collection plate at the left, center, and right positions, respectively to measure ionic current density. The pulse voltage wave form is measured by the high voltage probe (Pulse Electronics Engineering, Co., LTD. Type HV-50). The light activity of a corona spot is observed through a hole on the collection electrode using a photo-multiplier.

Fig. 2.3 illustrates a circuit diagram of the pulse power supply used, and its connection to the wire-to-duct corona transmission line of Fig. 2-2. Either a ceramic condenser or a coaxial cable is used as a wave forming element, the former producing a long-tailed pulse and the latter a trapezoidal pulse. It is charged through a rectifier, D, by an ac high voltage with a high charging efficiency, and discharged in the succeeding half cycle of its blocking polarity to the condenser coupled corona transmission line with the aid of the phase-selective synchronous rotating spark switch. This coupling condenser, C_1, is used to superpose the pulse voltage on the top of the dc bias voltage and its capacity should be large enough as:

$$C_1 > 10 \times T_h / Z_0 \qquad \text{-----(2.2)}$$

so that an undistorted pulse wave can be transmitted and the energy loss for dissipation of its accumulated charge remains small where T_h = pulse duration time and Z_0 = surge impedance of corona transmission line. The

surge impedance, Z_0, of the corona transmission line is determined experimentally by changing the magnitude of a resistance, R_4, terminating the line end to the ground, and observing the wave reflection from the end. No reflection occurs when $R_4 = Z_0$, and $Z_0 = 230$ ohm is obtained for both Cases I and II. A dc corona starting voltage is $V_c = -30$ kV in the case I (duct spacing p = 400 mm) and $V_c = -25$ kV in case II (p = 250 mm).

Throughout the present investigations the dc bias voltage, V_b, is set slightly below a dc corona starting voltage, V_c, so that only pulse-induced corona current is obtained ("back corona correction mode of operation [34]"), where $V_b = -30$ kV and -25 kV in Case I and II, respectively.

Three different wave forms are used: a sharp-rising moderate-duration pulse, a moderate-rising moderate-duration pulse, and an approximately trapezoidal pulse with a moderate duration. These are shown in Fig. 2.4.

The experiments are performed in room air at room temperature, with a pulse repetition frequency, $F_p = 50$ Hz.

2-2-3. Test Results by Bench Scale Unit

(A) Condition for Producing Pulse-Induced Negative Coronas:

Tests are made with the bench scale unit (Fig. 2.1) and the moderate-rising pulse to determine the condition for production of pulse-induced negative coronas, changing the dc bias-voltage, V_b, and pulse crest voltage, V_p. Fig. 2.5 shows a photograph of the streamer-like negative coronas appearing in this case. The hatched area in Fig. 2.6 indicate a region in which the pulse-induced negative coronas are produced on the entire length of this short corona wire. The horizontal line D represents the inception voltage of dc coronas, V_c. The threshold curve C in the figure indicates a significant effect of the dc bias-voltage, V_b, to enhance the pulse-induced negative corona by raising a local field on the

wire edges. Coronas can be induced at a comparatively low pulse voltage so far as V_b be kept close to V_c.

(B) Transverse Distribution of Ionic Current Density:

Fig. 2.7 indicates the transverse distribution of the ionic current density on the plane electrode in the direction perpendicular to the corona wire. Effects of V_p are examined in Fig. 2.7 with changing V_p in the formation region of pulse-induced negative coronas (see Fig. 2.6). An adequate level of current density is obtainable as far as V_p is in this region. The pattern of the current distribution remains unaltered, and it has a rather broad and symmetric range with a small dip at its center.

2-2-4. Test Results by Full Scale Unit

(A) Longitudinal Distribution of Ionic Current Density (under Matched Terminal Condition):

The longitudinal distribution of ionic current density on the plate electrode in the direction parallel to the corona wires is measured with the full scale unit of Fig. 2.2. Of special interest is the effect of the position-dependent change of pulse voltage, V_p, due to corona-induced attenuation, and reflection-induced peaking. This change is originally to be predicted from the data shown in Fig. 2.7, but there is some deviation due to many local weak spots existing on a long corona wire which produce coronas at lower levels of V_b and V_p. The investigation of the longitudinal distribution or decay of the ionic current distribution has a special importance for proper selection of the pulse parameters, V_p and T_h, as well as the design of the pulse power supply.

The wave form of ionic current detected by one of the current probes attached on the collection plate is shown in Fig. 2.8. A pulse-induced

first spike is followed by the displacement current by moving ion clouds with several milliseconds of duration time. This is determined by recombination of streamer plasmas and ion transition [35]. So far as the current pulse is concerned, its duration is independent of the voltage pulse duration.

Figs. 2.9(a) and (b) indicate for the Case I (L = 106.4 m; p = 400 mm) and Case II (L = 202.4 m; p = 250 mm) a distinct uniformity in light activity of the pulse-induced streamer-like negative coronas along the entire length of the long corona wires, appearing under a proper selection of V_b and V_p, whereas the negative dc coronas indicate a poor uniformity in its light activity along the wire even at a much higher level of average dc field, $\overline{E_{dc}}$ = -2.5 kV/cm (Fig. 2.9(c)). The current density on the plane electrode by the pulse-induced coronas indicates a concurrent remarkable uniformity in the longitudinal direction of the transmission line even at a very low current level, as shown in Fig. 2.10(a) (see Fig. 2.9(b)). Fig. 2.10(a) is measured under non-reflection condition with the end of the corona transmission line terminated with a resistance equal to its surge impedance (matched terminal). Fig. 2.10(b) indicates a very irregular distribution of the current density specific to the dc-induced negative coronas at a reduced overall current density, i, which is obtained at an even higher level of E = -3.5 kV/cm. This great improvement of current distribution provides the pulse-energization with distinguished features of improved particle charging and back corona correction.

Fig. 2.11 shows the effect of the pulse crest voltage, V_p, at the inlet on the longitudinal distribution measured with the sharply rising pulse with T_h = 400 ns. No appreciable difference appears in the range within x = 40 m from the pulse inlet, but it becomes more and more pronounced with distance in the downstream range. The curves at V_p less than -50 kV indicate a sharp drop, whereas that at V_p = -60 kV shows a much smaller decay in this particular case. The critical pulse voltage estimat-

ed from Curve C in Fig. 2.6 for V_b = -25 kV is V_p = -37 kV, which may provide a clue for understanding this difference. Note that not only in Fig. 2.11 but also in Figs. 2.12 and 2.16 shown later, the ionic current density measured are subject to statistical scatters and the curves shown indicate the rough decay characteristics of ionic current density.

Fig. 2.12 shows an effect of pulse duration time, expressed in its half-tail, T_h, on the longitudinal distribution of the ionic current density measured with V_b and V_p kept constant. Narrow pulses with $T_p < 200$ ns indicate a rapid drop in current density curve, whereas the curves for $T_h > 300$ ns show only a small decay in this particular case. The importance of using a broader pulse duration for getting an uniform current distribution is clearly recognized from Fig. 2.13.

(B) Pulse Voltage Wave Form Distortion:

Even with no dc bias voltage and a reduced pulse voltage, pulse voltage wave form modification takes place where no corona occurs. Fig. 2.13(a) indicates the results obtained with a wire-to-duct transmission line (case II) using a condenser-produced moderate rising pulse with T_r = 150 ns. An external trigger from the pulse at the line inlet is used to start the horizontal sweep, and the time origin is calculated assuming the pulse velocity to be c =0.3 m/ns. The part of wave forms before this time origin are considered as the parasitic components due to electro-magnetic coupling between different arms of the corona wire. The parasitic waves are induced on the adjacent wire arms both upstream and downstream, and the induction at the upstream are produces a faster signal in front of the main wave.

Fig. 2.13(b) shows the modification of pulse voltage wave form measured with the same wire-to-duct line (case II), using a condenser-produced fast rising pulse with T = 30 ns. The rising part of the pulse containing much high frequency components is greatly distorted in the

course of propagation. This is likely to be due to a rapid attenuation of the components beyond 2 MHz as a result of the skin-effect enhanced resistance loss in the line. The lowering of the rise time ceases when T_r = 120 ns is reached. It is concluded that the pulse with T_r = 120 ns is to be preferable for this type of pulse energization.

By raising either V_p or V_b, or both, up to a moderate level, the negative streamer takes place from the edges of the corona wire. The negative streamer induced wave distortion is shown in Fig. 2.14. The negative streamer erodes the region ahead of the pulse crest voltage. Fig. 2.15 shows the light signal from the negative streamer detected by a photo-multiplier tube as shown in Fig. 2.2. The photo signal induced by the negative streamers begins to develop after V_p reaches to the level of V_t which corresponds to the erosion starting point in Fig. 2.14 and also to the threshold of the corona formation region in Fig. 2.6 (V_p = -30 kV at V_b = -25 kV). These facts indicate that the negative streamer occurs at the leading edge of the pulse and erode this region little by little in the course of the propagation.

(C) Calculation of corona loss:

We consider a simple case when no reflection occurs. The power of a forward traveling wave at an arbitrary position x and time t is given by :

$$P(x,t) = V(x,t) \times I(x,t) \qquad \text{-----(2.3)}$$

Therefore, the pulse energy, w(x), carried by a single wave in the forward direction is:

$$W(x) = \int_T P(x,t)\, dt = 1/Z_0 \int_T V(x,t)^2\, dt \qquad \text{-----(2.4)}$$

where T : pulse period

The energy converted to the corona loss in a region between x_1 and x_2 is:

$$\text{Corona Loss} = W(x_1) - W(x_2) \qquad \text{-----(2.5)}$$

This corona loss can be estimated from the measured voltage wave form distortion.

The corona loss by the negative streamer per unit length of a corona wire is in the range of 0.001 - 0.002 J/m. In spite of the low energy consumption, the ionic current obtained is enough for its large-scale operation. This is because the pulse power is consumed only for triggering the negative streamers, and the succeeding substantially higher power required for separating and driving monopolar ions is supplied from the dc power supply.

(D) Effective Pulse Energy for Corona Production:

In the previous sections, the effects of T_h and V_p on the longitudinal decay of the ionic current density, and the wave form distortion by the negative streamer are shown. These facts lead to an assumption that only a fraction of the pulse energy localized in its top area above the critical corona inception level, V_t, can be effectively converted to streamer production energy. This energy, referred to as the "Effective Pulse Energy" and denoted by W_e, may provide a crude figure of merit for evaluation of the pulse voltage with different wave forms in terms of its corona production ability. The magnitude of W_e can be calculated from the following equation:

$$W_e = (1/Z_0)\int_{t_1}^{t_2} V(t)^2 dt - (V_t/Z_0)(t_2-t_1) \qquad \text{-----(2.6)}$$

where

$V(t)$: instantaneous pulse voltage at the inlet

$I(t)$: instantaneous line current at the inlet

t_1, t_2 : $V(t_1) = V(t_2) = V_t$

Z_0 : line surge impedance

The longitudinal decay of ionic current density measured with three different pulse voltages shown in Fig. 2.4 with the variation of V_p and T_h are plotted in Fig. 2.16 using the calculated value of W_e as a parameter. It can be seen that W_e may serve as a crude figure of merit to give a rule of thumb estimation of different pulses, and that W_e beyond 0.8 J may provide a reasonably uniform current distribution along a major part of the line. This value, 0.8 J, is about 2 to 4 times of the energy loss estimated from the modification of the pulse wave form which amounts to $W_e = (0.001 - 0.002) \times L = 0.2 - 0.4$ J in this case.

2-2-5. Pulse Peaking Technology

The electrode design of Case I in Fig. 2.2 with L = 106.4 m represents the most practical wire-to-duct corona transmission line applicable to a large scale precipitator. In other words, the practical total length of the wire in a single duct of one collection filed is about 100 m. Hence, it can be seen from Fig. 2.16 that more than 3 series collection fields could be energized with a single pulse power supply when a pulse voltage with W_e larger than 1.4 J with $V_p > -55$ kV is used. Whereas the use of a lower pulse voltage with a smaller W_e is very preferable to reduce the cost of a pulse power supply, provided its rapid decay can be technically improved. Since the pulse voltage after losing its corona-producing ability still possesses quite a large energy in its remaining trapezoidal

area, there is a possibility of regenerating its corona-active crest region by a proper exploitation of this energy. One of the method is to raise the surge impedance in the downstream direction, either continuously or stepwise, to produce a "peaking" of the pulse voltage. The pulse energy at a lower potential level is transferred to a higher potential level with the aid of the momentum of traveling wave in such a way that a continuous or stepwise wave reflection occurs and is superposed to the original wave. The simplest method of the "pulse-peaking" is to use a total reflection at the line end with an open terminal and a partial reflection to be made at an intermediate position of the line by inserting an inductance element in series.

Fig. 2.17 shows the effect of the total reflection made by opening the line terminal. A large peaking occurs in a region close to the terminal, and the regenerated area extends towards the inlet with increasing pulse duration time. It can be seen that a combination of a longer pulse duration time $T_h > 460 - 500$ ns with an open-ended wire provides quite a large improvement even at a lower pulse voltage, $V_p = -45$ kV.

The step-wise pulse peaking is also tested by inserting an inductance with $L = 21\ \mu H$ in series to a 100 m long corona wire (Case I) at a position $x = 72.8$ m. Wave forms are observed at 4 points of the open-ended transmission line. The results with the dc bias-voltage removed are shown in Fig. 2.18. In Fig. 2.18 (a) ($x = 0$) and (b) ($x = 32.6$ m), the original wave, the partially reflected wave, and the totally reflected wave are clearly discriminated. In Fig. 2.18(c)($x = 65.4$ m) the partial reflected wave is superposed on top of the crest of the oncoming wave to produce a distinct "peaking" with a resultant crest voltage higher than its original one. The partial reflection causes a drop of pulse voltage in the region downstream of the reflection point to cause a dip in corona current distribution. Hence, a successive reflection using coils with increasing inductance or a backup by the total reflection at the terminal is required to

avoid this degradation. Fig. 2.18(d) shows the effect of such a back-up by the total reflection.

Fig. 2.19 indicates the change in the longitudinal distribution of ionic current by a combination of the partial and total reflection. Curve 1 represents a baseline with only a total reflection at the terminal. Curve 2 indicates an example of the improper selection of the partial reflection point where an inductance L = 21 μH is inserted at point A. The drop of current density after A is too large. Curve 3 represents a proper selection of the reflection point B where the drop is effectively compensated by the total reflection from the terminal, and the sag in Curve 1 at the center is corrected.

2-2-6. Conclusions

(1) "Formation Region" of the pulse-induced negative coronas is determined in a $V_b - V_p$ domain. The dc bias voltage, V_b, has a large effect of enhancing streamer coronas, and lowering the critical pulse voltage of producing a pulse-induced streamer coronas.

(2) An extremely short pulse voltage propagates in a form of a traveling wave along a corona transmission line, and produces streamer coronas very uniformly on the line. As the results, a very uniform distribution of current density even at a very low current density level, which is by far impossible by a conventional dc energization.

(3) A pulse loses its energy gradually during propagation owing to corona production, finally to become inactive so as no to produce coronas any more. As a result, a longitudinal distribution of the ionic current shows a decay towards the end of the line.

(4) Even in the absence of corona production the wave form modification takes place in the corona transmission line in the rising part of the

pulse containing much high frequency components beyond 2 MHz as a result of skin effect enhanced resistance loss in the wire. The parasitic waves induced by electro-magnetic coupling also produces wave form modifications.

(5) The negative streamer is launched at the front region of the pulse crest voltage, and erodes this region. The corona losses per unit length of wires due to negative streamers are 0.001 - 0.002 J/m in wire-to-duct corona line, estimated from the wave erosion.

(6) To get a satisfactory current density distribution, a pulse should have enough "effective energy", at least beyond 0.8 J for L = 200 m.

(7) A "pulse peaking" concept is tested and its effectiveness confirmed. A partial reflection by means of a peaking inductance and a total reflection by an open terminal are used for this purpose. A reflected wave is superposed on top of an oncoming wave to produce the peaking so that an inactive pulse after decay regains a high corona activity. This results in a more effective conversion of a pulse energy to the streamer production.

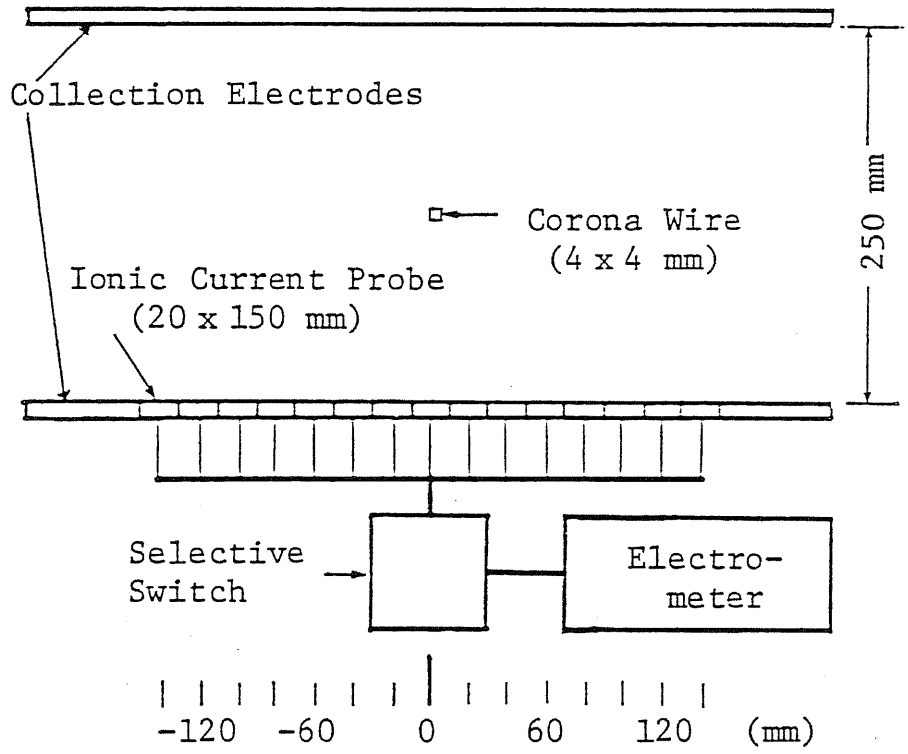

Fig. 2.1 Experimental Set-Up of Wire-to-Duct Electrode System in Bench Scale Unit (L = 400 mm)

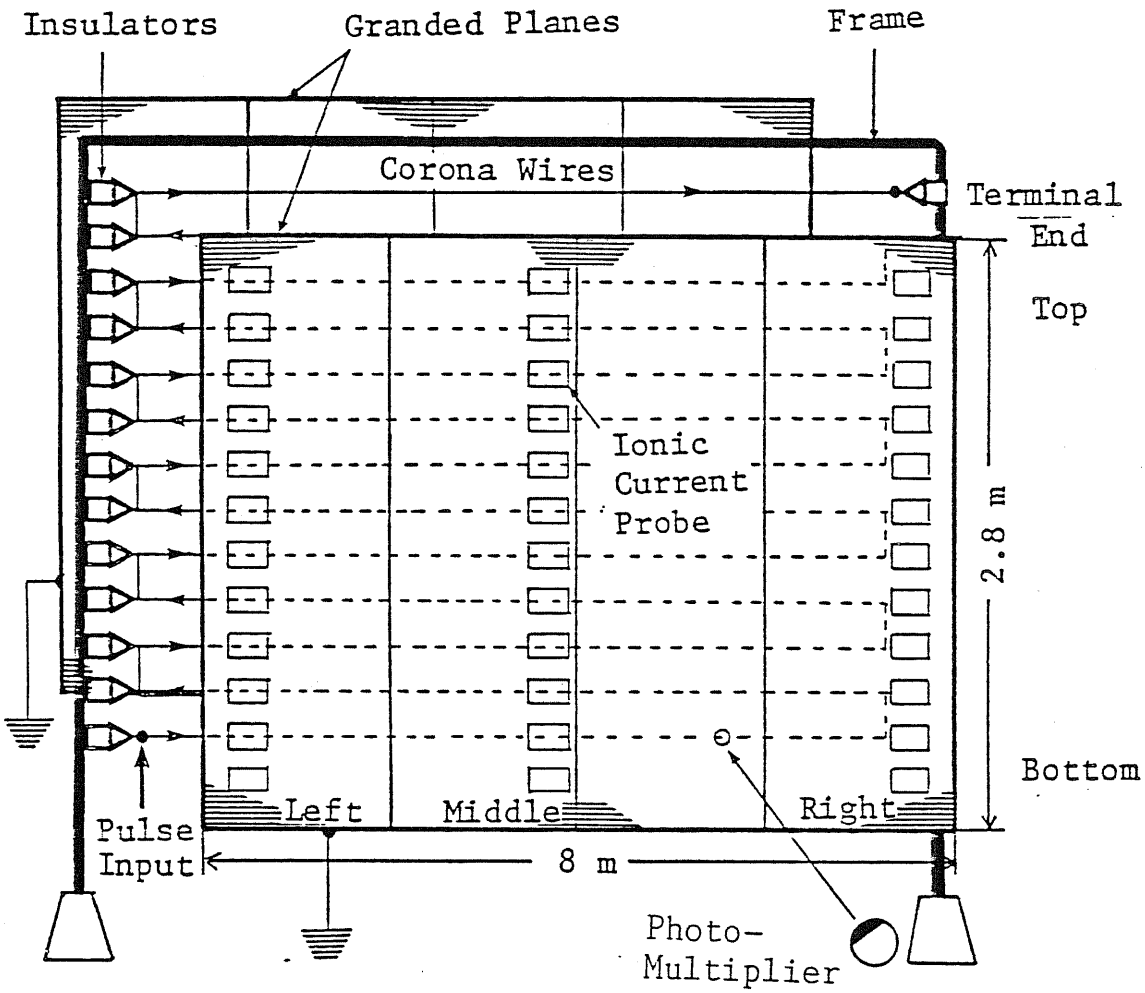

(case I) L = 106.4 m
p = 400 mm
g = 200 mm

(case II) L = 202.4 m
p = 250 mm
g = 100 mm

L : length of corona wire
p : duct spacing
g : wire-to-wire spacing

Fig. 2.2 Experimental Set-Up of Wire-to-Duct Corona Transmission Line in Full Scale Unit (surge impedance of the line = 23 ohm in both cases I and II)

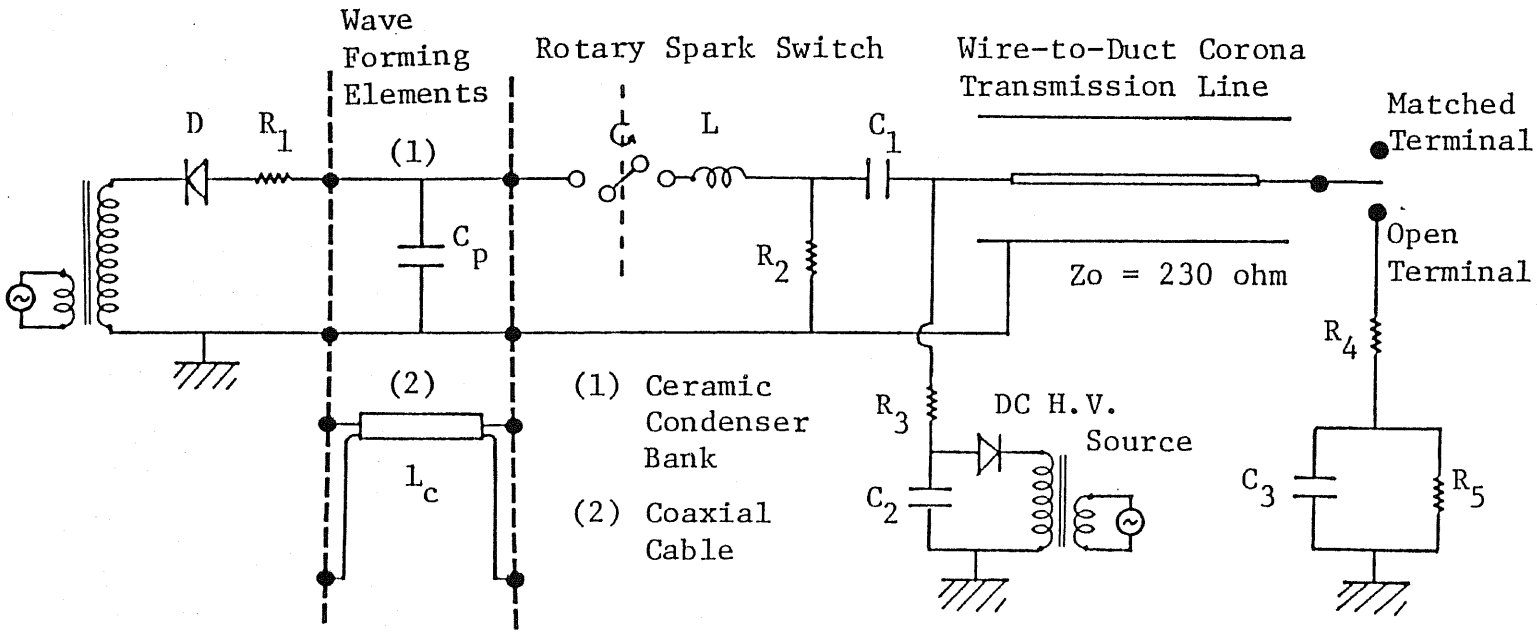

R_1 = 10 kΩ, R_2 = 100 kΩ, R_3 = 100 kΩ, R_4 = 230 Ω, R_5 = 100 MΩ,
C_p = 850 - 3400 pF, C_1 = 6.8 nF, C_2 = 1.5 μF, C_3 = 6.8 nF,
l_c = 7.5 - 50 m (50Ω), L = 2 - 10 μH,

Fig. 2.3 Pulse Power Supply and Its Connection to Wire-to-Duct Corona Transmission Line

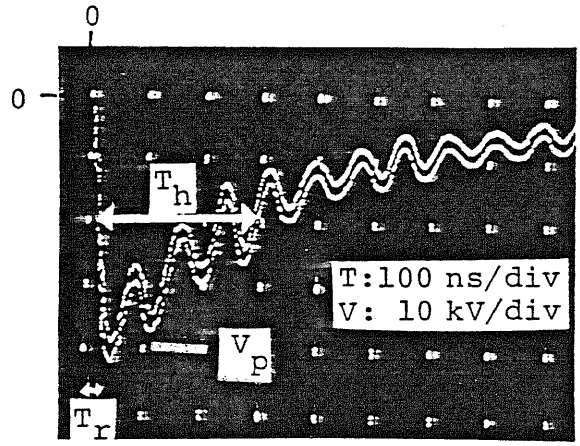

(a) Sharp Rising Pulse

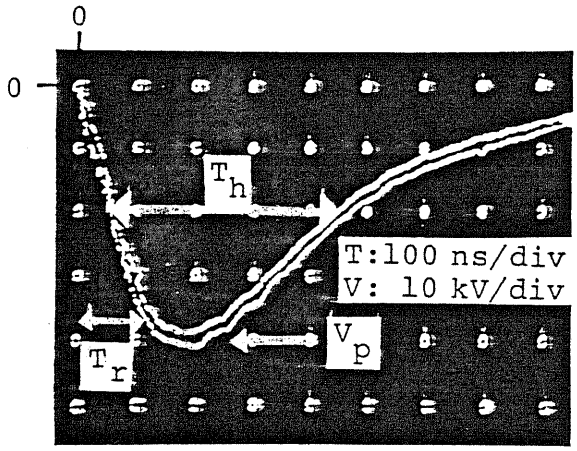

(b) Moderate Rising Pulse

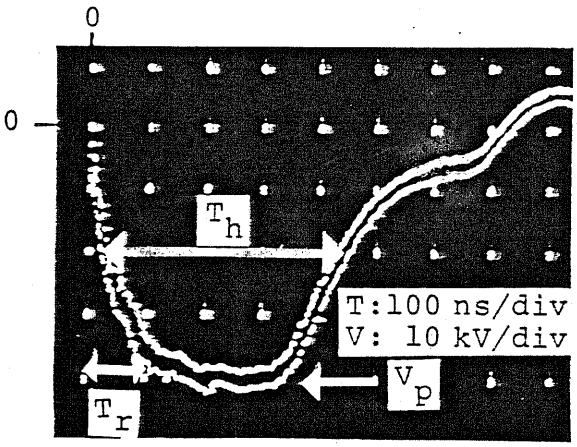

(c) Trapezoidal Pulse

Fig. 2.4 Pulse Voltage Wave Forms

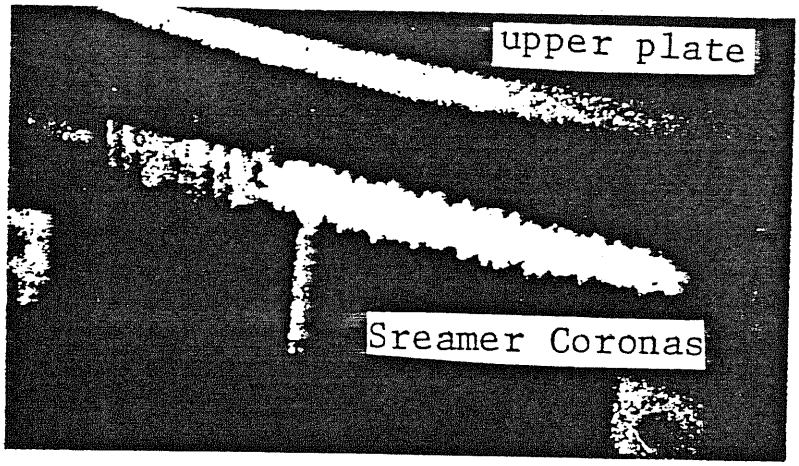

Fig. 2.5 Streamer Coronas Induced by Pulse in Bench Scale Unit (V_b = -25 kV; V_p = -50 kV; moderate rising pulse; T_h = 200 ns)

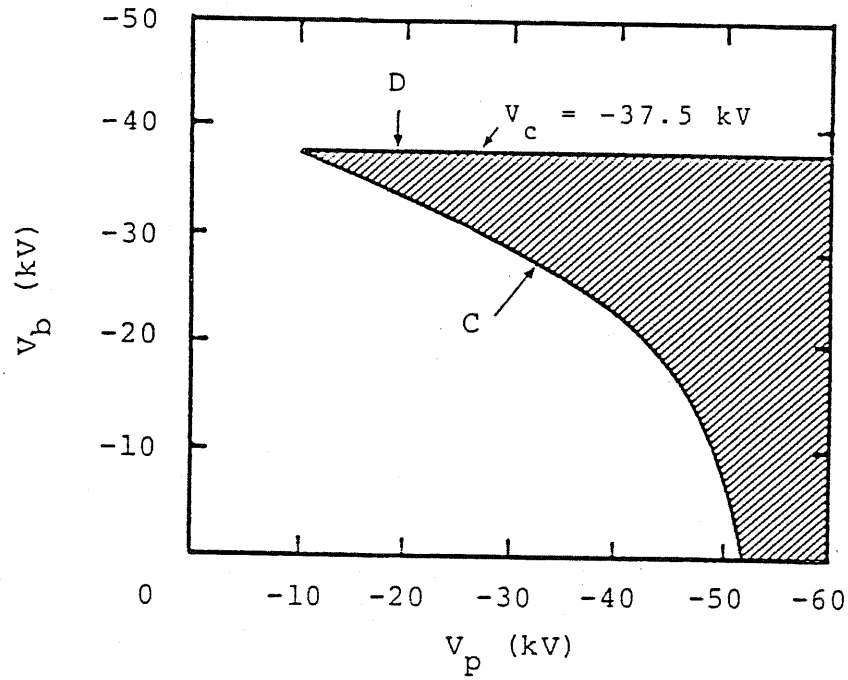

Fig. 2.6 Formation Region of Pulse-Induced Negative Coronas in V_b - V_p Domain (moderate rising pulse; T_h = 200 ns; p = 250 mm)

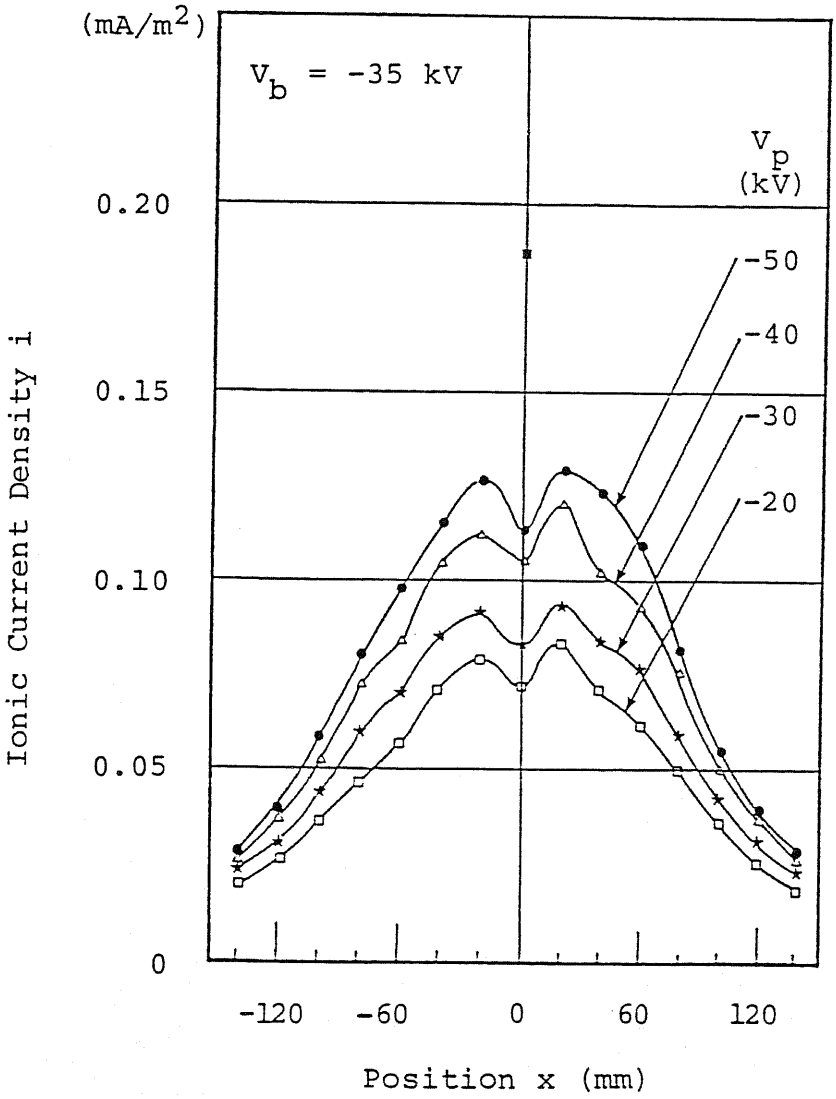

Fig. 2.7 Effects of V_p on Transverse Distribution of Ionic Current Density on Plate Electrode (moderate rising pulse; T_h = 200 ns; p = 250 mm)

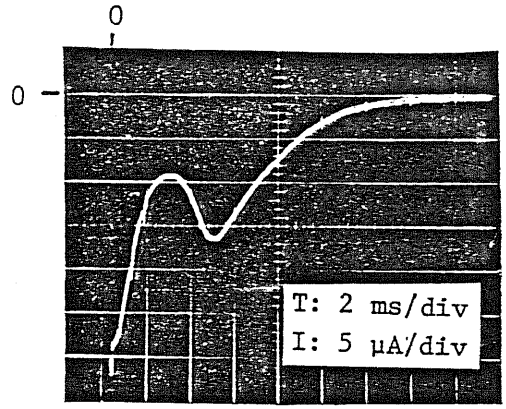

Fig. 2.8 Wave Form of Ionic Current on Plate Electrode (Case I; V_p = -40 kV; V_b = -30 kV; moderate rising pulse; ionic current probe = 200 x 100 mm)

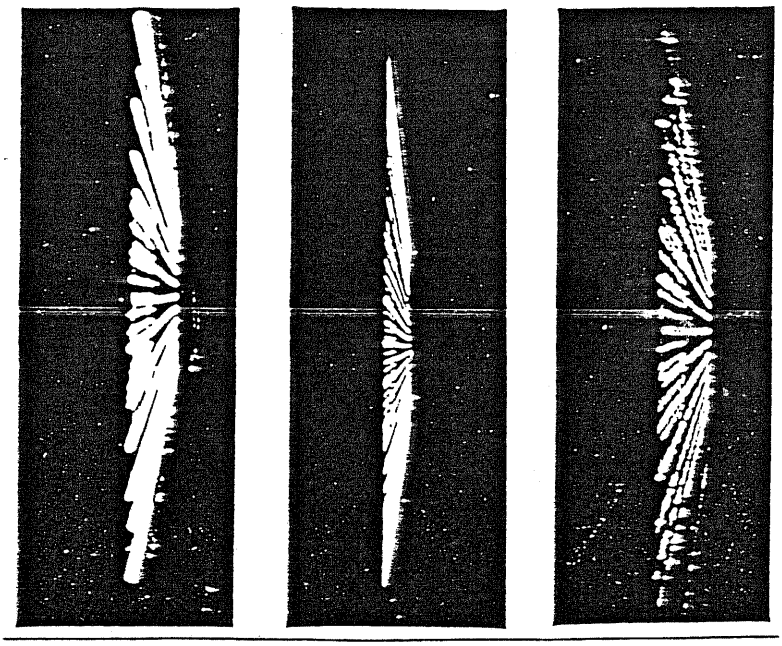

(a) Pulse-Energization (case I)
V_b = -30 kV, $\bar{E}_{dc}$ = -1.5 kV/cm, V_p = -40 kV

(b) Pulse-Energization (case II)
V_b = -25 kV, $\bar{E}_{dc}$ = -2.0 kV/cm, V_p = -50 kV

(c) DC-Energization (case I)
V_{dc} = -50 kV, $\bar{E}_{dc}$ = -2.5 kV/cm

Fig. 2.9 Uniformity in Light Activity on Pulse-Induced Corona As Compared to DC Corona

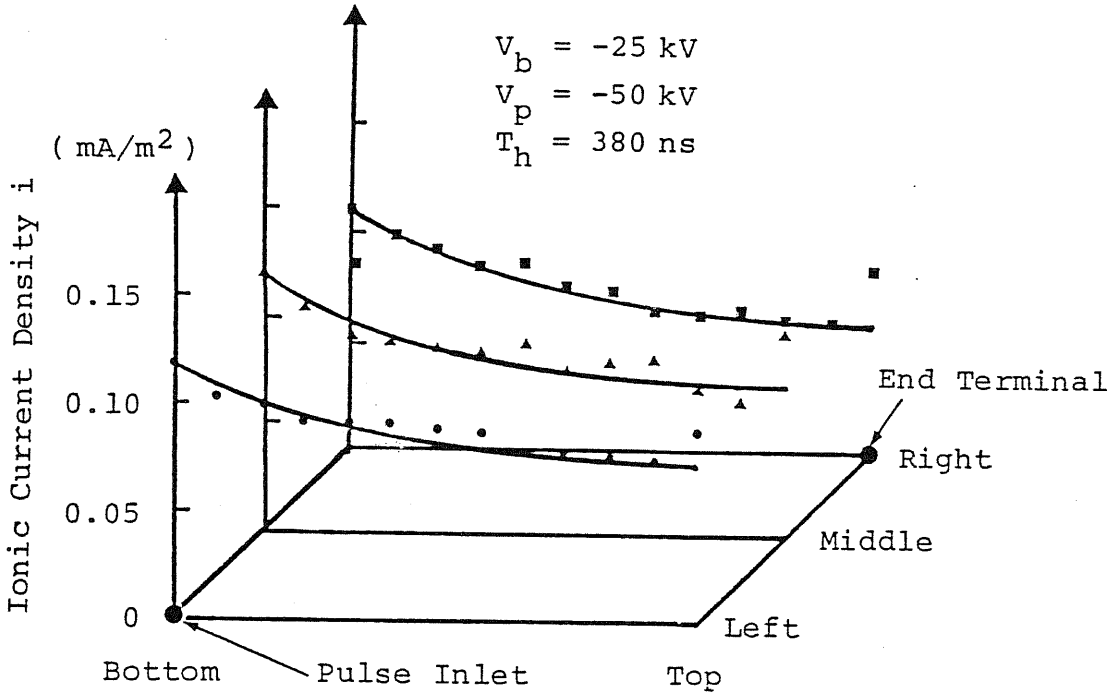

(a) Pulse-Energization (sharp rising pulse ; matched terminal)

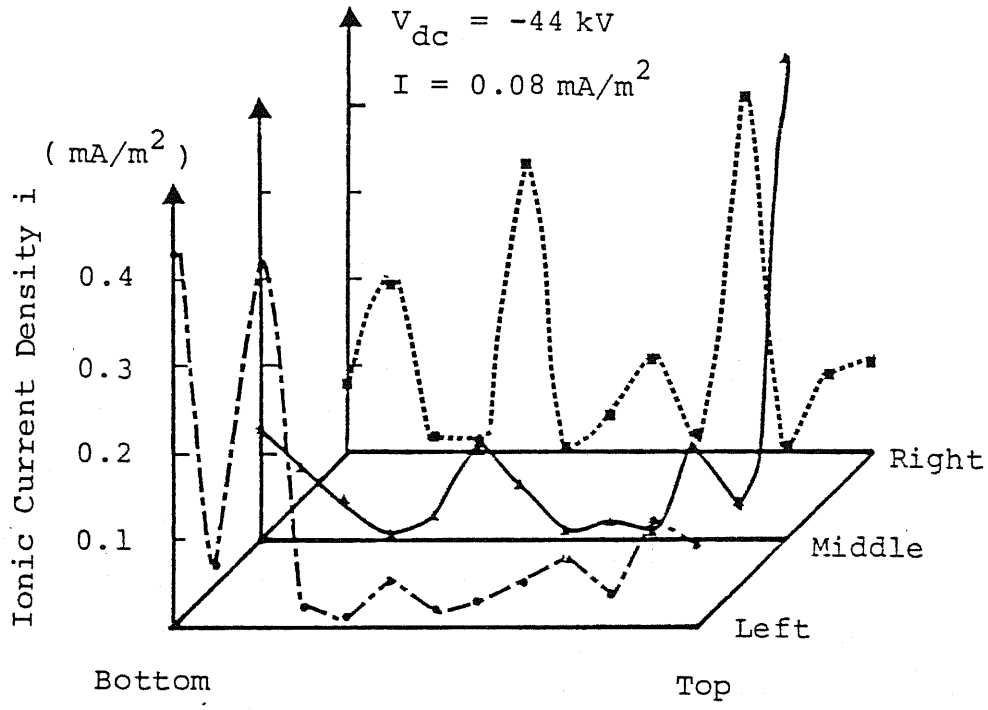

(b) DC-Energization ($\overline{E}_{dc}$ = -3.5 kV/cm)

Fig. 2.10 Ionic Current Density Distribution in Collection Plate (Case II; L = 202.4 m; p = 250 mm; g = 100 mm)

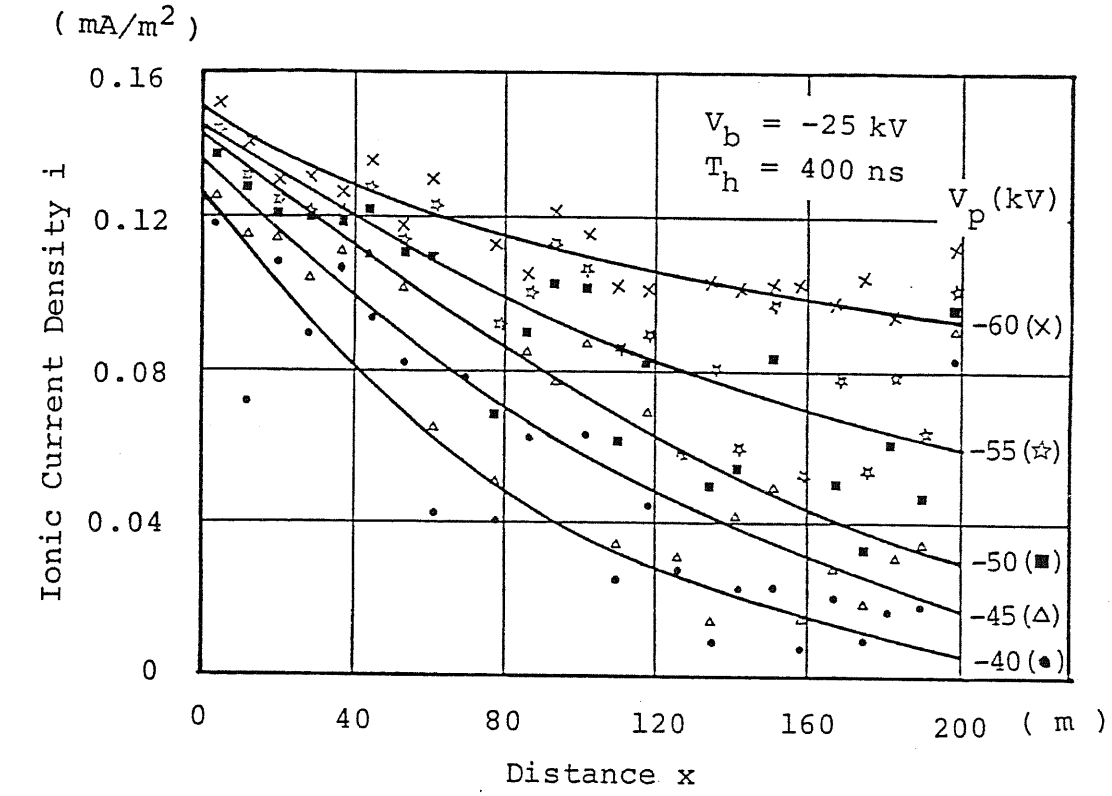

Fig. 2.11 Effects of V_p on Longitudinal Distribution of Ionic Current Density (Case II; sharp rising pulse; matched terminal)

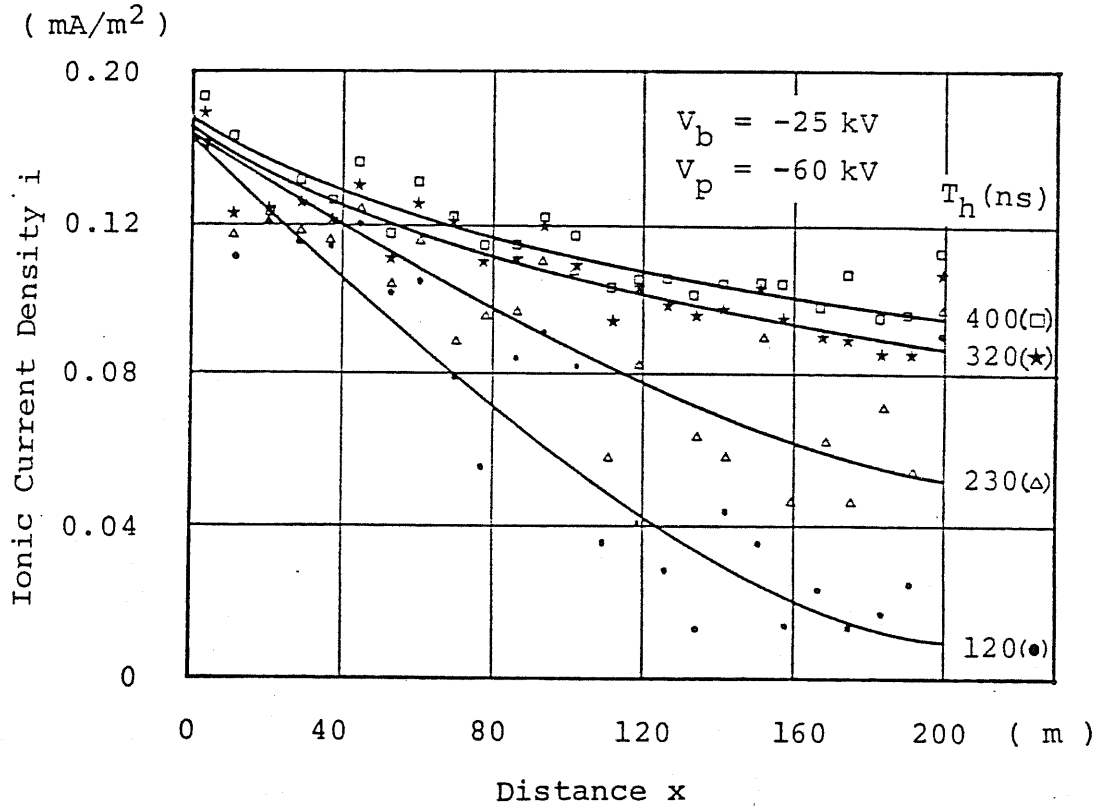

Fig. 2.12 Effects of T_h on Longitudinal Distribution of Ionic Current Density (Case II; sharp rising pulse; matched terminal)

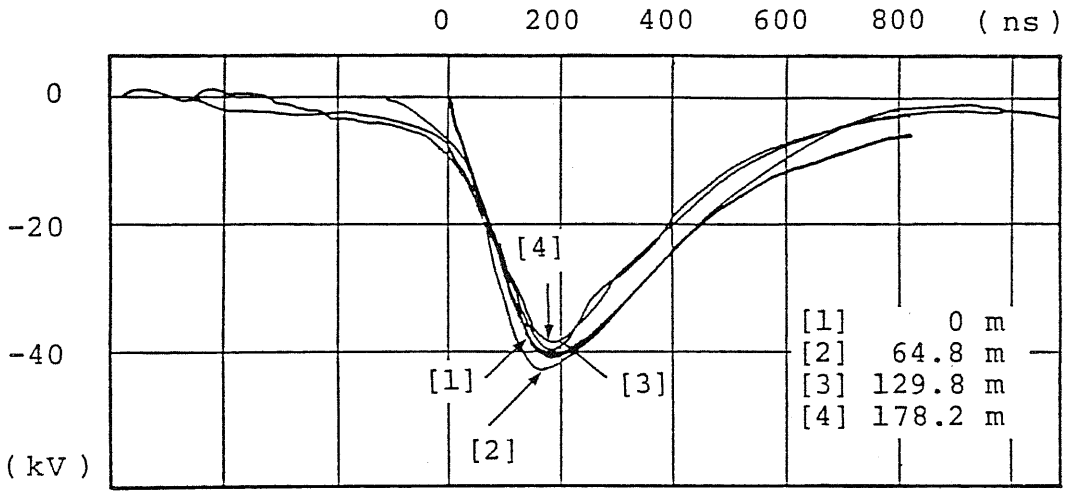

(a) Distortion due to Electro-Magnetic Coupling (Case II; V_b = 0 kV)

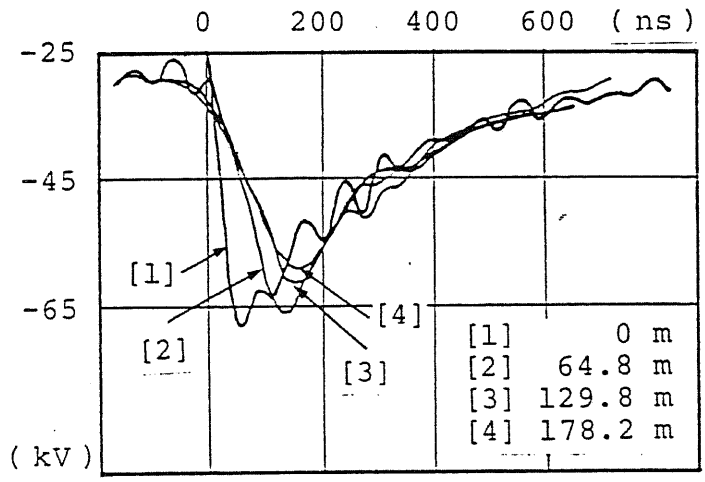

(b) Distortion due to Skin-Effect (Case II; V_b = 0 kV)

Fig. 2.13 Wave Form Distortion in the Absence of Coronas

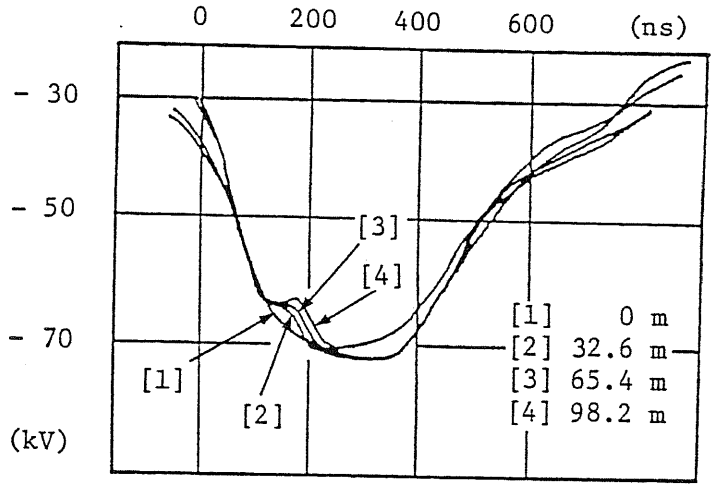

(a) Case I (V_b = -30 kV; T_h = 460 ns)

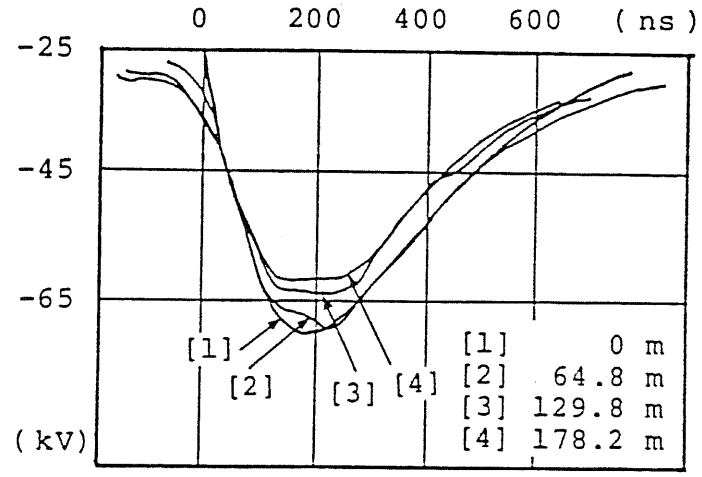

(b) Case II (V_b = -25 kV; T_h = 420 ns)

Fig. 2.14 Wave Form Distortion Caused by Negative Streamer

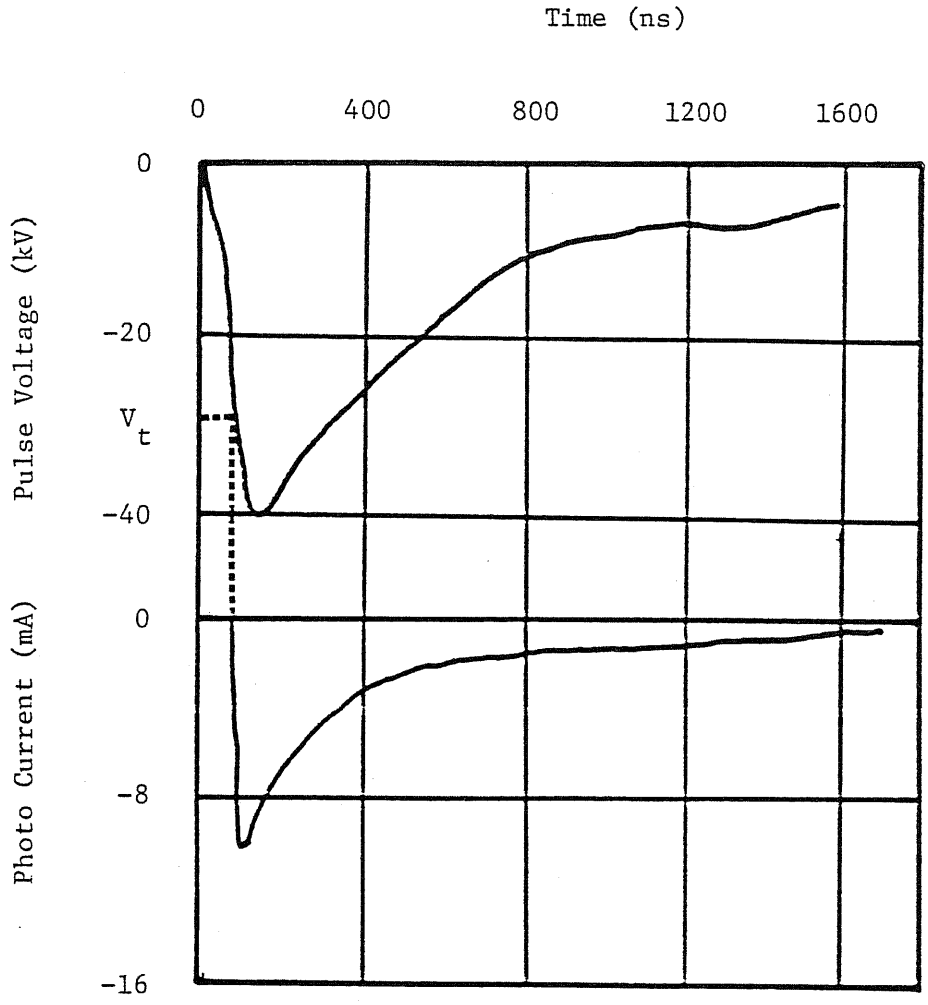

Fig. 2.15 Light Signal from Negative Streamer

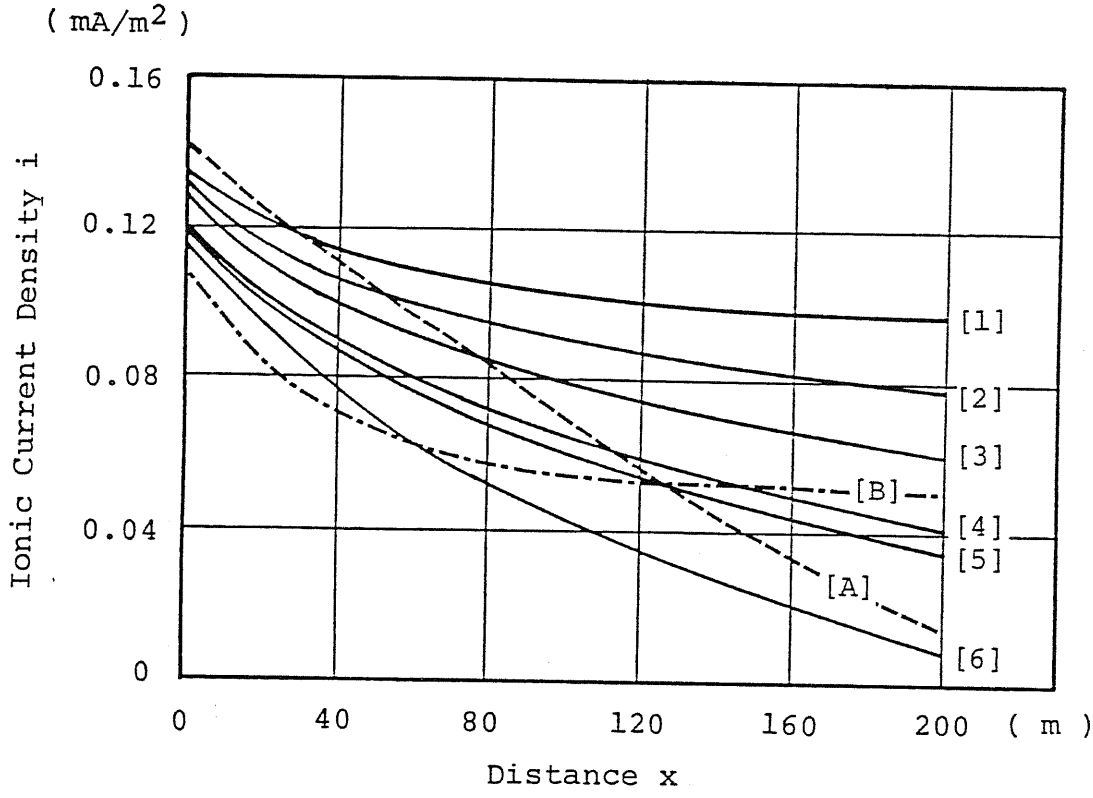

Key:

Curve	W_e (J)	V_p (kV)	T_h (ns)	
[1]	2.43	-60	390	
[2]	1.42	-55	390	
[3]	0.86	-50	390	Moderate
[4]	0.42	-45	390	Rising Pulse
[5]	0.37	-45	630	
[6]	0.26	-45	280	
[A]	0.38	-45	230	Sharp Rising Pulse
[B]	0.84	-45	560	Trapezoidal Pulse

Fig. 2.16 Effects of W_e on Longitudinal Decay of Ionic Current Density (Case II; V_b = -25 kV; matched terminal)

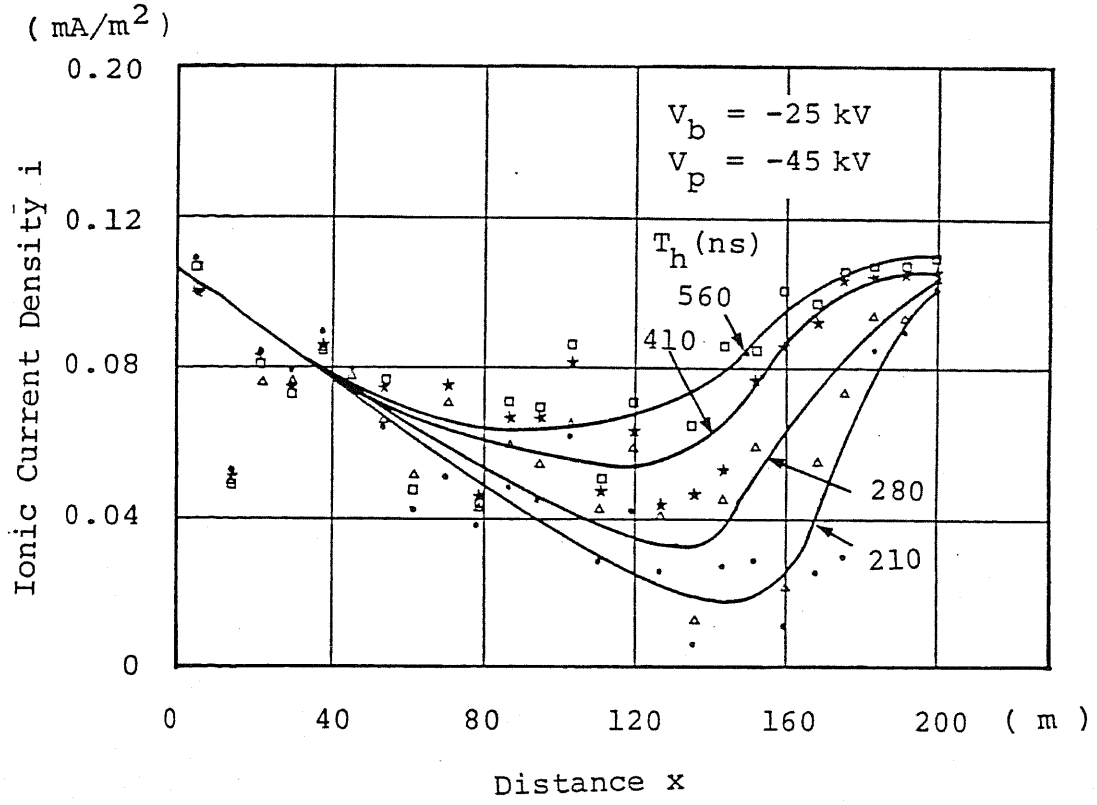

Fig. 2.17 Improvement of Uniformity in Longitudinal Distribution of Ionic Current Density with Total Wave Reflection at an Open Terminal (trapezoidal wave form; case II)

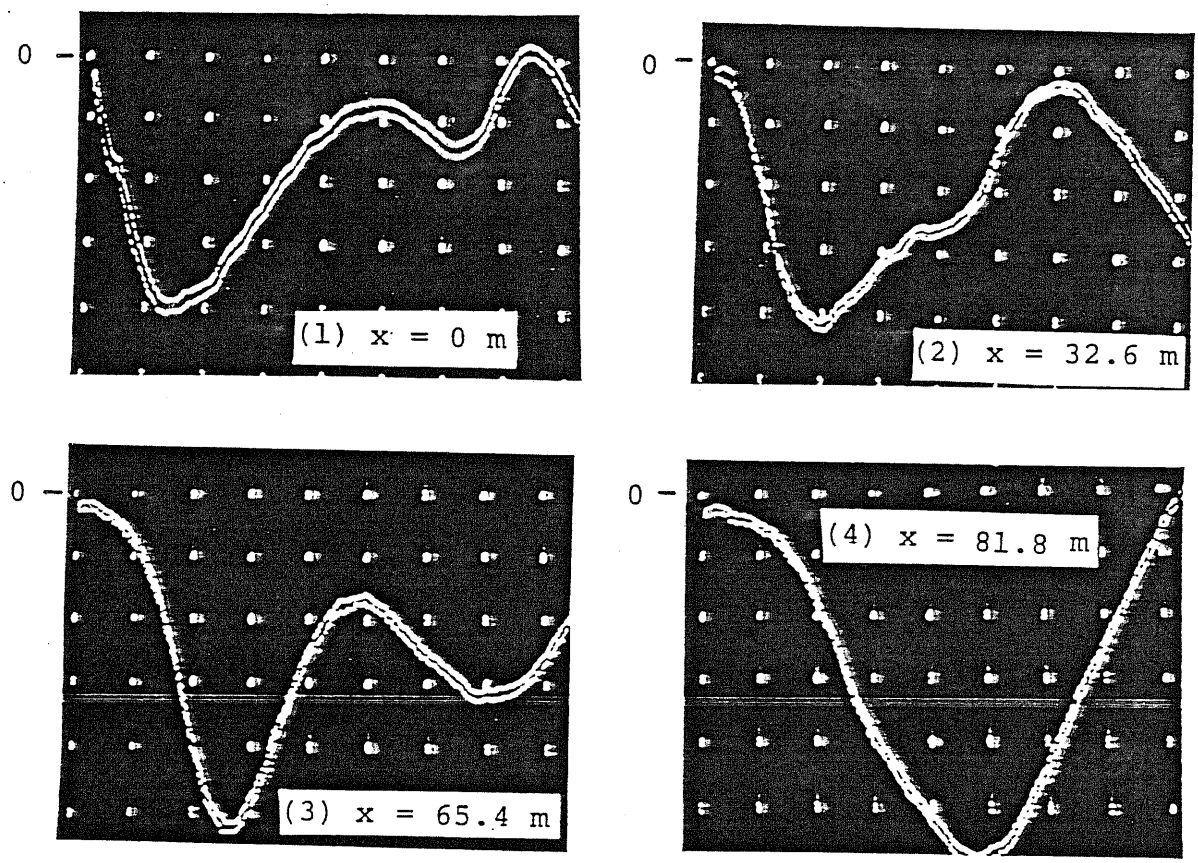

(T:100 ns/div ; V:10 kV/div)

Fig. 2.18 Pulse Peaking Using a Single Inductance and an Open Terminal (Case I; L = 106.4 m; V_b = 0 kV; moderate rising pulse; V_p = -40 kV; T_h = 260 ns; L_i = 21 μH inserted at x = 72.8 m)

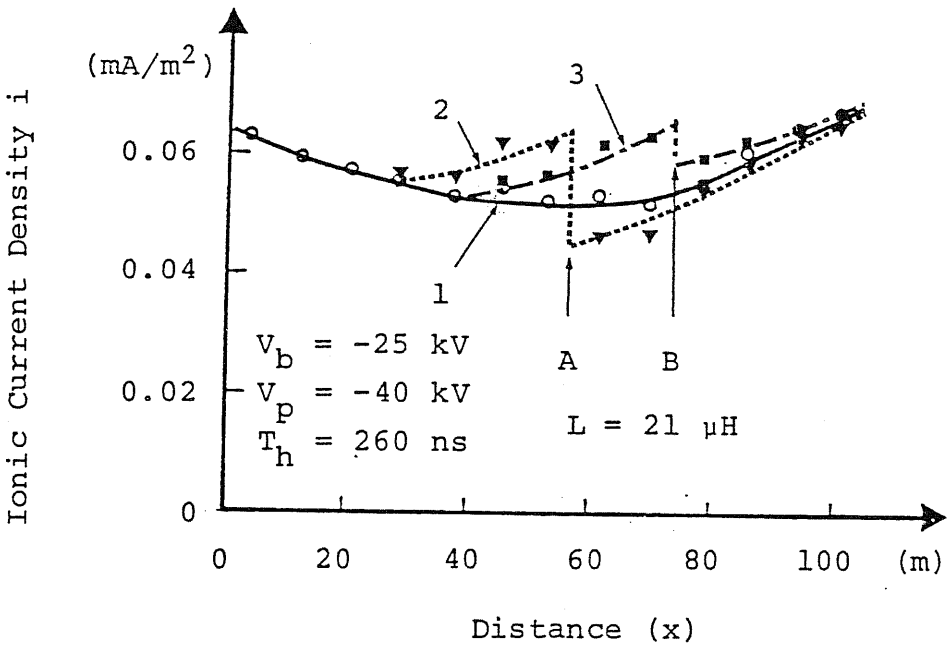

A, B : location of insertion of peaking inductance

Fig. 2.19 Effect of Pulse-Peaking on Longitudinal Distribution of Ionic Current Density (Case I; moderate rising pulse; V_b = -30 kV; V_p = -40 kV; T_h = 260 ns; peaking inductance L_i = 21 uH)

2-3. Condenser-Coupled Lumped-Constant-Circuit Pulse Energization

2-3-1. Introduction

There are many electrostatic precipitators suffering from performance degradation due to back corona problems. Therefore the retrofitting use without changing the precipitator construction is a very important application of pulse energization. In this case only the pulse power supply and its attachments are added. Even in a newly building precipitators the construction desgin is already confirmed and its drastical change is not easily accepted. So the pulse energization system to the conventional construction which is a lumped constant circuit as a load behavior should be developed.

The author take the note of the pulser developed for the traveling pulse energization and for the boxer-charger. It is out of only a pulse forming condenser bank and a rotating spark gap. Its simplicity and reliability is outstanding. Although the pulse impression to the capacitive load is not a easy matter, the author present two methods using this same pulser concept. One is the use of a pulse forming feeder, and another is the use of LC oscillation.

In the case of a feeder formed pulse ("Condenser-Coupled Feeder-Formed Pulse Energization"), a long feeder, its physical length longer than the wave electrical length (see Eq. (2.1)), is placed between the pulser and the electrostatic precipitator and the traveling pulse is produced on the feeder propagating toward the precipitator. At the feeder end terminal where the precipitator is connected, a wave reflection takes place. This can be modeled by the reflection due to the condenser short-circuited terminal. The proper selection of the feeder surge impedance, the traveling pulse shape, and the size of the precipitator to be energized, a pulse

with a submicrosecond rise time and a moderate pulse duration is obtained. As the result, a submicrosecond pulse energization can be possible.

In the case of a LC oscillatory pulse ("Condenser-Coupled LC-Oscillatory Pulse Energization"), the pulser is directly connected to the electrostatic precipitator through the coupling condenser. When the gap fires, LC oscillation takes places in the circuit of a series capacity of the pulse forming condenser, the coupling condenser, and the load capacity of the precipitator. The first cycle of the oscillation plays the role of a submicrosecond pulse. This pulse energization without using a pulse forming element such as a resistor and a feeder becomes very simple in construction.

In this paragraph, these two methods are introduced and their corona characteristics are shown.

2-3-2. Experimental Apparatus

In this series of experiments, the wire-to-duct system of full scale dimensions is again used, but the corona electrode is of a conventional construction where each corona wires are connected to the frame in parallel as shown in Fig. 2.20. Other constructions are same as Case II in Fig. 2.2. The inter-electrode capacity measured with a LCR meter (KOKUYOA ELECTRIC CO., LTD Type KC-534) and its value is C_{EP} = 3.17 nF. In these cases, pulse voltage wave forms, ionic current density distribution and light measurements of corona are performed by using the same instruments as referred in the paragraph 2-2.

Figs. 2.21 and 2.22 show the test circuit of the condenser-coupled feeder-formed pulse energization and the condenser-coupled LC-oscillatory pulse energization, respectively. In either cases, the pulser comprises a pulse forming capacitor, C_p, out of a number of ceramic-made condensers and

a rotating spark gap, which is synchronized to the ac charging voltage. Its output is connected to the feeder cable (10C2V; surge impedance Z_f = 75 ohm, and wave propagating speed v_w = 0.2 m/s, length of feeder = 160 m) and the cable is terminated by the condenser coupled corona electrode with dc bias voltage in the case of the condenser-coupled feeder-formed pulse energization (Fig. 2.21). The load characteristic of the pulser becomes resistive (surge impedance of the feeder cable) in this case.

In the case of the condenser-coupled LC-oscillatory pulse energization (Fig. 2.22), the pulser is directly connected to the condenser coupled corona electrode. The pulse circuit becomes the series LC circuit, where C is the total series capacity of the pulser, C_p, the coupling condenser, C_c, and the precipitator, C_{EP}. The load characteristic of the pulser becomes capacitive (series capacity of C_c and C_{EP}).

2-3-3. Test Results

(A) Pulse Voltage Wave Form:

The pulse voltage wave form is measured at the inlet terminal of the corona electrode. In the case of a feeder forming pulse, the pulse voltage wave form becomes as shown in Fig. 2.23 (solid line, V_b = 0 kV). Considering that the traveling wave on the feeder produced by the L-C_p-Z_f series oscillation reflects at the feeder end where the series capacity of C_c and C_{EP} is connected, its voltage wave form, $V_p(t)$ can be expressed by:

$$V_p(t) \fallingdotseq \frac{C_c}{C_0+C_{EP}} \frac{4\alpha}{\tau} \frac{1}{\gamma^2-\beta^2} e^{-\alpha t}\left(\cosh \gamma t - \frac{\beta}{\gamma} \sinh \gamma t - e^{-\alpha t}\right)V_0 \quad ---(2.7)$$

where

$$\alpha = Z_f/2L, \quad \gamma = \sqrt{\frac{Z_f}{4L}\frac{1}{LC_p}}, \quad \tau = \frac{C_c}{C_c+C_{EP}} Z_f, \quad \beta = \frac{1}{\tau}\alpha$$

V_0 : charging voltage of C_p

The dotted line in Fig. 2.23 shows the wave form calculated by Eq. (2.7). It agrees well with the measured curve, indicating that Eq. (2.7) is useful in designing the pulse voltage wave form.

In the case of a LC oscillatory pulse, the pulse voltage wave form is shown in Fig. 2.24, where the solid line (V_b = 0 kV) is the case without corona and the dotted line (V_b = -25 kV) the case with uniform corona as shown later. Considering C_p-L-C_c-C_{EP} series oscillation, the pulse voltage wave form, $V_p(t)$ is expressed by:

$$V_p(t) \fallingdotseq \frac{C}{C_p}(1 - e^{-\alpha t}\cos\omega t)\, V_0 \qquad \text{-----(2.8)}$$

where

$1/C = 1/C_p + 1/C_c + 1/C_{EP}$, $\omega = 1/\sqrt{LC}$,

$\alpha = r/2L$, r : total circuit loss

V_0 = charging voltage of C_p

The peak voltage V_p and the oscillation period, T, in Fig. 2.24 (V_b = 0) are in a good agreement as those calculated from Eq. (2.8). Eq. (2.8) also can be used to design the pulse parameters of V_p and T_r (= T/2; pulse rise time).

The wave form measured at other points of the corona electrode becomes almost same as the one at the pulse inlet terminal as shown in Figs. 2.23 and 2.24, but a small deviation can be recognized. The difference occurs probably because the electrode system becomes a distributed constant circuit to the high frequency components. In this mean Eqs. (2.7) and (2.8) treating it as a lumped constant capacitive load give the first approximation.

(B) Corona Characteristics:

Ionic current density distribution in both types of pulse energization systems are shown in Figs. 2.25 and 2.26, respectively. In these cases,

these data are obtained again by "back corona correction mode of operation" where V_b is set slightly below the dc corona onset voltage. Figs 2.25 and 2.26 indicate as good uniformity as obtained by the condenser-coupled traveling-pulse energization (see Fig 2.7(a)).

The photo signal from the pulse induced corona is shown in Figs. 2.27 and 2.28, respectively. In these cases, the photo signal starts at the leading edge of the pulse voltage, which is also recognized in the traveling pulse (see Fig. 2.15). It is very interesting that the photo signal is observed only once in a pulse period, and the following peak of a LC oscillatory pulse although beyond the threshold voltage, V_t, can not emit corona (Fig. 2.28). This is probably because of the corona quenching effect of prasma formed by the first corona. As a result, the first half cycle plays a role of the submicrosecond pulse.

The light activity of pulse induced corona observed in the whole corona electrode is same in both cases as that of the traveling pulse as shown in Fig 2.6(b). As the result, the corona characteristics of these three pulse energization systems are recognized to be almost same.

(C) Calculation of Corona Loss:

Fig. 2.29 shows the voltage wave form measured at the middle of the feeder cable, V_f, in the case of the condenser-coupled feeder-formed pulse energization (V_f in Fig. 2.21). V_f is out of the forward traveling pulse and the backward one. The backward traveling pulse caused by the reflection from the feeder end terminal appears after t = 800 ns. The case of V_b = 0 with no corona is shown by a solid line. When V_b is raised to -25 kV and uniform corona takes place in the entire corona wires, it is modified as shown in the dotted line. The total energy of the backward pulse in the case of V_b = -25 kV decreases compared to the case of V_b = 0 kV and this decrease can be calculated from Eqs. (2.4) and (2.5). This corresponds to corona forming energy (corona loss) and it is estimated to

be 0.38 J.

In the case of the condenser-coupled LC-oscillatory pulse energization, the difference in the pulse voltage wave form in V_b = 0 kV and V_b = -25 kV can be recognized as shown in Fig. 2.24. This is again caused by the corona forming loss. The rough estimation of corona loss is made by:

$$\text{Corona Loss} \fallingdotseq \frac{1}{2} C_{EP} (V_p^2 - V_p'^2) \qquad \text{-----(2.9)}$$

where

V_p : peak voltage in case of V_b = 0 kV

V_p': peak voltage in case of V_b = -25 kV

The corona loss estimated from this equation becomes 0.51 J. These values of the corona losss (0.38 J and 0.51 J) are very close to the one by the condenser-coupled traveling pulse energization (0.2 - 0.4 J).

2-3-4. Comparison of Three Pulse Energization Systems

Using these results, we can estimate the pulser capacity necessary for these three condenser-coupled pulse energization systems. Assuming that the capacity of the pulser, C_p, is 20 nF, the total inductance in the pulse circuit, L, is 1 μH, and the charging voltage of the pulser is same (V_0 = -64 kV), we can estimate the collection area of the precipitator to be energized becomes:

	Collection Area	Capacitance of Coupling Condenser
Traveling Pulse	1000 m^2	250 nF

Feeder Formed Pulse	600 m^2	120 nF
LC Oscillatory Pulse	450 m^2	35 nF

The stored energy in the pulser is most effectively transferred to the corona formation by the traveling pulse energization system (without using a peaking inductance). The conversion efficiency in this case is estimated to be about 8 - 15 %. This mean also the operation cost is minimum. However it requires the replacement of the corona electrode and a larger coupling condenser. The efficiency of the pulser degrades in both lumped constant circuit types where the existing precipitator can be used. The feeder forming pulse requires a long pulse forming feeder in addition to the pulser and the coupling condenser. The cost of a long and reliable feeder is another problem. Although the pulser efficiency of the LC oscillatory pulse becomes worst but it is most simple and the initial cost is expected to be smallest in these three.

2-3-5. Conclusion

(1) Submicrosecond pulse energization is possible even in the case of the conventional electrode system using either by the feeder formed pulse or the LC oscillatory pulse.

(2) In this case the load characteristic of the precipitator is considered to be the lumped constant circuit in the first approximation.

(3) In the case of the condenser-coupled feeder-formed pulse energization, the pulse voltage is formed by the reflection of the traveling wave at the feeder end terminal where the condenser coupled corona electrode is connected.

(4) In the case of the condenser-coupled LC-oscillatory pulse energization, the first cycle of the LC series oscillation acts as a submicrosecond

pulse where L is the total inductance in the pulse circuit and C is the series capacity of the pulser, the coupling condenser, and the precipitator.

(5) Uniformity in ionic current density distribution is excellent in both cases as in the condenser-coupled traveling-pulse energization. Corona activity is also very uniform in the entire corona wires.

(6) The light measurements indicate that corona takes place only once in one pulse cycle and starts at the leading edge of the pulse voltage where the applied voltage exceeds the threshold voltage.

(7) Corona loss estimated from the pulse voltage modification becomes 0.38 J and 0.51 J in the feeder forming pulse and the LC oscillatory pulse, respectively. This agrees well to corona loss obtained by a traveling pulse (0.2 - 0.4 J).

(8) The pulse to convert the capacitive energy of the pulser to the corona formation in the precipitator becomes largest in the traveling pulse type, and the initial cost becomes smallest in the LC oscillatory pulse in these three pulse energization systems.

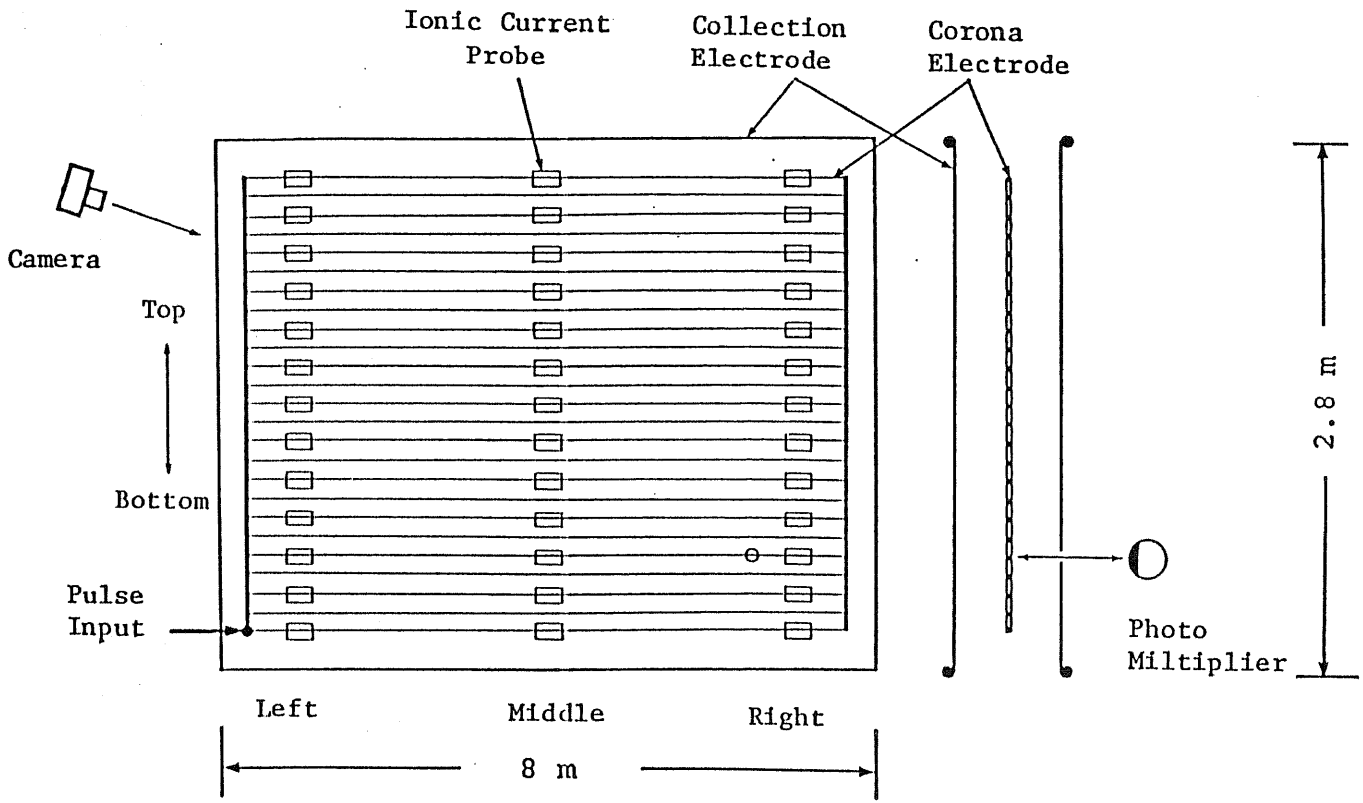

duct spacing : 250 mm ; wire-to-wire spacing : 100 mm
corona electrode : 25 wires ; wire : 5 x 5 mm cross section

Fig. 2.20 Single Duct Electrode System with Full Dimensions
(clean electrode; twin-electrode; lumped constant circuit)

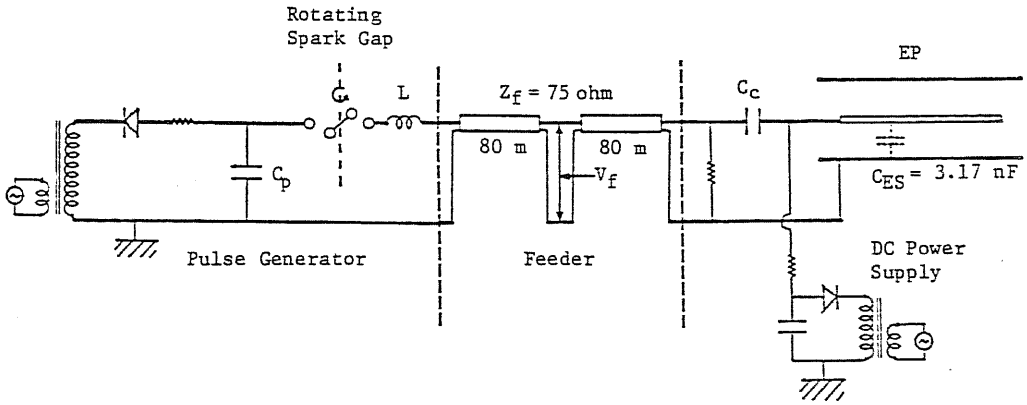

Fig. 2.21 Pulse Power Supply and Its Connection to DC Biased Precipitator in Condernser-Coupled Feeder-Formed Pulse Energization

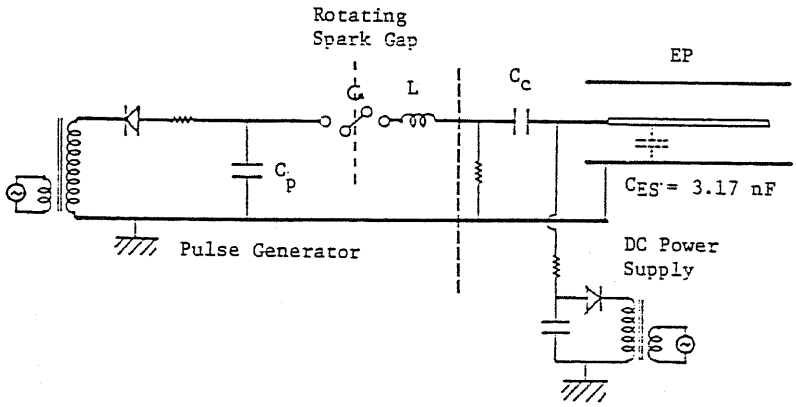

Fig. 2.22 Pulse Power Supply and Its Connection to DC Biased Precipitator in Conderser-Coupled LC-Oscillatory Pulse Energization

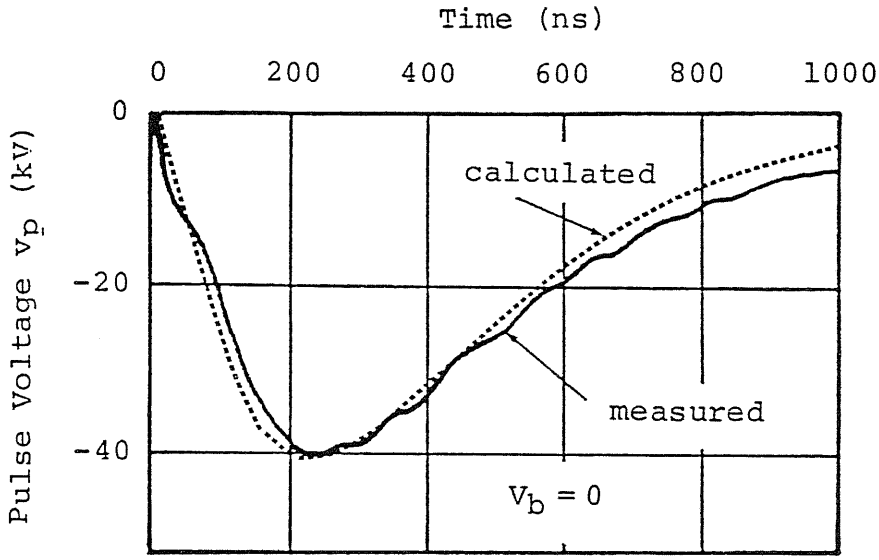

Fig. 2.23 Pulse Voltage Wave Form of Condenser-Coupled Feeder-Formed Pulse Energization

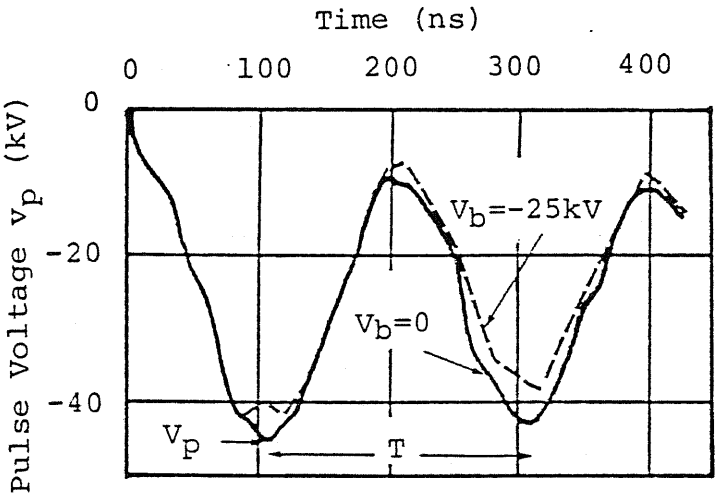

Fig. 2.24 Pulse Voltage Wave Form of Condenser-Coupled LC-Oscillatory Pulse Energization

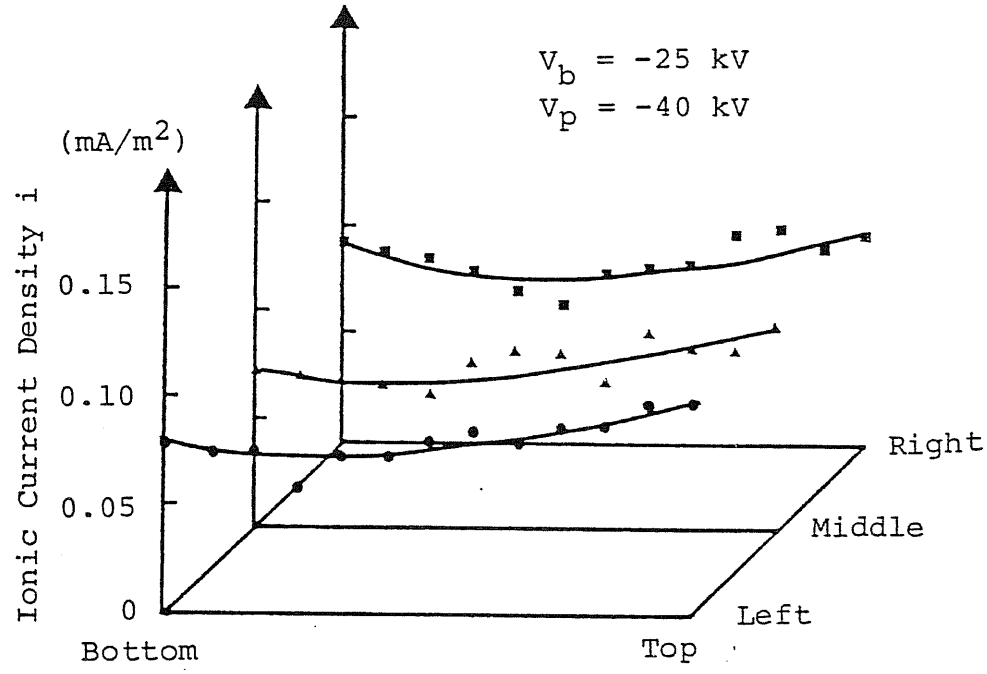

Fig. 2.25 Uniform Current Density Distribution Obtained by Condenser-Coupled Feeder-Formed Pulse Energization

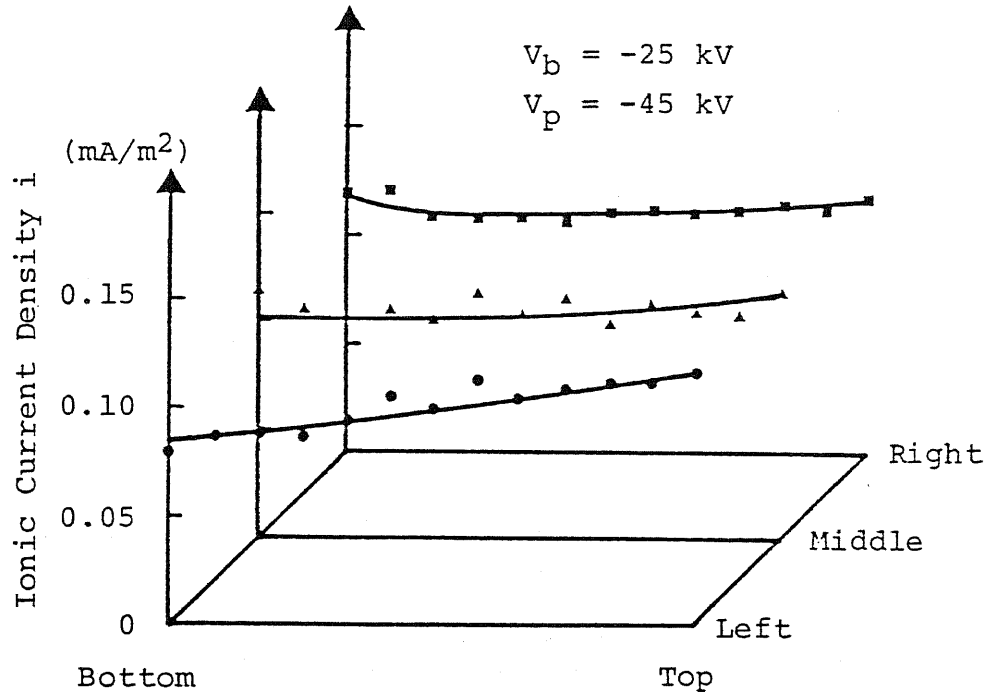

Fig. 2.26 Uniform Current Density Distribution Obtained by Condenser-Coupled LC-Oscillatory Pulse Energization

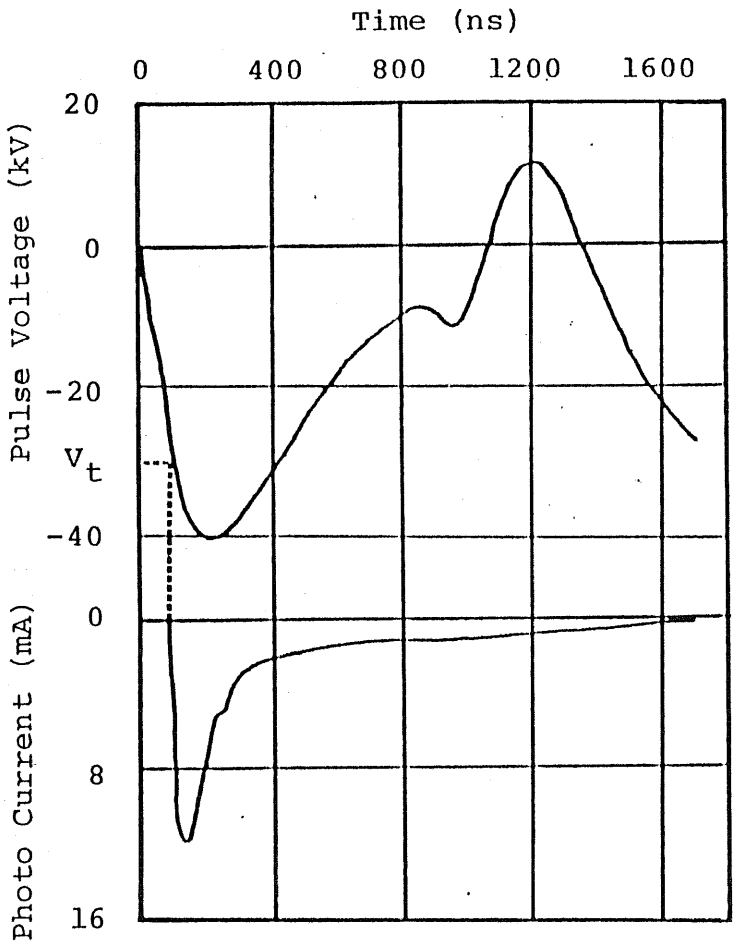

Fig. 2.27 Photo Signal of Pulse-Induced Corona in Condernser-Coupled Feeder-Formed Pulse Energization

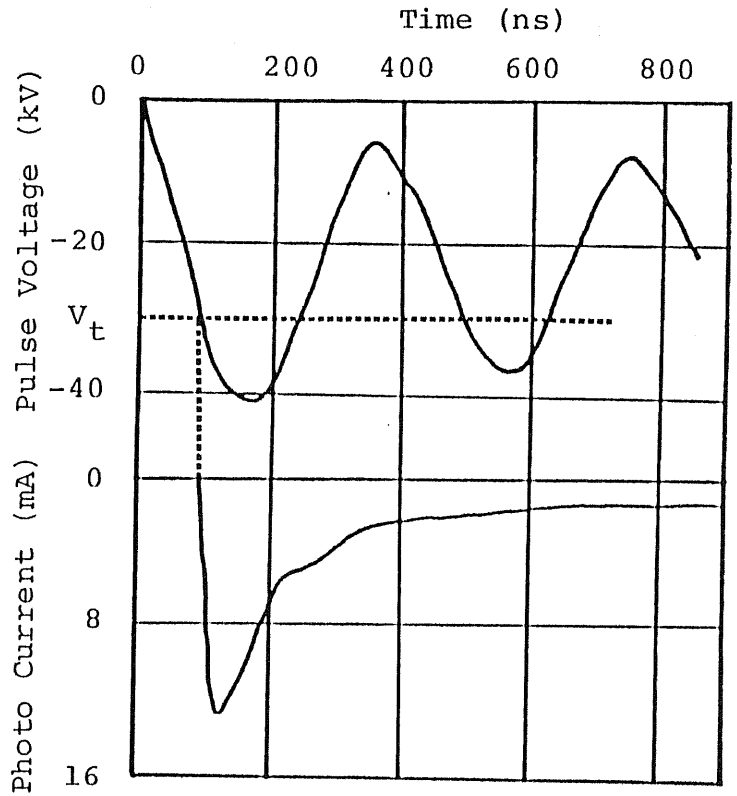

Fig. 2.28 Photo Signal of Pulse-Induced Corona in Condenser-Coupled LC-Oscillatory Pulse Energization

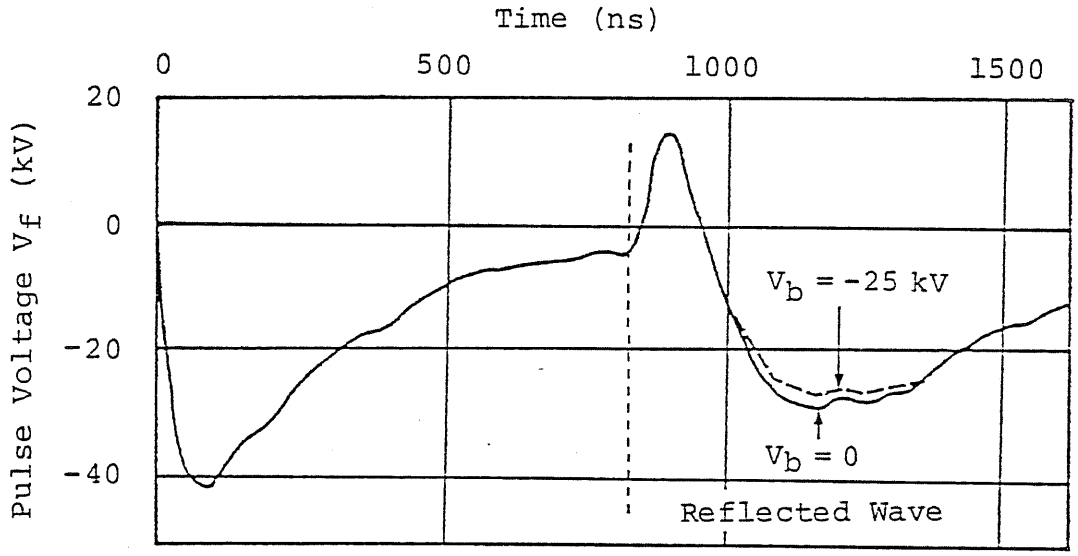

Fig. 2.29 Difference in Reflected Voltage Wave Form Measured at the middle of the Feeder between with and without Corona in Condenser-Coupled Feeder-Formed Pulse Energization

2-4. Direct-Coupled Pulse Energization

2-4-1. Introduction

In the past two paragraphs, the effectiveness of submicrosecond pulse for the corona production in the electrostatic precipitators is shown. The pulser efficiency becomes best by the condenser-coupled traveling pulse energization and the initial cost will be smallest by the condenser-coupled LC-oscillatory pulse energization in the three systems treated in the last paragraphs. However, the costs of the coupling condenser and a separate power source needed to charge the pulse-forming condenser are still the problem. In consideration of the great effectiveness of high-frequency LC oscillation and the potential of reducing the cost of the pulse system, both the dc bias voltage and the coupling condenser are removed from the condenser-coupled LC-oscillatory pulse energization, and connected the pulser directly to the corona electrode of the conventional construction. Surprising to say. the saw-teeth like wave form with a switching frequency having a very sharp peak of the LC oscillation at its leading edge is obtained. This sharp peak acted as a submicrosecond pulse to produce a very active streamer coronas uniformly distributed over the entire length of corona wires when properly designed, and remaining voltage stored in the inter-electrode capacity of the precipitator after the spark gap turns off produces charging field. It decays slowly due to the ionic current and increases sharply when the gap fires, resulting a saw-teeth wave form. The current distribution is also very uniform. This direct-coupled pulse energization enables the use of the existing dc power supply and corona electrodes by just inserting the cassette type pulser module shown later (Chapter 4), so that it can be used in the retrofitting applications for upgrading the existing precipitators.

This paragraph describes the basic corona characteristics of the direct coupled pulse energization.

2-4-2. Experimental Apparatus

Various kinds of corona measurements are made using the same system as described in the paragraph 2-3-2 (see Fig. 2.20). The test pulse power supply becomes very simple as shown in Fig. 2.30. The pulser output is is directly connected to a bottom corner of the corona electrode. The pulse rise time, T_r, is altered by inserting a coil, L_i, in series to the gap.

2-4-3. Experimental Results and Their Analysis

(A) Pulse Wave Form and Equivalent Circuit:

Fig. 2.31 shows the pulse voltage wave form in three different time scales measured at the inlet terminal of the corona electrode. After the spark gap fired, the LC oscillation starts to occur, and the voltage takes its first maximum, V_M, at $t = T_r$. The oscillation decays quickly and stops at $t = T_d$ when the spark channel is opened to disconnect the pulse-forming capacitor C_p from the corona electrode. Then, the voltage of the corona electrode decays in a saw-teeth fashion, which consists of a first rapid decay (decay phase I) and the second slower one (decay phase II). Approximate characteristics of the oscillation can be considered in terms of an equivalent circuit as shown in Fig. 2.32(a). The oscillation phase lasts for sereral tens microseconds, whereas the main negative streamers are produced only in the first half cycle of the oscillation as described later. The oscillation decays quickly by the losses in the circuit, spark channel and corona plasmas due to ion oscillation. The ion

migration towards collecting electrodes is negligible in the oscillation period, so that we can assume $R_{EP} \to \infty$ in this period. Then, we get the following expression for the damped oscillation:

$$V_{EP} \fallingdotseq V_R + (V_0 - V_R) \frac{C_p}{C_p + C_{EP}} (1 - e^{-\alpha t} \cos \omega t) \qquad \text{-----(2.10)}$$

$$0 \leqq t \leqq T_d, \quad r << 4L/C$$

where

V_R : final voltage of one pulse cycle

$\alpha \fallingdotseq r/2L$, r : overall loss in pulse circuit

$\omega \fallingdotseq 1/\sqrt{LC}$, $C = C_p C_{EP}/(C_p + C_{EP})$

and the equivalent pulse rise time, T_r, is given by:

$$T_r \fallingdotseq T/2 = \pi/\omega = \pi\sqrt{LC} \qquad \text{-----(2.11)}$$

Finally, the spark channel turns off at $t = T_d$ as shown in Fig. 2.31(b), and the decay phase starts. The initial voltage of the decay phase I, V_D, may be taken as:

$$V_D = V_R + \frac{C_p}{C_p + C_{EP}} (V_0 - V_R) \qquad \text{-----(2.12)}$$

and the voltage decay in the phases I and II will follow the following equations, (see equivalent circuit of Fig. 2.32(b)):

$$\text{Phase I} : V_{EP}(t) = V_D \, e^{-t/\tau_I} \qquad \text{-----(2.13)}$$

$$\tau_I = (R_{EP})_I C_{EP}$$

$$\text{Phase II} : V_{EP}(t) = V_D \, e^{-T_I/\tau} \, e^{-(t-T_I)/\tau_{II}} \qquad \text{-----(2.14)}$$

$$\tau_{II} = (R_{EP})_{II} C_{EP}$$

Fig. 2.33 shows the ionic current wave form measured at one of the

ionic current probes. It can be seen that the ionic convection current lasts as long as several milliseconds. This time corresponds to that of the decay phase I (Fig. 2.31(a)) with a decay time constant, τ_1. A substantial fraction of energy stored in the inter-electrode capacity is consumed in this process with a concurrent sharp decay of V_{EP} in the phase I.

In the decay phase II, V_{EP} decays much more slowly because only leakage current and, in some cases, dc coronas are existing. As described later, the decaying speed in the phase I is enhanced with the increase in pulse voltage and decrease in the pulse rise time.

(B) Factors Affecting Pulse Voltage Wave Form:

It is observed that among the factors affecting the pulse wave form in the present pulse energization the following two are the most dominant in the clean electrode system and the room air condition : the magnitude of the pulse peak voltage, V_M, and the pulse rise time, T_r. The effects of the high resistivity dusts on the collection electrode (back corona) and the very fine dusts in the gas (corona quenching effect) will be treated later (Chapters 3 and 5).

Figs. 2.34(a) and (b) indicates the effect of V_M. It should be noted that the use of a higher charging voltage of the pulse forming capacitor, V_0, and a concurrently higher V_M produce a sharp drop of the voltage in the phase I to the dc residual voltage which remains almost constant in phase II and is substantially lower level than that obtained when a lower magnitude of V_M is used (Fig. 2.34(b)). Whereas the use of lower V_0 and V_M produces a much less voltage drop in the phase I and a long lasting gradual drop in the phase II (Fig. 2.34(a)).

This difference may be explained by the difference in the carrier production in corona plasmas. The lower peak voltage will produce less carriers available for the discharge of the inter-electrode capacity, C_{EP},

resulting in a smaller voltage drop in the phase I, which in turn will produce a low level dc corona current and a concurrently slower, but long lasting voltage drop in the phase II. Contrarily, the higher peak voltage, V_M, will produce enough carriers to discharge the inter-electrode capacity down to the level below corona starting threshold only by the ion convection current in the phase I.

Figs. 2.34(b) and (c) show that effect of T_r, which is identical to that of V_M. The use of a shorter T_r corresponds to the use of a higher V_M. The difference may again be understood when the difference in carrier production in the corona plasma is considered. A shorter rise time produces a much more uniform and intense coronas with a greatly enhanced carrier production.

(C) Ionic Current Density Distribution:

The ionic current density on the collection electrode is measured by 39 probes shown in Fig. 2.20. Two typical results are shown in Figs. 2.35(a), and (b): one with a sharp rising submicrosecond pulse (T_r = 200 ns, T_h = 280 ns), and another with a slower rising microsecond pulse (T_r = 2 us, T_h = 2.7 us). For the purpose of comparison, the results by the the condenser-coupled traveling pulse energization and by the conventional dc energization are shown in Figs. 2.35(c) and (d), respectively. It is evident in the present pulse energization, that the use of a very sharp pulse with submicrosecond rise and duration times (Fig. 2.35(a)) is the essential factor to obtain a good uniformity in current distribution next to the ideal uniformity obtainable by the condenser-coupled traveling pulse energization (Fig. 2.35(c)). However, even with the microsecond rise and duration times(Fig. 2.35(b)), the degradation in current uniformity by the dc energization (Fig. 2.35(d)) can be fairly improved by the present pulse energization. Fig. 2.36 shows the concurrent difference in the uniformity of corona light activity on the wires (see Fig. 2.20). Several peaks in

current distribution in Fig. 2.35(b) occur at the points opposite to the bright corona spots probably produced by dc coronas.

(D) Light Measurement:

The light signals from the corona induced by the present pulse energization are detected by a photo-multiplier (Fig. 2.20), and shown in Fig. 2.37. Measurements are performed with and without attaching a small needle to the corona wire. This needle simulates active spots on the wire easy to cause bright points of Fig. 2.35(b). The light signal is initiated in all of the cases at the rising phase of the first half-cycle of the high frequency oscillation of voltage as shown Figs. 11(a) and (b). This is the common feature of the negative streamer coronas energized by a fast rising pulse as shown before. The photo signal appears only once in the case when a first rising submicrosecond pulse (T_r = 200 ns) is used with and without the needle (Fig. 2.37(a)), or a slower rising microsecond pulse (T_r = 1.2 μs) is used without the needle (Figs. 2.37(b) and (c)). The photo signal takes its maximum intensity around the crest of the first voltage cycle, followed by an after glow lasting 1 - 4 μs. This may be caused by the corona-choking effect of the electrons and negative ions which are produced in the streamers to accumulate at their periferal region and weaken the field inside the plasma region. The succeeding crests of voltage cannot produce streamers before these negative carriers (mostly slow-moving negative ions) are removed from the periferal region by Coulombic force. However, the succeeding light signals, weak in intensity, appears in the case when the needle is attached and the slow rising microsecond pulse is used (Fig. 2.37(b)). A strong field around the needle will enhance the removal of the negative ions, now substantially small in number as a result of weaker carrier production by the slow rising pulse. An exceptional case is Fig. 2.37(a) when T_r = 200 ns is used in combination with the needle. In this case, so many carriers are produced that the

shield effect of the periferal negative ions could last to the end of the oscillation even with the existence of a needle-intensified field.

Fig. 2.38 shows the wave forms of ionic current at T_r = 1.2 μs with and without the needle (see Figs. 2.37(b) and (c)). Without the needle the current contains only a single pulse lasting several milliseconds. With the needle, however, the pulse current is succeeded by dc corona current, resulting in a much greater average current density.

(E) Design Parameters:

Fig. 2.39 shows the magnitude of the residual voltage, V_R, plotted as a function of V_0 and C_p. It can be seen that V_R drops with increasing V_0, and that this tendency is enhanced by the increase in C_p. As already indicated in the previous section, with the increase in the pulse crest voltage, V_M, the pulse-induced coronas become more intense and uniform to produce a larger ionic convection current, resulting a greater reduction in V_R.

Assuming r = 0 in Eq. (2.10), we get

$$V_M/V_0 = V_R/V_0 + (1-V_R/V_0)\frac{2(C_0/C_{EP})}{1+(C_p/C_{EP})} \qquad \text{-----(2.15)}$$

Fig. 2.40 indicates the calculated values of V_M/V_0 as a function of C_p/C_{EP} for various values of V_R/V_0 assumed. It can be seen that C_p/C_{EP} has to be increased to increase the magnitude of V_M, whereas its increasing rate becomes diminished beyond C_p/C_{EP} = 1. Hence, in consideration of the cost of the pulse forming condenser, the value of C_p should be selected in the range of:

$$C_{EP} \leq C_0 \leq 1.5\ C_{EP}$$

Fig. 2.41 indicates the change of V_R as a function of V_0 and T_r. T_r is changed by inserting a coil with an inductance L_i in series to the spark gap. With decreasing T_r, V_R indicates a rapid drop with V_0, again because

of an increase in carrier production in the streamer coronas. Fig. 2.42 shows the effect of T_r on the ionic current density measured at the points opposite to the center of the wires. Here again a smaller T_r gives a better uniformity in the current distribution with its magnitude also increased. Thus, it is concluded that the use of submicrosecond pulse rise time is essential in the present pulse-energization. However, it is difficult to reduce the overall circuit inductance, L_s (spark channel and feeding wires), below a certain level. Hence, the magnitude of C_{EP}, i.e. the number of parallel ducts, to be energized with a single pulse power supply (number of parallel ducts) should be limited under a certain level so as to keep T_r at a desired submicrosecond level.

Fig. 2.43 shows the effect of V_0 on the distribution of ionic current density measured at the points opposite to the centers of corona wires. It is recognized that, even with T_r = 200 ns an uniform current distribution can be obtained only at a sufficiently high pulse voltage, obtainable at $|V_0| > 70$ kV in this particular case. Thus it is imperative in the present pulse energization system to use a sufficiently high V_0 and a sharp rising submicrosecond pulse to obtain a satisfactory uniformity in current distribution, which, however, is always accompanied by the reduction in the average field intensity.

Under these constrictions the average current density on the collecting electrode, a parameter determining the initiation of back corona, can be altered only by changing the pulse frequency, F_p.

2-4-4. Conclusions

The pulse energization system of electrostatic precipitators suitable to retrofitting applications (Direct-Coupled Pulse Energization) is developed and the following conclusions derived from its test results:

(1) The submicrosecond pulse energization becomes possible by connecting the pulser comprizing of the pulse forming capacitor and the rotating spark gap directly to the corona electrode of the electrostatic precipitator.

(2) A transient LC oscillation occurs when the gap fires, and its sharp first peak acts as a first rising short pulse voltage with a submicrosecond rise time, producing streamer coronas at its first rising phase. This LC oscillation decays rapidly to disappear when the gap is switched off. At this instance there remains a sufficiently high voltage between the corona and the collection electrodes, to separate negative ions form the corona plasmas and drive them toward the collecting electrodes. The ion convection current lasts several milliseconds, with a concurrent rapid decay in the voltage. This fast decay of the voltage is succeeded by a much slower decay due to leakage and dc corona current.

(3) A very uniform distribution of ionic current density is produced by the present direct-coupled pulse energization when the short pulse rise time below 1 μs and a sufficiently high peak voltage are used. At the same time the inter-electrode voltage indicates a sharp drop because of copious carriers produced, resulting in a low average dc voltage.

(4) The photo signal from the streamer coronas indicates that the main streamer with intense carrier production occurs only once, at the first crest of the LC oscillation.

(5) The final voltage V_R decreases with increasing V_0, and decreasing pulse rise time T_r.

(6) The optimum value of C_0 lies in the range $C_{EP} \leq C_p \leq 1.5\ C_{EP}$. As the uniformity in corona current distribution is improved by only using a smaller T_r, the overall inductance of the pulse and feeder circuits must be kept as low as possible. In addition, the number of parallel ducts to be energized by a single pulser should also be restricted.

The level of average current density is to be controlled by changing pulse frequency, F_p.

In conclusion, the present direct-coupled pulse energization system is found to be a useful and economical means in particular for retrofitting applications.

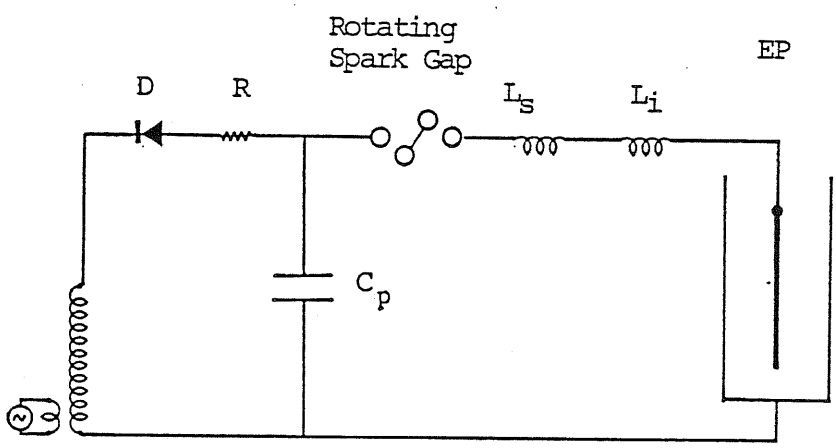

D : diode
C_p : pulse forming capacitor
L_s : overall circuit inductance of connecting wires and spak channel
L_i : inductance of inserted coil

Fig. 2.30 Pulse Power Supply and Its Connection to Precipitator in Direct-Coupled Pulse Energization

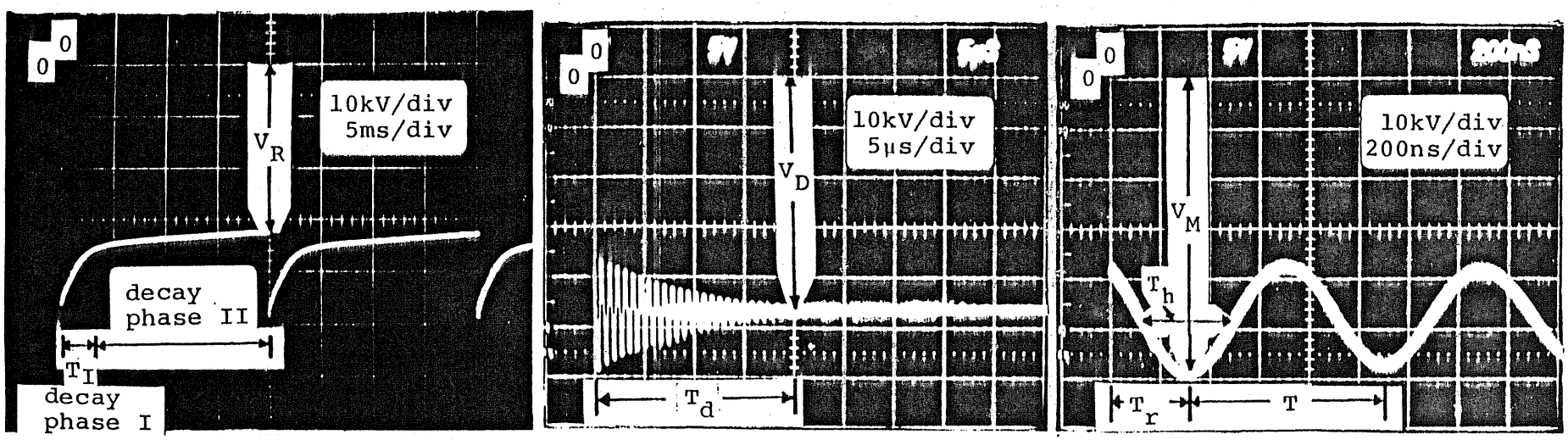

(a) Saw-Teeth Like Pulsating Wave with Sharp Initial Peaks

(b) Transient LC Oscillation

(c) Magnified Oscillating Part

Fig. 2.31 Voltage Wave Form, V_{EP}, Measured at the Inlet Terminal of Corona Electrode in Direct-Coupled Pulse Energization

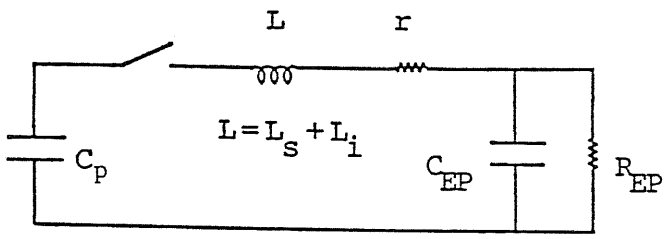

(a) Oscillation Phase

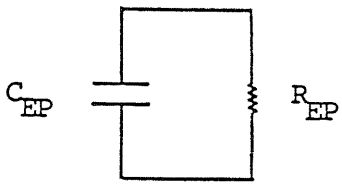

(b) Decay Phase

Fig. 2.32 Equivalent Circuit of Precipitator in Direct-Coupled Pulse Energization

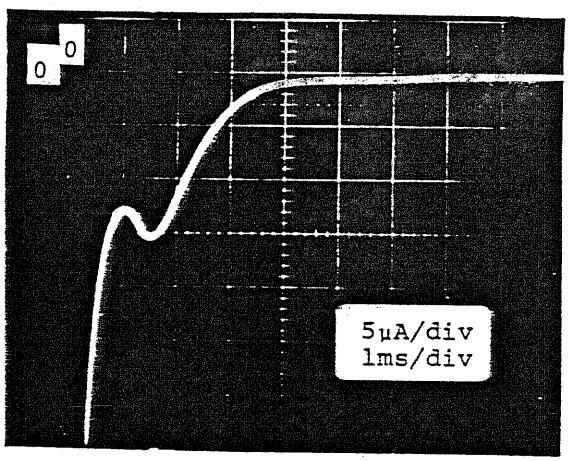

Fig. 2.33 Wave Form of Ionic Current Measured at Collection Electrode

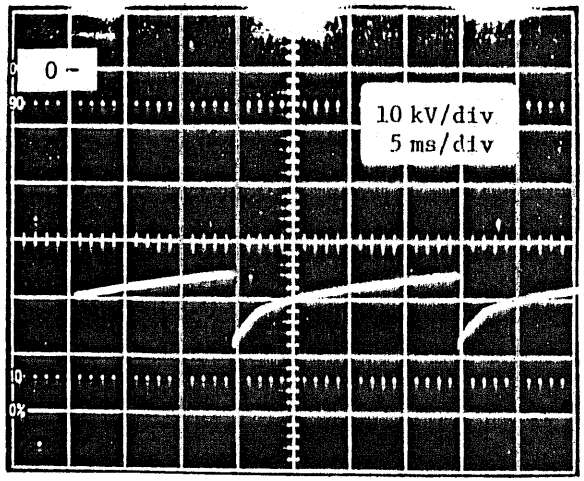

V_0 = -60 kV; T_r = 200 ns
V_M = -57 kV; T_h = 250 ns

(a) Low V_M and Short T_r

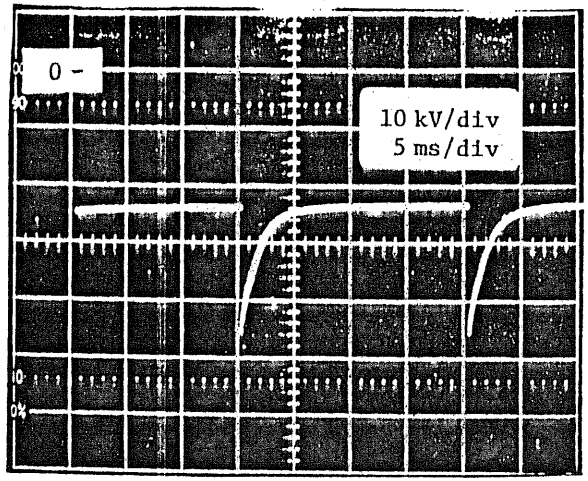

V_0 = -70 kV; T_r = 200 ns
V_M = -62 kV; T_h = 280 ns

(b) High V_M and Short T_r

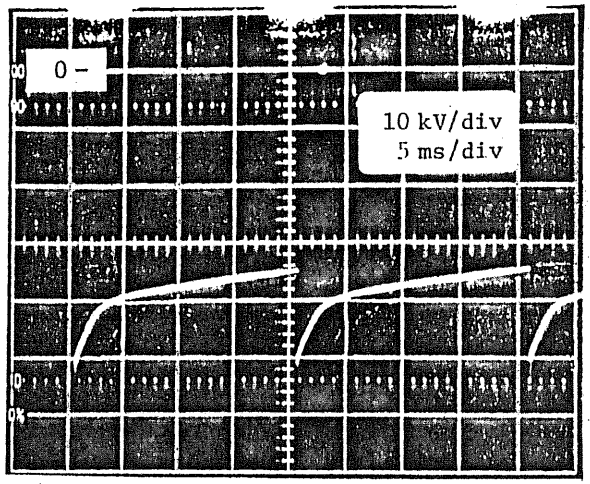

V_0 = -70 kV; T_r = 2.0 μs
V_M = -64 kV; T_h = 2.7 μs

(c) High V_M and Long T_r

Fig. 2.34 Effects of V_M and T_r on Pulse Voltage Wave Form

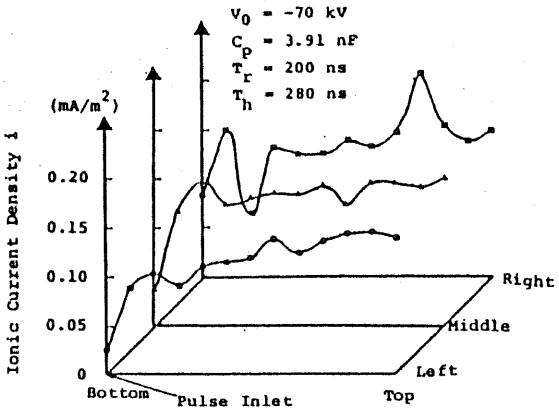

(a) Direct-Coupled Pulse Energization (sharp rising submicrosecond pulse)

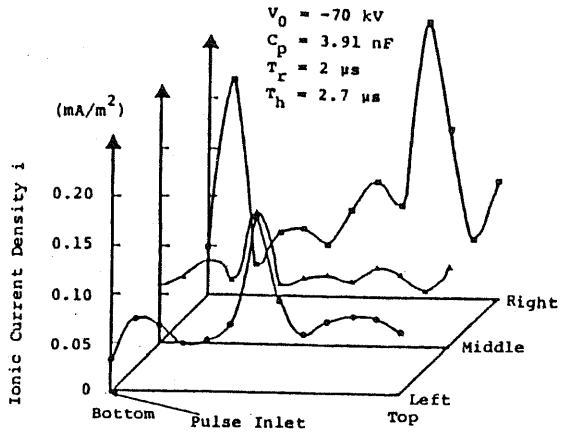

(b) Direct-Coupled Pulse Energization (slower rising microsecond pulse)

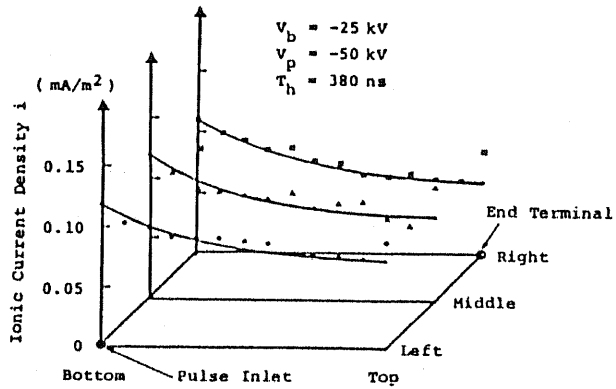

(c) Condenser-Coupled Travelling Pulse Energization (L = 200 m)

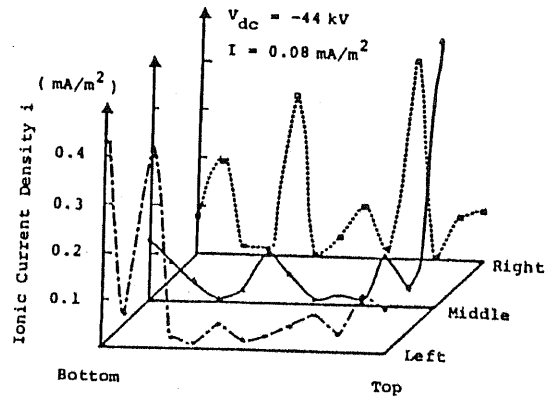

(d) DC-Energization

Fig. 2.35 Ionic Current Density Distribution in Collection Electrode

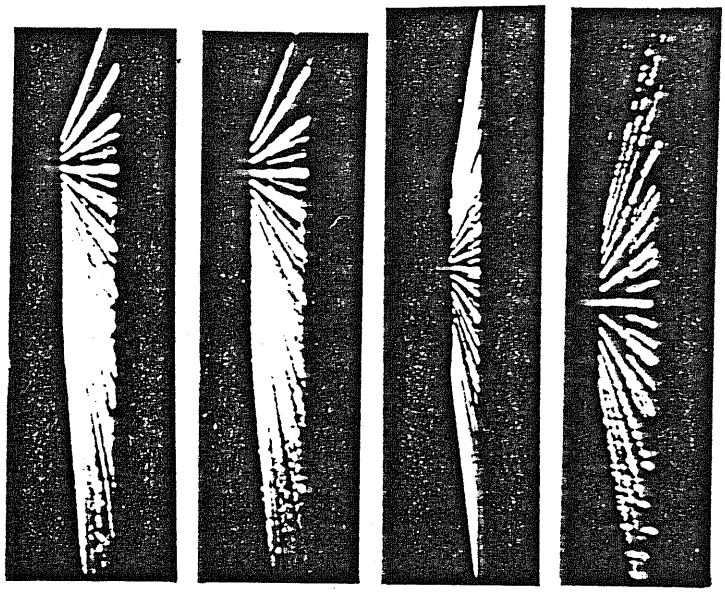

(a) (b) (c) (d)

(a) Direct-Coupling Pulse Energization; T_r = 200 ns, T_h = 280 ns, V_0 = -70 kV

(b) Direct-Coupling Pulse Energization; T_r = 2 μs, T_h = 2.7 μs, V_0 = -70 kV

(c) Condenser-Coupled Travelling Pulse Energization; V_b = -25 kV, E_{dc} = -2.0 kV/cm, V_p = -50 kV

(d) DC-Energization; V_{dc} = -50 kV, E_{dc} = -2.5 kV/cm

Fig. 2.36 Light Activity of Coronas

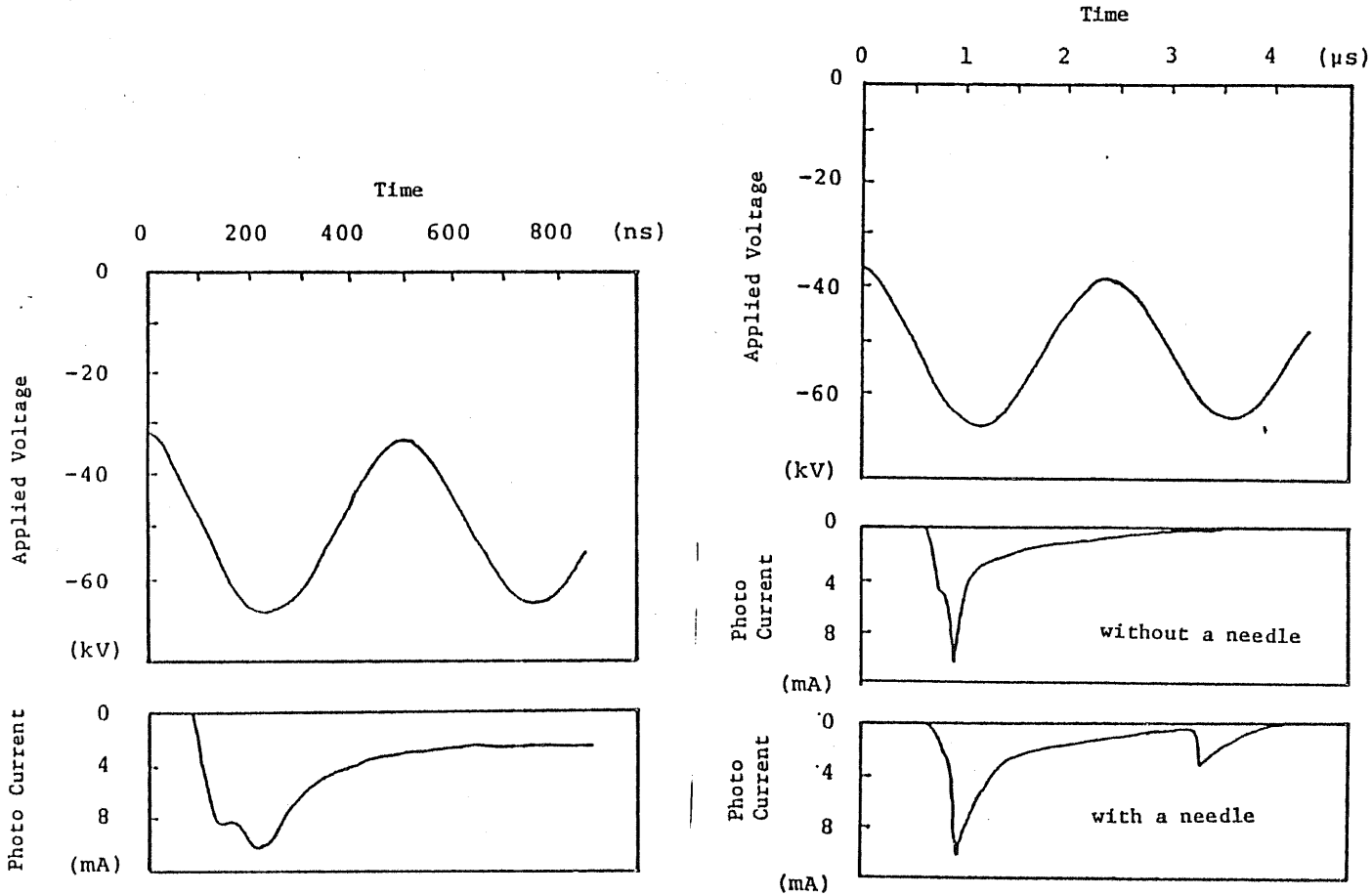

(a) T_r = 200 ns (with and without a needle)

(b) T_r = 1.2 μs (fast sweep)

Fig. 2.37 Light Signals from Coronas of Direct-Coupled Pulse Energization

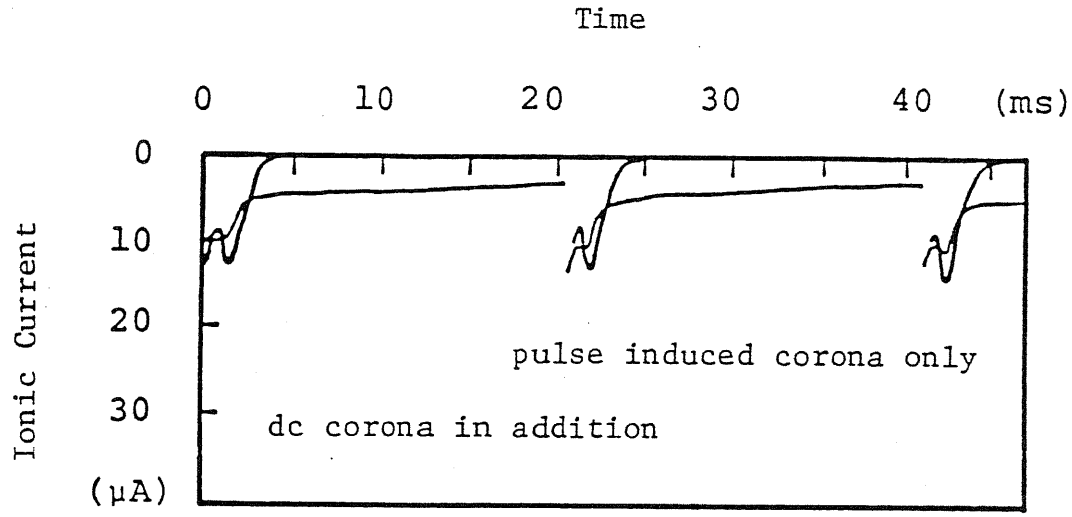

Fig. 2.38 Wave Form of Ionic Current With and Without a Needle (T_r = 1.2 μs; V_M = −70 kV)

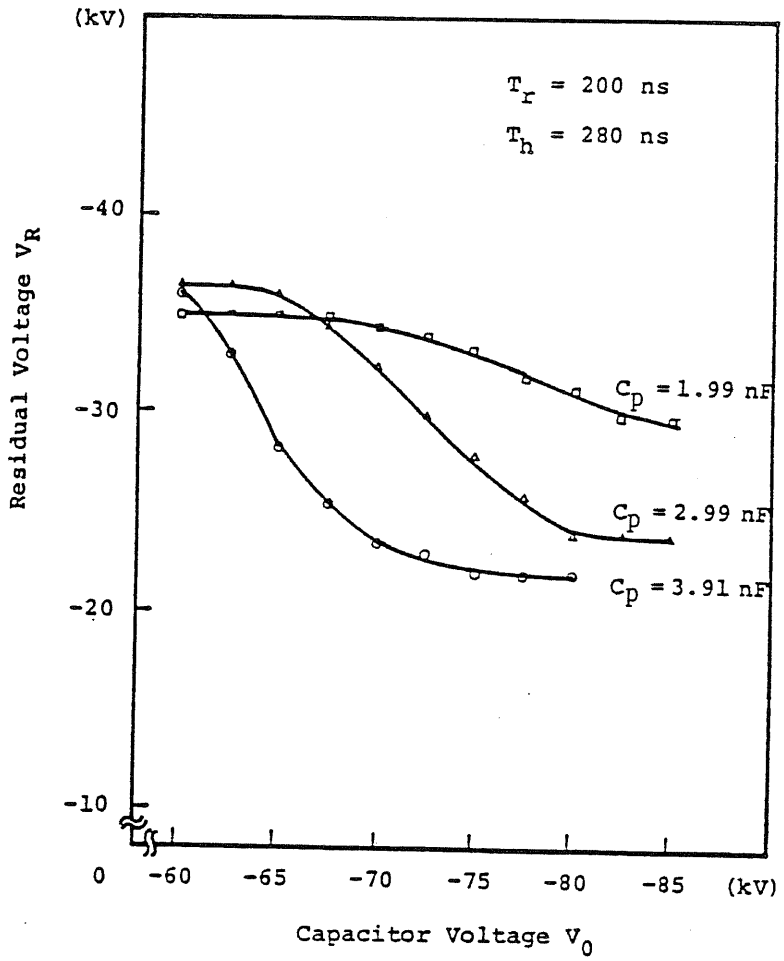

Fig. 2.39 Effects of Capacity and Voltage of Pulse Forming Condenser, C_p, on Final Voltage, V_R

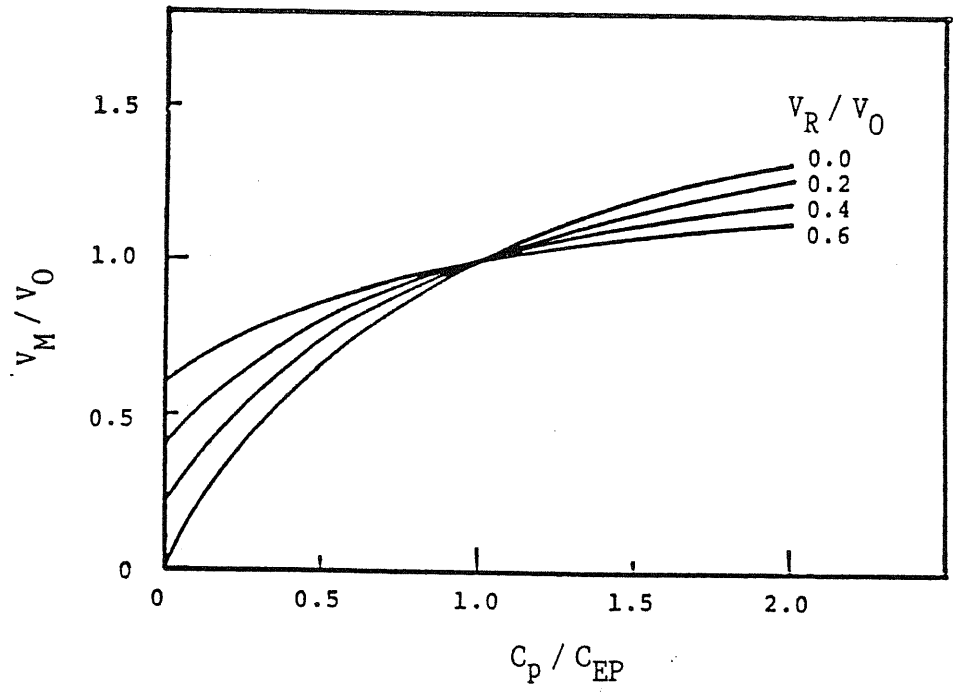

Fig. 2.40 V_M / V_0 vs. C_p / C_{EP}

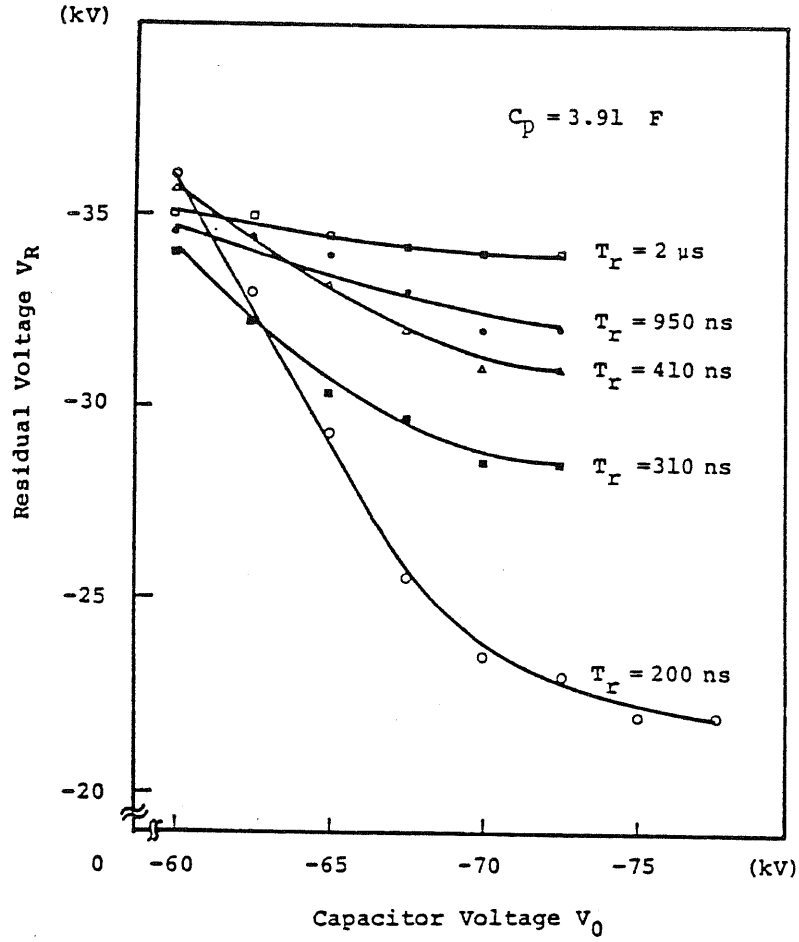

Fig. 2.41 Effects of Pulse Rise Time, T_r, and Voltage of Pulse Forming Condenser on Final Voltage, V_R

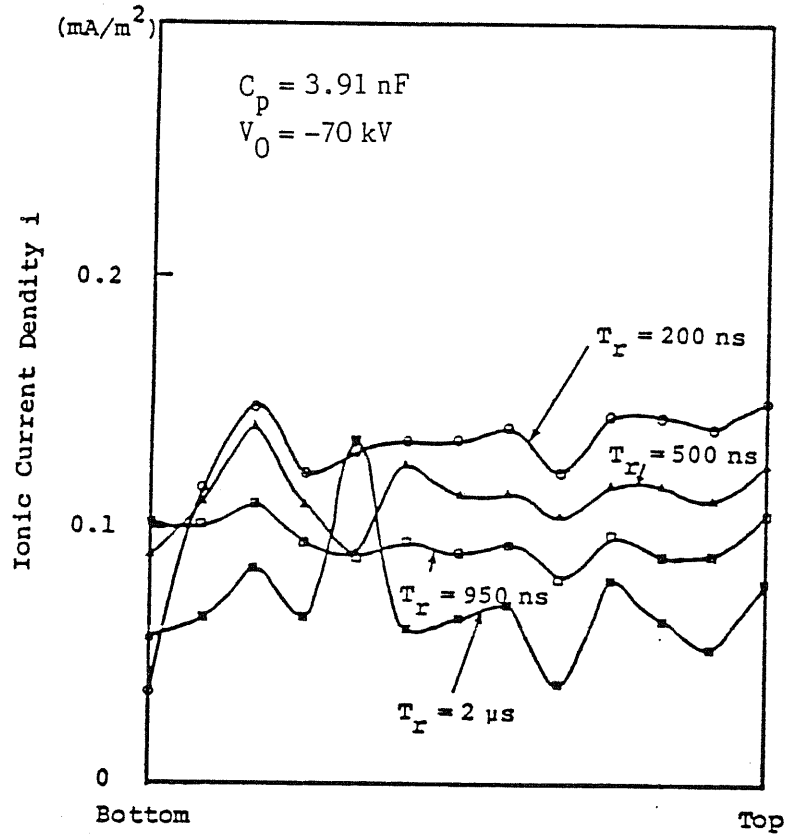

Fig. 2.42 Effects of T_r on Distribution of Ionic Current Density Measured at the Points on a Vertical Line Opposite to Centers of Corona Wires

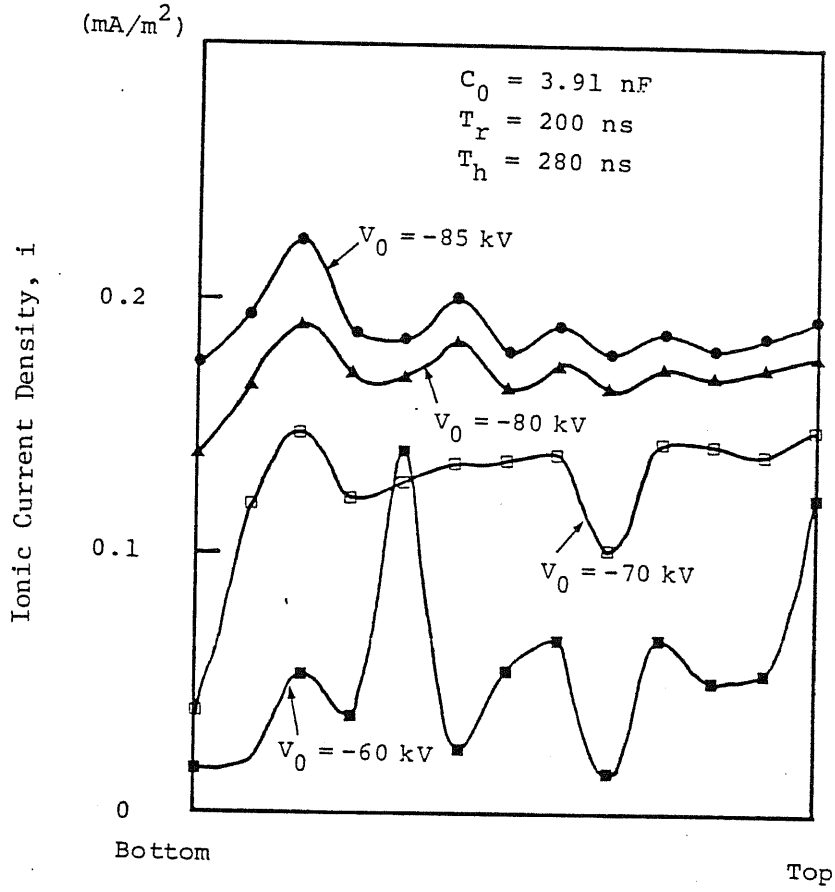

Fig. 2.43 Effects of V_0 on Distribution of Ionic Current Density Measured at the Points on a Vertical Line Opposite to Centers of Corona Wires

CHAPTER 3. COLLECTION PERFORMANCE OF DIRECT COUPLED PULSE ENERGIZATION

3-1. Introduction

In order to reduce the back corona problems, ionic current density should be controled in the level below the back corona threshold its distribution as uniform as possible. The direct-coupled pulse energization system meets not only these conditions but also the requirement of smallest initial cost.

To confirm the effectiveness of the direct-coupled pulse energization in correction of back corona, the collection test of fly ash from coal burning boilers are made using the laboratory test precipitators. Two series of tests are made, one in a race track system and another in a coal combation rig.

As expected the collection performance is enhanced by the pulse energized collection field in a wide range of dust resistivity, from a low resistivity range of 10^{10} - 10^{11} ohm-cm where the dc energized field shows a normal high efficiency to a high resistivity rang of 5 x 10^{13} ohm-cm where the dc energized fields suffers from severe back corona troubles.

In this chapter are reported the results obtained by these two series of collection tests.

3-2. Test by Race-Track Type Laboratory Precipitator

3-2-1. Introduction

Collection tests of the direct-coupled pulse energization are made by the race-track type laboratory precipitator. The fly ash sample is dispersed in the circulating gas heated by the electric heater. Collection performance is tested in the precipitating parts out of two parallel ducts with a standard duct spacing (2D = 300 mm) and corona electrode smooth round wires with 3 mm in diameter). Although the precise simulation of the real plant is impossible because the gas used is room air without steam injection, and the circulation of the gas causes a reentry of difficult dust particles with a smaller size into the precipitating section, it provides a rough estimation of collection performance of the direct-coupled pulse energization.

Two comparison tests are also made by changing the power supply, one by the dc energization and another by the condenser-coupled submicrosecond pulse energization (simulating the condenser-coupled traveling pulse energization) which is to be expected as the best means of back corona correction from corona characteristics as shown in the paragraph 2-2.

The direct-coupled pulse energization gives the exactly same collection performance as one by the condenser-coupled submicrosecond pulse energization. The performance enhancement is recognized in the fly ash samples with the dust resistivity of $r_d = 5 \times 10^{11}$ ohm-cm and $r_d = 2 \times 10^{12}$ ohm-cm as far as tested here where back corona is suppressed. The enhancement factor based on Deutsch migration velocity (precise migration velocity) compared with the dc energization becomes $H_{eff} = 1.45$ and 1.35, respectively. Once severe back corona takes place in the case of $r_d = 1 \times 10^{13}$ ohm-cm in this particular test, even the pulse energized collection

fields can not improve the performance.

3-2-2. Experimental Apparatus

Fig. 3.1 illustrates a laboratory test precipitator of race-track type used for measuring the performance enhancement produced by the direct-coupled pulse energization. For the purpose of comparison tests are also made with a conventional dc-energization and a condenser-coupled submicro-second pulse energization (back corona correction mode of operation). Two fly ash samples are used, one with the resistivity of 5×10^{11} ohm-cm at T_g = 130 °C, and another with 2×10^{12} ohm-cm at T_g = 50 °C and 1×10^{13} ohm-cm at T_g = 100 °C.

Three collection fields are energized with a common power supply. Each field consists of 2 parallel ducts each spaced at 0.3 m, and being 0.76 m high, 0.5 m long in the gas flow direction, and 0.46 m^2 in the total duct cross-section. The total collection area of these three fields is F = 4.56 m^2 with f (specific collection area) = 12.1 $m^2/(m^3/s)$ at 0.82 m/s standard gas velocity. Three corona wires with 3 mm in diameter are installed in a each duct with a 80 mm wire-to-wire spacing. The carrier gas is air, and its temperature can be raised by an electric heater up to 200 °C. Steam injection is not performed. The inlet dust mass loading (W_i) is kept constant by using a constant dust feeder, monitored by a dustmeter (Konitest) based on the tribo-electrification. The dust mass-loading is measured at the outlet (W_0) by a sampling filter.

The occurrence of back corona is observed by the light emitted from the dust layer. And its severity expressed in terms of a ratio of the positive current density to the negative one, (I_+/I_-), is measured by the bi-polar current probe [36-39].

3-2-3. Collection Performance

The collection performance of the direct-coupled pulse energization is tested at T_r = 800 ns. Other test conditions are indicated in Table 3.1. The collection efficiency, η, is shown in Table 3.2, together with the back corona severity, I_+/I_-, measured with the bi-polar current probe. Here, I_+ and I_- denote the current densities of back corona induced positive ions and normal negative ions, respectively.

The apparent migration velocity, w_{total}, is calculated from the Deutsch equation:

$$\eta = 1 - \exp(-w_{total} f) \qquad \text{-----(3.1)}$$

where

η : collection efficency

f : specific collection area

And the precise migration velocity, w_{eff}, is estimated from the gradient of In $(1 - \eta)$ - f curve. In the cases of the dc energization and the condenser coupled submicrosecond energization, the number of collection fields energized is altered from one to three sections, and In $(1 - \eta)$ - f curve is plotted. In the case of the direct-coupled pulse energization, three sections are energized in parallel to obtain enough inter-electrodes capacity, so that the values of w_{eff} are evaluated from the data of the condenser-coupled pulse energization. w_{total} includes the mechanical collection effects such as gravitational precipitation, while w_{eff} excludes them and gives only the electrical collection effect. These are shown in Table 3.3 where the enhancement factors, H_{total} and H_{eff}, based on w_{total} and w_{eff}, respectively, are also indicated.

As the values of I_+/I_- indicate, the dc-energization causes back corona at all of the three resistivity levels, and the back corona severity in

terms of I_+/I_- becomes larger, and the collection performance lower with the increase in dust resistivity. The collection performance in the dc energization is the worst in the three energization modes. On the other hand, a distinct improvement is produced by both modes of the pulse energization. However, practically no difference exists between the two pulse-energization modes in the dust resistivity range tested. The performance enhancement factor becomes H_{eff} = 1.45, 1.35, and 1.1 at $r_d = 5 \times 10^{11}$, 2×10^{12}, and 1×10^{13} ohm-cm, respectively. The performance enhancement is pronounced in the first two cases where back corona can be corrected by the pulse energization. In contrast back corona can not be corrected by any mode of the two pulse energization in the case when $r_d = 1 \times 10^{13}$ ohm-cm, and the performance enhancement is only H = 1.1. It should be added that the use of a precharger (Boxer-Charger) [40-42] in combination with the pulsed collection fields produces a substantial performance improvement even at $r_d = 1 \times 10^{13}$ ohm-cm.

Once back corona occurs, V_R, drops drastically in the present direct coupled pulse-energization as shown in Table 3.1 (from -30 kV at $r_d = 5 \times 10^{11}$ ohm-cm to -9 kV at $r_d = 1 \times 10^{13}$). The back corona extinguishing voltage, V_e, is found to be so low when $r_d = 1 \times 10^{13}$ ohm-cm that it is hardly interrupted and even tends to propagate in the lateral direction to cover the wide area of the collection electrode. Hence, a careful control of corona current is required at this extremely high resistivity level so as not to initiate back corona.

3-2-4. Voltage Wave Modification Due To Back Corona

As indicated that V_R drastically drops in the case of severe back corona, the voltage wave form is also modified. Fig. 3.2 indicates the difference in the pulse wave form measured in the course of the present

collection tests.

The wave form without back corona is essentially the same as that observed with clean electrode system as shown in the previous chapter (see Figs. 2.31(a) and 2.34(b)) but it indicates a drastic change when back corona takes place. The voltage continues to drop during an entire period of a pulse cycle, and the difference between the phase I (see Fig.2.31(a)) produced by the convection of pulse induced ions and phase II after depletion of these initial ions disappears. A large contribution of positive ions by back corona is recognized to the continuous discharge of the inter-electrode voltage in this particular case of extremely high dust resistivity, resulting in a very low level of the final voltage, V_R.

3-2-5. Conclusion

(1) The direct-coupled pulse energization shows the same collection performance for high resistivity fly ash as the condenser-coupled submicrosecond pulse Energization operated in the back corona correction mode.

(2) The performance enhancement factor in terms of Deutsch migration velocity (precise migration velocity, w_{eff}) for two pulse-energization mode becomes H_{eff} = 1.45, 1.35, and 1.1 at $r_d = 5 \times 10^{11}$, 2×10^{12}, and 1×10^{13} ohm-cm, respectively.

(3) At an extremely high dust resistivity of $r_d = 1 \times 10^{13}$ ohm-cm, back corona can not be corrected even with any of the two pulse energization modes operated at f_p = 50 Hz, with a concurrently a small performance enhancement of H = 1.1.

(4) In this case, the voltage wave form is drastically modified, and the voltage continues to drop in the entire period of the pulse cycle and V_R drops to the very low level.

Table 3.1 Test Conditions of Laboratory Precipitator in Race-Track System

Dust Resistivity	DC-Energization	Condenser-Coupled (a) Submicrosecond Pulse Energization	Direct-Coupled (b) Pulse Energization
5×10^{11} ohm-cm ($^{\text{sample I}}_{T_g = 130\ ^\circ C}$)	$V_{DC} = -42$ kV $I = 0.2$ mA/m^2	$V_b = -35$ kV $V_p = -20$ kV $I = 0.06$ mA/m^2	$V_0 = -60$ kV $V_M = -59$ kV $V_R = -30$ kV $I = 0.09$ mA/m^2
2×10^{12} ohm-cm ($^{\text{sample II}}_{T_g = 50\ ^\circ C}$)	$V_{DC} = -38$ kV $I = 0.2$ mA/m^2	$V_b = -30$ kV $V_p = -32$ kV $I = 0.04$ mA/m^2	$V_0 = -56$ kV $V_M = -65$ kV $V_R = -20$ kV $I = 0.09$ mA/m^2
1×10^{13} ohm-cm ($^{\text{Sample II}}_{T_g = 100\ ^\circ C}$)	$V_{DC} = -32$ kV $I = 0.2$ mA/m^2	$V_b = -22$ kV $V_p = -32$ kV $I = 0.04$ mA	$V_0 = -50$ kV $V_M = -62$ kV $V_R = -9$ kV $I = 0.08$ mA/m^2

(a) $T_r = 40$ ns, $T_h = 180$ ns, $f_p = 50$ Hz

(b) $T_r = 800$ ns, $T_h = 900$ ns, $f_p = 50$ Hz

Table 3.2 Back Corona Sererity and Collection Performance
(Laboratory Precipitator in Race-Track System)

Dust Resistivity	DC-Energization		Condenser-Coupled Submicrosecond Pulse Energization		Direct-Coupled Pulse Energization	
	Back Corona Sevirity (I_+/I_-)	Collection Performance η	Back Corona Sevirity (I_+/I_-)	Collection Performance η	Back Corona Sevirity (I_+/I_-)	Collection Performance η
5×10^{11} ohm-cm (sample I $T_g = 130$ °C)	8.2 %	85.5 %	0 %	92.6 %	0 %	92.6 %
2×10^{12} ohm-cm (Sample II $T_g = 100$ °C)	2 - 15 %	84 %	0 - 2 %	89 %	0 - 2 %	89 %
1×10^{13} ohm-cm (sample II $T_g = 50$ °C)	27 %	73 %	24 %	76 %	25 %	75 %

Table 3.3 Dust Migration Velocity and Enhancement Factor

Dust Resistivity (ohm-cm)	DC-Energization		Condenser-Coupled Submicrosecond Pulse Energization		Direct-Coupled Pulse Energization		Enhancement Factor	
	w_{total} (cm/s)	w_{eff} (cm/s)	w_{total} (cm/s)	w_{eff} (cm/s)	w_{total} (cm/s)	w_{eff} (cm/s)	H_{total}	H_{eff}
5×10^{11} ($^{sapmle\ I}_{T_g = 130\ °C}$)	16.0	12.4	21.5	18.0	21.5	18.0	1.34	1.45
2×10^{12} ($^{sample\ II}_{T_g = 50\ °C}$)	15.1	8.6	18.2	11.6	18.2	11.8	1.21	1.35
1×10^{13} ($^{sapmple\ II}_{T_g = 100\ °C}$)	10.8	6.6	11.8	7.6	11.5	7.2	1.08	1.10

Note: w_{total} = Aparent Migration Velocity (include mechanical collection effect)

w_{eff} = Precise Migration Velocity (exclude mechanical collection effect)

Enhancement Factor, $H_{total} = w_{total}$ (pulse) / w_{total}(dc)

$H_{eff} = w_{eff}$(pulse) / w_{eff}(dc)

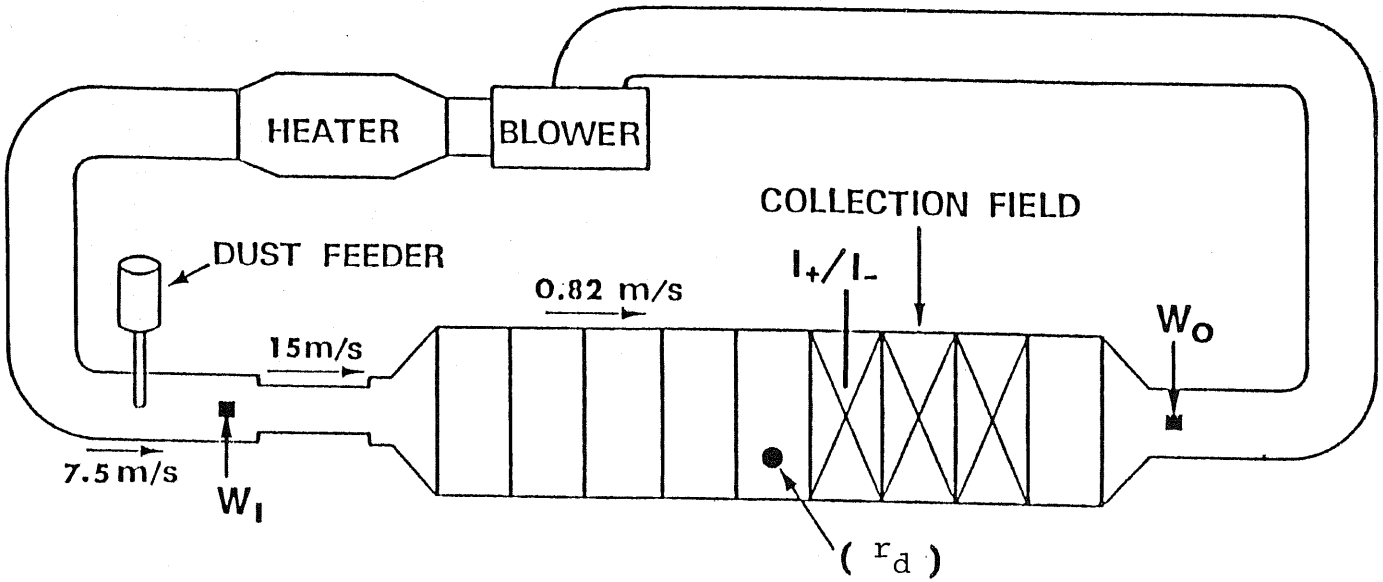

W_i : inlet dust loading
W_o : outlet dust loading
I_+/I_- : back corona sevirity measured by bi-polar ion current probe
r_d : dust resistivity

Fig. 3.1 Laboratory Precipitator in Race-Track System

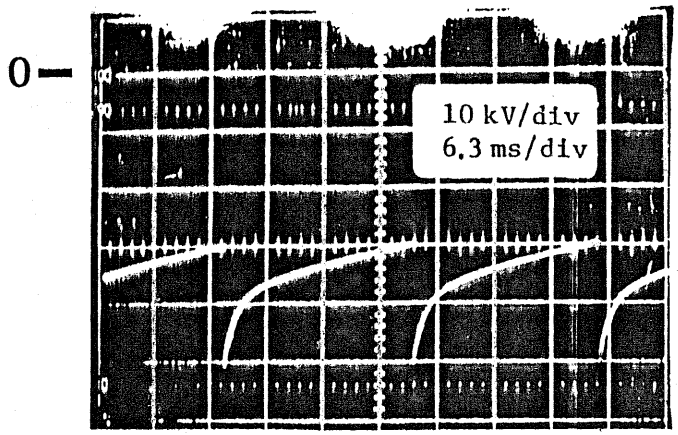

V_M = -60 kV V_0 = -60 kV
V_P = -30 kV T_r = 700 ns
V_R = -30 kV T_h = 900 ns

(a) Without Back Corona

(r_d = 5 x 10^{11} ohm-cm)

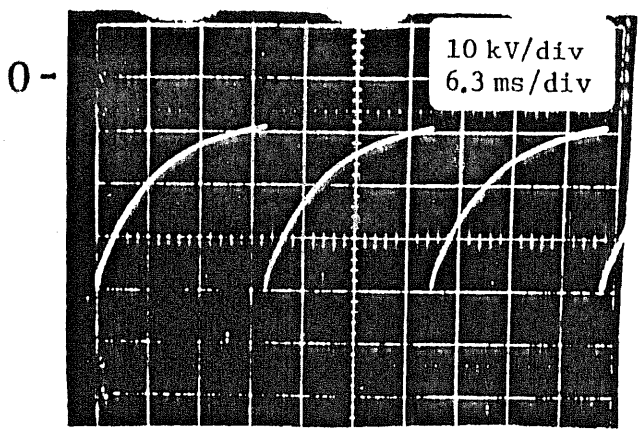

V_M = -62 kV V_0 = -50 kV
V_P = -53 kV T_r = 700 ns
V_R = - 9 kV T_h = 900 ns

(b) With Back Corona

(r_d = 1 x 10^{11} ohm-cm)

Fig. 3.2 Effect of Back Corona on Pulse Voltage Wave Form

3-3. Test by Coal-Fired Test Rig of Electrostatic Precipitator

3-3-1. Introduction

The performance enhancement has been confirmed in the first series of collection tests by the race-track type laboratory precipitator with f = 12.1 s/m where the fly ash samples with the resistivity level of 5×10^{11} - 1×10^{13} ohm-cm are used. The test has continued using the test facility simulating more precisely a practical electrostatic precipitator comprizing of a furnace burning 50 kg of pulverized coal per an hour, gas cooling system, and the elecrostatic precipitator with a collection duct spaced in 300 mm with f = 35 s/m and the corona electrode with barbed wires.

In order to confirm the effectiveness of the direct-coupled pulse energization in the high resistivity level of more than 10^{13} ohm-cm where the conventional dc-energized collection field causes severe back corona, a difficult coal is supplied and the exhaust gas is cooled down to T_g = 150 °C to obtain $r_d = 2 \times 10^{13}$ ohm-cm. The test is also made at T_g = 110 °C where r_d is reduced to the lower level and the dc-energized field can achieve a normal operation with a high efficiency. In both cases the pulse energized field shows performance enhancement with a high collection efficiency of more than 99 %. In this paragraph, are reported the results in this pilot plant test.

3-2-2. Experimental Apparatus

Fig. 3.3 shows the pulser circuit of this direct-coupled pulse energization system. The pulser used here again consists of the high voltage transformer with the half-wave rectifier diode and the resistor to

two cases as shown latter. The resistivity is affected by SO_3 in the exhaust gas especially in the lower gas temperature (T_g < 120 °C in this case) and the dust resistivity at T_g = 110 °C is probably in much lower level of less than 10^{11} ohm-cm. The dust mass loading is measured by the constant dust monitor based on the light scattering which is calibrated by filtering occasionally. The charge-to-mass ratio at the outlet, q/m, is also measured by a suction type Faraday cage.

3-3-3. Test Results

(A) Back Corona Suppression Effect:

Fig. 3.5 shows the V-I characteristics in the conventional dc-energized collection field. Here V denotes the average voltage applied to the precipitator and I the average output current of the high voltage transformer outlet. In the case of Fig. 3.53(a) with T_g = 110 °C, the V-I curve shows the ordinally corona characteristics indicating no back corona takes place in the dc-energized collection field. On the other hand in the case of Fig. 3.5(b) with T_g = 150 °C, a distorted hysteresis curve typical to severe back corona appears.

Fig. 3.6 shows the light activity of both the corona electrode and the collection electrode in the case of T_g = 150 °C. This is observed from the downstream side of the precipitator where the gas channel duct is removed just after the gas flow is stopped. In the case of the dc-energized field as shown in Fig. 3.6(a), the light induced by the negative dc corona can be seen only in parts of the corona electrode opposite to the dust layer where back corona induced light is observed. This phenomena may be explained by the positive feed back between the negative dc corona and back corona. Once back corona in the dust layer takes place, positive ions from the back corona points are driven by the dc field to the corona electrode. Although

the amount of positive ions is reduced during the traverse in the bi-polar ionic field due to recombination and diffusion, they form a sheath around the corona points of the wires and enhance the local field. As the result, dc corona activity is enhanced to produce more excess negative ions, which again enhance back corona. The vertical line in a hysteresis curve of Fig. 3.5(b) is produced by this process. It should be noted that the non-uniformity in gas temperature distribution caused by corona wind in the no gas flow condition also enhances the partiality of dc corona activity.

Fig. 3.6(b) shows the light activity in the pulse-energized fields. A luminous region in collection electrode caused by back corona is still observed, yet its extent and luminosity is remarkably reduced. The most significant difference from the dc-energized field is the uniformity in corona activity of the corona electrode. Even in this case of very high resistivity and non-uniform gas temperature distribution, the light of pulse-induced corona becomes very uniform in the entire corona electrode. Moreover not only from the spikes of the barbed wires but also from the wire edges, pulse-induced corona is emitted. The ionic current distribution becomes very uniform in the entire collection electrode, consequently.

(B) Pulse Voltage Wave Forms:

Fig. 3.7 shows the voltage wave forms, V_{EP}, measured at the pulse inlet of the corona electrode in the direct-coupled pulse energization. Figs. 3.7(a-1) and (b-1) indicate the magnified LC oscillation part existing in the tip of the saw-teeth wave forms as shown in Figs. 3.7(a-2) and (b-2). The pulse rise time, T_r, defined by the time of the first half cycle of the LC oscillation is adjusted to be $T_r = 2$ μs which can be obtained in a practical full-scale elecrostatic precipitator of, say, 5000 m^2 collection area. The effect of T_r is discussed latter.

The difference in the saw teeth wave forms between Figs. 3.7(a-2) and

(b-2) can be noticed, especially in the final voltage, V_R, of one pulse period. In the case of Fig. 3.7(a-2) (T_g = 110 °C) without back corona in the collection field, V_R = -25 kV and the average of the saw teeth voltage, V_{EP} = -30 kV are obtained. On the other hand in the case of Fig. 3.7(b-2) (T_g = 150 °C), a continuous rapid decay in the saw teeth voltage wave form produces V_R = -10 kv and V_{EP} = -15 kV. The decay continues even in the lower voltage level below the dc corona threshold, V_c = -18 kV in this case. This is one of the evidence that back corona takes place even in the pulse-energized field, yet the collection performance is in a very high level as described in the next paragraph.

(C) Collection Performance Enhancement:

In Table 3.4 are shown the test results in the typical cases of I = 0.3 mA/m^2 and V_M = -65 kV where I is the average current density in the dc-energized field, V_M the maximum voltage in the pulse-energized field, the collection efficiency, w the Deutsch migration velocity (apparent migration velocity), and H the enhancement factor by the pulse-energization base on w. The dc-energized collection field without back corona (T_g =110 °C) shows a reasonably high collection performance (η = 99.48 %, w = 15.1 cm/s). But the collection performance declines to η = 84.2 % and w = 5.3 cm/s when severe back corona takes place. The pulse-energized collection field shows a high collection efficiency in both cases of T_g = 110 °C and 150 °C (η = 99.83 % and 99.02 %, respectively). Even in the case of T_g = 110 °C where dc-energized collection field shows a high performance, the pulse-energized field enhances the performance (H = 1.21). The significant performance enhancement is obtained in case of T_g = 150 °C (H = 2.50). The direct-coupled pulse energization can cope with a wide dust resistivity range to enhance the collection performance.

Even in the pulse-energized field as described previously, back corona, although its severity is reduced, can be recognized in the case of

T_g = 150 °C. But the collection performance is kept in a high level. This fact leads us to an assumption that back corona emits positive ions in the low field domain in the voltage wave form shown in Fig. 3.7(b-2), and negative ions on the other hand are existing in a higher field domain of the first 2 - 3 ms of the pulse cycle and moves in a mass toward the collection electrode. As the result negative charging becomes more effective in the pulse-energized field due to the higher charging field which is, moreover, enhanced by the space charge effect of a negative ion cloud of high concentration and the charge elimination due to back corona becomes less effective than in the dc-energized field. This difference between the dc-energized and the pulse-energized fields comes from the difference in corona features. The pulse-induced corona occurs once in one pulse period at the leading edge of the first half cycle of the LC oscillation, but the plasma density is much higher. The ionic current becomes again pulsive with a very high peak to produce a stronger space charge field in front of the cloud of ions. On the other hand the dc-corona is in the fashion described as the Trichel pulse which occurs very frequently (up to several kHz). The total amount of the negative ions is larger than in the pulse-induced corona, but the ionic current becomes again a continuous dc flow. The details of this assumption are to be inspected. Needless to say the uniformity in corona discharge in the corona electrode as shown in Fig. 3.6(b) enables the collection field in the precipitator to be fully used as designed as to achieve a high collection performance.

Fig. 3.8 shows the effects of I and V_M on the collection efficiency of the dc-energized field and the pulse-energized field respectively in the case of T_g = 110 °C, and Fig. 3.9 in the case of T_g = 150 °C. The collection efficiency of the dc-energized collection field increases as increasing the current density, I, in both cases of Figs. 3.8(a) and 3.9(a), but the value of w increases only 2 cm/s in both cases by increasing current from I = 0.1 mA/m^2 to 0.5 mA/m^2 indicating that the high

current operation of dc-energized field is not a very effective mean especially in considering energy consumption. The collection efficiency of the pulse-energized field rises in both cases of Figs. 3.8(b) and 3.9(b) with increasing V_M. This is because the uniformity and the intensity of the pulse-induced corona are raised with a higher V_M. In the case of Fig. 3.9(b), the flash over voltage in the collection field is measured to be -70 kV. V_M with 80 % of the flash over voltage (V_M = -56 kV) which is considered to ensure the no sparking operation in practical plants shows a very high collection efficiency of $\eta > 98$ % (Fig. 3.9(b)). Moreover surprisingly to say, even with the very low peak voltage in pulse energization such as V_M = -45 kV and -35 kV in Figs. 3.8(b) and 3.9(b), respectively, maintains the same level of collection performance of dc-energized field. These values are same as the peak voltages of dc-energization, whereas the current level is much reduced. This is again due to the difference between the pulse-induced corona and the dc corona.

(D) Charging Performance Enhancement:

Figs. 3.10 and 3.11 show the charge-to-mass ratio, q/m, expressed in relation of the dust mass loading, W_o, both measured at the outlet of the precipitator. In the case of Fig. 3.10 (T_g = 110 °C), the data of both the dc-energization and the pulse-energization lie on the same line. On the other hand, in the case of Fig. 3.11 (T_g = 150 °C) the curve of the dc-energization lies below the one of the pulse-energization which still follows the curve of Fig. 3.10. The reduction in q/m in the case of the dc-energization in Fig. 3.11 is due to severe back corona to produce a bi-polar ionic field with high positive ion content. But the charging performance is again recovered in the pulse-energized field to the level in the normal operation. Here again the superiority of the pulse-energization is proved.

current operation of dc-energized field is not a very effective mean especially in considering energy consumption. The collection efficiency of the pulse-energized field rises in both cases of Figs. 3.8(b) and 3.9(b) with increasing V_M. This is because the uniformity and the intensity of the pulse-induced corona are raised with a higher V_M. In the case of Fig. 3.9(b), the flash over voltage in the collection field is measured to be -70 kV. V_M with 80 % of the flash over voltage (V_M = -56 kV) which is considered to ensure the no sparking operation in practical plants shows a very high collection efficiency of $\eta > 98$ % (Fig. 3.9(b)). Moreover surprisingly to say, even with the very low peak voltage in pulse energization such as V_M = -45 kV and -35 kV in Figs. 3.8(b) and 3.9(b), respectively, maintains the same level of collection performance of dc-energized field. These values are same as the peak voltages of dc-energization, whereas the current level is much reduced. This is again due to the difference between the pulse-induced corona and the dc corona.

(D) Charging Performance Enhancement:

Figs. 3.10 and 3.11 show the charge-to-mass ratio, q/m, expressed in relation of the dust mass loading, W_o, both measured at the outlet of the precipitator. In the case of Fig. 3.10 (T_g = 110 °C), the data of both the dc-energization and the pulse-energization lie on the same line. On the other hand, in the case of Fig. 3.11 (T_g = 150 °C) the curve of the dc-energization lies below the one of the pulse-energization which still follows the curve of Fig. 3.10. The reduction in q/m in the case of the dc-energization in Fig. 3.11 is due to severe back corona to produce a bi-polar ionic field with high positive ion content. But the charging performance is again recovered in the pulse-energized field to the level in the normal operation. Here again the superiority of the pulse-energization is proved.

(E) Effect of Pulse Rise Time on Collection Performance:

The effect of the pulse rise time, T_r, on the collection performance is tested in the case of T_g = 150 °C. The inductance inserted in the pulse circuit as shown in Fig. 3.3 is removed to get the shorter T_r. A very sharp rising pulse with T_r = 150 ns is obtained and the saw-teeth pulse wave form becomes as shown in Fig. 3.12. A very sharp drop in the decay phase (see Fig. 2.31(a)) and two tips in the saw-teeth caused by the secondary spark in the gap due to a very sharp decay in V_{EP} to produce an enough voltage difference in the gap can be recognized. These are the obvious evidence of very active pulse-induced corona. The spark voltage in the precipitator is recognized to be higher (V_s > -70 kV at T_g = 150 °C; V_s = -70 kV in case of T_r = 2.0 μs). The shorter pulse rise is preferrable in order to operate the precipitator stable without sparking. But the collection performance itself can not be raised as compared to the case of T_r = 2.0 μs in this particular case. Probably because the uniformity and the ionic current density even in the case of T_r = 2.0 μs is satisfactory to get a good performance. This fact encourages us to apply this direct-couple pulse energization to an electrostatic precipitator with a very large dimensions where T_r could not be reduced than 2 μs because of a very large capacity between the corona electrode and the collection electrode.

3-3-4. Conclusion

The pilot plant test of the direct-coupled pulse-energization is performed and the following conclusions are obtained.

(1) In the case of $r_d = 2 \times 10^{13}$ at T_g = 150 °C, the dc-energized collection field causes severe back corona and V-I characteristics becomes a hysteresis curve. The corona activity of the corona electrode in

this case is restricted in the back corona region. The direct-coupled pulse energization corrects the corona activity and the entire corona electrode becomes active to produce corona very uniformly.

(2) Even in the pulse-energized field, back corona weaker than in the dc-energized field can be recognized and the saw teeth pulse wave form shows a continuous decay to the low voltage level of V_R which is far below the dc corona threshold. But the collection performance is in the high level (η = 99.02 % at V_M = -65 kV) and the performance enhancement becomes also remarkable (H = 2.50).

(3) In the lower resistivity level at T_g = 110 °C, the performance can be raised in the pulse-energized field to η = 99.83 % and the performance enhancement can be still expected as large as H = 1.21.

(4) The collection performance of the pulse energization is increased as increasing the peak voltage, V_M, in both cases of T_g = 110 °C and 150 °C. In the latter case, more than 98 % collection efficiency can be achieved by V_M = 80 % of the spark voltage in the collection field.

(5) The relation between the charge-to-mass ratio, q/m, and the dust mass loading, W_0, both measured at the outlet of the EP can be expressed in the same curve both in the dc-energized field and in the pulse-energized field in the case of T_g = 110 °C. In the case of T_g = 150 °C, q/m - So curve of the pulse-energized field still follows the same curve of T_g = 110 °C. But one obtained by the dc-energized field lies blow it indicating that back corona reduces the charging performance.

(6) The effect of the pulse rise time, T_r, on the collection performance can not be recognized in the case of T_g = 150 °C. The change in the saw-teeth voltage indicates the shorter T_r with 150 ns produces the better corona characteristics. But the collection efficiency can not be raised compared to the case with T_r = 2.0 μs.

Table 3.4 Comparison of Collection Performance of DC Energization and Pulse Energization in Test Precipitator of Coal Combusion Rig

Gas Temperature T_g (°C)	DC-Energization ($I = 0.3$ mA/m^2)		Pulse-Energization ($V_M = -65$ kV)		Enhancement Factor H
	η(%)	w(cm/s)	η(%)	w(cm/s)	
110	99.48	15.1	99.83	18.2	1.21
150	84.19	5.3	99.02	13.2	2.50

key

I : ionic current density in dc-energized collection field

V_M : maximum voltage applied in pulse-energized collection field (peak voltage in the first cycle of LC oscillation)

η : collection efficiency

w : Deutsch migration velocity

H = w (pulse-energization) / w (dc-energization) : enhancement factor

$r_d = 2 \times 10^{13}$ ohm-cm at $T_g = 150$ °C

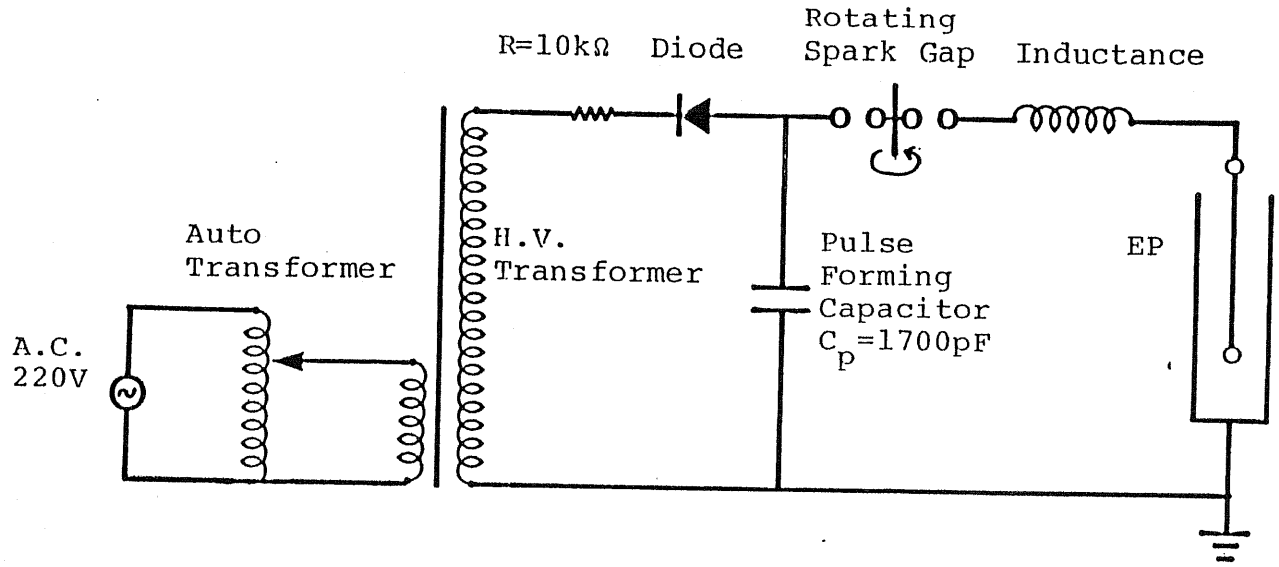

EP: 2D = 300 mm (duct spacing)
Corona Electrode: Berved Wires
$F = 5.57\ m^2$ (collection area)
$f = 35\ s/m$ (specific collection area)
$V_g = 0.9\ m/s$ (gas velocity)

Fly Ash: $w_i = 4.5 - 5.5\ g/Nm^3$ (inlet dust mass loading)
$d_m = 6.5\ \mu m$ (mass median diameter)
$r_d = 2 \times 10^{13}$ ohm-cm (dust resistivity at 150°C)

Fig. 3.3 Test Circuit and Conditions of Direct-Coupled Pulse Energization for Test Precipitator of Coal Combustion Rig

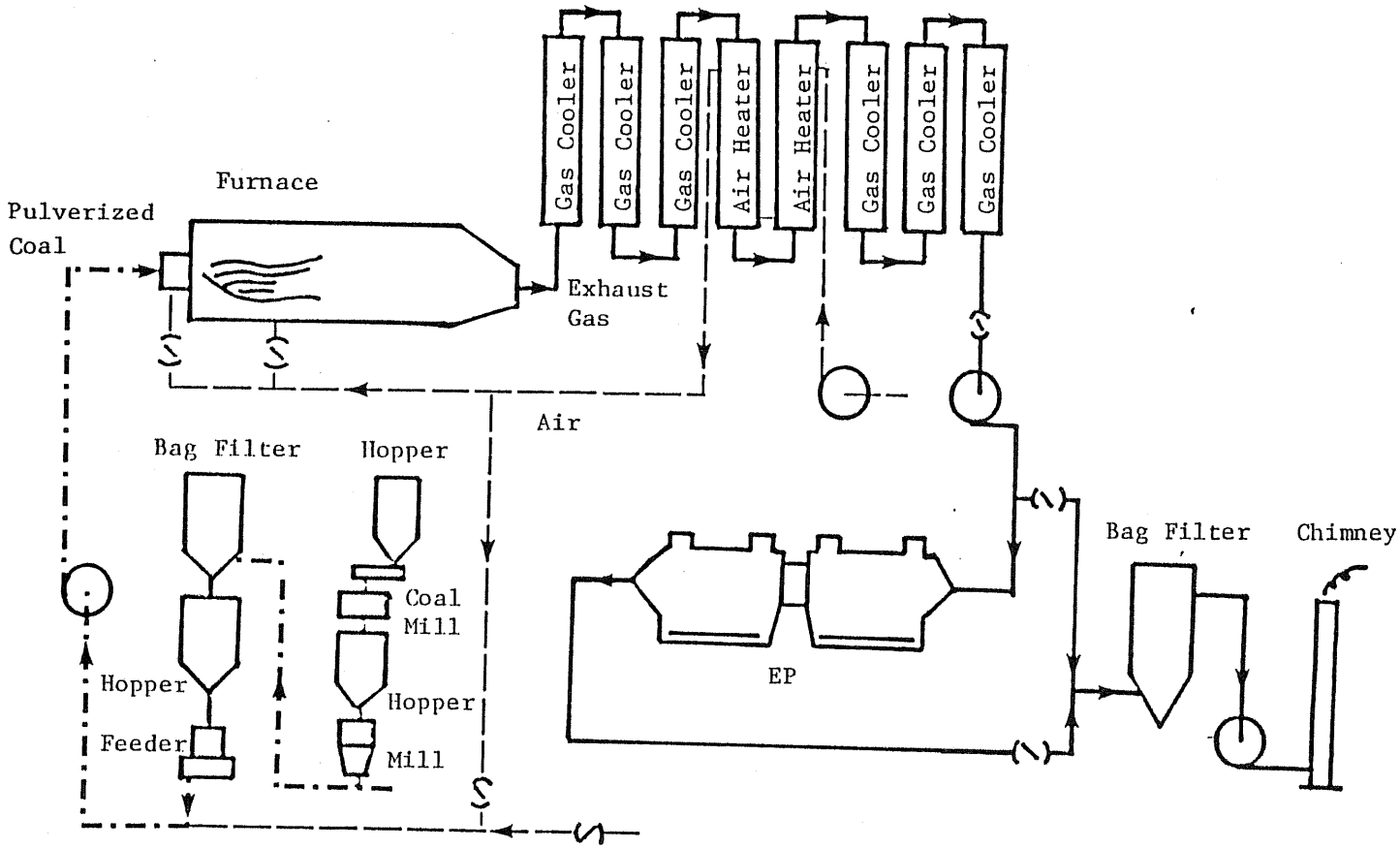

Fig. 3.4 Experimental Set-Up of Electrostatic Precipitator of Coal Combustion Rig

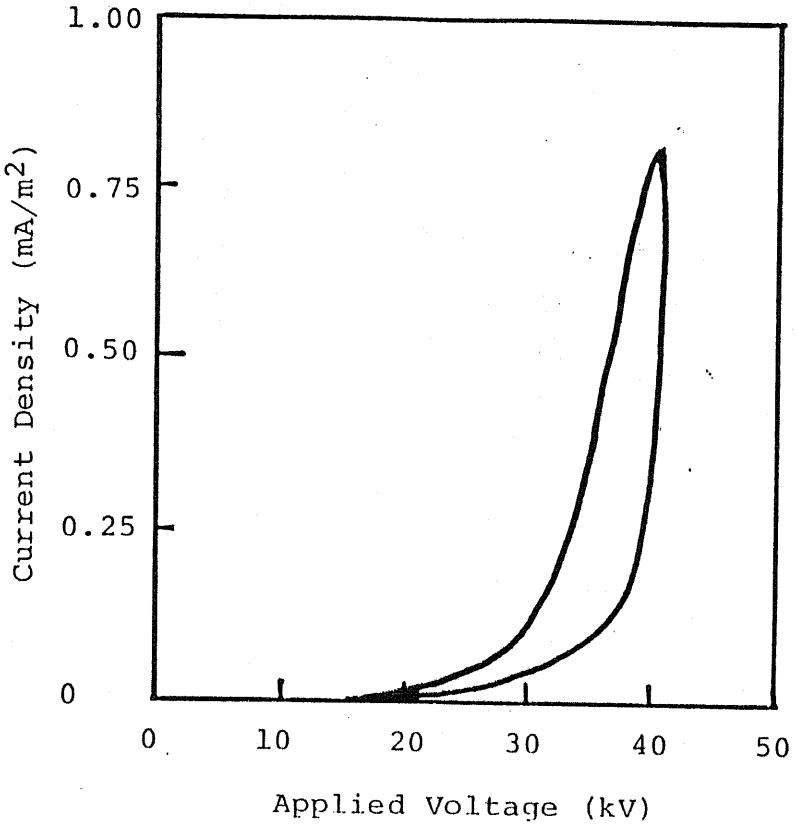

(a) normal curve without back corona
(T_g = 110 °C)

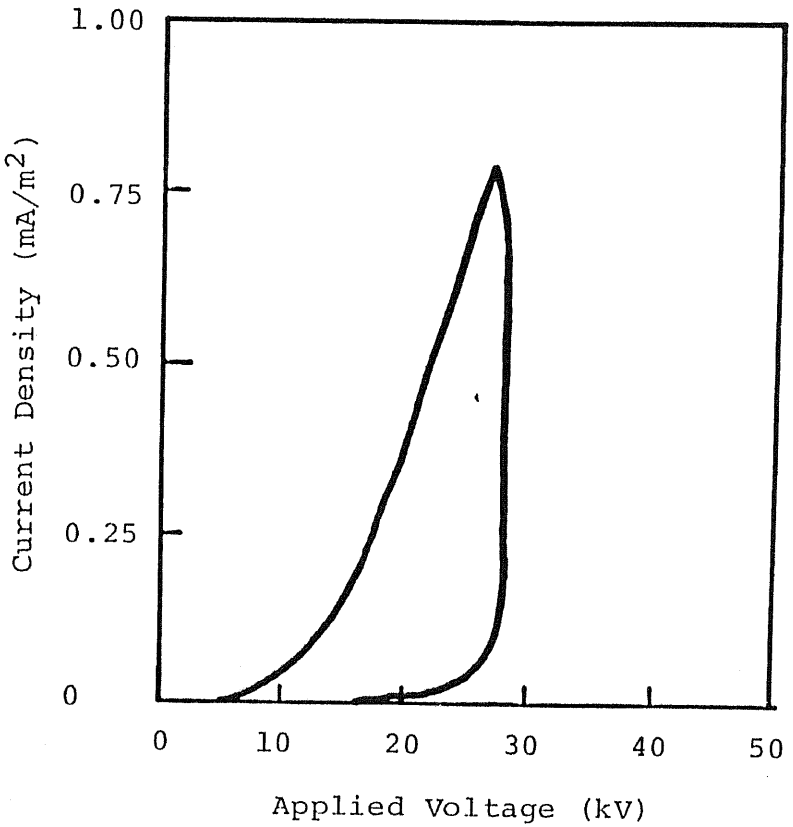

(b) hysteresis cure with severe back corona
(T_g = 150 °C)

Fig. 3.5 V - I Characterisitics in DC Energized Collection Field

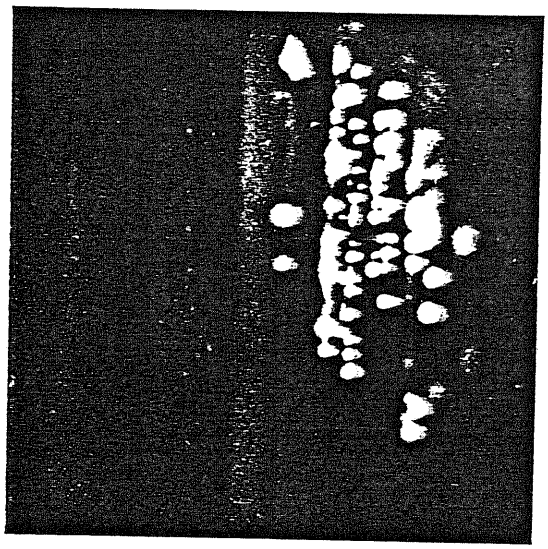

(a) dc-energized field

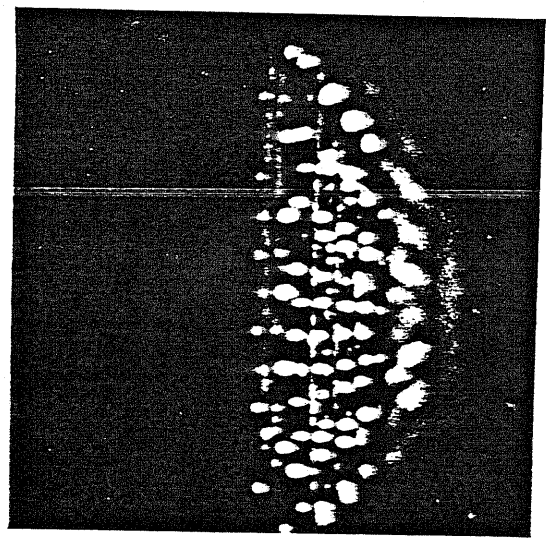

(b) pulse-energized field

Fig. 3.6 Correction of Back Corona and Enhancement of Uniformity in Light Activity of Corona Wires by Pulse-Energization (T_g = 150 °C)

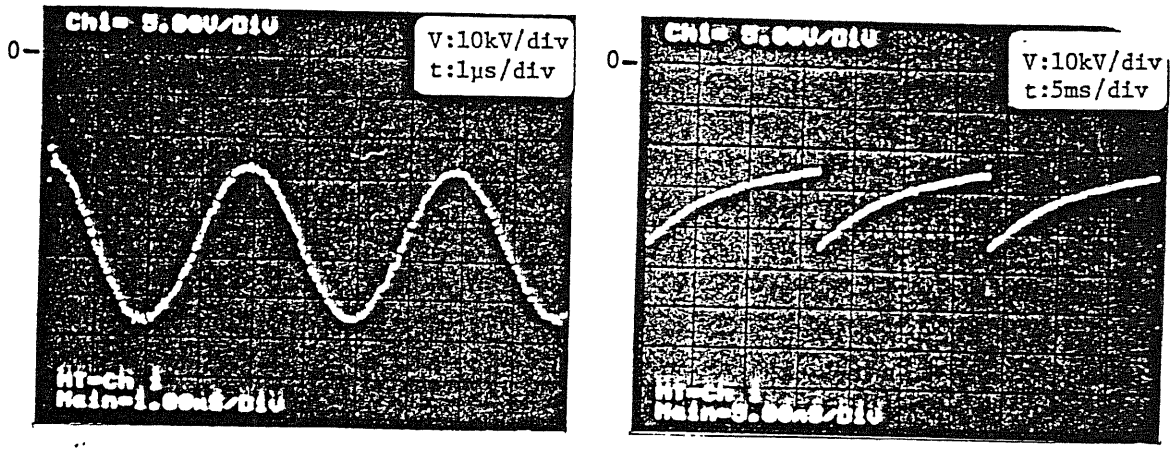

(a-1) Magnified LC Oscillation (a-2) Saw-Teeth Pulse Wave Form

(a) No Back Corona, $T_g = 110$ °C

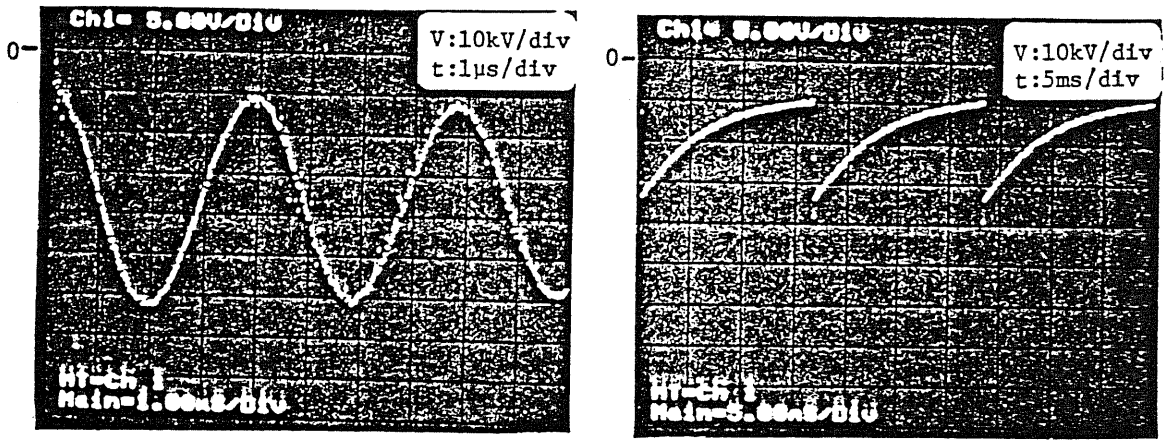

(b-1) Magnified LC Oscillation (b-2) Saw-Teeth Pulse Wave Form

(b) Slight Back Corona, $T_g = 150$ °C

Fig. 3.7 Pulse Voltage Wave Form, V_{EP}, Measured at the Inlet Terminal of Corona Electrode

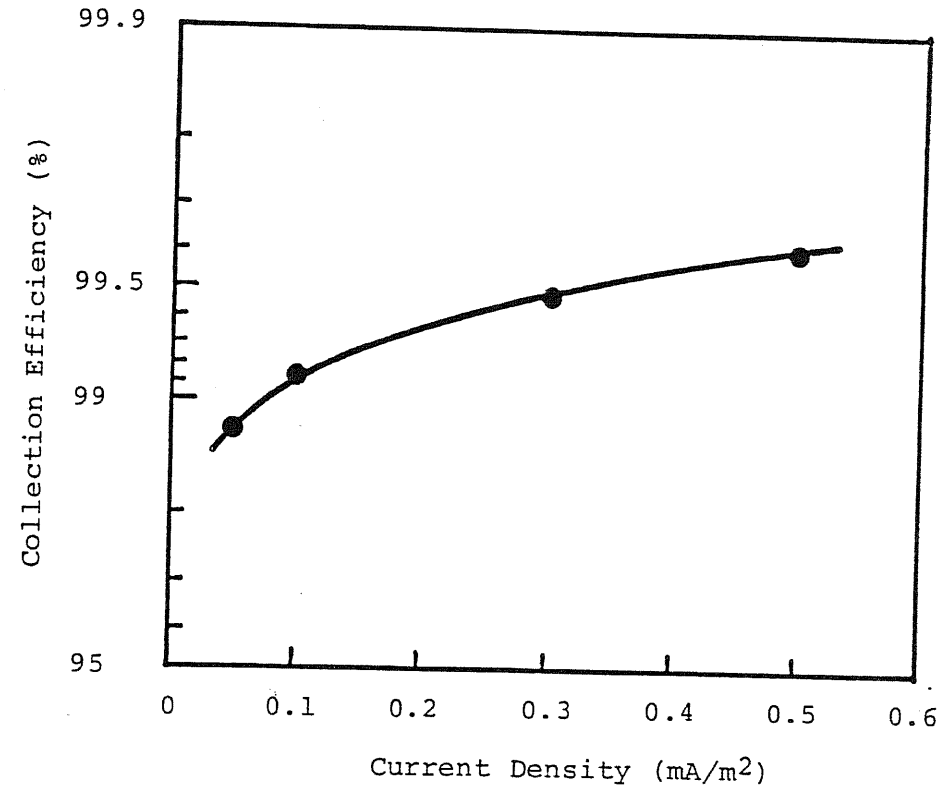

(a) dc-energization

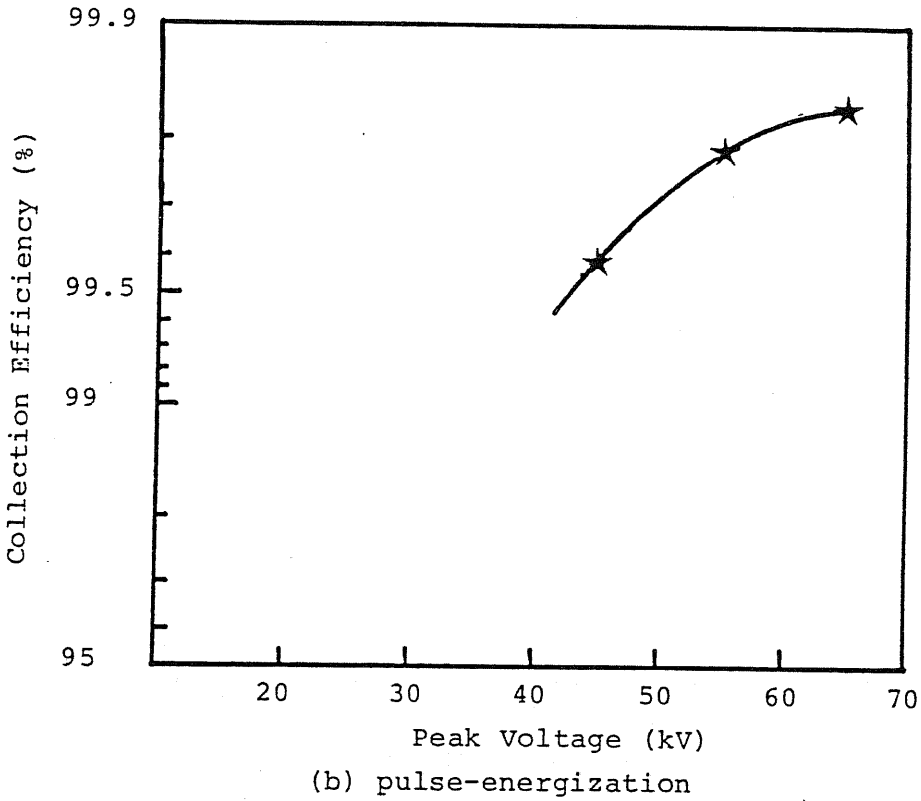

(b) pulse-energization

Fig. 3.8 Enhancement of Collection Performance by Pulse Energization (no back corona in both dc- and pulse-energized fields; T_g = 110 °C)

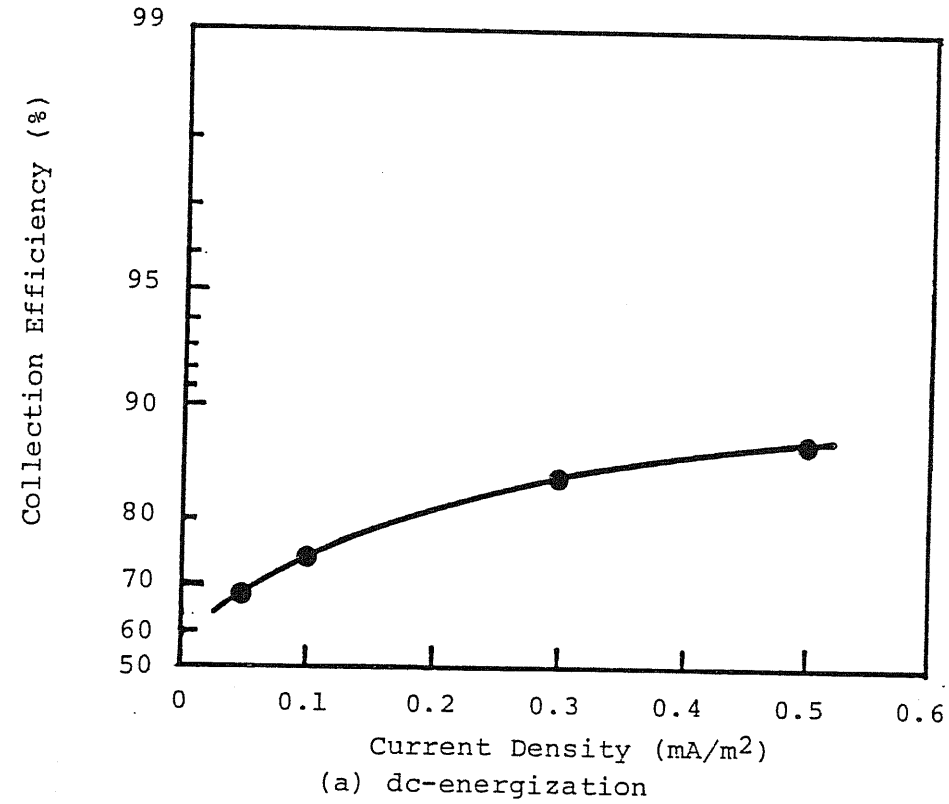

(a) dc-energization

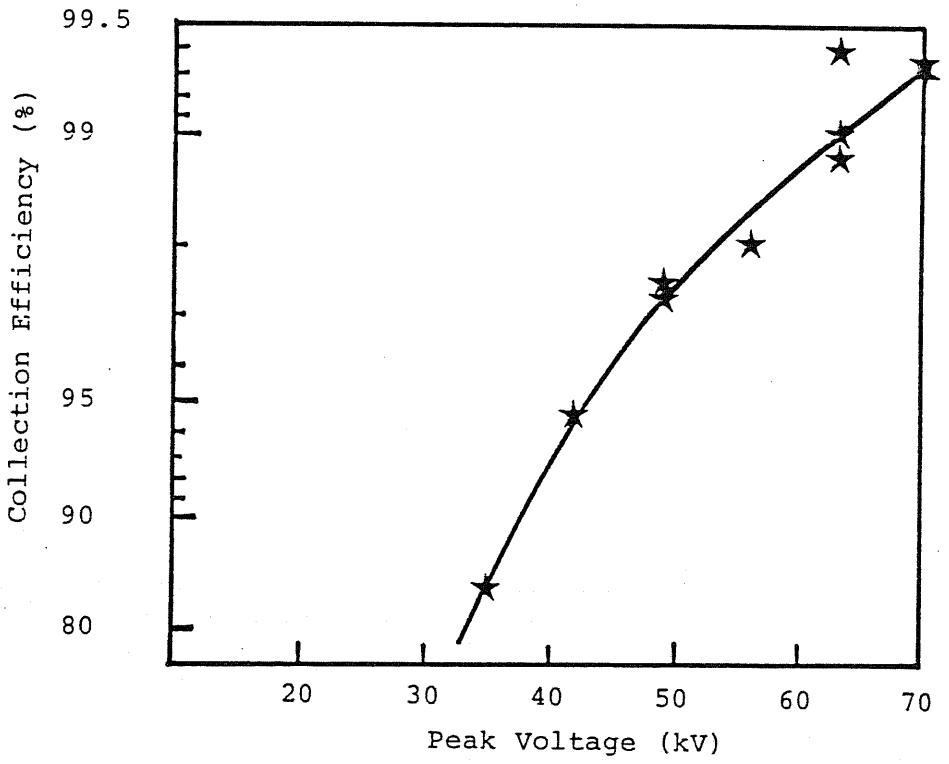

(b) pulse-energization

Fig. 3.9 Enhancement of Collection Performance by Pulse-Energization (severe back corona in dc-energized field and slight back corona in pulse-energized field; T_g = 150 °C)

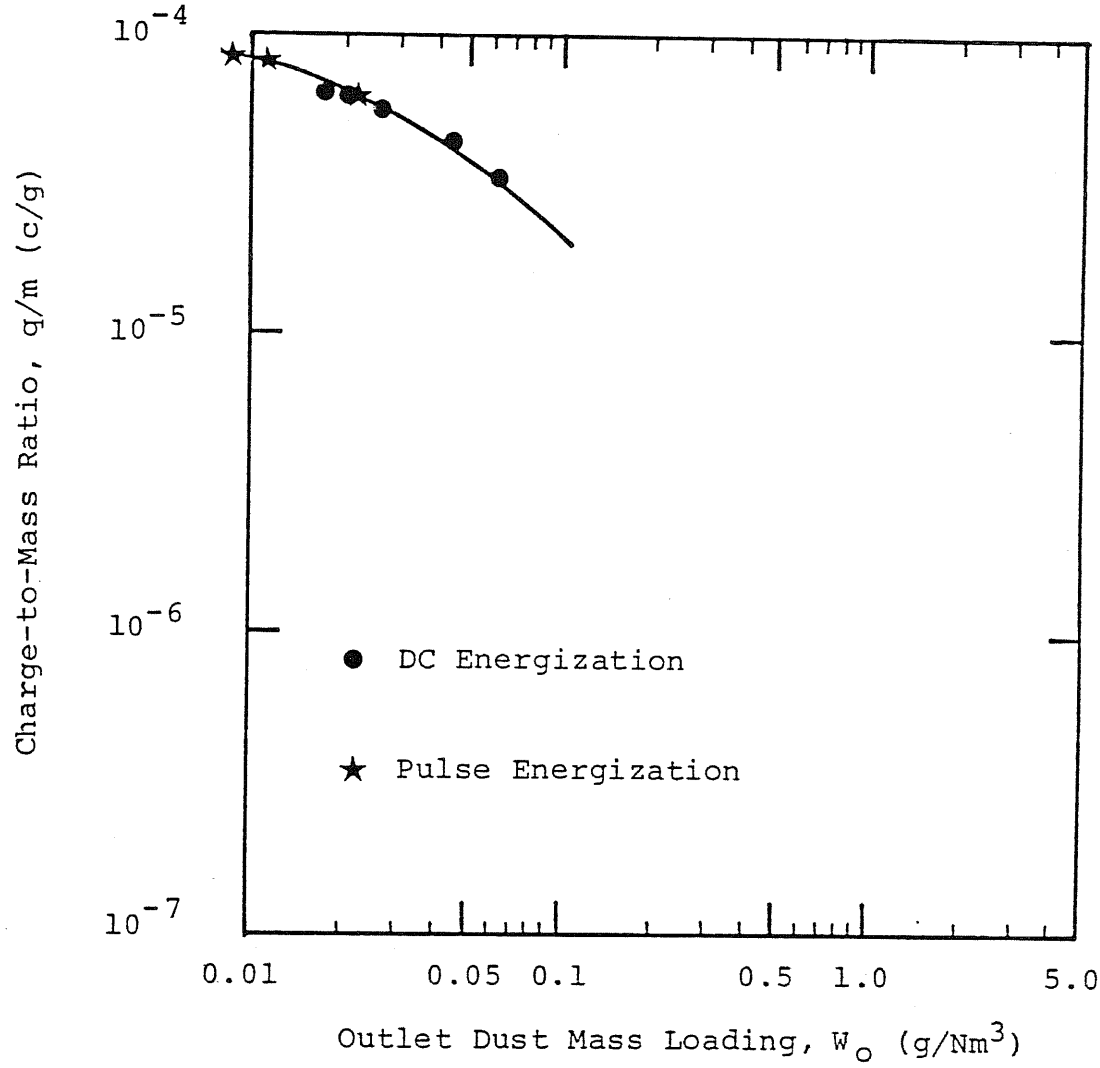

Fig. 3.10 Relation Between Outlet Mass Loading and Charge-to-Mass Ratio (no back corona in both dc- and pulse-energized fields; T_g = 110 °C)

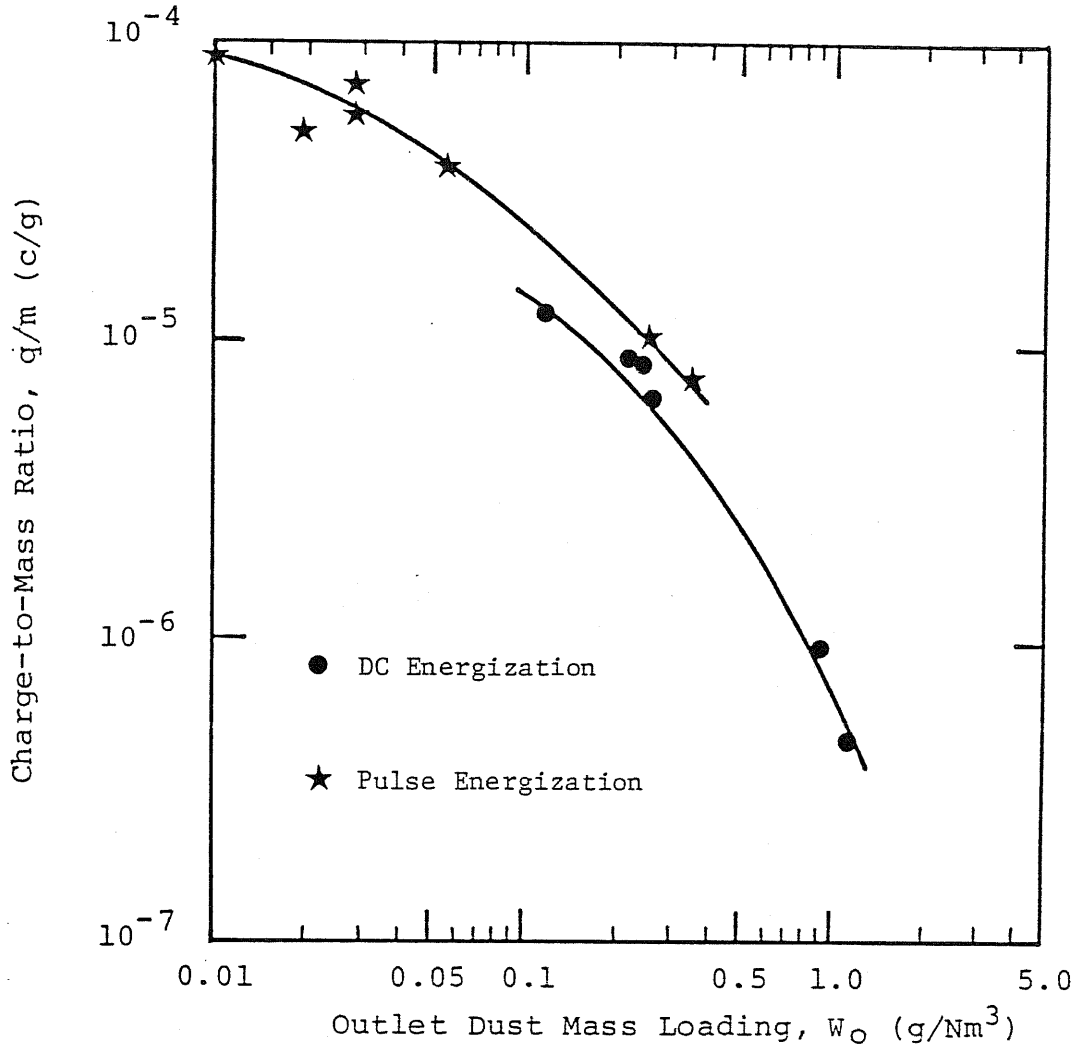

Fig. 3.11 Difference in Charging and Collection Performance between DC-Energized and Pulse-Energized Collection Fields (severe back corona in dc-energized field and slight back corona in pulse-energized field; T_g = 150 °C)

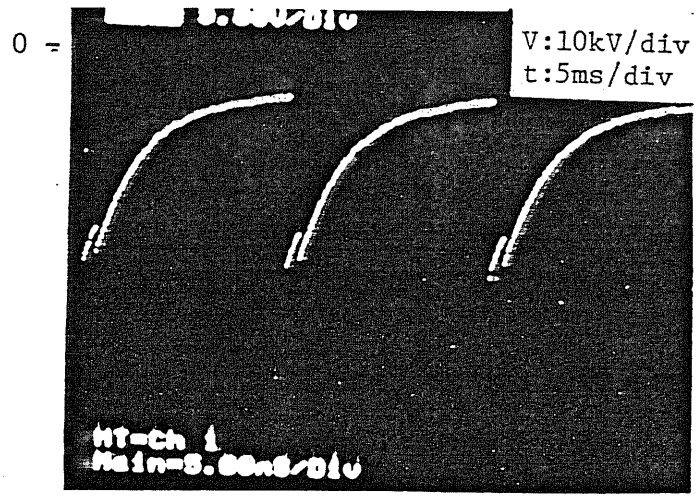

Fig. 3.12 Change of Pulse Voltage Wave Form Caused by Very Fast Rising Pulse (T_r = 150 ns; T_g = 150 °C)

CHAPTER 4. Cassette Type Pulser Module for Direct-Coupled Pulse Energization

4-1. Introduction

As shown in the previous two chapters, the direct-coupled pulse energization possesses the supriority in back corona correction and the inherent possibility of reduction in an initial cost. In order to apply it to the existing electrostatic precipitators of the practical scale, the pulse power supply is developed. As the initial cost is the most important factor in introducing it to the practical use, the existing dc power supply is used as the power source for the cassette type pulser module to be inserted between the existing dc power supply and the existing precipitator.

Fig. 4.1 shows the basic concept of the cassette type pulser module developed. The output voltage of the existing dc power supply is usually below the necessary charging voltage, V_0, of the pulse forming condenser, C_p. The voltage-doubling circuit using LC charging allows to charge C_p up to the necessary level. The rotating spark gap is driven by a servo motor so as to change the revolutions. By controlling both the thyristor of the voltage doubling circuit and the servo moter, a pulse repetition frequency is changed up to 200 Hz continuously.

In this chapter, are shown the design and the test results in the laboratory using a simulated load, of the pulser module capable to energize a practical precipitator of up to 1800 m^2 collection area.

It should be noted that the main constructions of the pulser are in common in all of the pulse energization systems shown in the chapter 2, and

the pulser module developed here for the direct-coupled pulse energization can be also used for the other pulse energization systems by connecting a coupling condenser unit, a separate dc power supply, and other attachments.

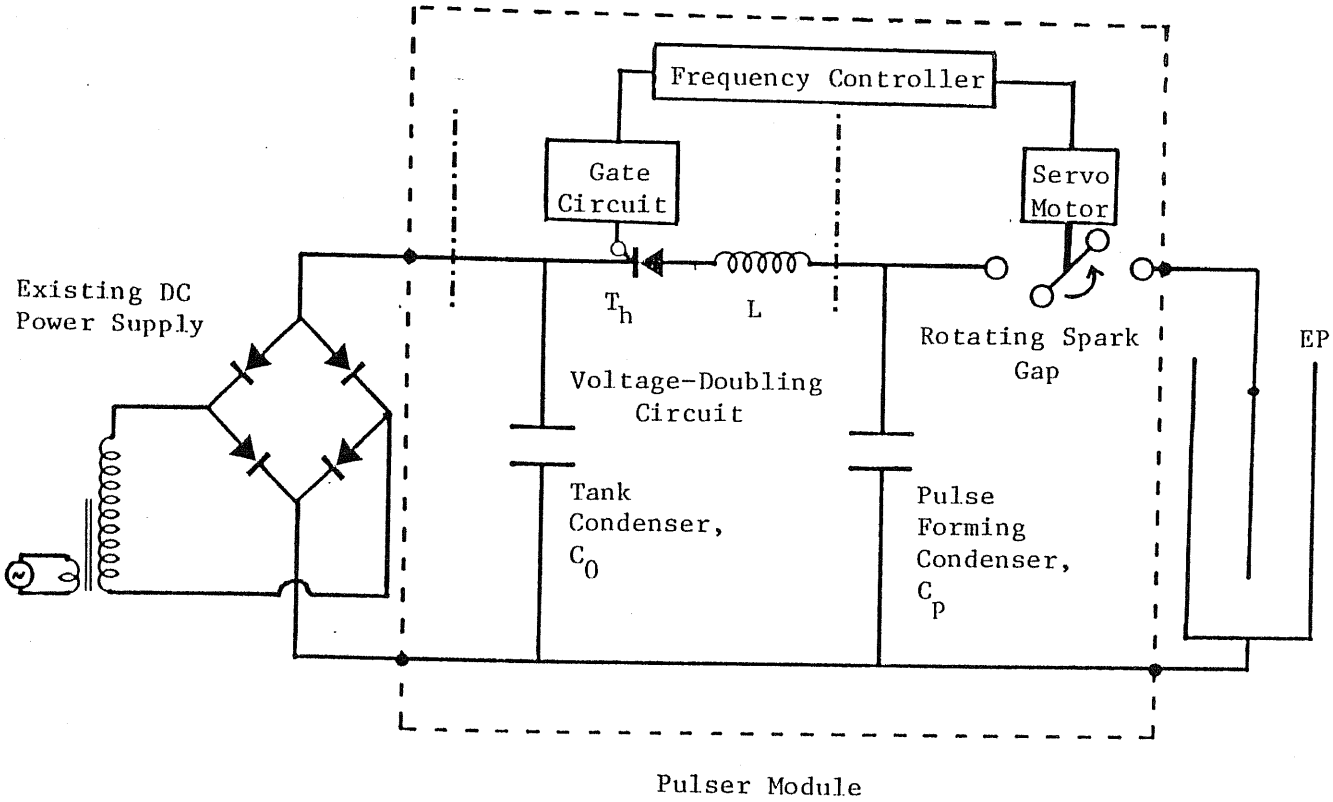

Fig. 4.1 Basic Circuit Diagram of Cassette Type Pulser Module Inserted between Existing DC Power Supply and Existing Precipitator For Direct-Coupled Pulse Energization

4-2. Design of Pulser Module

4-2-1. Practical Circuit Diagram

A medium size electrostatic precipitator of a 1200 - 1800 m^2 collection area and a standard duct spacing of 300 mm is chosen as a target of the pulser to be constructed.

Fig. 4.2 shows the practical circuit diagram of the cassette type pulser module inserted between the existing dc power supply and the simulated load out of a capacitor and a resistor. In this case, the module is divided into two tanks, one for the voltage doubling unit and another the pulse forming condenser unit with the rotating spark gap on its top, in order to reduce in the circuit inductance, to shield each other, and to be easily moved and set. Fig. 4.2 also shows the circuit diagram of the standard dc power supply for a electrostatic precipitator used in this series of tests, and the simulated load whose capacity of 63 nF (about 1200 - 1300 m^2 collection area in standard duct spacing).

There are protection components (F, M, and O in Fig. 4.2) and the gate triggering unit (I, J, and K) added to Fig. 4.1. The effect of these components will be shown later.

In the case of the standard electrostatic precipitators with a 300 mm duct spacing and the operating temperature of 100 - 200 °C, the necessary voltage of the direct-coupled pulse energization is assumed to be V_R = -20 kV, and V_M = -60 kV where V_R is the final voltage in one pulse period and V_M the peak voltage of the first LC oscillation cycle (see Fig. 2.31(a)). In Table 4.1 are shown the specifications of the main elements and the requirements calculated for the output condition of C_{EP} = 63 nF (capacity of the simulated load), V_M = -60 kV, and V_R = -20 kV. In this paragraph are reported the designing process, and the estimation of the

requirement of each elements based on the output condition above.

Fig. 4.3 shows the appearance of the pulser module constructed ((a): the hood duct removed, (b): connected to the dc power supply and the simulated load). The total weight of the pulser unit is about 1,500 kg.

4-2-2. Rotating Spark Gap

Fig. 4.4 shows the rotating spark gap. There are two stator electrodes supported by the insulators in both sides, and four rotor electrodes attached on the insulated shaft. It is rotated by the ac servo motor in a speed of up to 3000 rpm. A spark takes places when a pair of the rotor electrodes draw near to the stator ones and their gap distances become small enough. Four sparks are produced in one revolution in this case, so that the pulse repetition frequency is altered up to 200 Hz.

The electrodes are made of tungsten-copper sinter alloy, so as to reduce the erosion due to numerous sparks with 2 - 3 kA of the peak current. And they are designed to be easily replaced. The tests on the electrode erosion will be reported later.

4-2-3. Pulse Forming Condenser Tank

(A) Pulse Forming Condenser Bank:

As shown in Fig. 2.40, the total capacity of the pulse forming condenser, C_p, should be in the range of $C_{EP} \leqq C_p \leqq 1.5\, C_{EP}$ to get a satisfactory pulse peak voltage. The pulse forming condenser unit installed in this pulser has $C_p = 93.3$ nF. As a result, C_{EP} satisfying the above condition becomes,

$$62.2 \text{ nF} \leqq C_{EP} \leqq 93.3 \text{ nF}$$

Assuming that the capacity of the unit collection area of a precipitator with a standard duct spacing (2D = 300 mm) is c = 50 pF/m^2, C_{EP} in the above range amounts to

$$1244\ m^2 \leqq F \leqq 1866\ m^2$$

where F is the total collection area.

A ceramic condenser made from strontium titanate coated by epoxy resins is used as the condenser element. A number of ceramic condensers (420 pieces are used) are carefully assembled as shown in Fig. 4.5. The rating of this condenser unit becomes V = 120 kV. It is noted that this rating of V = 120 kV provides an enough allowance even in the worst case as shown later (V_{pp} in Table 4.1).

(B) Surge Absorbing Diode Unit:

It is a common feature of high voltage condensers, that they are fragile to a surge voltage with the opposite polarity to the charging one. Such a surge voltage is produced by a spark in the precipitator, and the occurrence of a spark is not avoidable in the practical precipitators so that the precaution is needed to avoid the impression of such a surge on the pulse forming condenser unit.

Fig. 4.6 shows the circuit diagram of a spark simulation, and the precaution by the surge absorbing diode unit. The gap distance of the spark controlling gap is changed and a spark is adjusted to occur at around the crest of V_{EP} (applied voltage in the precipitator) and at the instance when the rotating spark gap fired (dead short). The wave forms without the surge absorbing diode unit become as shown in Fig. 4.7(a). It indicates that the spark produces the surge voltage with an opposite polarity in these two cases. Its magnitude becomes largest in the case of a dead short between a corona electrode and a collection electrode (the worst case), as large as the charging voltage.

The element which can absorb a such sharp surge for a long term

operation is the fast recovery diode. As shown in Fig. 4.6, the surge absorbing diode unit is inserted in parallel to the pulse forming condenser unit. Fig. 4.7(b) shows its effect on the reduction in the magnitude of the surge (the worst case) where the resistance of the series resistor, r_s, is changed. This resistor is used to reduce the surge current in the diode unit as shown in Fig. 4.7(c). The magnitude of the surge voltage is reduced by the surge absorbing diode and the smaller value of the series resistor is better in its reduction. If the diode is carefully chosen to bear the surge current, the series resistor can be took off. The surge current, $i_s(t)$, in the worst case becomes:

$$i_s(t) = \frac{C_p}{L} V_0 \exp(-\frac{t}{L/r}) \qquad \text{-----(4.1)}$$

where

L : total circuit inductance

r : total circuit loss

The rating of a surge forward current of a diode is indicated by the product of (current)^2 and time, I^2t. It is roughly estimated by:

$$I^2t = \frac{C_p}{L} V_0{}^2 \frac{2L}{r} \qquad \text{-----(4.2)}$$

and it becomes I^2t = 267 A^2s in the case shown in Table 4.1.

A fast recovery diode with the sufficient rating (rating : 800 V, I^2t = 1000 A^2s) is chosen and 200 pieces are connected in series. Fig. 4.5(b) shows the surge absorbing diode unit (under the insulator) thus assembled, and the resistor to equalize the voltage between the series condensers (also used as a divider to measure the charging voltage).

These elements shown in Figs. 4.5(a) and (b) are put in a tank filled with insulating oil (pulse forming condenser tank).

4-2-4. Voltage Doubling Tank

(A) Tank Condenser:

The voltage doubling circuit is formed by C_0 - T_h - L - C_p as shown in Fig. 4.1. When the thyristor turns on LC oscillation takes place, and when the current becomes zero the thyristor turns off. As the result C_p is charged up to as much as twice of the voltage difference between C_0 and C_p if C_0 is chosen to be $C_0 >> C_p$. Considered that there is no loss in the circuit, the charging voltage of C_p follows:

$$V_0 = V_{OR} + f_d\,(V_{CO} - V_{OR}) \qquad \text{-----(4.3)}$$

where

$f_d = 2C_0/(C_0+C_p)$: voltage doubling factor

V_0 : charging voltage of C_p

V_{CO} : charging voltage of C_0

V_{OR} : minimum voltage of C_p (This changes according to the precipitator operation conditions.)

and the current rise time, T_{dr}, becomes:

$$T_{dr} = (\pi/2)\ L\frac{C_0C_p}{C_0+C_p} \qquad \text{-----(4.4)}$$

C_0 is charged by the dc power supply with a full-wave rectification system and in the case of F_p > 100 Hz (or 120 Hz), C_0 is required to charge C_p twice before charged. C_0 by the second charging is reduced resulting in the reduction of V_M (peak voltage of V_{EP}). To limit the reduction of V_M in less than 10 %, the tank condenser is required to have C_0 > 0.63 F in the condition of Table 4.1. A paper condenser carefully designed for pulsive operation is used as the tank condenser (rating: working voltage = 80 kV, capacity = 0.75 μF) where enough allowance is considered. As a

result, f_d in Eq. (4.3) becomes $f_d = 1.78$.

(B) Coil:

In order to use the cheaper normal type thyristor, the current rise time is needed to be $T_{dr} > 100$ μs. By inserting a series coil, L, as shown in Fig. 4.1, this requirement is satisfied. In this case, the coil current becomes one-way so that the air core is used. The inductance of this air core coil actually made is L = 64 mH. As a result, T_{dr} in Eq. (4.4) becomes $T_{dr} = 114$ μs.

(C) Thyristor Unit:

120 pieces of the thyristors with the rating of V = 1200 V and I(average) = 20 A are assembled in series to provide the total maximum rating of V = 144 kV. In this case also, this unit has enough allowance to the requirements of both the normal conditions and the worst case (Table 4.1).

The current transformer is used to trigger the thyristor. The gate triggering circuit is carefully designed so that all of 120 pieces are simultaneously triggered. Otherwise, a high voltage exceeding the rating appears in an element transiently to destroy it. Insulation of 53.5 kV between the primary and the secondary of the current transformer is needed even for the normal conditions in Table 4.1, if the primary circuit is placed on the grand potential. To reduce the necessary insulation level, it is placed on the potential level of the C_0. The control signals are transmitted by the optical fiber and the insulated transformer is used to supply power for the gate signal amplifier. As the result, the insulation level becomes 8.6 kV in the normal conditions and 45 kV in the worst case (see Table 4.1).

(D) Protection Diode Unit:

The existing dc power supply for an electrostatic precipitator, especially the diode unit of the full-wave rectification system is designed under a condition of the output voltage wave form with a ripple caused by corona current. However, in this case the output voltage wave form is flattened to be almost dc by C_0, the reinforcement to the diode unit of the power supply is needed. A fast recovery diode unit with a total maximum rating of V = 160 kV is inserted between the conventional dc power supply and the tank condenser, C_0.

These units of F, G, H, I, J, K, and H indicated in Fig.4.2 are assembled in one tank as shown in Fig. 4.8 and inserted in a tank filled with oil for insulation (voltage doubling tank).

Table 4.1 Specifications of Main Components of Pulse Module

Element (Fig.4.2)	Rating	Designed [a]	
		normal condition	worst case [b]
F	V = 160 kV I_a = 3 A	V < 90 kV I_a = 250 mA	---------
G (C_0)	V = 80 kV C = 0.75 μF	V = 45 kV (V_{C0}) I_{max} = 5.8 A	I_{max} = 33 A
H (T_h)	V = 144 kV I_a = 26 A	V = 8.6 kV I_a = 252 mA	V = 45 kV I_{max} = 33 A
L (L)	I_a = 2.7 A L = 64 mH	I_a = 252 mA	I_{max} = 33 A
N (C_D)	V = 120 kV C = 93.3 nF	V = 53.5 kV (V_0)	V_{pp} = 107 kV
O	V = 160 kV I^2t = 1000 A^2s	V = 53.5 kV	I^2t = 267 A^2s

Note:

a) The designed values shown here are estimated under the following operation conditions: C_{EP} = 63 nF, V_M = -60 kV, V_R = -20 kV, and F_p = 200 Hz. (C_{EP} = 63 nF : capcity of the simulated load used for the performance cofirmation test in the laboratory ; see the paragraph 4-3)

b) electrode short between corona and collection electrodes

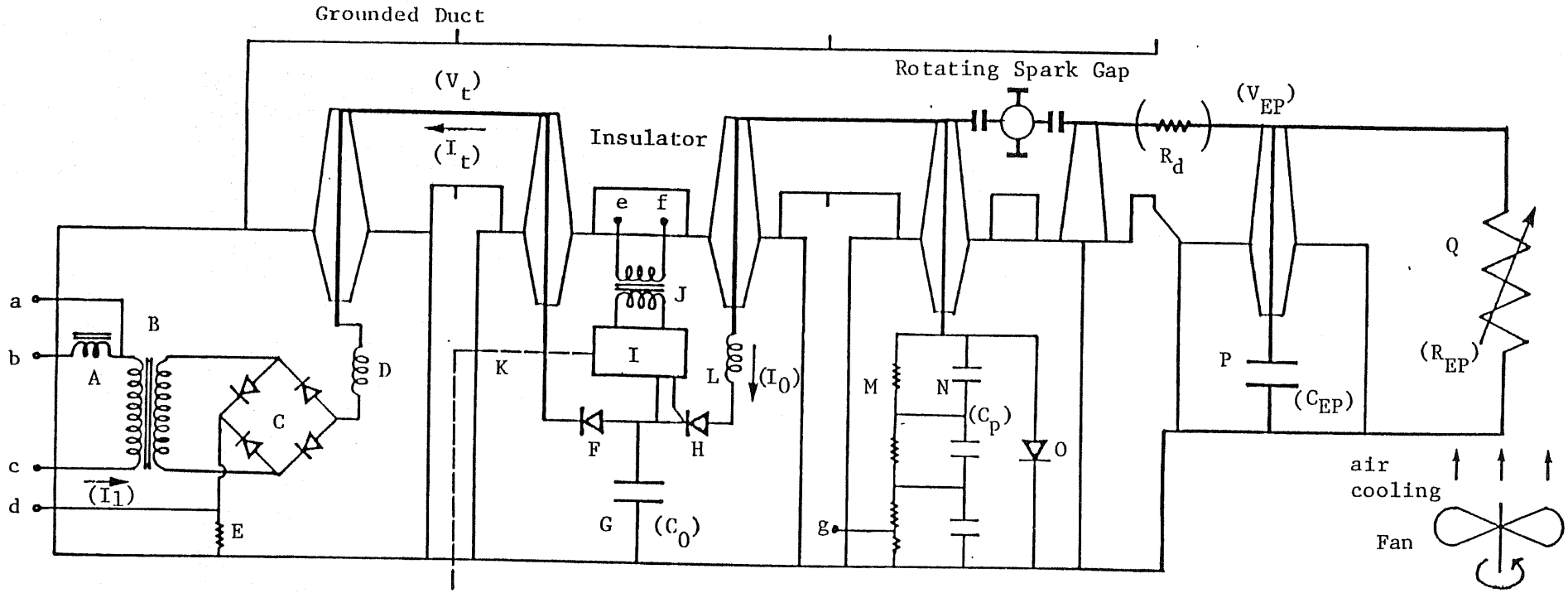

A: Current Limitting Reactor
B: High Voltage Transformer
C: Full-Wave Rectification System
D: Air Core Reactor
E: Shunt Resistor (0.5ohm)
F: Fast Recovery Diode Unit

G: Paper Condenser
H: Thyristor Unit
I: Gate Trigger Amprifier
J: Power Supply for I
K: Opitical Fiber
L: Air Core Reactor

M: Balancing Resistor
N: Ceramic Condenser Unit
O: Surge Absorbing Diode Unit
P: Ceramic Condenser Bank
Q: Resistor
R_d: Dumping Resistor

b-c: Main Power Supply (0 - 400V)
e-f: AC Power Supply (15V)
a,d,g: Wave Form Measuring Terminal

V_1: voltage between b and c
V_2: voltage between a and c
V_3: voltage between a and b

Fig. 4.2 Precise Circuit Diagram of Cassette Type Pulser Module and Its Test Circuit

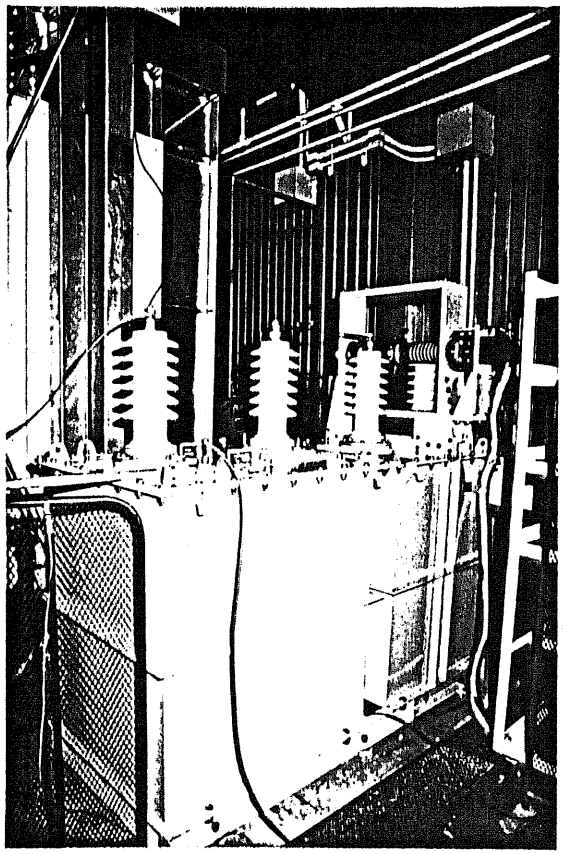

(a) Top hood Removed

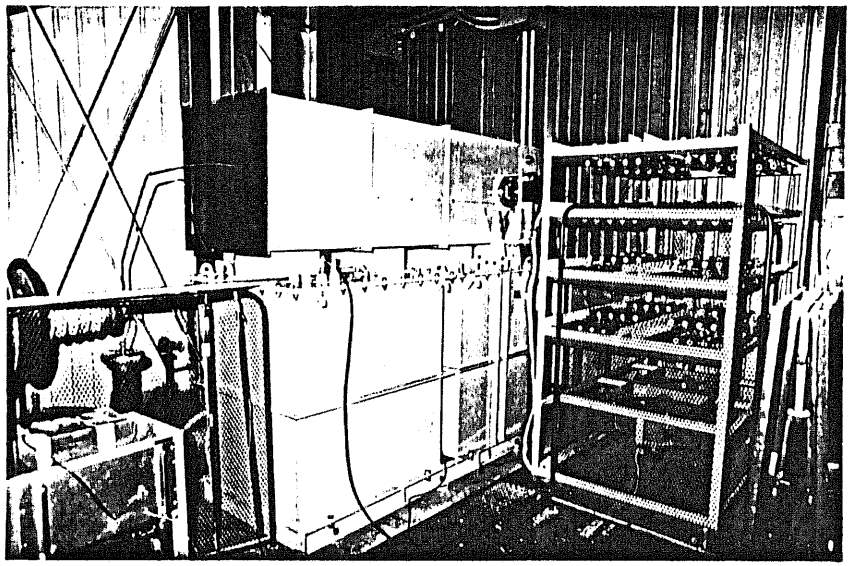

(b) Connected to DC Power Supply
and Simulated Load

Fig. 4.3 Appearance of Pulser Module

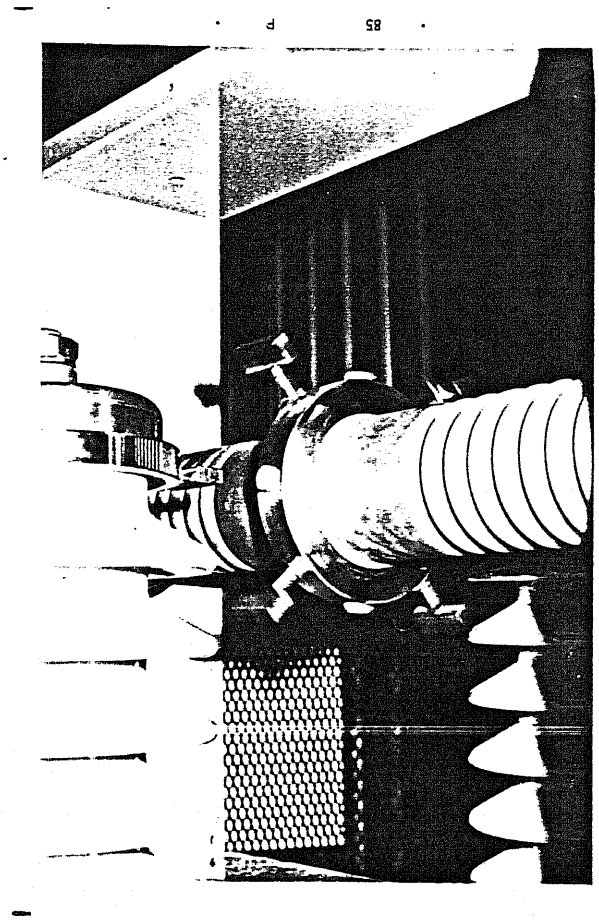

Fig. 4.4 Ratating Spark Gap with Four Rotor Electrodes

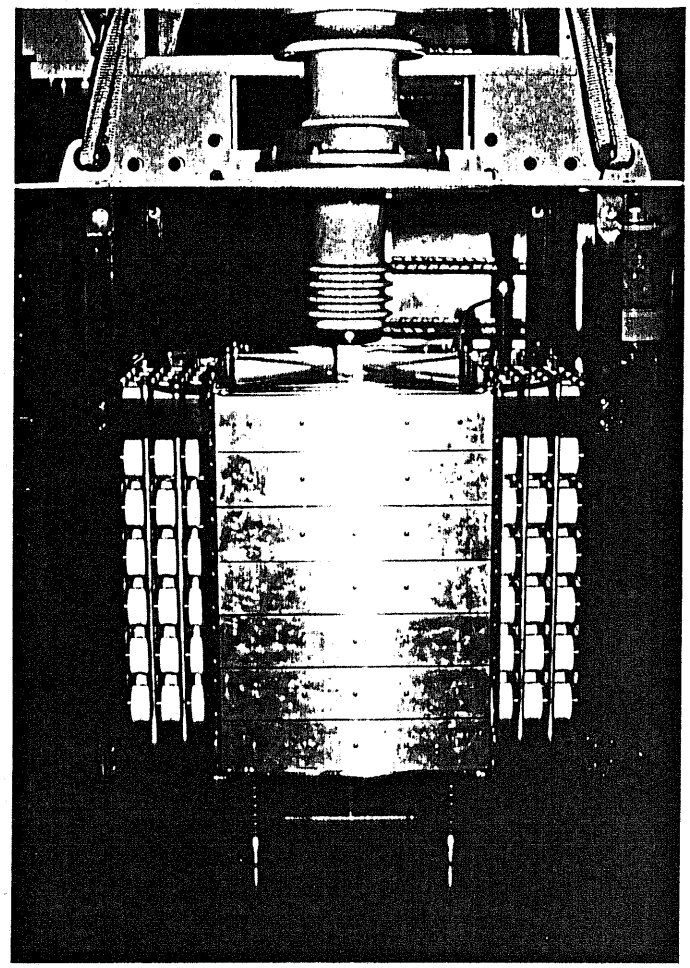

(a) Pulse Forming Condenser Out of 420 Pieces of Ceramic Condensers

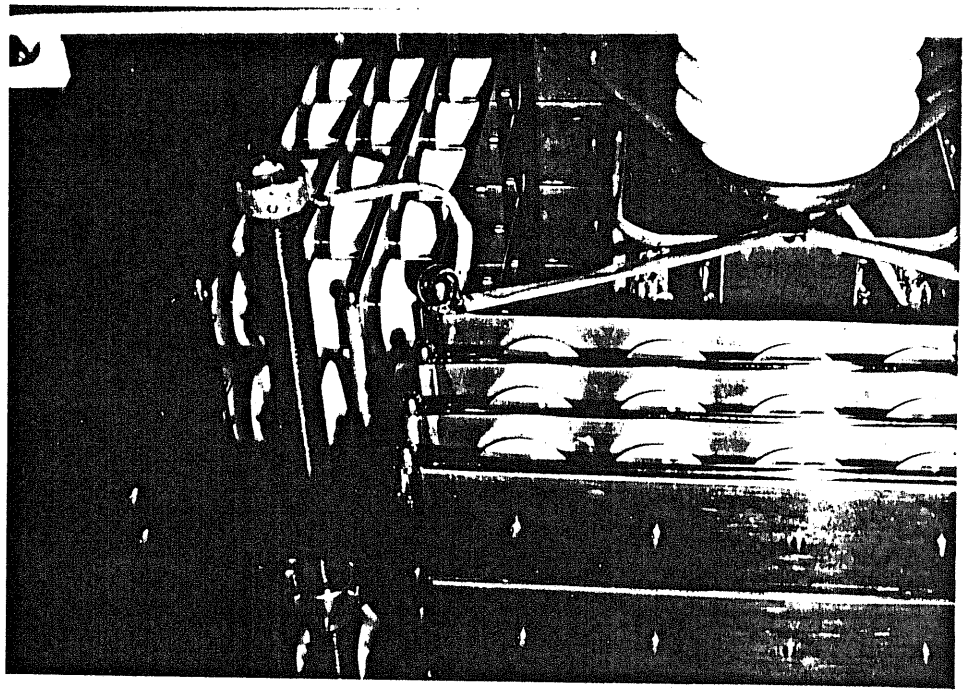

(b) Surge Absorbing Diode Unit Installed Inside of Condenser Unit and Balancing Resistor

Fig. 4.5 Pulse Forming Condenser Unit

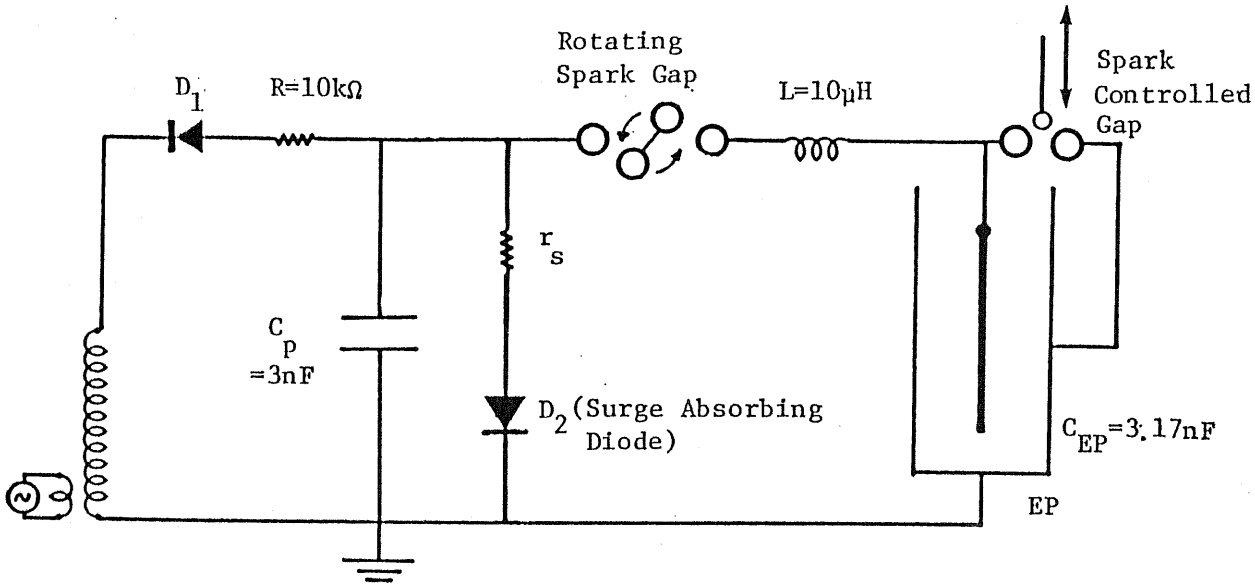

Fig. 4.6 Circuit Diagram of Spark Simulation
(spark is produced by spark controlled Gap

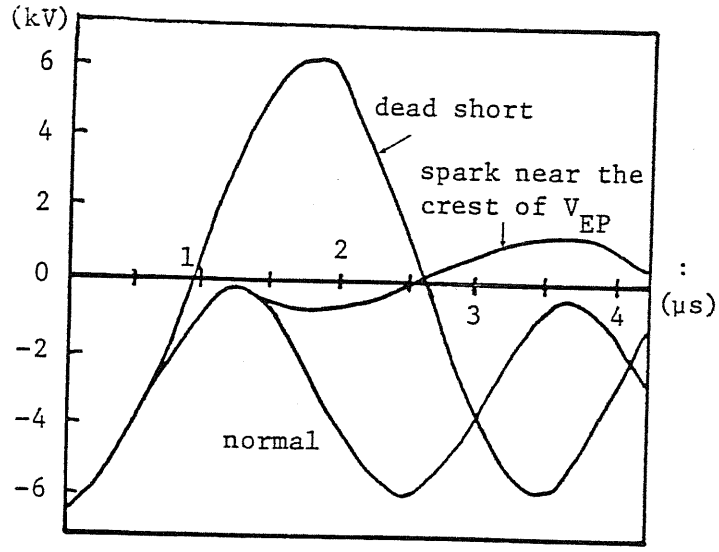

(a) Voltage Wave Form of C_p Without Surge Absorbing Diode

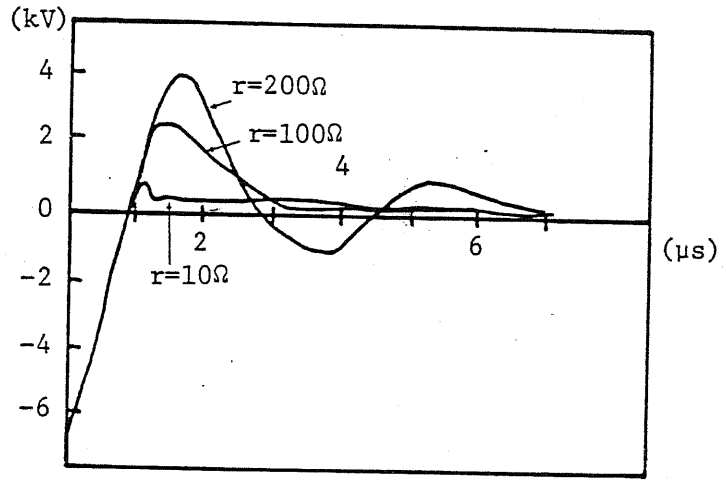

(b) Voltage Wave Form of C_p With Surge Absorbing Diode

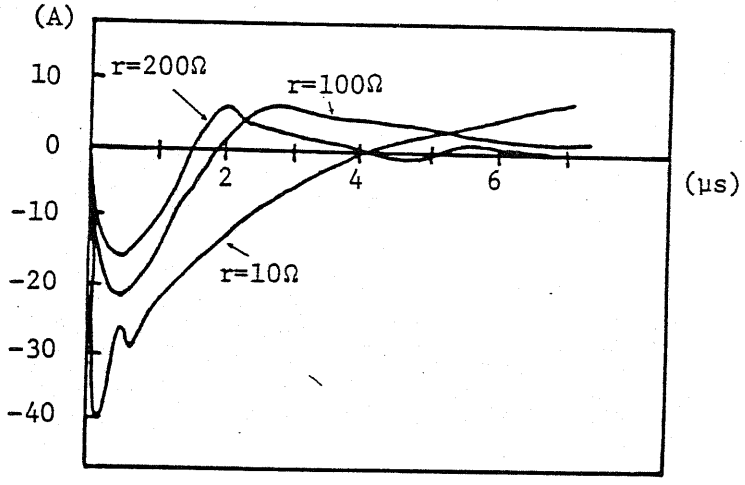

(c) Current Wave Form of Surge Absorbing Diode

Fig. 4.7 Effect of Surge Absorbing Diode, r_s, on Voltage Wave Form of C_p (surge produced by sparking in precipitator)

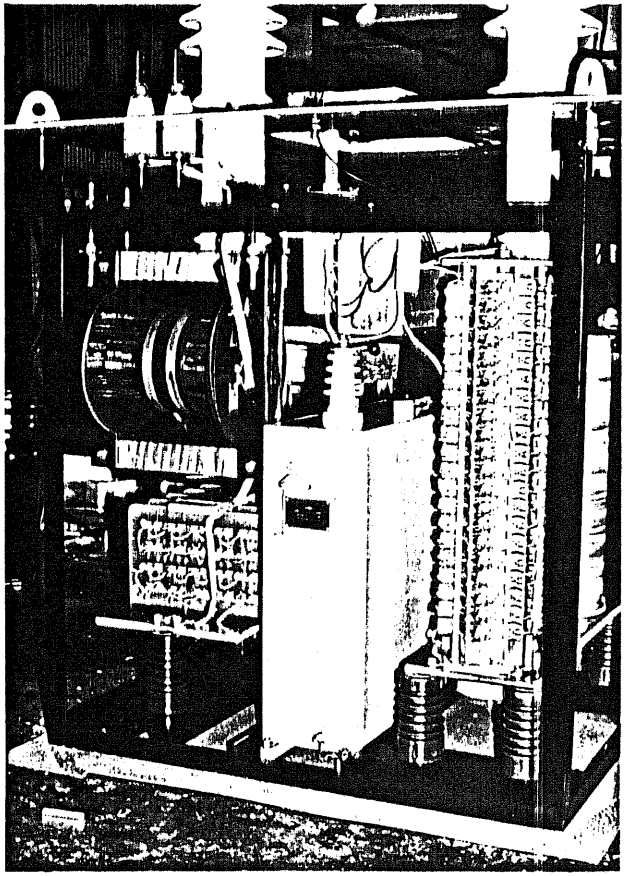

(a) Front View

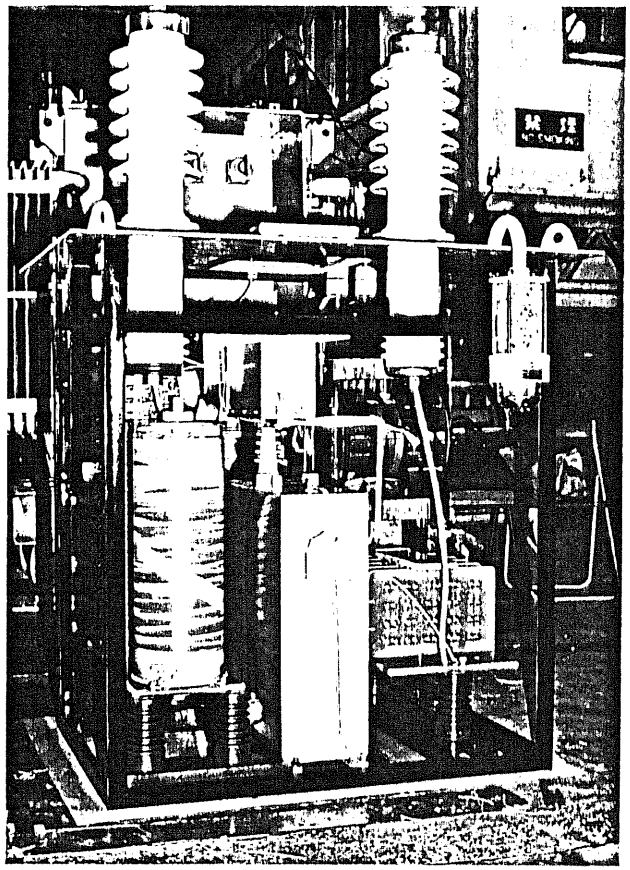

(b) Back View

Fig. 4.8 Voltage Doubling Circuit Unit

4-3. Pulser Performance Confirmation Test

4-3-1. Experimental Set-Up

The test to confirm the performance of the cassette type pulser module constructed is made in a laboratory using the dummy load simulating the practical electrostatic precipitator. As shown n Fig. 4.2, the cassette type pulser module is inserted between the dc power supply and the simulated load. The simulated load is out of a ceramic condenser bank of C_{EP} = 63 nF (equivalent capacity of a precipitator with a collection area of F = 1200 - 1300 m^2), and a resistor unit, R_{EP}, cooled by a fan. R_{EP} is adjusted so that an output voltage wave form becomes the designed one.

4-3-2. Output Voltage Wave Form

Figs. 4.9 - 4.12 show the voltage wave forms and the current wave forms measured at various places (see Fig. 4.2). Two typical cases (F_p = 50 Hz and 100 Hz) are shown in Figs. 4.9 - 4.11 where the pulser is operated under the conditions of Table 4.1 (C_{EP} = 63 nF, V_M = -60 kV and V_R = -20 kV) and in Fig. 4.12 the case of F_p = 100 Hz shown.

Fig. 4.9 shows the pulse voltage wave form measured at the inlet terminal of the dummy load condenser bank (see Fig. 4.2) As expected, the dumped LC oscillation is obtained in both cases (Figs 4.9(a-1) and (b-1)) follows Eq.(2.10).

Table 4.2 shows the pulse voltage parameters measured (Figs. 4.9 - 4.11) and also the circuit components calculated from these measurement (L and r). L and r are the non-linear function of a pulse current and also change according to the wiring. In this sence, L and r in Table 4.2 are

only rough estimation.

Comparing Table 4.1 and Table 4.2, it is recognized that the measured values of V_0 and V_{C0} are larger than designed. This is because r is neglected in the process of designing as described in the previous paragraph 4-2. Although larger values of V_0 and V_{C0} are needed than designed, they are still within the rating and an enough allowance exists. The data obtained by the field test shown latter, are to be used and the design becomes more precise and provides a moderate level of allowance to every element.

Fig. 4.10 shows the voltage wave form of the pulse forming condenser. In this case, the designed value of the voltage doubling factor is f_d = 1.78. From Figs. 4.9 and Table 4.2, f_d is calculated to be f_d = 1.75 and 1.74 in the case of F_p = 100 Hz and 50 Hz, respectively. These are very close to the designed value and it is concluded that the voltage doubling circuit works as designed. In order to measure the current rise time of the voltage doubling circuit, the experiment using the current probe (Tektonix Type-6022) in a lower voltage level is made and the result is shown in Fig. 4.13. The current rise time is measured to be T_{dr} = 105 μs where the designed value is 114 μs. This also indicates that the voltage doubling circuit works as designed.

Figs. 4.11 shows the output (secondary) voltage and current wave form of the dc power supply (V_t, I_t). The tank condenser is charged by I_t and the charging is made by 100 Hz in both cases of F_p = 50 Hz, and 100 Hz. Fig. 4.12 (a) shows the primary voltage and current wave forms of the dc power supply (V_1, I_1), and Fig. 4.12(b) shows the primary voltage wave form of the high voltage transformer, V_2 (see Fig. 4.2). The difference between V_1 in Fig. 4.12(a) and V_2 in Fig. 4.12(b) is caused by the current limiting reactor (A in Fig. 4.2). The current limiting reactor is used to limit the rash current when a spark takes place and the run-away characteristics caused by severe back corona in a precipitator in the dc energization. In

this case, where this dc power supply is used for charging the tank condenser, it acts as a current limiter of charging current, I_t, resulting in increase of an overall charging time. Moreover there is not appreciable difference between the positive and the negative polarities of the primary current, I_1. This indicates the high voltage transformer is used in the full-wave system with a better utility than in the half-wave system.

It should be noted that the charging efficiency of both C_0 by the dc power supply and C_p by the voltage doubling circuit is close to 100 %.

Table 4.2 Pulse Parameters Measured and Pulse Circuit Paramers Estimated (compare with Table 4.1)

Capacitance of Pulse Forming Condenser: C_p = 93.3 nF Capacitance of Simulated Load: C_{EP} = 63 nF
Pulse Parameters Measured: V_M = -60 kV (Maximum Voltage of V_{EP}) V_R = -19 kV (Residual Voltage) V_0 = -55.4 kV (Charging Voltage of C_p) V_{CO} = -49.5 kV (Charging Voltage of C_0) T_r = 1.95 μs (Pulse Rise Time) $\alpha = 1 \times 10^5\ s^{-1}$ (Dumping Factor)
Circuit Parasitic Parameters: L = 2.6 μH (Total Circuit Inductance) r = 0.5 ohm (Total Circuit Loss)

Note: Pulse Repetition Frequency, F_p = 100 Hz

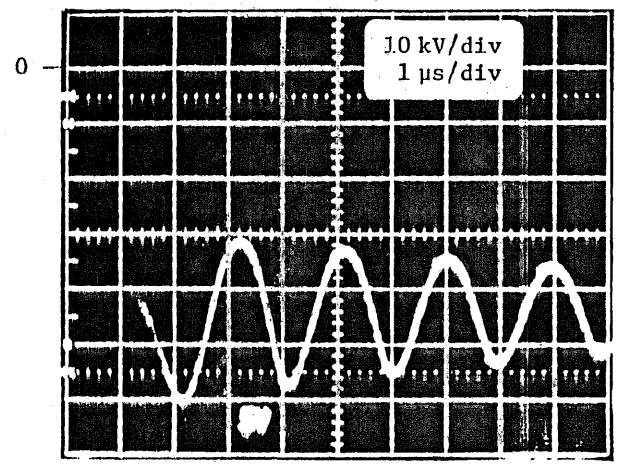

(a-1) Transient LC Oscillation (F_p=50Hz)

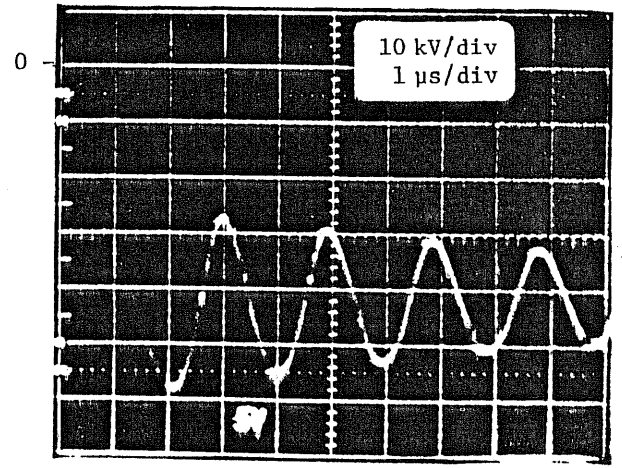

(b-1) Transient LC Oscillation (F_p=100Hz)

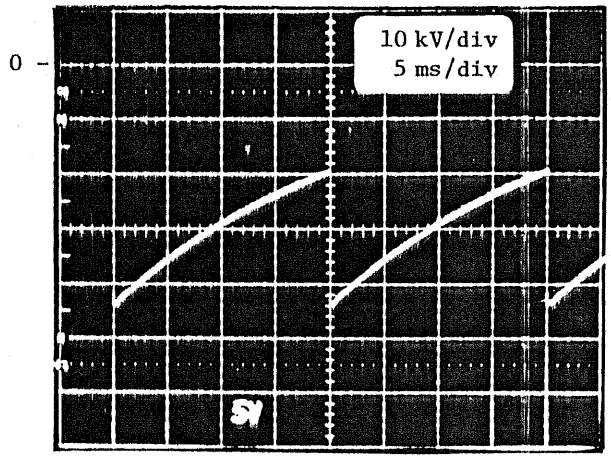

(a-2) Saw-Teeth Pulse Wave Form (F_p=50Hz)

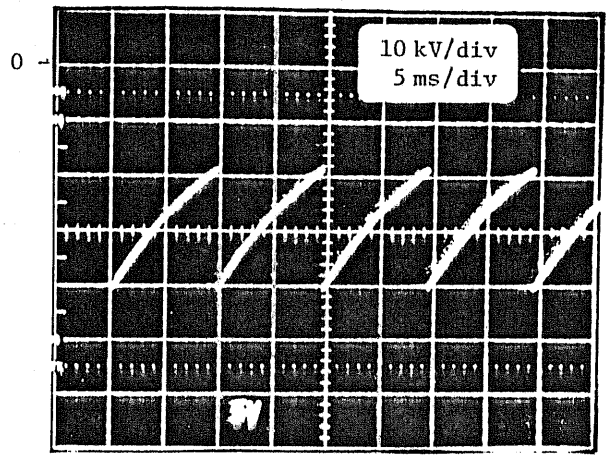

(b-2) Saw-Teeth Pulse Wave Form (F_p=100Hz)

Fig. 4.9 Pulse Voltage Wave Form, V_{EP}, Measured at the Inlet Terminal of Simulated Load (C_{EP} = 63 nF, $V_M \fallingdotseq$ -60 kV, $V_R \fallingdotseq$ -20 kV)

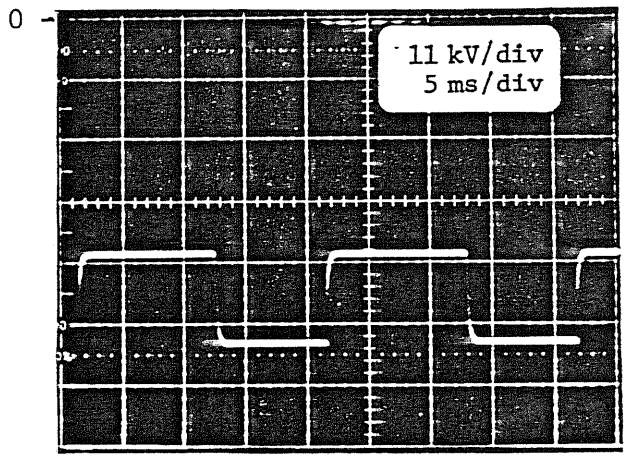

(a) F_p = 50 Hz

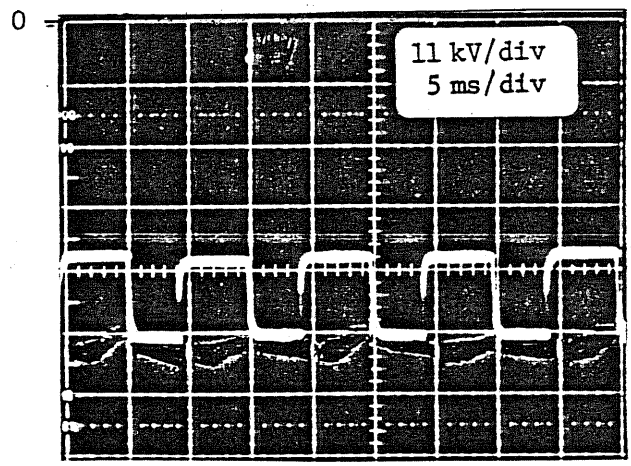

(b) F_p = 100 Hz

Fig. 4.10 Voltage Wave Form of Pulse Forming Condenser
(C_{EP} = 63 nF, $V_M \fallingdotseq$ -60 kV, $V_R \fallingdotseq$ -20 kV)

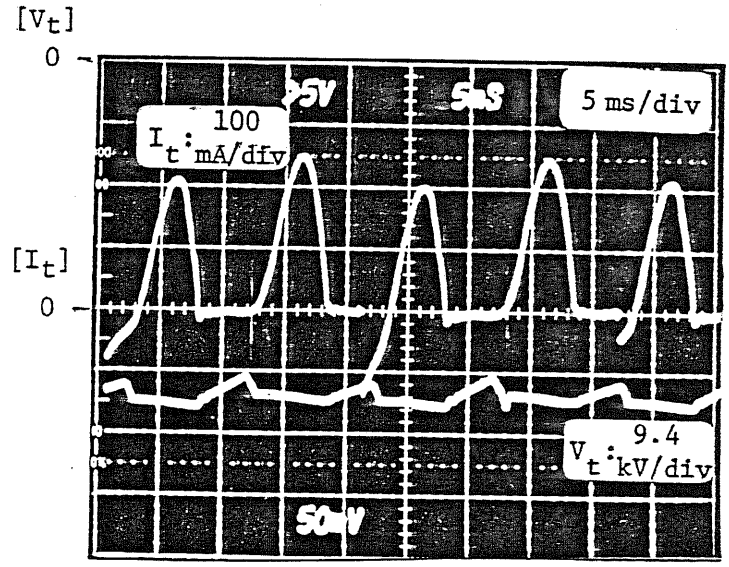

(a) F_p = 50 Hz

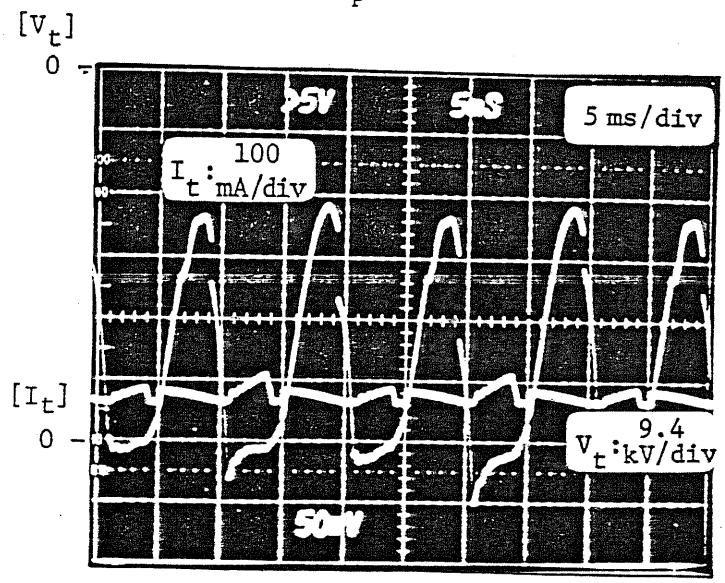

(b) F_p = 100 Hz

Fig. 4.11 DC Power Supply Output Voltage Wave Form, V_t, and Current Wave Form, I_t
(C_{EP} = 63 nF, $V_M \doteqdot$ -60 kV, $V_R \doteqdot$ -20 kV)

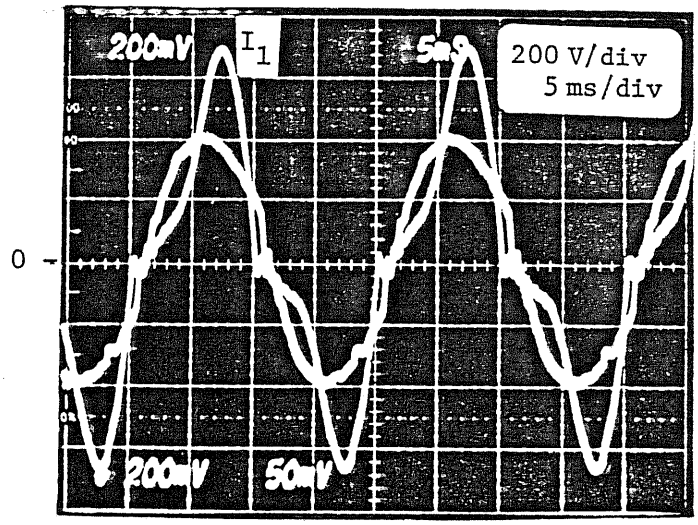

(a) Primary Voltage of DC Power Supply, V_1

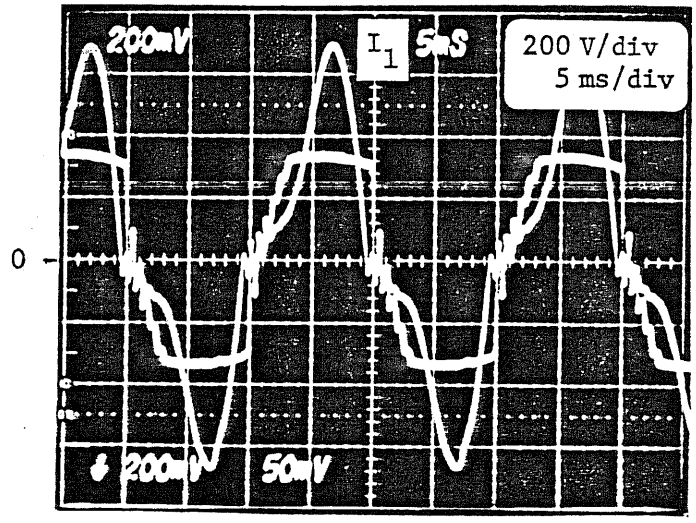

(b) Primary Voltage of Transformer, V_2

Fig. 4.12 Primary Voltage and Current Wave Form of Both DC Power Supply, V_1, and I_1, and High Voltage Transformer, V_2 and I_1 (V_1, V_2, I_1 : see Fig. 4.2)
(C_{EP} = 63 nF, $V_M \doteqdot$ -60 kV, $V_R \doteqdot$ -20 kV, F_p = 100 Hz)

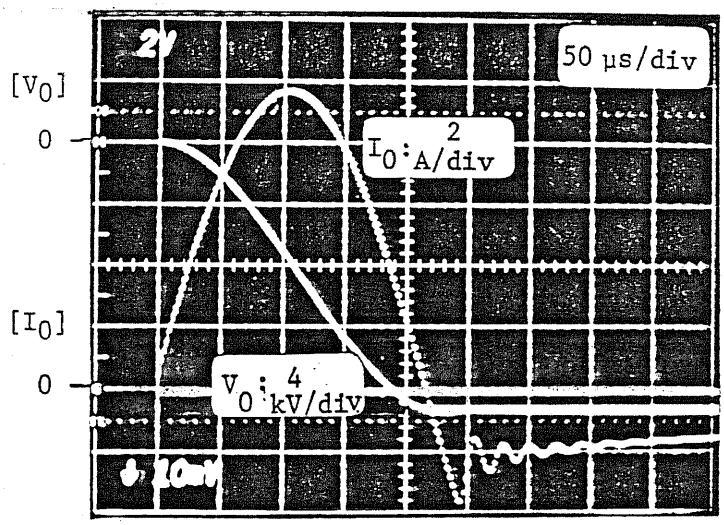

Fig. 4.13 Voltage and Current Wave Forms in Charging of Pulse Forming Condenser by Voltage Doubling Circuit
(V_{CO} = -10 kV : voltage of tank condenser of voltage doubling circuit
No switching in rotating spark gap)

4-4. Electrode Erosion Test

4-4-1. Experimental Apparatus

In the practical appliction of this pulser system, the electrode erosion of the rotating spark gap becomes one of the problems. An electrostatic precipitator is operated continuously without any stops at least for one year (more than 8700 hours) and a regular maintenance is made once a year which is the only chance to replace the electrodes of the gap. As the result, the electrodes should last at least one year.

The electrode erosion test is made by the experimental set-up as shown in Fig. 4.2. The electrode is made from copper-tungsten sinter alloy (W : 70 %, Cu : 30 %) with a very small erosion and a reasonable cost. It is cut in a size to be measured by the electric balance. The pulser is operated in the condition of C_{EP} = 63 nF, V_M = -60 kV, V_R = -20 kV, and F_p = 100 Hz.

4-4-2. Electrode Erosion

Fig. 4.14 shows the erosion rate of 6 electrodes (A, B : stator electrode, 1 - 4 : rotor electrode). The electrode B is eroded most quickly in those 6 electrodes, and the next is the electrode A. The electrodes 1 - 4 are almost same in erosion rate. The stator electrodes erode about 4 times as large as the rotor electrodes. Although it is taken into account that the stator electrodes receives twice as much sparks as the rotor electrode (the stator electrodes receive 4 sparks in one revolution and the rotor electrodes 2 sparks), the stator electrodes still erodes much more. This figure provides a necessary amount of the initially installed

electrode to be operated for one year without replacement. In the most severe case of the electrode B, it amounts to about 2.6 kg (160 cm^3) when operated in this mode of V_M = -60 kV, V_R = -20 kV, and F_p = 100 Hz. Although it is not a small amount, it is possible to install such electrode as a stator electrode. In the case of the rotor electrode, the size is reduced to 1/4. Moreover the operation pulse repetition frequency may be 50 - 60 Hz in the practical cases, the required size of the electrodes is reduced.

Table 4.3 shows the electrode elosion rate summarized. In the case of the traveling pulse produced by the same type of the rotating spark gap, the erosion rate is largest in the electrode B, next in the rotor electrodes, and smallest in electrode A. In this case of the direct coupled pulse, the erosion rate is more than 10 times as large as that of the traveling pulse (see Apparent in Table 4.3, Apparent : based on charge consumed). In this case, charge is exchanged many times between the pulse forming condenser and the load capacity causing a dumped LC oscillation. Considering the total charge passing the spark channels during the LC oscillation, the electrode erosion rate becomes those as shown in Table 4.3 (see Overall). These values are almost as same as those by the traveling pulse [43].

It is reported that the electrode erosion in a spark gap out of twin electrodes is larger in a cathode electrode than in an anode electrode [44] (see Table 4.3). In these cases of the rotating spark gap, an anode electrode (stator electrode A) are eroded more than a cathode electrode (stator electrode B). The reason of the erosion rate difference in polarities is not clear yet. At any rate, the overall erosion rate is in the rage of 20 - 50 μg/c in the practical cases using the rotating spark gap.

4-4-3. Effect of Dumping Resistor

Even in this case of the direct coupled pulse, the gap electrodes last for one year without replacement, but the demand of reduction in electrode erosion is large. In order to reduce the apparent electrode erosion rate, a dumping resistor, R_d = 1.1 ohm, is inserted between the output of the pulser and the load.

Fig. 4.15 shows the pulse voltage wave forms in three different time scale. Comparing Fig. 4.9(b-1) and Fig. 4.15 (a), it is clearly recognized that the dumping in the LC oscillation is enhanced by R_d.

Table 4.4 indicates the effects of R_d on the dumping factor, α, the total charge of the oscillatory current in the spark gap, Q, the necessary charging voltage of C_p to achieve V_M = -60 kV, V_0, and the total energy used in one pulse period, E. α becomes about 3.5 times as large as the one without R_d resulting in the drastical reduction in Q. It can be expected that the electrode erosion rate is also reduced as much as the reduction of Q. However, the quicker dumping also reduces V_M (peak voltage). As a result, a higher charging voltage of C_p is necessary to keep V_M = -60 kV. Also the total energy E increases by 17 %.

The electrode erosion test is made using this dumping resistor under the operation conditions of C_{EP} = 63 nF, V_M = -60 kV, V_R = -20 kV, and F_p = 100 Hz. The test result is shown in Table 4.5. The overall electrode erosion becomes less than 20 % of that without R_d which is better than expected. It means that the initially installed electrode becomes 20 % in volume or the electrode of the same size as the one used in the case of no dumping resistor lasts for 5 times longer.

However the initial cost of the dumping resistor becomes another problem. In this particular case, the heat capacity of the resistor should be larger than 2.3 kW, because most of the circuit loss is produced here. And the operation cost is also increased because the necessary charging

voltage of the pulse forming condenser, V_0, increases as shown in Table 4.4.

It is concluded that the use of the dumping resistor should be considered in case by case according to the required conditions of each electrostatic precipitator. If the long term operation without a maintenance is a important factor, then the dumping resistor becomes a good solution.

Table 4.3 Electrode Erosion Rate

Rotating Spark Gap	Stator Electrode		Rotor
	A	B	Electrode
Direct Coupled Pulse			
Apparent	500	600	280
Overall	35	40	20
Traveling Pulse	30	50	40

	Cathode	Anode
Twin Electrode Spark Gap	20	4 - 8

Unite : μg/c

Apparent : based on condenser charge used (condenser : C_p)

Overall : based on charge of oscillatory current in gap

Traveling Pulse : H.Nakatani, Doctoral Dissertation, University of Tokyo, 1983.

Twin Electrode Spark Gap : A.L.Donaldson, M.O.Hagler, M.Kristiansen, G.Jackson, and L.Hatfield, Electrode Erosion Phenomena in a High-Energy Pulsed Discharge, IEEE Trans. on Plasma Science, vol. PS-12, pp28-38, 1984.

Table 4.4 Effect of Dumping Resistor on α, Q, V_o, and E

	α (1/s)	Q (coulomb)	V_0 (kV)	E (J)
No Dumping Resistor	1.0×10^5	0.02	55.0	66.5
Dumping Resistor (1.1 ohm)	3.5×10^5	0.006	61.0	77.4

Note: α = dumping factor (see Eq.(2.10)

Q = total charge of oscillatory current in gap per one pulse

V_0 = charging voltage of C_p

E = energy used in one pulse (energy supplied from power supply)

Operation Conditions = C_{EP} = 63 nF, V_M = -60 kV, V_R = -20 kV, F_p = 100 Hz

Table 4.5 Electrode Erosion Rate Reduced by Dumping Resistor

	Stator Electrode		Rotor Electrode
	A	B	
No Dumping Resistor	250	300	70
Dumping Resistor (1.1 ohm)	32	41	14

Operation Mode : V_M = -60 kV, V_R = -20 kV, F_p = 200 Hz

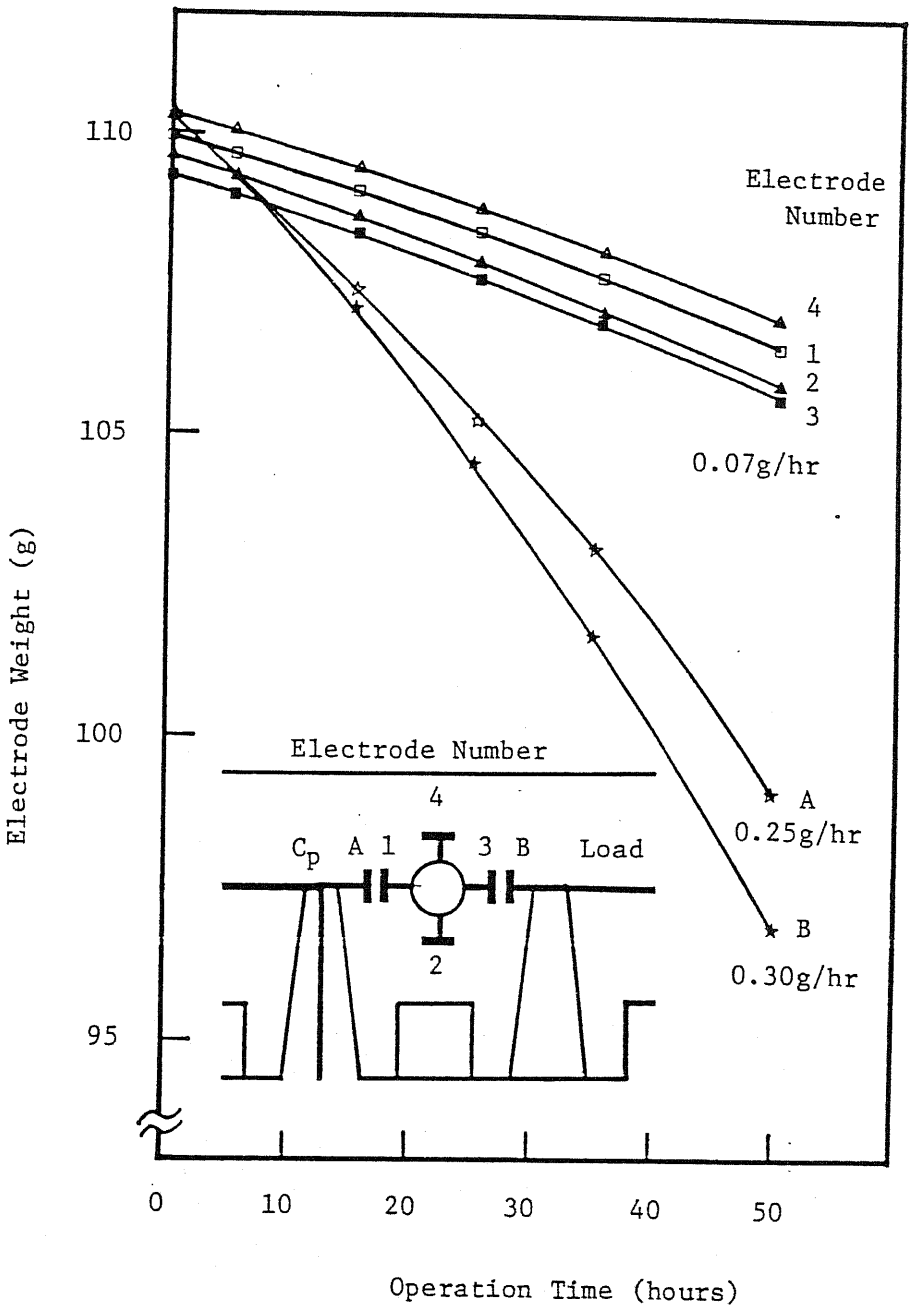

Fig. 4.14 Electrode Erosion of Rotating Spark Gap of Pulser Module (C_{EP} = 63 nF, V_M = -60 kV, V_R = -20 kV, F_p = 100 Hz)

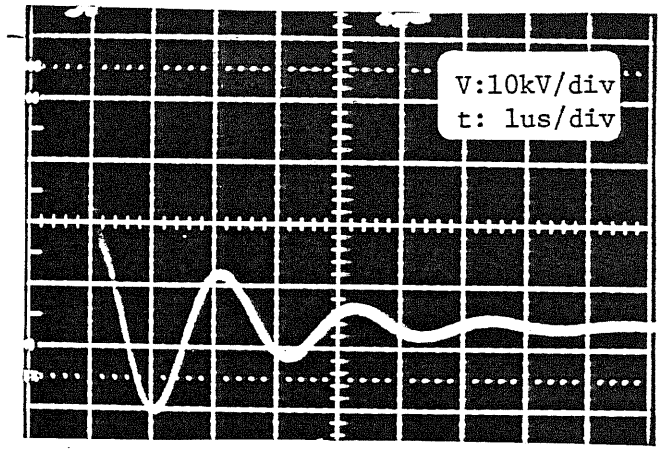

(a) Magnified Dumped LC Oscillation

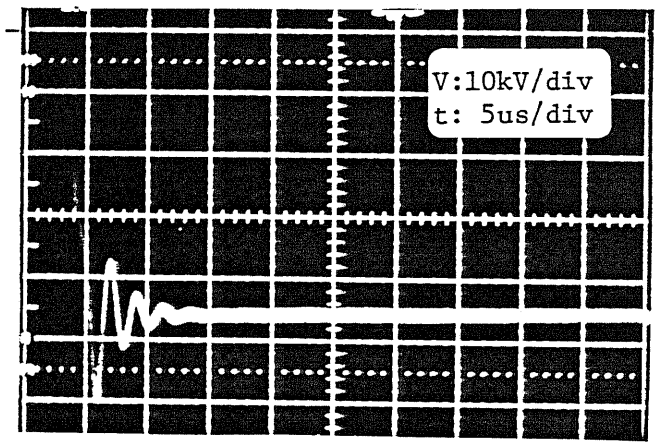

(b) Dupmed LC Oscillation Followed by Slowly Decaying Voltage

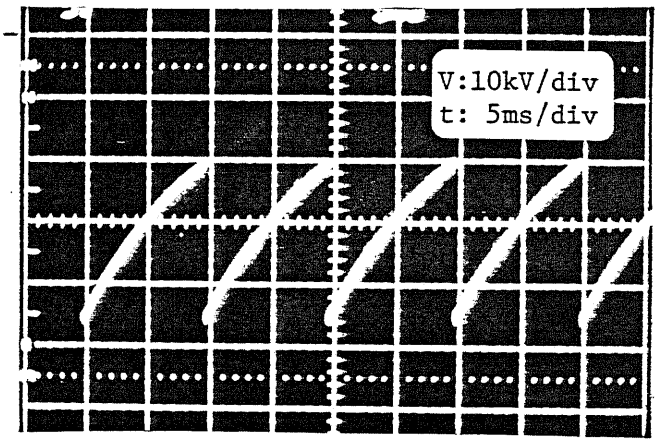

(c) Saw-Teeth Like Pulse Voltage Wave Form Produced by Simulated Load

Fig. 4.15 Effect of Dumping Resistor, R_d, on Pulse Voltage Wave Form Especially on LC Oscillation

(C_{EP} = 63 nF, V_M = -60 kV, V_R = -20 kV, F_p = 100 Hz)

4-5. Conclusion

The pulser system based on the direct coupled pulse energization concept is developed for the practical use, and its performance is confirmed to be as the one designed in the laboratory test using a simulated load. The essential points in this chapter are shown in following:

(1) A cassette type pulser module to be inserted between an existing dc power supply and an electrostatic precipitator is constructed, for the retrofitting application.

(2) It consists of the voltage doubling tank, the pulse forming condenser tank, and the rotating spark gap.

(3) It has a capacity to energize an electrostatic precipitator of the standard duct spacing of 2D = 300 mm with the collection area of F = 1200 - 1800 m^2.

(4) The performance is confirmed in the laboratory test using the simulated load out of a condenser and a parallel resistor and the designed output is obtained. The charging voltage of the pulse forming resistor to achieve the designed output becomes about 10 - 15 % higher than the designed where the circuit loss is neglected.

(5) The dumping factor is measured to be $\alpha = 1 \times 10^5$ and an equivalent circuit loss is estimated to be r = 0.5 ohm. The pulse rise time is also measured to be T_r = 1.1 μs from which the total circuit inductance is estimated to be L = 2.6 μH in this particular test circuit.

(6) The voltage doubling circuit works as designed. The voltage doubling factor is measured to be f_d = 1.75 (designed : 1.78) and the current rise time, T_{dr} = 105 μs (designed : 110 μs).

(7) The current limiting reactor of the existing dc power supply plays as

the current limiter of the charging of the tank condenser, also in this case. And the equivalent charging time constant becomes large and a full wave charging is possible even in a lower pulse repetition frequency. As the result, the utility of the high voltage transformer becomes better.

(8) In both cases of charging C_0 and C_p, charging efficiency is very high (almost 100 %).

(9) Electrode erosion test of the rotating spark gap is made and it is found that the stator electrode in the load side is eroded most, then the stator electrode in the pulse forming condenser side, and the rotor electrodes are least eroded in these electrodes. In the worst case of the stator electrode in the load side, the necessary initial amount of the electrode lasting for one year without replacement is estimated to be 2.6 kg (160 cm^3) in the operation condition of C_{EP} = 63 nF, V_M = -60 kV, V_R = -20 kV, and F_p = 100 Hz.

(10) In order to reduce the electrode erosion rate, the dumping resistor, R_d, is inserted between the load and the output of the rotating spark gap. The LC oscillation is much more quickly dumped by inserting R_d = 1.1 ohm, and the erosion rate is reduced to 20 % of that without R_d.

CHAPTER 5. FIELD TESTS OF DIRECT-COUPLED PULSE ENERGIZATION

5-1. Introduction

In the tests of the laboratory precipitators, test conditions are ideal. For example, the size of the precipitator is small and the corona conditions become uniform in the entire corona electrode. The ash conditions are also stable and the performance degradation problem is specified due to back corona. However, in a practical plant the size of the precipitator is large and its electrode system becomes complicated. The corona conditions can be different from those observed in a small size laboratory set-up. The ash conditions are very much affected by the furnace conditions. For example another difficult problem of the corona quenching effect of space charge produced by a very fine dusts comes out when a boiler produces a large amount of unburnt carbon soot. This is one of the "Hidden Variables" to cause the performance degradation. Consequently there exists the limit of performance enhancement only by the pulse energization.

Two series of the field tests for evaluation of the direct-coupled pulse energization are made at the practical plants. One is the precharger of the electrostatically augmented granular bed filter collecting flyash from the wooden-chips burning boiler. Although the size of the precharger is small ($F = 117\ m^2$: total collection area), it is in the practical system and possessing a problem of a lower performance than designed. Another is the electrostatic precipitator in the exhaust gas cleaning system of the glass furnace. It is also suffering the performance degradation. It has 3 series precipitating fields and the first two sections have $F = 1520\ m^2$ of

collection area in total and a standard duct spacing of 300 mm. The cassette type pulser module constructed as shown in the chapter 4, is possible to be applied to this system.

In both cases the observation from the man-hole at the ceiling of the precipitator by both naked eyes and the image intensifier indicates that the light is emitted from the collection electrodes (much brighter than the light from the corona electrode). This fact leads the assumption that the performance degradation is due to the back corona problem. The direct-coupled pulse energization is expected to be a remedy in these systems.

In the former case, the collection performance itself could not raised by the pulse energization, although the back corona problem is solved. There comes out the problem due to the "Hidden Valuable", that is a corona quenching effect produced by unburnt carbon soot. In the latter case, the dust resistivity is so high as $r_d = 10^{14}$ ohm-cm and back corona can not be removed by the present pulse energization. Moreover the condensation of boron compounds from the vapor phase provides another problem. However, the energy saving effect of the present direct-coupled pulse energization is confirmed to be very large in the normal conditions (the exhaust gas is changed). The consumed energy in the pulse energized collection fields becomes 1/16 of that in the dc energized fields.

In this chapter are shown the results of these field tests and their analysis.

5-2. Electrostatic Precharger for Granular Bed Filter

5-2-1. Introduction

The small-size electrostatic precipitator is installed as a precharging section of an electrostatically augmented granular bed filter of moving bed type for cleaning of an exhaust gas from the wooden-chips burning boiler. Fig. 5.1 shows the appearance of this system. The wooden chips from the plywood factory are burned as fuel and fed into the furnace by the conveyor belt from its top. The feeding rate is changed by its revolutions from the steam demand of the factory. The optimum burning conditions could not maintained due to the fuel property and the furnace equipments. As the result, a very large fluctuation in exhaust gas temperature and ash property is produced. This is the reason why the granular-bed filter of a moving bed type augmented by precharging is selected as it is considered a more reliable control means to cope with such large temperature surge.

Silica is a main component of the flyash, but unburnt carbon soot is contained in the exhaust gas due to incomplete combustion in the furnace. The dust resistivity is about 10^{11} - 10^{12} ohm-cm to cause back corona and the soot concentration is quite high and fluctuates owing to the unstable operation of the furnace. Moreover needle-like chars having a size with about 50 mm in length and 3 mm in diameter also enter the collection field to produce excessive sparking.

The test of the direct-coupled pulse energization is made in this bad condition where the high resistivity of dust and the high surface loading problem due to carbon soot are coexisting. It removes the back corona troubles but reveals the high surface loading problem hidden behind the back corona trouble.

In this paragraph describes the results of this series of test.

5-2-2. Test Facility

Fig. 5.2 shows the schematic of the test facility which consists of a small one-field electrostatic precharger and a granular bed filter of moving bed type. The exhaust gas from the wooden-chips burning boiler is introduced through two screen grid for gas flow distribution into the electrostatic precharging section where dust particles are precharged, and then to the filter section of a moving type granular bed where charged particles are collected on the surface of pebbleds. The direct-coupled pulse energization is applied to this precharger. Fig.5.2 also shows the dimensions and specification of this precharger.

The gas load is changed by the screw revolutions of the fuel feeding belt converyor, R_s. The full gas load is produced by R_s = 1000 rpm.

Fig. 5.3 shows the circuit diagram of the direct-coupled pulse energization system where the existing dc power supply with a full-wave rectification system is used. The rotating spark gap with twin contacts in one revolution is synchronized to fire in the blocking period of the diode and produces the pulse repetition frequency of F_p = 60 Hz.

5-2-3. Primary Test Results

The behaviors of this precharger under the dc-energization are shown here as the preparation for the introduction of the direct-coupled pulse energization.

(A) V-I Curves:

Fig. 5.4 shows V-I characteristics of the electrostatic precharger under no load condition, indicating a smooth curve without back corona and corona quenching.

Fig. 5.5 indicates V-I curves measured under the operating conditions. The solid curves show the characteristics with a full gas load (R_s = 1000 rpm) and a half gas load (R_s = 500 rpm) measured on the same day and the dotted curves with a full gas load (R_s = 1000 rpm) and 1/3 gas load (R_s = 330 rpm) measured on the other day. Although the exhaust gas conditions fluctuates and the data schatter, it is clearly recognized that back corona is taking place in this precharger in operation.

(B) Wave Forms of Voltage and Current:

Fig. 5.6 shows the wave forms of the voltage applied to the corona electrodes of the precharger, and of the output current from the dc power supply. This indicates that voltage continues to drop in the entire period during the dc power supply is in the pause (zero output current period). This tendency is enhanced in higher current operation. It indicates again the large back corona induced current to exist.

(C) Dust Resistivity:

Fig. 5.7 shows the resistivity of the flyash sampled from the hopper of the precharging section and measured at a laboratory with the absolute humidity being kept constant at 15 vol% and temperature changed from 100 °C to 350 °C. It can be seen that the resistivity lies around 10^{12} ohm-cm at an operating temperature of 220 °C. However, it is anticipated that the working resistivity in the precharger under operation is about one order of magnitude lower because of the existence of a much higher water vapor. The flyash containes a substantial amount of carbon soot, however the dust resistivity does not seem to affected much by carbon mixture. Silica with very small particle size is a major chemical component.

(D) Visual Observation of Back Corona:

Visual observation is made with both naked eyes and the image

intensifier from the man-hole installed at the ceiling of the precharger. The back corona is recognized in a form of many tiny breakdown points on the entire grounded electrode. Its ligth activity is very active and bright, while negative corona on the wires are so feeble that they can not be observed by naked eyes. The corona wires with 4 mm in diameter were covered with dust deposit of 1 - 2 mm thickness.

It is noted that the state of back corona changes in time due to the furnace conditions resulting a concurrent change in operating voltage and current of the precharger. When streamer mode back corona is taking place, the voltage is higher level of V_{dc} = -30 kV and the current fluctuates because of the sparking. While glow mode back corona, the voltage is lowered in the level of V_{dc} = -20 - -24 kV and the current is stable in I = 50 mA (0.42 mA/m^2).

5-2-4. Pulse Energization Test

(A) No Load Tests:

At first no load tests of the direct-coupled pulse energization tests are made with the gas flow stopped. The gas is still the exhaust gas and its temperature is T_g = 205 °C. Both the grounded electrode and the corona electrode are covered with the high resistivity dust deposit.

Fig. 5.8 shows the wave form of the voltage on the precharger measured at its pulse inlet terminal in three different time scale. The typical wave form of the direct-coupled pulse energization, a saw-teeth like wave form with a dumped LC oscillation in its leading edge and a CR-decay in the first part of the decaying phase followed by a flat period, is obtained.

All the corona wires produced very active light activity of pulsed coronas, while back corona on the grounded electrode disappears completely in the condition as shown in Fig. 5.8.

Fig. 5.9 shows the wave forms of the transformer primary voltage and the charging voltage of the pulse forming condenser. From these two figures, the pulse parameters can be measured and the geometric parameters of this pulse system can be estimated. These are shown in Table 5.1.

It is concluded that, so far as no particles are existing, all of the wires can produce equally active pulsed coronas, and that the present direct-coupled pulse energization is effective to produce very active and uniform coronas and to remove back corona completely. In addition, a great reduction in corona current is also achieved by the present pulse energization (0.081 mA/m^2 in the case of Fig. 5.8).

(B)Load Tests:

The load test is carried out by allowing the exhaust gas to pass through the precharger. The load is changed by changing the screw revolutions, R_s.

Fig. 5.10 shows the voltage wave form change in accordance with increasing the load expressed by R_s, while the peak voltage is kept in the range of V_M = -45 - -48 kV. In Fig. 5.11, the mean current density of the precharger estimated from the saw-teeth voltage wave forms is plotted against the screw revolutions, R_s. It can be seen from these two figures, that with increasing R_s the decay speed of the voltage is lowered, resulting a reduction of corona current. The excessive sparking takes place in the case of R_s > 800 rpm, especially when the smoke from the chimney becomes noticeably black.

The visual observation of the inside of the precharger indicates that back corona is not taking place even in any case of the load test. However, there is a drastic change in the negative corona activity of the corona wires. The first wire in each duct indicates an active pulsed corona, but the second and third wires become feeble and the succeeding wires much less of not at all in light activity of pulsed corona. Fig.

5.11 indicates that the mean current density in the case of R_s = 1000 rpm becomes about one half of that at no load test(R_s = 0 rpm) which corresponds to the reduction in number of active corona wires confirmed by the visual observation.

These evidences indicate that the corona quenching effect is taking place in the precharger. Its severity increases in accordance with the increase of fuel feeding rate, R_s. Carbon soot produced in the furnace due to incomplete combustion is charged in the region of the first two or three corona wires and forms space charge in the charging field of the succeeding corona wires. The field intensity around these wires is reduced to stop corona production (corona quenching effect). Moreover, the field across the corona electrode and the grounded electrode becomes more flattened and once a micro discharge usually from the ground electrode takes place it bridges over to cause sparking. In this sense, the electrode system of both 4 mm corona wires and the mesh grounded electrode are most easily suffers from the space charge problem.

(C) Measurement of Collection Performance:

Table 5.2 shows the test results by both the pulse energization and the dc energization. The emission concentration of dust is measured at the outlet of the granular bed filter, and the precharging performance should be estimated from these data by assuming that the total collection performance is related to the charging performance of the precharger. The peak voltage, V_M, in the direct-coupled pulse energization is kept as high as possible (V_M = -45 - -48 kV in the test number 1,2,and 5-9, and V_M = -52 kV in the test number 10-12).

No difference can be seen in the emission concentration in Table 5.2 between the pulse energization and dc energization when a large fluctuation of the combustion conditions is considered. The peak voltage is limited by the sparking voltage, and the higher voltage operation in order to increase

corona current is not possible.

(D) Discussion:

The level of the corona current density is very small compared with its ordinary level (i = 0.43 mA in this case), but its charging time constant is calculated by

$$\tau_{ch} = 4 \varepsilon_0 E_0 / i \qquad \text{-----(5.1)}$$
$$= 4 \times 8.85 \times 10^{-12} \times (30000\,V / 0.125\,m) / (5 \times 10^{-5}\,A/m^2)$$
$$= 0.15\ s$$

which is still much shorter than the residence time of dust in corona field, t = 1.2 s. Even though the active corona field is limited to the region of the first corona wire as the visual observation indicates and the effective residence time becomes 1/6 (6 wires in one duct), the saturation charge may be given to the dust particles because the charging time constant becomes also 1/6 in considering the simple case of Pauthenier's equation.

A picture of what is going on in this particular case of severe space charge effect might be drawn as described in following:

(1) The gas containing a large quantity of S (total surface loading) due to carbon soot are introduced to the first corona wire region of the precharging field where active pulsed corona is taking place. Although the current density in this region is high enough to satisfy the saturation charging condition of Pauthenier's equation, the amount of negative ions is not sufficient to provide saturation charge or at least adequate level of charge to all of the particles due to a very large quantity of S.

(2) Dust particles poorly charged in the first wire region are brought to

the succeeding corona wire region, forms space charge with very high density in spite of a low charge level of indivisual particles. They reduce the field intensity around the wire below the corona level. Especially in this case of round and smooth wires this effect is distinguished. In the worse cases, the field across the corona and the ground electrode is flattened and a micro discharge from the grounded electrode triggers a spark. In this case of the mesh electrode again produces more easily a micro discharge.

(3) The poorly charged particles can not acquire additional charge in these region nor be collected due to shortage in particle charge.

(4) The overall collection performance can not be enhanced by the pulse energization because of the shortage of particle charge.

5-2-5. Space Charge Effect

It is essential to evaluate the level of the dust surface loading, S, to estimate the severity of space charge effect. Assuming that the all the dust particles are sphere,

$$S = \sum_i 4\pi a_i^2 n_i \qquad \text{-----(5.2)}$$

$$Q_{total} = \sum_i Q_i n_i = S \varepsilon_0 \frac{3\varepsilon}{\varepsilon_s + 2} E_0 \qquad \text{-----(5.3)}$$

where

Q_{total} : total charge of dust particles

a_i : radius of dust particle

n_i : number of particles with a_i

Q_i : saturation charge of dust particles with a_i

When the surface loading meter comprizing of the charger to provide the saturation charge to every particle and the Faraday cage to measure the

total charge, Q, the direct measurement of the total surface loading becomes possible. It is under construction and S in this case will be measured and the assumption shown above should be confirmed.

Space charge effect is also reported to occur in coal burning utility boilers by the use of low NO_x burners operated at the combustion condition of a lower excess air in order to reduce the thermal NO_x. It produces unburnt carbon soot to cause space charge trouble in the electrostatic precipitator.

In this case of the precharger operated in the dc energization mode, the space charge effect seems not to appear and the back corona trouble is dominant. Back corona takes place first in the precharger, and provides positive ions to the space filled with negatively charged particle cloud to decrease its space charge density. As a result, the high surface loading effect is masked due to lower charge density in the field and the level of overall current density consisting of both negative and positive ions remains high.

However, in the pulse energization mode, back corona is completely removed and the space charge effect is revealed. In order to solve both troubles of back corona and space charge effect electrostatically, the use of the preagglomerater in front of the pulsed collection field is recommended. The preagglomerater [45] out of the back corona free precharger and the parallel plane collection field produces larger particles in size than the original. And the pulsed collection field without back corona can achieve its maximum efficiency in absence of space charge effect.

5-2-6. Conclusion

In this series of experiments, the following conclusions are obtained:

(1) The precharger operated in the dc energization, back corona is clearly observed by both the visual observation and V-I characteristics. The dust resistivity level is estimated in the order of 10^{11} -10^{12} ohm-cm.

(2) By the direct-coupled pulse energization mode, back corona is completely disappears in both cases with and without gas load in the precharger.

(3) In the case without gas load, the wave form of the direct-coupled pulse energization is ideal as obtained in the previous tests. The corona activity is very uniform in the entire corona wires.

(4) Under the gas load condition, where unburnt carbon soot is contained, only the first wires are producing active corona, but the succeeding wires indicate feeble or no corona. As s result the current density dropps a half of the no gas load condition. These are due to the space charge effect.

(5) Even in this case the charging time constant is small enough to give the saturation charge according to the calculation using the data of current density. However, the outlet dust mass loading measured at the downstream of the granular bed filter can not be reduced by the pulse energization. This suggests that the dust particles can not acquire enough charge due to the very large quantity of the surface loading.

(6) The space charge effect seems to masked by back corona in the case of dc energization and it appears when back corona trouble is removed.

Table 5.1 Pulse Parameters Measured and Circuit Parameters Estimated (No Gas Load Conditions)

Capacity of Pulse Forming Condenser: C_p = 9 nF Collection Area of Precharger: F = 117 m^2
Measured Value (No Gas Load Condition): V_M = -44 kV (maximum voltage of V_{EP}) V_R = -4.5 kV (final voltage in pulse period) V_D = -27 kV (dc residual voltage when gap turned off) V_0 = -45 kV (charging voltage of C_p) T = 800 ns (oscillation period of LC oscillation) α = 1.8×10^5 s^{-1} (dumping factor)
Estimated Value: L = 4.1 μH (total circuit inductance) r = 1.5 ohm (total circuit loss) C_{EP} = 7.2 nF (inter-electrode capacity of precharger) c = 62 pF/m^2 (capacity of unit collection area)

Table 5.2 Results of Comparative Measurement of Dust Emission by Direct-Pulse Energization and by DC-Energization

Test NO.	Mode of Energization	Speed of Fuel Feeding Screw R_s (rpm)	Gas Volume Q_g (Nm^3/h)	Gas Temparature T_g (°C)	Outlet Dust Mass Loading W_o (g/Nm^3)	Average Current Density i (mA/m^2)	Remarks
1	pulse	800	21,100	190	0.107		
2	pulse	800	20,500	195	0.088		
3	dc	800	21,600	190	0.083		
4	dc	800	22,900	200	0.060		
5	pulse	1000	21,600	180	0.101	0.052	
6	pulse	900	23,100	220	0.092	0.054	
7	pulse	850	23,600	215	0.117	0.058	
8	pulse	800	23,800	220	0.156	0.037 - 0.060	Excesive Sparking
9	pulse	800	24,000	230	0.094		
10	pulse	850	23,400	200	0.159	0.043	Excesive Sparking
11	pulse	850	23,600	205	0.115	0.041	
12	pulse	850	23,000	210	0.219	- 0.052	Excesive Sparking
13	dc	850	20,600	200	0.083		
14	dc	850	23,200	205	0.196		
15	dc	850	22,400	215	0.110		

Note: Soot appears from the stack in Test NO. 8, 10, 12, and 14.

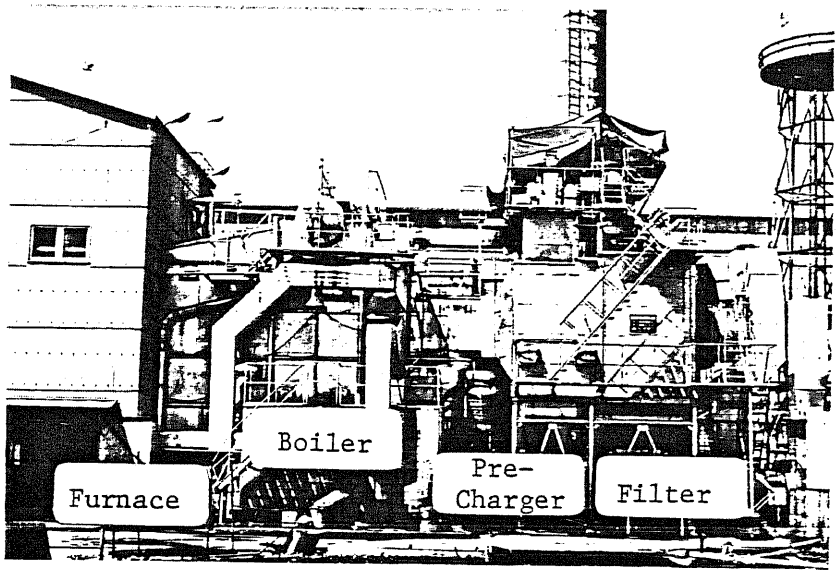

Fig. 5.1 Wooden-Chips Burning Boiler and Its Gas Cleaning System (Electrostatically Augmented Granular Bed Filter of Moving Bed Type)

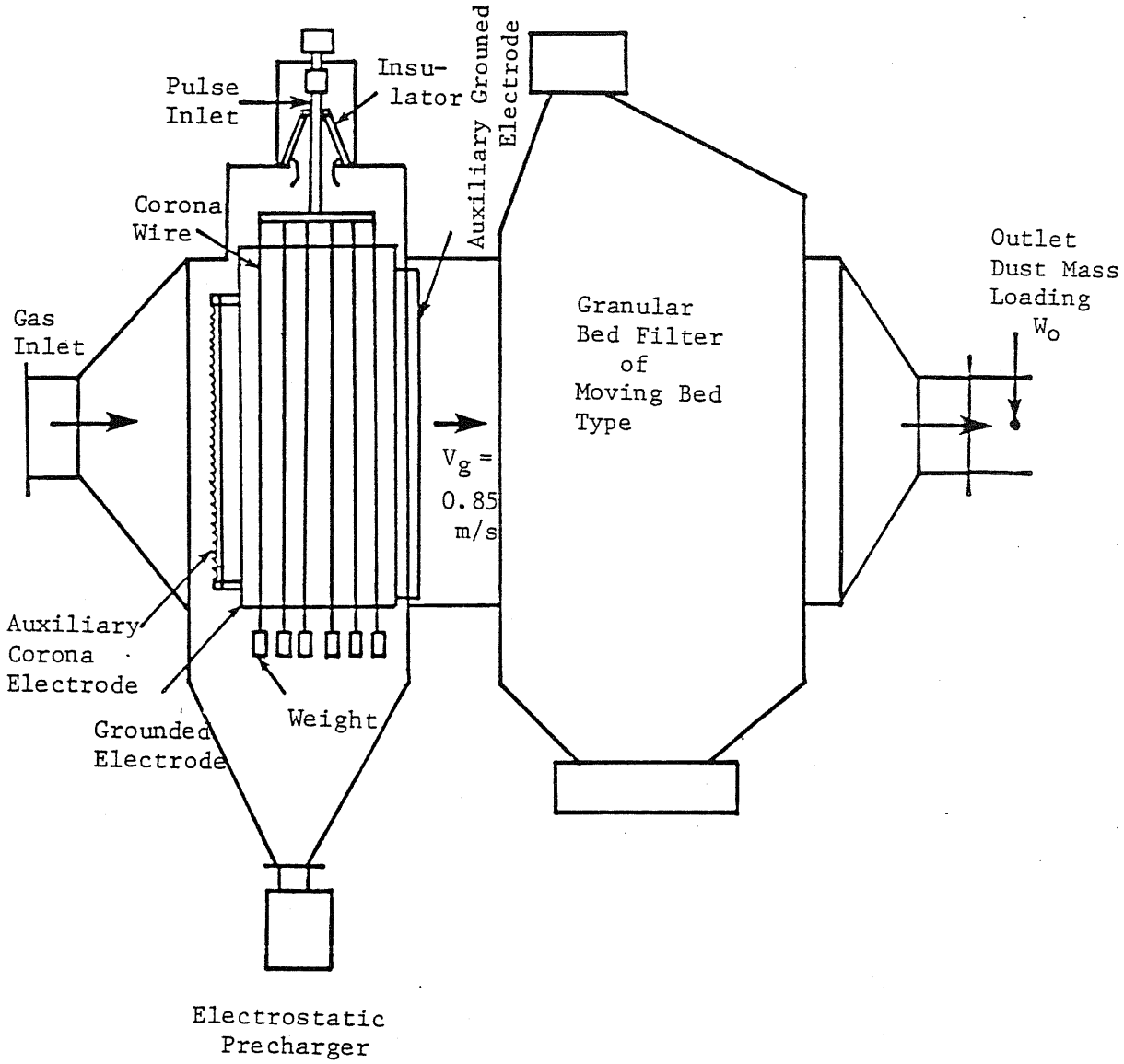

Specifications of Electrostatic Precharger

Gas Flow Rate: Q = 24,500 Nm^3/h
Gas Temperature: T_g = 200 - 250 °C
Inlet Dust Mass Loading: W_i = 5.0 g/Nm^3
Duct Spacing: 2D = 250 mm
Total Surface Area of Grounded Electrode:
F = 117 m^2
Grounded Electrode: Mesh
Length in Gas Flow Direction: L = 1 m
Residence Time of Dust: t = 1.2 s
Corona Wire: Smooth Round Wire with d = 4mmo
6 wires spaced at 140 mm

Fig. 5.2 Test Facility of Electrostatic Precharger for Granular Bed Filter

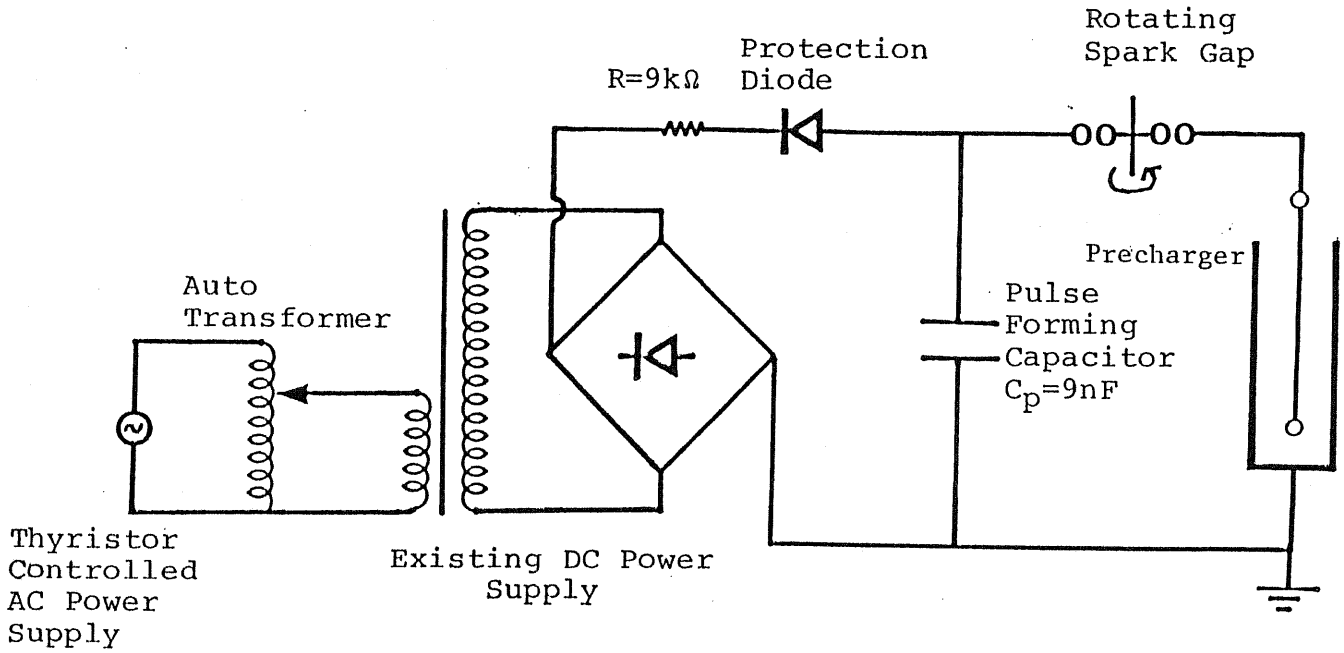

Fig. 5.3 Pulse Power Supply of Direct-Coupled Pulse Energization Using Existing DC Power Supply with Full-Wave Rectification System
(load capacity of precharger estimated: C_{EP} = 7.2 nF)

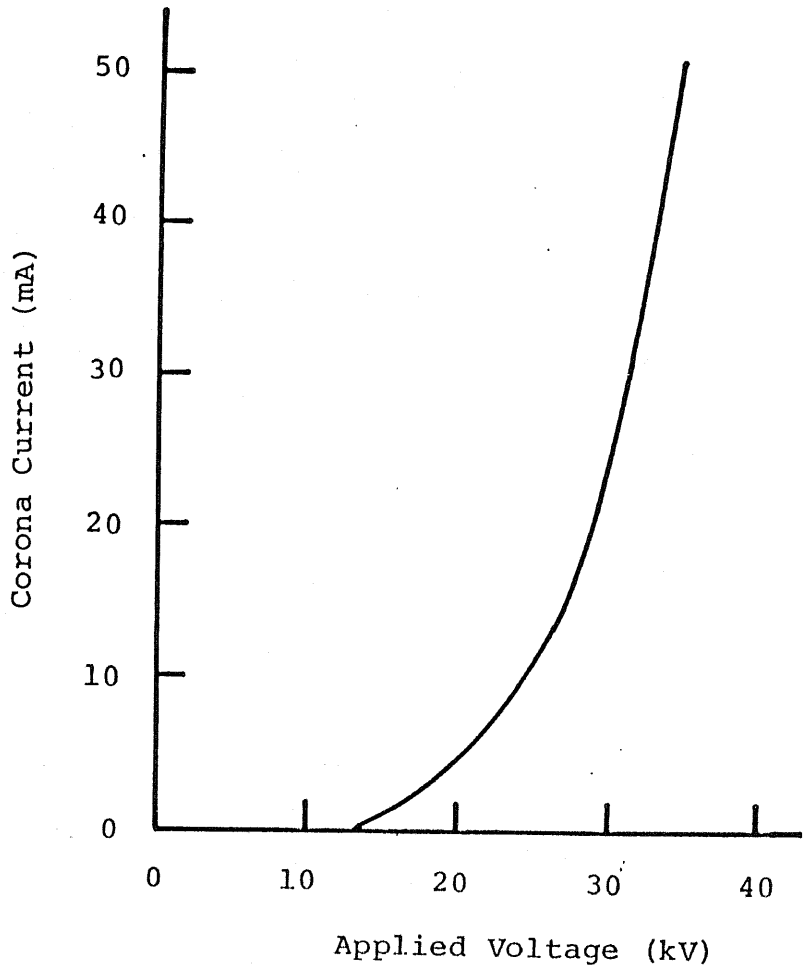

Fig. 5.4 V-I Characteristics of Electrostatic Precharger with DC-Energization under No Gas Condition (T_g = 250 °C)

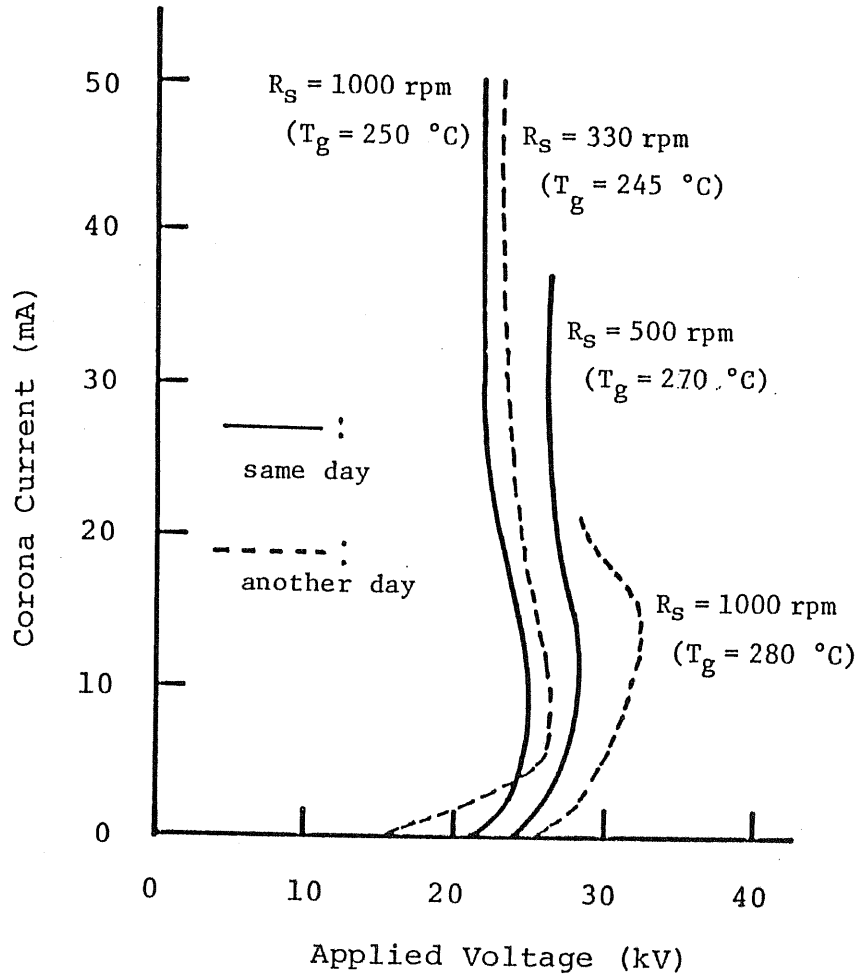

Fig. 5.5 V-I Characteristics of Electrostatic Precharger with DC-Energization under Gas Load (Load conditions are chaneged by the screw revolutions of wooden-chips feeder, R_s; full load: R_s = 1000 rpm)

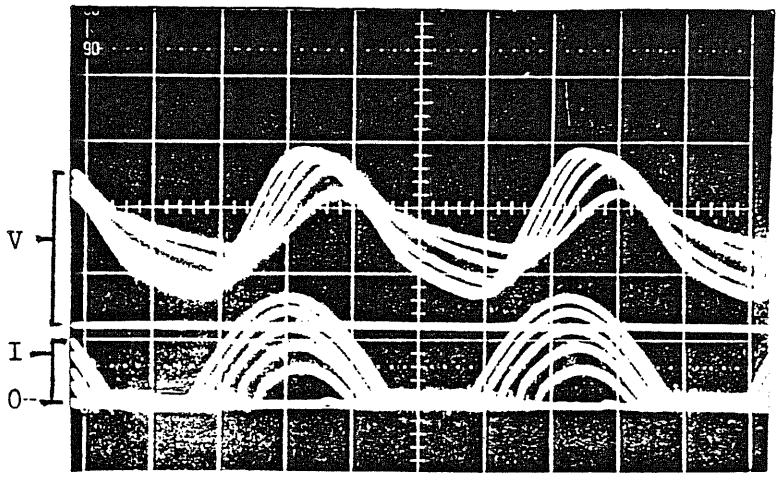

key: from larger peak to lower
1: $\overline{V}$ = 26 kV, $\overline{I}$ = 50 mA
2: 26 kV, 40 mA
3: 27 kV, 30 mA
4: 28 kV, 20 mA
5: 28 kV, 10 mA
6: 13 kV, 1 mA
($\overline{V}$, $\overline{I}$: average value)

Fig. 5.6 Wave Forms of Precharger Voltage and Output Current of DC Power Supply with DC Energization under Full Gas Load (R_s = 1000 rpm)

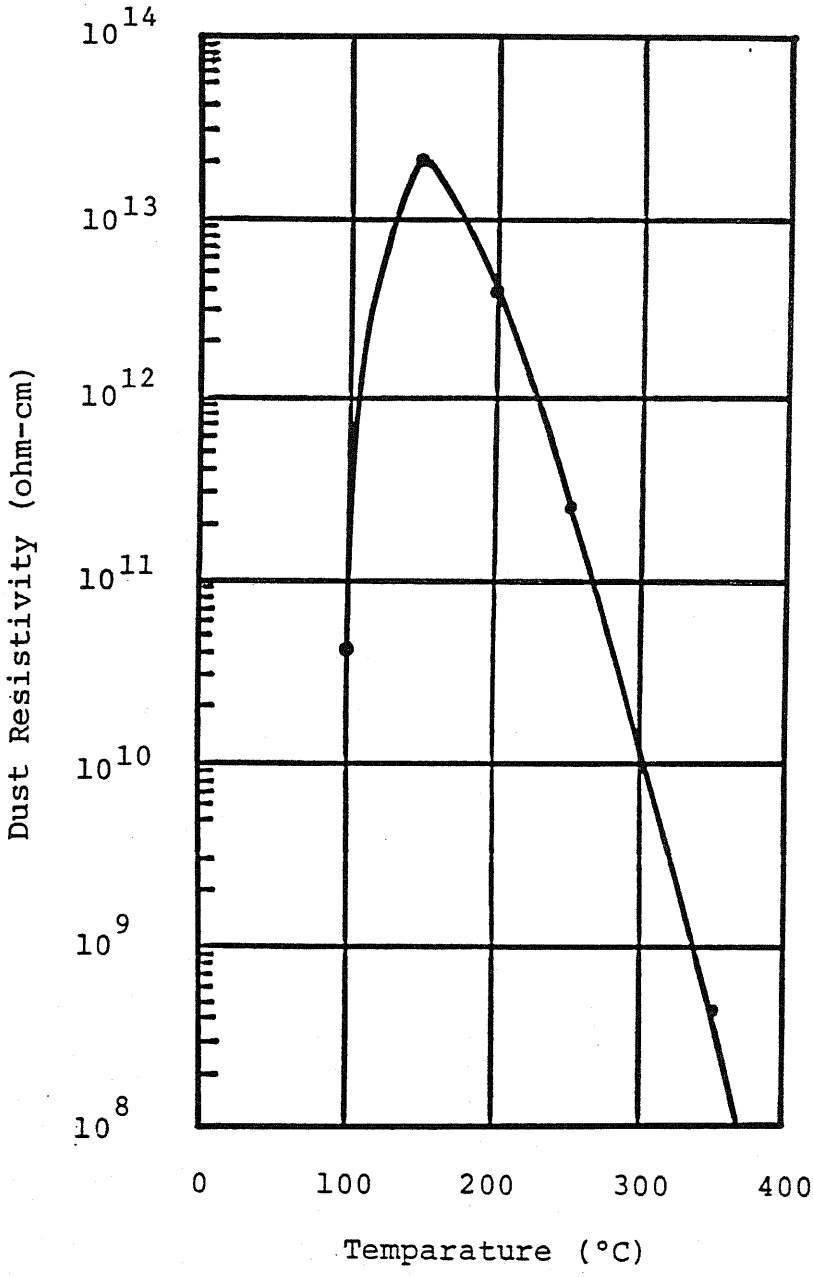

Fig. 5.7 Dust Resistivity vs. Temparature
(Humidity : 15 vol%)

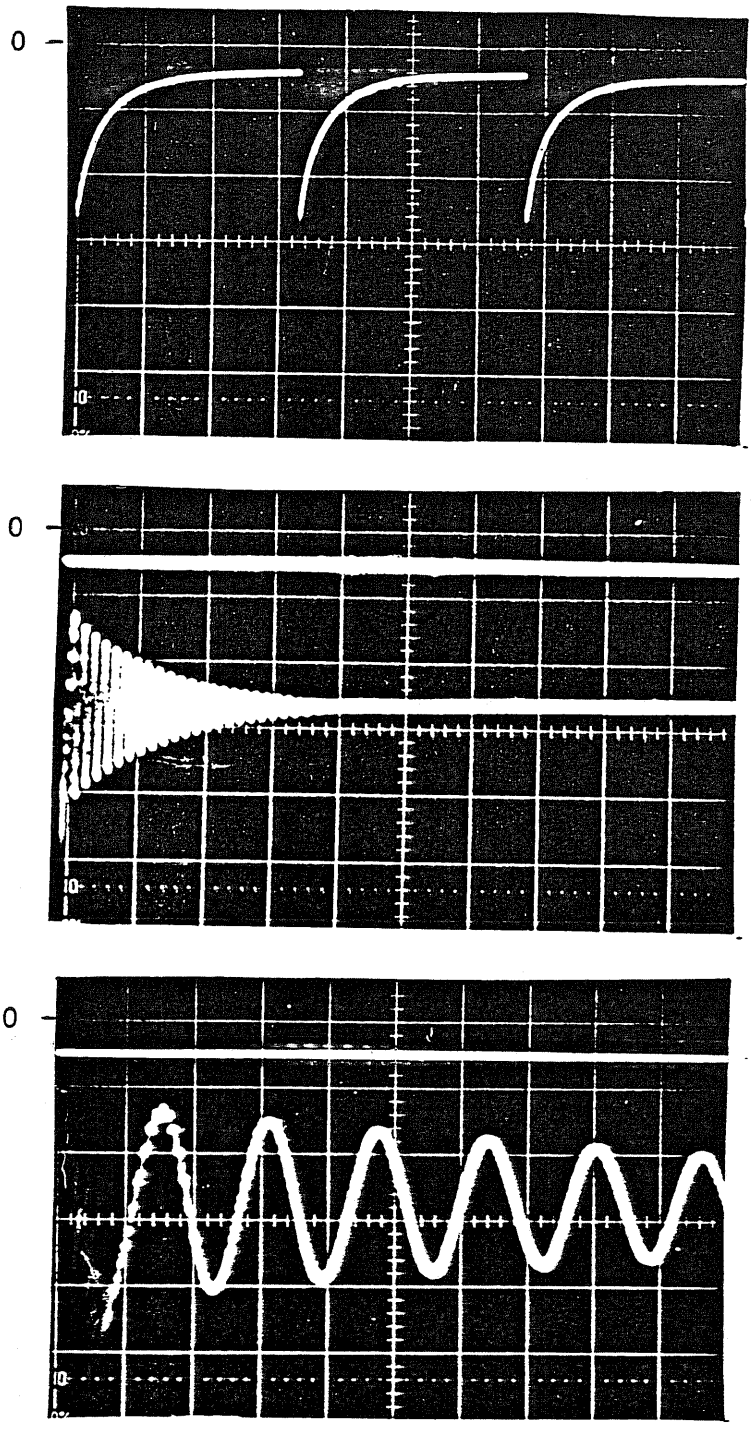

(a) Saw-Teeth Like Pulse Wave With Sharp Initial Peal (V:10kV/div, T:5ms/div)

(b) Transient LC Oscillation (V:10kV/div, T:5μs/div)

(c) Magnified Oscillating Part (V:10kV/div, T:500ns/div)

Fig. 5.8 Pulse Voltage Wave Form Measured at the Inlet Terminal of Corona Electrode Under No Gas Load Condition (T_g = 205 °C; exhaust gas in precharger)

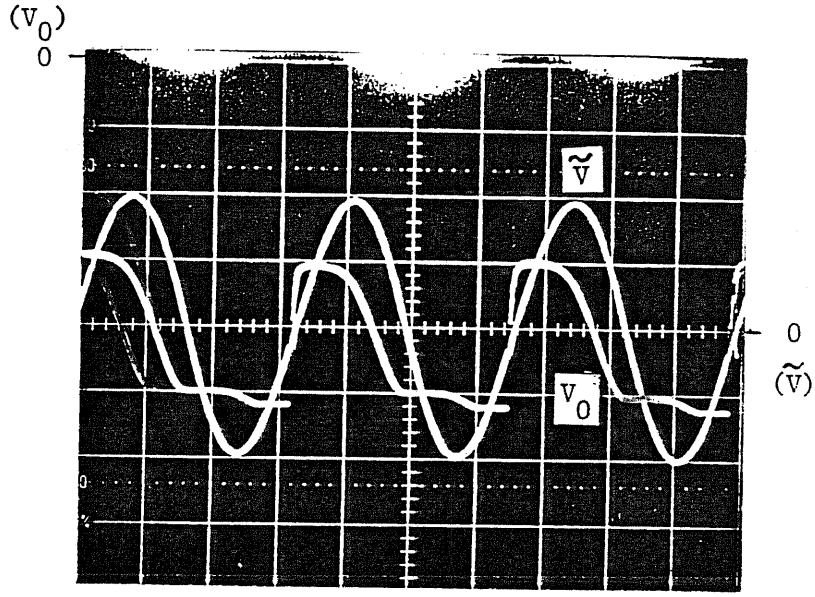

T : 5 ms/div

V_0 : charging voltage wave form of pulse forming condenser (8.8 kV/div)

$\tilde{V}$: transformer primary voltage wave form (100 V/div)

Fig. 5.9 Charging Voltage Wave Form of Pulse Forming Condenser and Transformer Primary Voltage Wave Form Indicating Timing of Spark and Charging (No Load Condition; T_g = 205 °C)

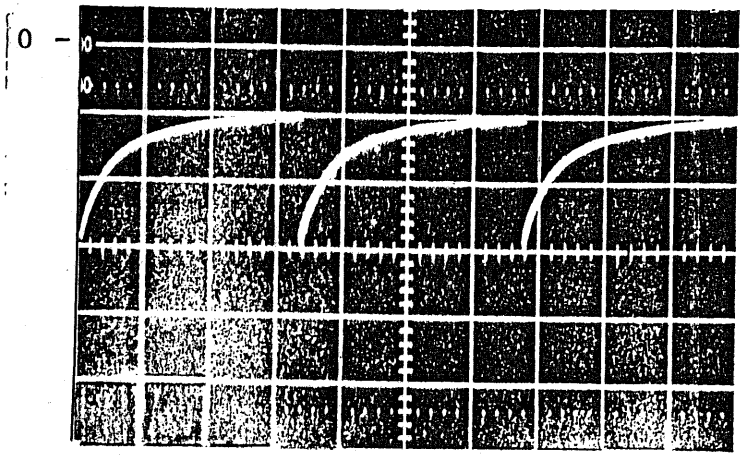

(a) R_s = 100 rpm

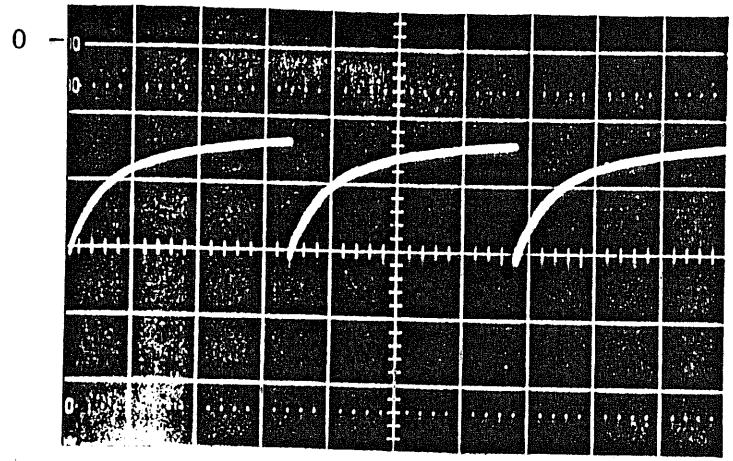

(b) R_s = 400 rpm

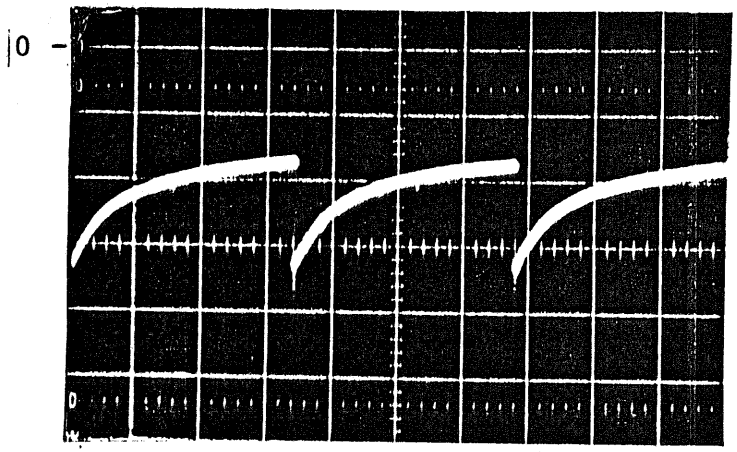

(c) R_s = 800 rpm

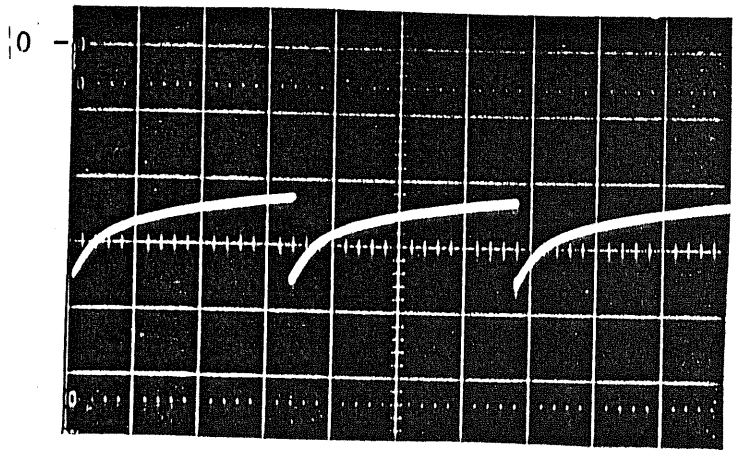

(d) R_s = 1000 rpm

Fig. 5.10 Change of Pulse Voltage Wave Form in Direct-Coupled Pulse Energization with increase in Gas Load (Gas load is changed by screw revolutions of fuel feeder, R_s.)

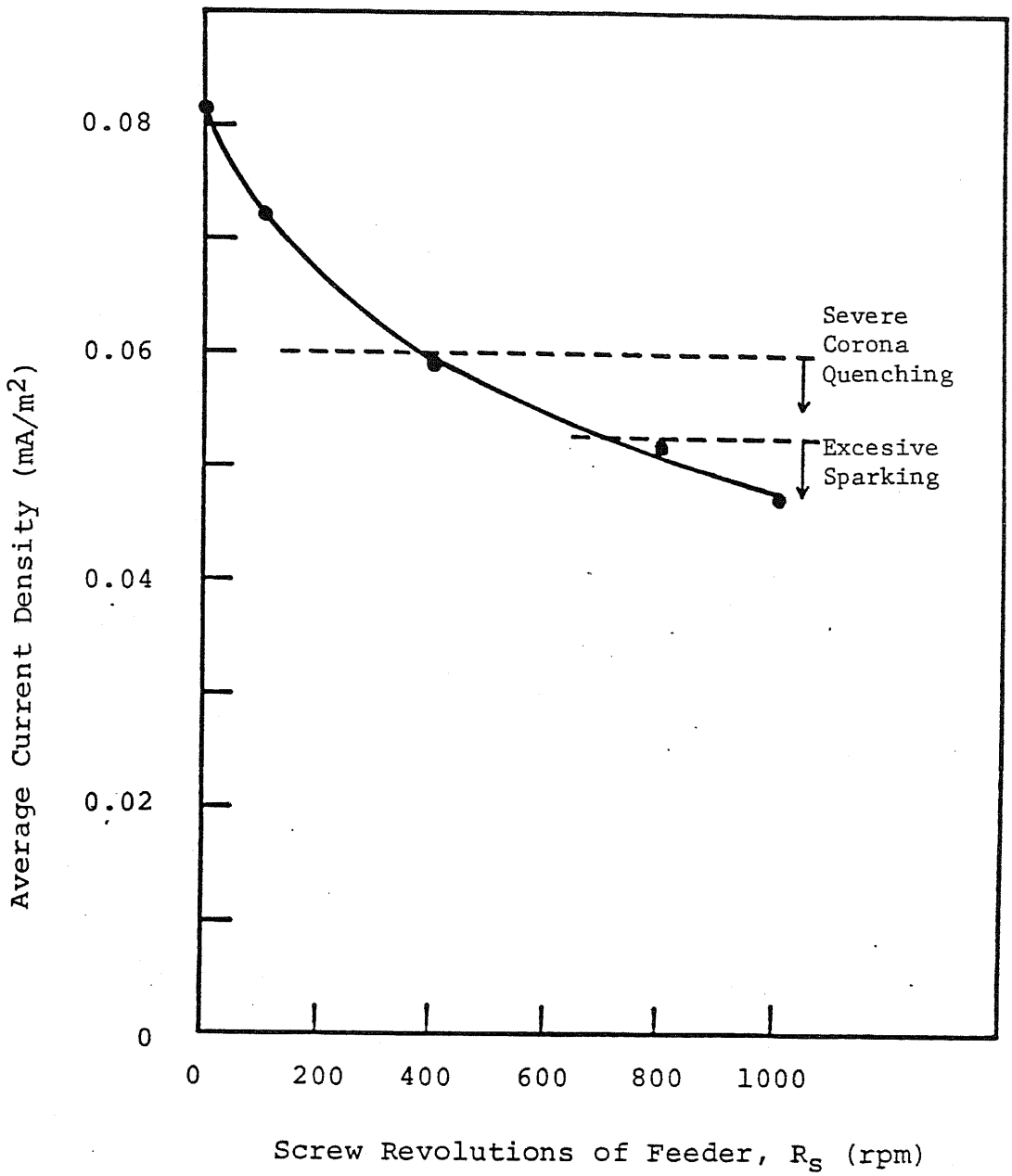

Fig. 5.11 Change in Current Density Due To Space Charge Effest (Severity of space charge effect increases with increase in gas load changed by screw revolutions of fuel feeder, R_s.)

5-3. Electrostatic Precipitator for Glass Furnace

5-3-1. Introduction

The second series of the field tests is carried out at a medium size electrostatic precipitator as shown in Fig. 5.12. It is used for cleaning the exhaust gas from the glass melting furnace. Two series of tests are made using the same precipitator. One is the exhaust gas from the glass fiber furnace, and another from the cathode-ray tube furnace.

In the former case, the electrostatic precipitator with conventional dc energization fails to achieve the designed dust emission. The visual observation and the V-I characteristics indicate that severe back corona is taking place in the entire collection field. By the direct-coupled energization, the back corona correction and the performance enhancement is expected. However, at this extremely high level of dust resistivity (r_d = 10^{14} ohm-cm) even the pulse energized collection field can not remove back corona. Moreover, a large quantity of extremely fine fume of boron (B_2O_3 and H_3BO_3) is continuously condensed from the vapor phase in passing through the precipitator. As the result, the collection performance can not be enhanced. This series of tests indicates the threshold level of dust resistivity where the pulse energization can be applicable for the purpose of back corona correction.

In the latter case, the dust resistivity is in a moderate level and the condensation of fine fumes do not take place. Even in the dc energized collection field the dust emission of lower than 10 mg/Nm^3 (more than 99 % collection efficiency) is achieved. The main target in this case is to test the reduction in energy consumption of the electrostatic precipitator by the direct-coupled pulse energization. It is recognized that the great reduction in energy consumption as low as 1/16 of that by the dc energi-

zation is achieved without lowering the collection performance.

Another big target of these series of tests is to confirm the direct-coupled energization concept in the practical precipitator with a larger scale, and to check the performance of the pulser module constructed. The cassette type pulser module as shown in the chapter 4 is installed on its roof. It is confirmed that the voltage wave form as well as the corona characteristics are same as those in the laboratory and the pulser works as designed.

In this chapter, these tests results as well as their analysis are described.

5-3-2. Test Facility

Fig. 5.13 shows the gas cleaning system for the glass melting furnace. It consists of the lime reaction chamber which is aimed to remove HF in the exhaust gas (lime conditioning) and the electrostatic precipitator out of 3 fields. Water spray is made before the lime conditioning. At both of the inlet and the outlet ducts of the precipitator are measured the dust mass loading and the boron loading in the vapor phase. Two series of tests are made by changing the gas flow from the glass fiber furnace and from the cathode-ray tube furnace. The gas conditions are shown also in the figure.

Fig. 5.14 shows the schematic top view of the precipitator in the pulse energization mode. Fields 1 and 2 are energized in parallel using the cassette type pulser module as shown in the chapter 4. They have a standard duct spacing of D = 300 mm and their total collection area becomes F = 1523.2 m^2 which is within the capacity of the pulser module. Not only the direct-coupled pulse energization but also the dc-biased pulse energization by connecting an additional dc power supply directly are also tested. The dc-biased pulse energization in this case is used to raise the

average voltage (namely increase V_R as described later) and the other behaviors are same as those by the direct-coupled pulse energization. Field 3 has a wide duct spacing of 2D = 500 mm and is operated in the dc energization.

In the dc energization mode, the dc power supply is automatically controlled to maintain the corona current in the level of

Fields 1 and 2 : I = 400 mA (i = 0.53 mA/m^2)

Field 3 : I = 400 mA (i = 0.81 mA/m^2)

however sparking especially in Fields 1 and 2 prevents the stable operation and both the current and the voltage fluctuate.

5-3-3. Back Corona Correction Test

Here the experimental results of the former case of cleaning the gas from the glass fiber furnace are described.

(A) V-I Curves in DC Energization:

Fig. 5.15 shows the V-I characteristics of Field 3 with the lime conditioning stopped. Two examples measured on the same day are shown. The curve shows a very steep rise and a tendency of hysteresis even in this case of the wide duct spacing of 2D = 500 mm. The visual observation indicates that a very severe back corona is occurring in the entire collection plates as shown in Fig. 5.16 which is taken in this condition by using a potable image intensifier. Even in this wide spacing precipitator, the positive feedback of enhancing back corona from the dust layer and negative corona from the corona wires each other is recognized as this picture indicates that the dust layer opposite to the corona wires emitts especially bright lights of back corona.

In the case of lime conditioning off, the excessive sparking in Fields

1 and 2 prevents to measure V-I characteristics. With increasing the voltage, the current suddenly jumped to a high level of say 140 mA, and sparking takes place concurrently. As the results, the stable operation becomes impossible and the voltage and the current in the automatic control become a cyclic mode of the current jump from 0 mA to 140 mA when the voltage reaches V = 30 -32 kV and sparking resulting V = 0 kV and I = 0 mA for a while. This extremely unstable V - I characteristics of excessive sparking is usually observed in the case of a lower dust resistivity range of $r_d = 10^{10} - 10^{11}$ ohm-cm due to back corona. But judging from various data shown later and the V-I characteristics of Field 3, the dust resistivity is in the very high level of $r_d = 10^{14}$ ohm-cm and another mechanism causes this funny characteristics of excessive sparking. This mechanism is not clear yet, however a hypothesis can be drawn. As described later, a large quantity of extremely fine fumes of boron compounds exists and also condenses from the vapor phase continuously. They suppress the corona current by forming space charge to produce a considerably high electric field near the dust layer. In this stage, however, enough ionic current can not reaches to the dust layer. By raising the applied voltage the corona current reaching to the layer exceeds the threshold, and back corona suddenly takes place which is enhanced by the high field near the layer to turns into sparking. This hypothesis should be supported by the more precise experiments.

It is noted that in the earlier stage of the operation (within 6 months since its start) with the lime conditioning a stable operation of all fields are reported as:

Field 1 : V = -31.5 kV, I = 200 mA, ($i = 0.26$ mA/m^2)

Field 2 : V = -32.5 kV, I = 200 mA, ($i = 0.26$ mA/m^2)

Field 3 : V = -53.0 kV, I = 200 mA, ($i = 0.41$ mA/m^2)

with few sparking. And the visual observation in all the fields reveals that the entire collection electrode is growing due to back corona. It is

not sure whether the time dependent characteristics of the precipitator such as formation of the permanent dust layer changed the operation condition or not. These funny aspects may be due to coexisting of extremely high dust resistivity and high dust surface loading.

(B) Dust Resistivity:

Fig. 5.17 shows the dust resistivity measured in the laboratory at the humidity of 15 vol% with temperature changed. The lime conditioning does not alter the value of dust resistivity. It is assumed that the $Ca(OH)_2$ particles are covered with boron compounds and the dust resistivity becomes one of the boron compounds with very high resistivity. In the precipitator temperature range, the measurement shows $r_d = 10^{13}$ ohm-cm. However, the humidity in operation is much less between 7 - 10 vol%, so that it is likely the working resistivity lies about $r_d = 10^{14}$ ohm-cm. The state of back corona in the pulse energized field as shown later where no light can be observed from the collection electrode. This type of back corona appears in the extremely high resistivity of say $r_d > 10^{14}$ ohm-cm.

(C) Pulse Voltage Wave Forms:

The direct-coupled pulse energization using the pulser module is performed as shown in Fig. 5.14 and the pulse voltage is measured at the inlet terminal of Field 2. Fig. 5.18 shows the pulse voltage wave in three different time scales when the lime conditioning is off. A saw-teeth pulsating wave form with a transient LC oscillation at its leading edge is obtained which is essentially same as the one obtained in the laboratory test with a clean electrode system. Fig. 5.19 shows the voltage wave form of the pulse forming condenser in the pulser module which is also as same as the one obtained in the laboratory test of the pulser with a sudden voltage drop due to switching of the rotating spark gap and a rapid voltage rise due to charging through the voltage doubling circuit. It is confirmed

that the direct-coupled pulse energization concept is applicable in a practical plant with a full scale, and the cassette type pulser module developed by the author also shows its designed performance.

However, there is a distinct difference in the pulse voltage in the continuous decay resulting a very low level of the final voltage of V_R = - 10 kV, caused by back corona induced positive current. The problem of back corona is explained later in detail.

Table 5.3 shows the pulse parameters measured from the voltage wave form of Fig. 5.18 and the estimated value of the pulse circuit componets of the load and the wiring. It should be noted that the value of c = 49 pF/m^2 is very close to c = 50 pF/m^2 used in designing the pulser module. A proper installation enables to reduce the total inductance in the pulse circuit (L = 1.98 μH). If it is in this level, the pulse rise time in a larger precipitator with a collection area of F = 5000 m^2 becomes T_r < 2 μs which is essential for the uniform corona formation and raising the sparking threshold.

(D) Factors Affecting to Pulse Voltage Wave Form:

The effect of the lime conditioning to the pulse voltage wave form is tested. Fig. 5.20 shows the pulse voltage wave form measured during the lime conditioning (V_M = -50 kV and F_p = 50 Hz). However, there is no distinct difference between Figs. 5.18 and 5.20. indicating that the corona production in the corona wires, the back corona severity as explained later, and probably the high dust surface loading do not change by the lime conditioning.

Fig. 5.21 shows the effects of the peak voltage, V_M, on the pulse voltage wave form, especially to the decay phase with keeping F_p = 50 Hz. In this case also, the decaying speed of the decay phase I as defined previously (see Fig. 2.31(a)) is enhanced by increase of V_M and as a result V_R is decreased. However, the voltage drop continues in the decay phase II

in all cases of Fig. 5.21. This is one of the evidence of back corona occurrence which provides a large quantity of positive ions to produces a continuous decay even in the decay phase II.

Fig. 5.22 indicates the effect of the pulse repetition frequency, F_p, on the voltage wave form measured at V_M = -50 kV. It is astonishing to see that the decay speed in the decay phase rises with increasing F_p and, concurrently, the magnitude of the final voltage remains unchanged at about V_R = -10 kV, although V_R shows a slight increase with F_p. It is anticipated that with increasing F_p the average number of negative ions arriving at the surface of the dust layer in an unit time rises proportionally, tending to raise its surface potential. However, with the increase in the surface layer potential beyond the breakdown threshold of the layer, which is originally a statistical value scattering around its average, the number of the breakdown points would increase to produce an increased emission of positive ions, and thereby keeping the magnitude of the surface potential almost unaltered. As a result, the supply of the positive ions by back corona per each pulse should be increased in proportion with F_p, and the decay time is increased with F_p, concurrently. This is an only possible explanation of Fig. 5.22 and such a instrument as to measure the time dependent change of both negative current and positive one is needed to support this assumption.

Fig. 5.23 show the change of the voltage wave form due to the time dependent fluctuation of the furnace condition where V_M = -50 kV and F_p = 50 Hz is being kept. The burner in the furnace changes every 15 min. to produce a fluctuation in the gas volume, gas temperature, and the dust loading resulting a slight change in the voltage wave form. However, the continuous decay in the decay phase is seen in all cases of Fig. 5.23 indicating that the back corona do not stop and moreover its severity do not seem to be change by the furnace fluctuation.

(E) Effect of DC Bias Voltage:

By connecting dc power supply to the direct-coupled pulse energization system (see Fig. 5.14) without using any coupling means, the dc-biased pulse energization is tested. Fig. 5.24 shows the voltage wave forms in two different pulse repetition frequency. There is no difference in transient LC oscillation between these figures and Fig. 5.20(b) except in their magnitude. However, a great difference is recognized in the saw-teeth wave form. Its bottom is increased by the aid of dc bias voltage, which, however, is not flat but fluctuating in accordance with the frequency of the dc power supply (full-wave rectification : 120 Hz). It should be noted that the dc corona onset voltage in this particular case is V_c = -24 kV and the dc voltage is flat without pulse superposition up to this level. The negative ionic current induced by the pulse voltage should be distinguished in the first 2 - 4 ms and the voltage fluctuation in the dc bias voltage is caused by the positive current produced by back corona. This is another clear evidence of back corona in the pulse energized field. The back corona distinguishing voltage in this case should be very low as blow -10 kV resulting the continuous voltage decay when the dc bias voltage removed (Fig. 5.20 etc.).

(F) Visual Observation of Pulse Energized Field:

Although the pulse voltage wave form indicates that there is severe back corona taking place, light activity in the collection electrode can not be recognized in the pulse energized fields (Fields 1 and 2) with the lime conditioning on and off by the visual observation both by naked eyes and by the potable image intensifier from the man-holes on the roof of both Field 1 and 2. Fig. 5.25 shows the light activity of Field 2 with the pulse energization. All the corona wires emitts lights with good uniformity. According to the author's experience, such a mode of back corona with such feeble light activity is caused by an extremely high

resistivity dust with say $r_d > 10^{14}$ ohm-cm.

(G) Measurements of Collection Performance:

The collection performance of the pulse energized field is tested using the sampling filter with the lime conditioning on and off. The comparison tests of the dc energized fields are also made. These results are shown in Tables 5.4 and 5.5. The inlet condition fluctuates and the collection efficiency is difficult to estimate, however it is recognized that the collection performance can not be increased by the pulse energization in any cases. The change of the operation mode of the pulse energization does not indicates any distinct difference in collection performance. In the case of no lime conditioning, about 40 % of the dust components is the boron compounds. On the other hand in the case of the lime conditioning on, about 60 - 70 % of its components becomes the calcium compounds, and about 10 % the boron compounds.

The second series of measurements of the collection performance of the dc-biased pulse energization (see Fig. 5.24) together with an extremely low current operation of the direct-coupled pulse energization is made. The voltage wave form of the direct-coupled pulse energization with the extremely low current operation is shown in Fig. 5.26. Fig. 5.26(a) indicates that back corona induced voltage decay is stopped, in this case of extremely low current of pulse-induced negative corona. Table 5.6 shows the test results. However, the effect of the dc-bias voltage could not be seen at all. The best performance in the pulse energization mode is obtained by the extremely low current operation and the collection efficiency becomes 62.5 %. In this operation mode, the initial negative current seems too small to cause back corona and also to charge dust particles effectively. The test of the dc energization is made on the other day and the condition may changes. But the collection efficiency is the highest of all these tests in this table. It should be noted that the

boron compounds (shown by conversion of B_2O_3 in the table) in vapor phase decreases in the precipitator due to condensation to the fine fume. The quantity of the condensation is estimated by:

$$(B_{in} - B_{out}) \times \frac{Q_{in}}{Q_{out}} \quad \text{(see Table 5.6)} \quad \text{-----(5.4)}$$
$$= (1240 - 871) \times (19800/23300) = 220 \text{ mg/Nm}^3$$

which is the same amount as the inlet dust mass loading. The collection efficiecy should be taken into account of this condensation and the efficiency shown above is only estimated from the dust mass loading at the inlet and the outlet which becomes lower than the actual value.

According to the investigation, the boron compounds condense from the vapor phase continuously in accordance with the decrease of the gas temperature down to about 70 °C. It is very difficult to lower the gas temperature below 70 °C before the electrostatic precipitator in the existence of the boron compounds which may cause a trouble of reduction of heat transfer efficiency of a heat exchanger by deposition. The continuous condensation produces a large quantity of very fine fumes to produce a large dust surface loading in the precipitator. Fig. 5.27 shows the picture of the dust on the sampling filter sampled at the outlet. It can be seen that there are a considerably large amount of needle like particles with a very small diameter and also a very fine particles with less than 1 μm in diameter.

(H) Discussions:

This is another unfavorable condition for the electrostatic precipitators which may be characterized by co-existence of extremely high resistivity and continuous condensation of very fine particles. The space charge effect produced by such fine particles is masked by extremely severe back corona and can not be clearly seen. However, a very unstable

operation in the dc energization at Fields 1 and 2 with a standard duct spacing seems to indicate the space charge effect.

This series of tests indicates that back corona can not be removed even by the pulse energization when the dust resistivity level is beyond about 10^{14} ohm-cm. In such cases, the parallel plane collection fields [46] or the pulse energized collection fields in a very low current operation both combined with a back corona free precharger may be one of the solutions. A suitable chemical agent to lower the dust resistivity in one order to the level of $r_d = 10^{13}$ ohm-cm at which the pulse energization can work is another solution.

However, the remedy for the condensation of boron compouds should be provided in order to achieve the complete solution for this particular gas cleaning system.

5-3-4. Tests on Energy Saving Effect

The second series of tests using the same electrostatic precipitator is made by changing the gas flow, and the exhaust gas from the furnace producing cathode-ray tube glass is introduced. The lime conditioning is also maintained in order to remove HF components in the gas. The dust contained in the exhaust gas has lower dust resistivity and there is no condensation in the temperature range of the precipitator. The collection performance even by the dc energization is very high as more than 99 % of collection efficiency. The main target of this series of tests is therefore in the reduction of energy consuption of the electrostatic precipitator by the pulse energization.

(A) V-I Characteristics of DC Energization:

Fig. 5.28 shows the V-I characteristics of each fields. Every curve

indicates the normal corona V-I characteristics where no hysteresis tendency is recognized.

(B) Pulse Voltage Wave Forms:

Figs. 5.29, 5.30, and 5.31 show the pulse voltage wave forms in two different time scales and the voltage wave forms of the pulse forming condenser operated in F_p = 25Hz, 50 Hz, and 100 Hz, respectively. It is clearly recognized that the saw-teeth voltage wave forms where the decay phases I and II are clearly discriminated in all cases becomes the typical one when back corona does not exist. The decaying speed in the decay phase I lasting 3 - 4 ms is almost same in these three different pulse repetition frequency and in the decay phase II the voltage wave form shows almost flat resulting the same value of the final voltage, V_R = -20 kV. This also indicates a quantity of the negative current produced by one pulse becomes almost same and the ionic current increases in proportional to the pulse repetition frequency in this range of F_p (see Table 5.7).

It should be noted that the voltage wave forms of Fig. 5.18 etc, in the previous series of tests using the same facility indicate severe back corona in comparison with Figs. 5.29 - 5.31.

(C) Reduction in Energy Consumption:

The collection performance tests are made with the pulse energization in three different pulse repetition frequency and the dc energization. The maximum voltage in the pulse energization is kept as high as possible within no sparking condition (V_M = -50 kV). Table 5.7 shows the test results. The outlet mass loading is below 10 mg/Nm^3 in all cases tested and the collection efficiency is higher than 99 %. In this range of very low dust mass loading, there is no difference in collection efficiency of all cases in taking account of the measuring error.

The total energy used in Fields 1 and 2 for energization and excluding

for the hammering, the blower, the controller, and so on are shown also in Table 5.7. In the dc energization of automatic control, 22.2 kWh is consumed. On the other hand a great reduction is obtained in the direct-coupled pulse energization. The reduction rate increases in accordance with decrease in pulse repetition frequency and it becomes as high as 94 % in F_p = 25 Hz is obtained, while the collection performance is not decreased.

Energy saving effect is also expected even in the dc energization with such a control as the intermittent energization as mentioned as "semi-pulse concept" in the chapter 1. However, the reduction rate is probably up to 25 %. The reason of high collection efficiency of the direct-coupled energization in the very low current operation may be explained by the difference in the state of corona discharge as shown in the paragraph 4-3. Pulsed corona is produced only once at the instance of pulse impression with a very high intensity to increase the effective field intensity by the space charge effect. On the other hand, dc corona is in a form of Trichel pulse to produce continuous current.

5-3-5. Conclusions

This series of the field test made at the electrostatic precipitator of the gas cleaning system for the glass melting furnace provides following conclusions:

(1) The direct-coupled pulse energization can be applied to the practical electrostatic precipitators with a full equipment. The saw-teeth voltage wave form with a transient LC oscillation acting as a submicro-second pulse at its leading edge is obtained.

(2) The cassette type pulser module made by the author is installed for

this test and its performance is confirmed to be the one as designed. A proper installation gives a smaller circuit inductance in wiring. It indicates the application of this direct-coupled pulse energization method to a very large precipitator with say 5000 m^2 collection area is also possible without much enlargement of pulse rise time.

(3) Even in the pulse energized collection field can not remove back corona nor enhance the collection performance in the case in cleaning the gas from the fiber glass furnace with the lime conditioning on and off. The dust resistivity in this case is $r_d = 10^{14}$ ohm-cm. The pulse voltage wave form shows a continuous decay throughout the decay phase produced by back corona induced positive current. As a result, the final voltage becomes a very small of $V_R = -10$ kV.

(4) In this case a very low current density operation with $V_M = -38$ kV, $F_p = 10$ Hz, and $i = 0.005$ mA/m^2 show the best performance in all the conditions of the pulse energization tested.

(5) The space charge effect due to a very high dust surface loading produced by a large quantity of fine particles of boron compounds condensing continuously from the vapor phase in the precipitator does not appear clearly as the back corona induced positive current masked it.

(6) The energy saving effect of the direct-coupled pulse energization is tested in the lower resistivity level where even the dc energization shows a good collection performance. The power consumption by the condition of $V_M = -50$ k, $F_p = 25$ Hz, and $i = 0.023$ mA/m^2 becomes as low as 1/16 of that by the dc energization.

Table 5.3 Pulse Parameters Measured and Circuit Parameters Estimated

Capacity of Pulse Forming Condenser: C_p = 93.3 nF Total Collection Area of Field 1 + Field 2: F = 1523.2 m^2
Measured Value of Puls Parameters: V_M = -50 kV (macimum voltage of V_{EP}) V_R = -10 kV (final voltage in pulse period) V_D = -33 kV (dc residual voltage when gap terned off) V_0 = -46 kV (charging voltage of C_p) T = 1.8 us (oscillation period of LC oscillation) α = 1.4×10^5 s^{-1} (dumping factor)
Estimated Value: L = 1.98 μH (total circuit inductance) r = 0.55 ohm (total circuit loss) C_{EP} = 74.7 nF (inter-electrode capacity of EP) c = 49 pF/m^2 (capacity of unit collection area)

Table 5.4 Collection Performance of Pulse Energized Fields
(Furnace: Glass Fiber, Field 3: DC Energization)

Test Conditions of Direct Coupled Pulse Energization	No Conditioning (mg/Nm^3)			Lime Conditioning (mg/Nm^3)		
	Dust Mass Loading	Dust Components		Dust Mass Loading	Dust Components	
		$Ca(OH)_2$	B_2O_3		$Ca(OH)_2$	B_2O_3
Outlet Conditions V_M=-50kV, F_p=50Hz, i=0.056mA/m^2	88.6	3.26	36.0	662	444	71.3
	81.5	2.79	36.9	540	389	67.8
Outlet Conditions V_M=-50kV, F_p=25Hz, i=0.029mA/m^2	104	3.81	35.0	468	333	69.7
	111	5.00	43.9	550	350	56.6
Outlet Conditions V_M=-50kV, F_p=100Hz, i=0.100mA/m^2	127	5.35	48.0	755	551	91.6
	119	4.75	43.3	683	481	91.0
Outlet Conditions V_M=-40kV, F_p=50Hz, i=0.035mA/m^2	92.2	3.42	38.8	421	292	63.6
	96.1	3.40	42.0	487	279	62.4
Inlet Conditions	214	10.1	78.9	1960	1249	192.8
				2670	1321	167.7

Table 5.5 Collection Performace of DC Energized Fields

Test Conditions of DC Energization	No Conditioning (mg/Nm^3)			Lime Conditioning (mg/Nm^3)		
	Dust Mass Loading	Dust Components		Dust Mass Loading	Dust Components	
		$Ca(OH)_2$	B_2O_3		$Ca(OH)_2$	B_2O_3
Outlet Conditions All of Three Sections Energized	114	14.7	72.2	337	211	50.6
	129	11.9	66.2	316	202	54.7
Outlet Conditions Only Third Section Energized	328	91.9	123.8	1010	829	144.5
	315	67.7	109.1	952	740	119.0
Inlet Conditions	324	30.2	148.6	1360	925	162.3
	431	43.8	183.9	773	438	169.9

Note: Water Spray of 6 ℓ/min is performed in all cases.

Operation voltage and current in all fields fluctuate due to excesive sparking.

	maximum voltage	maximum current
Field 1	30 kV	140 mA
Field 2	31 kV	160 mA

Table 5.6 Comparative Collection Performance of DC-Biased Pulse Energization, Direct-Coupled Pulse Energization with Extremely Low Current Operation, and DC Energization (Furnace: Glass Fiber)

Test Conditions		Dust Mass Loading (mg/Nm^3)	Dust Components		B_2O_3 in Vapor Phase (mg/Nm^3)
			$Ca(OH)_2$ (mg/Nm^3)	B_2O_3 (mg/Nm^3)	
DC Biased Pulse Energization	Inlet	220	7.2	82.1	1240 (B_{in})
V_M=-55kV, V_{bias}=-20kV, F_p=50Hz	Outlet	100	3.2	42.9	871 (B_{out})
DC Biased Pulse Energization	Inlet	230	7.1	93.1	1150
V_M=-55kV, V_{bias}=-20kV, F_p=25Hz	Outlet	96	3.1	41.3	784
Direct Coupled Pulse Energization	Inlet	200	5.6	87.9	1140
V_M=-38kV, F_p=10Hz, i=0.005mA/m^2	Outlet	75	1.7	31.9	781
DC Energization	Inlet	250			
	Outlet	63			

Note: Water Spray = 6 ℓ/min in all cases

Gas Volume Q_{in} = 19,800 Nm^3/h (EP inlet)

Q_{out} = 23,300 Nm^3/h (EP outlet)

Table 5.7 Reduction of Energy Consumption by Direct-Coupled Pulse Energization (Furnace: Cathode-Ray Tube)

	Energy Comsumption (kWh)	Dust Mass Loading		Collection Efficiency (%)
		Inlet (mg/Nm^3)	Outlet (mg/Nm^3)	
Direct Coupled Pulse Energization V_M=-50kV, F_p=25Hz, i=0.023mA/m^2	1.4	916	10.6	98.84
		869	5.4	99.38
Direct Coupled Pulse Energization V_M=-50kV, F_p=50Hz, i=0.044mA/m^2	2.3	896	----	-----
		974	9.1	99.07
Direct Coupled Pulse Energization V_M=-50kV, F_p=100Hz, i=0.078mA/m^2	4.8	959	4.9	99.49
		1010	9.8	99.03
DC Energization	22.2	926	2.2	99.76
		1080	3.8	99.65

Note: Water Spary = 6 ℓ/min, Lime Consumption = 25 kg/h.

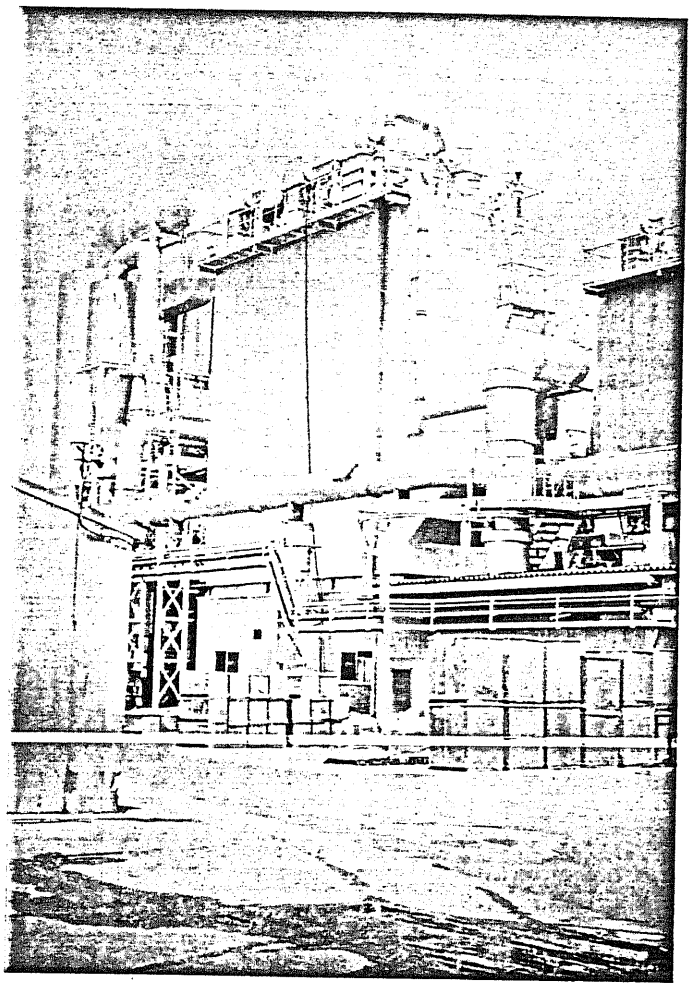

Fig. 5.12 Gas Cleaning System of Glass Furnace (Lime Conditioning Chamber and Electrostatic Precipitator)

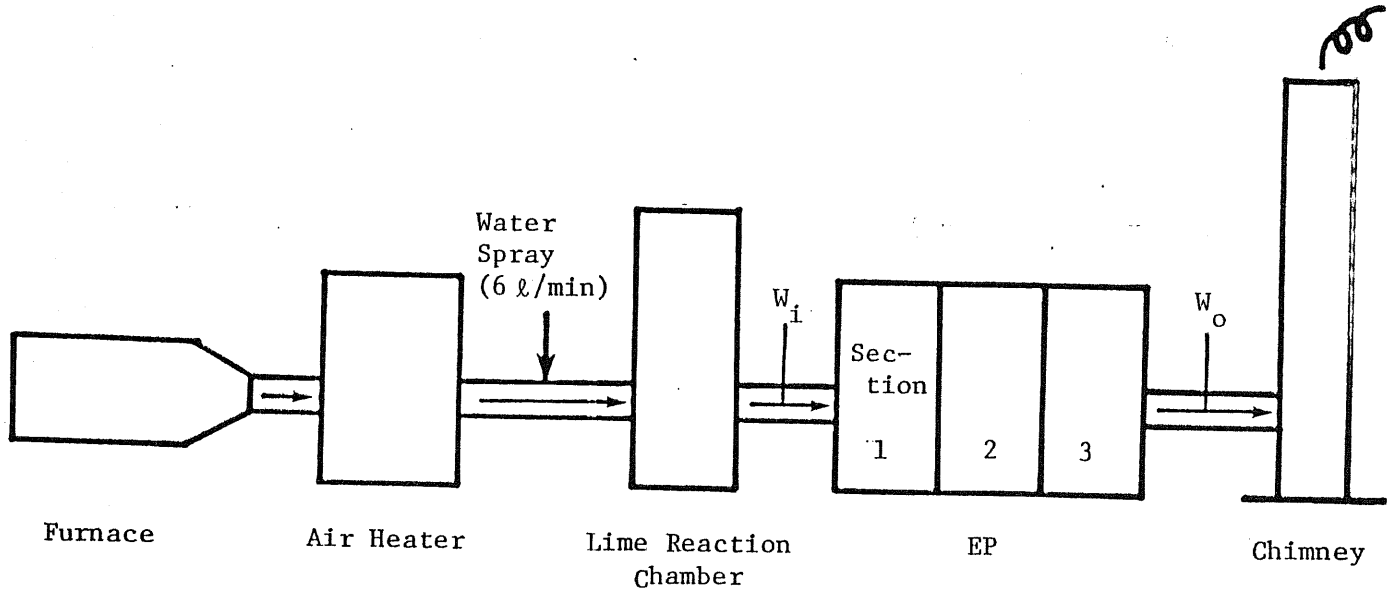

Furnace	Lime Consumption	Gas Temperature (EP Inlet)	Gas Volume (EP Inlet)
Glass Fibler	50 kg/h	T_g = 250 °C	Q = 17,000 - 20,000 Nm^3/h
Cathode-Ray Tube	25 kg/h	T_g = 340 °C	Q = 17,00 - 19,000 Nm^3/h

Fig. 5.13 Schematic Diagram of Gas Cleaning System of Glass Furnace

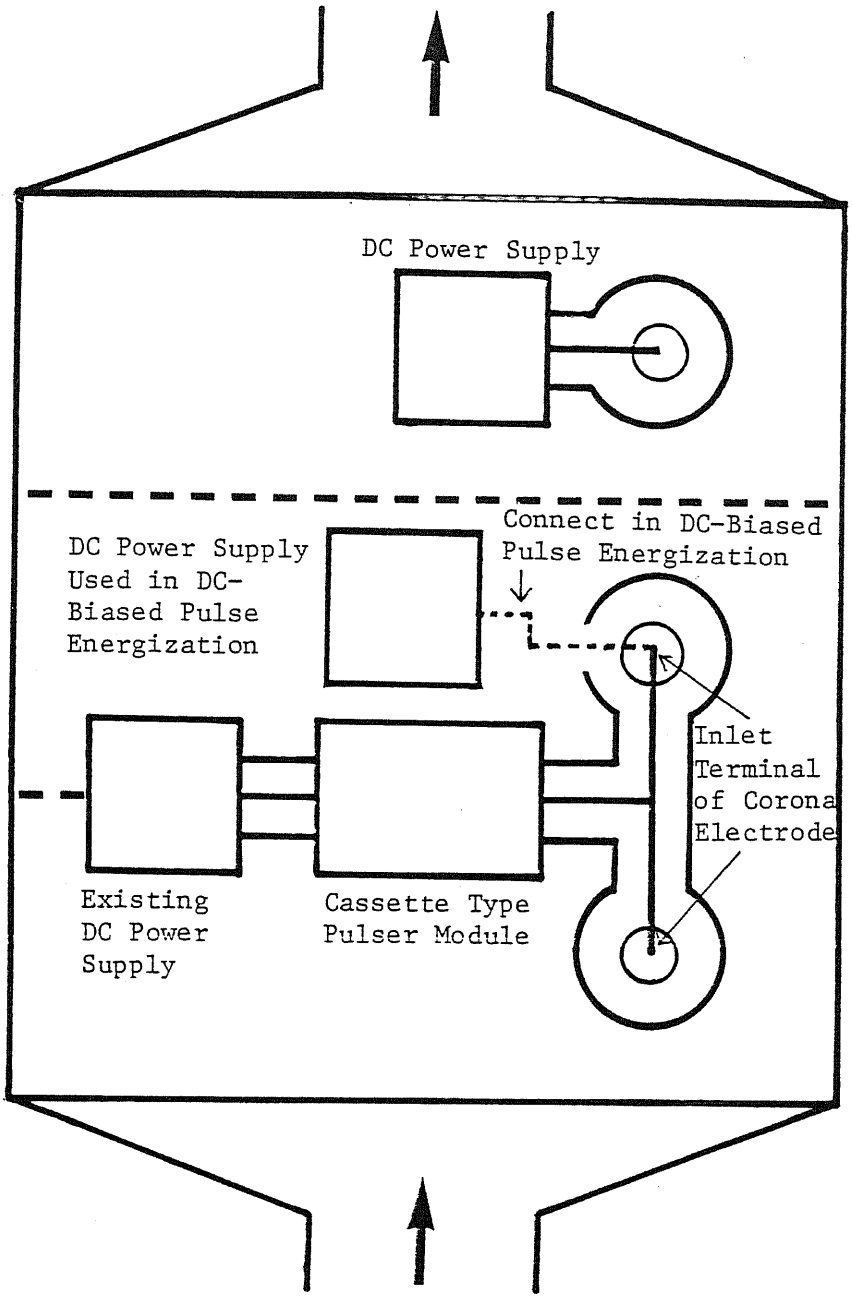

Field 1 : collection area, F_1 = 761.2 m^2; duct spacing, 2D = 300 mm
Field 2 : collection area, F_2 = 761.2 m^2; duct spacing, 2D = 300 mm
Field 3 : collection area, F_3 = 492.8 m^2; duct spacing, 2D = 500 mm

Fig. 5.14 Schematic Top Vie of EP in Pulse Operation
Fields 1 and 2 : Direct-Coupled Pulse Energization or DC-Biased Pulse Energization
Field 3 : DC Energization

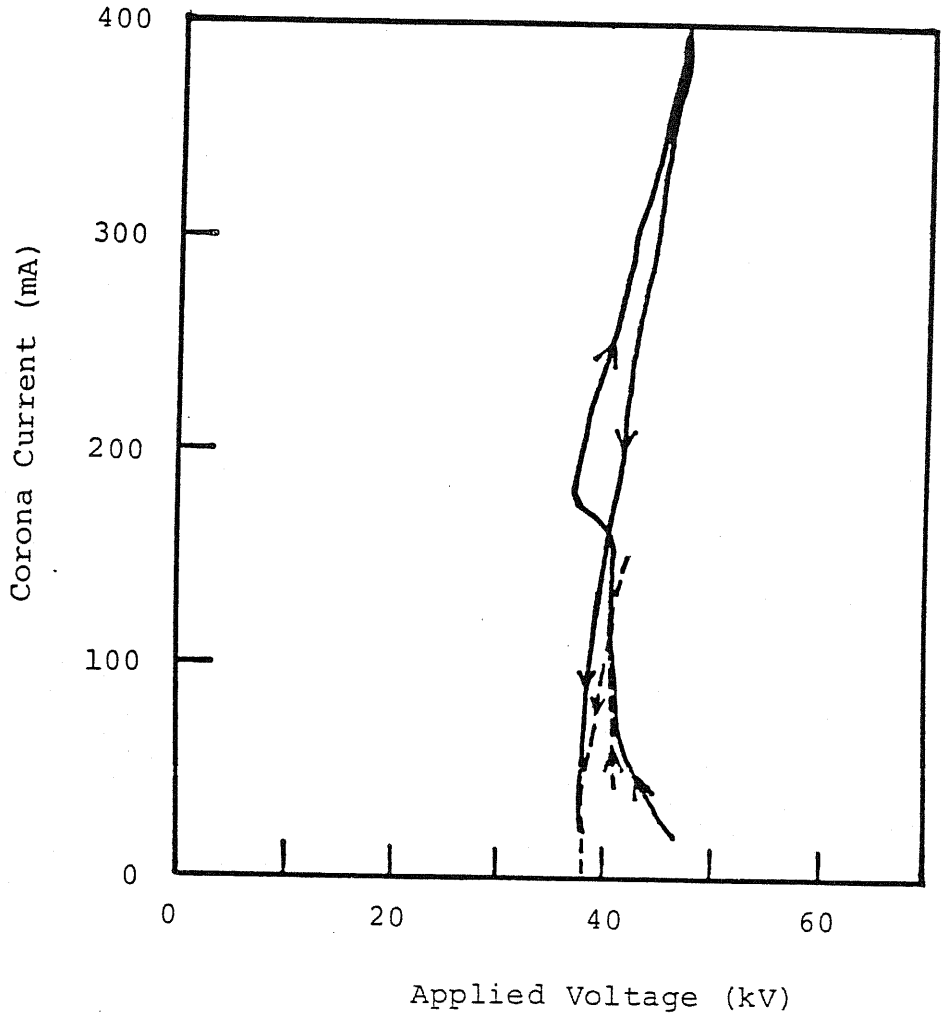

Fig. 5.15 V-I Characteristics of Field 3 under DC Enerigzation (Furnace: Glass Fiber, Lime Conditioning: Off, Water-Spray: Off, Gas Temperature: T_g = 210 °C)

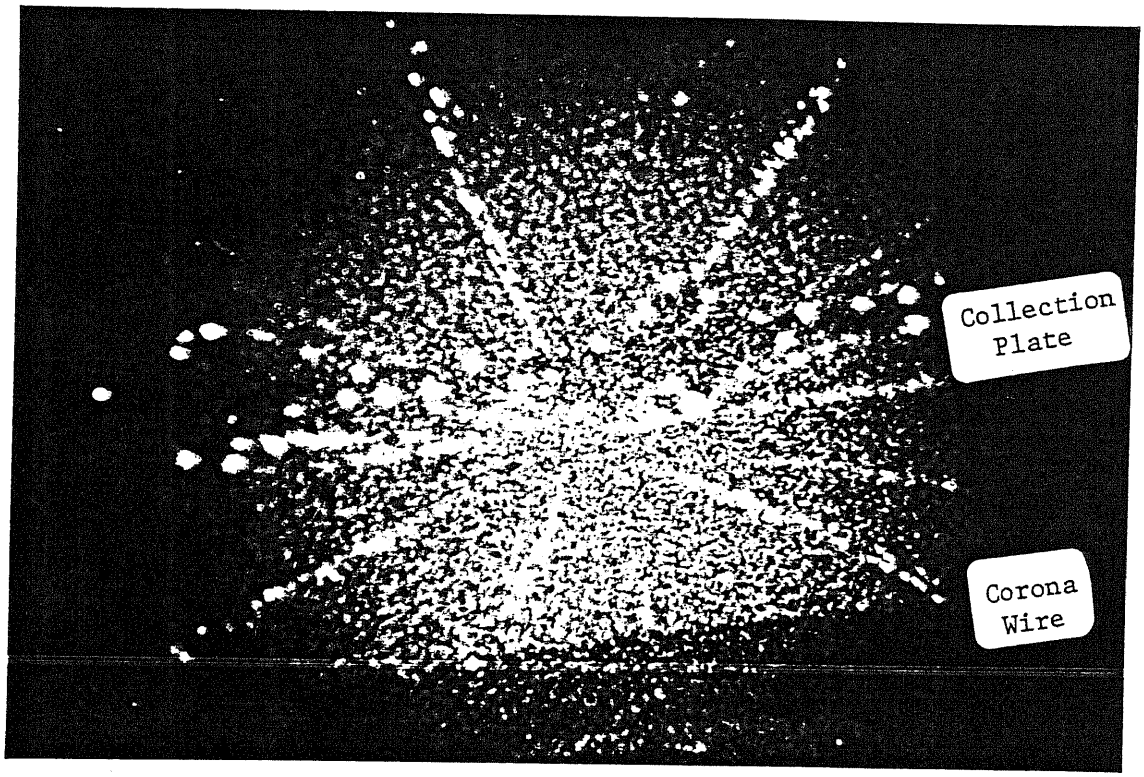

Fig. 5.16 Photograph of Severe Back Corona Occuring in Field 3 under DC-Energization
(furnace: Glass Fiber, Lime Conditioning: Off, Water Spray: Off, Gas Temperature: T_g = 210 °C)

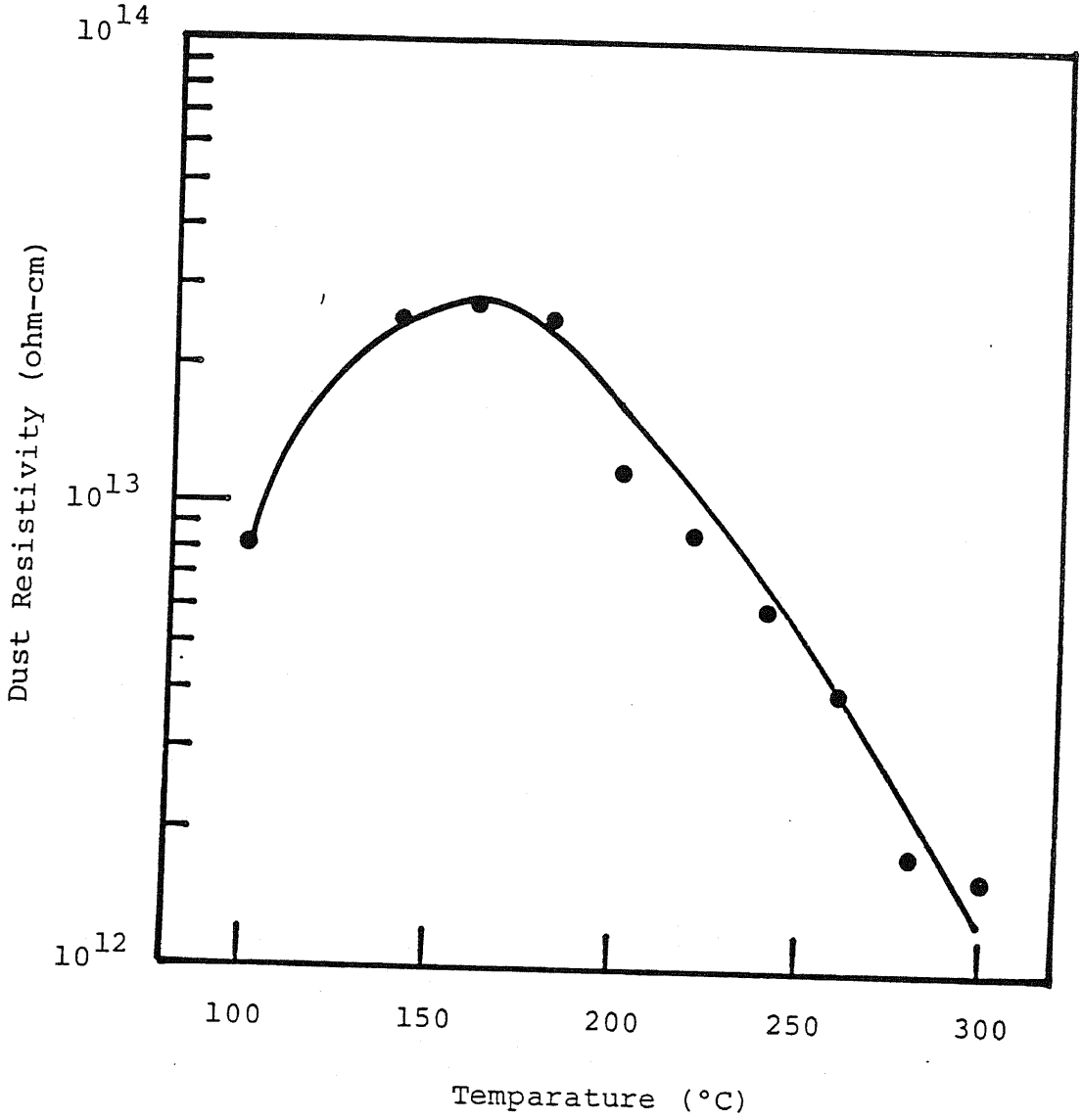

Fig. 5.17 Dust Resistivity vs. Temperature Measured in Laboratory (Dust: from Glass Fiber Furnace with Lime Conditioning, Humidity: 15 vol%)

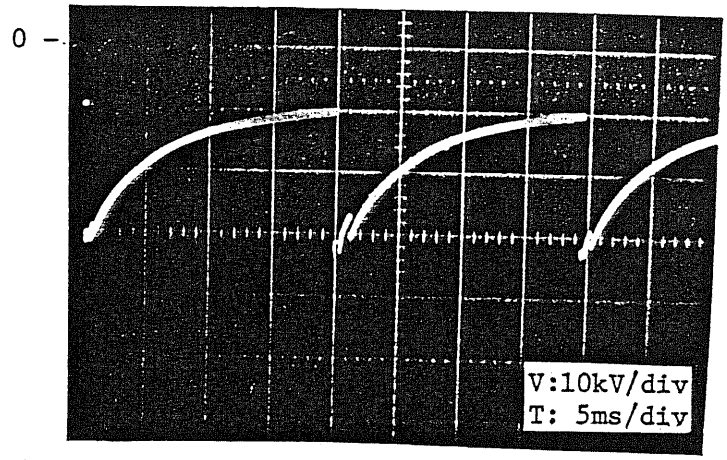

(a) Saw-Teeth Like Pulsating Wave Form

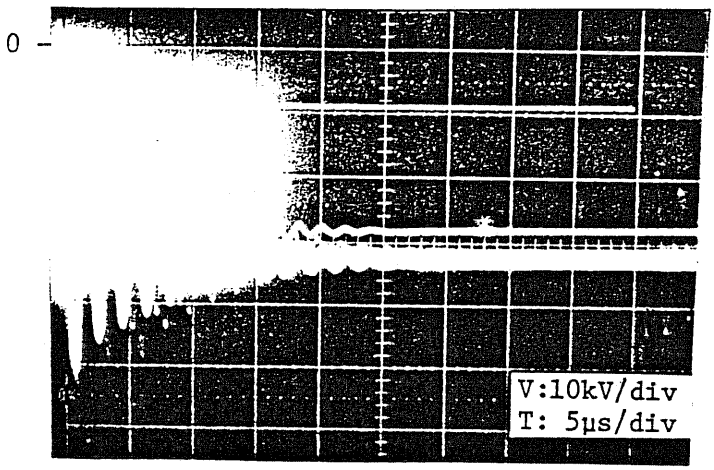

(b) Transient LC Oscillation

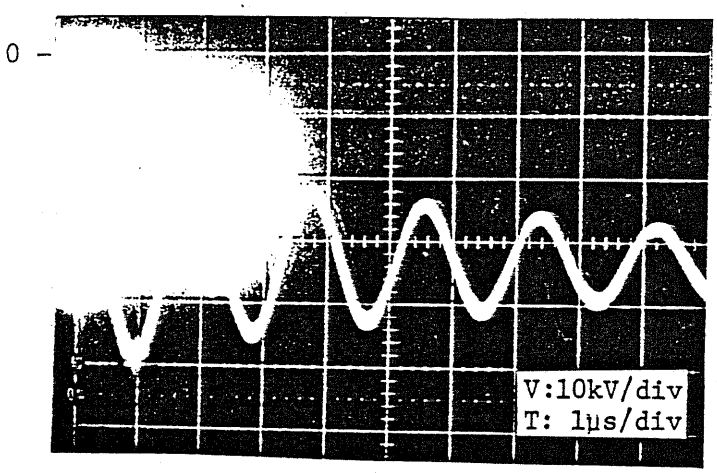

(c) Magnified LC Oscillating Part

Fig. 5.18 Pulse Voltage Wave Form of Direct-Coupled Pulse Energization Measured at the Inlet Terminal of Field 2 (Furnace: Glass Fiber, Lime Conditioning: Off, Water Spray: On, Gas Temperature: T_g = 210 °C, Pulse Conditions: V_M = -50 kV and F_p = 50 Hz)

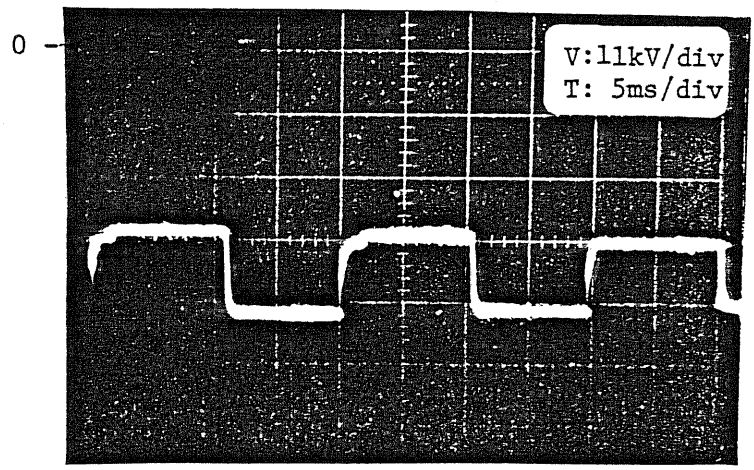

Fig. 5.19 Voltage Wave Form of Pulse Forming Condenser
(Conditions : see Fig. 5.18)

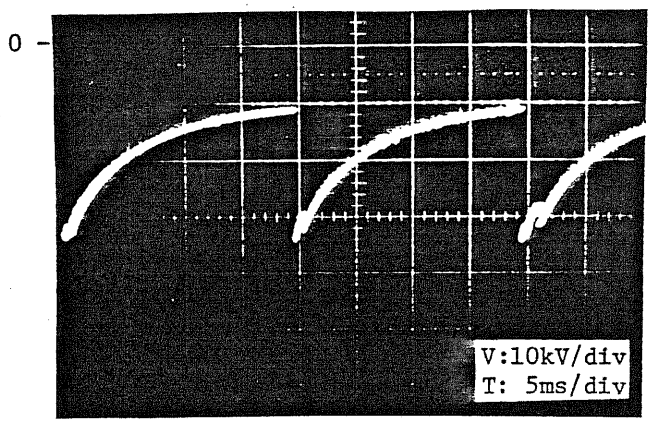

(a) Saw-Teeth Voltage Wave Form

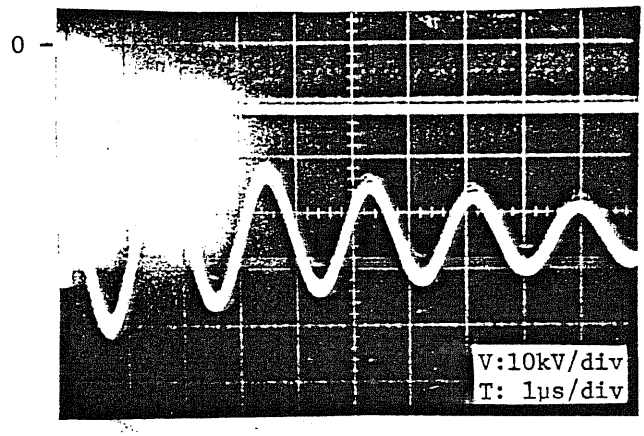

(b) Magnified LC Oscillating Part

Fig. 5.20 Effect of Lime Conditioning on Pulse Voltage Wave Form (Furnace: glass Fiber, Lime Conditioning: On, Water Spray: On, Gas Temperater: T_g = 240 °C, Pulse Conditions: V_M = -50 kV and F_p = 50 Hz)

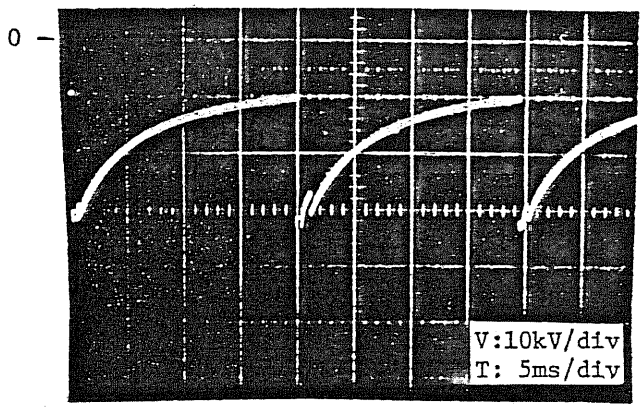

(a) V_M = -50 kV

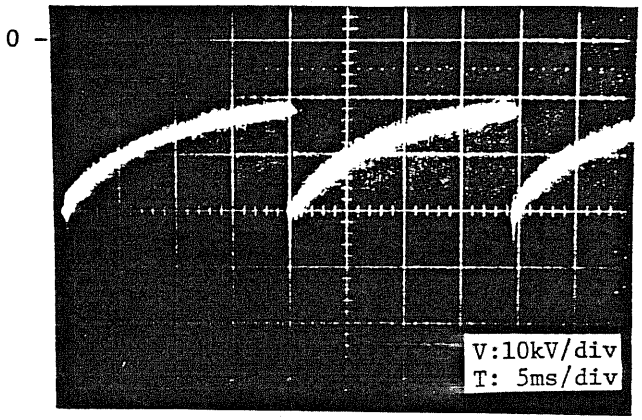

(b) V_M = -45 kV

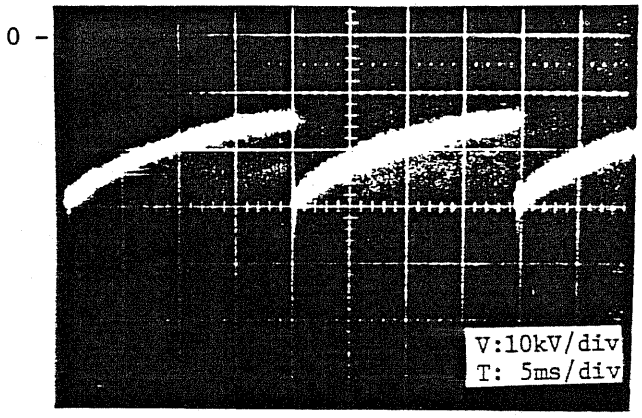

(c) V_M = -40 kV

Fig. 5.21 Effect of Pulse Peak Voltage, V_M, on Pulse Voltage Wave Form
(Furnace: Glass Fiber, Lime Conditioning: Off, Water Spray: On, Gas Temperature: T_g = 210 °C, Pulse Condition: F_p = 50 Hz)

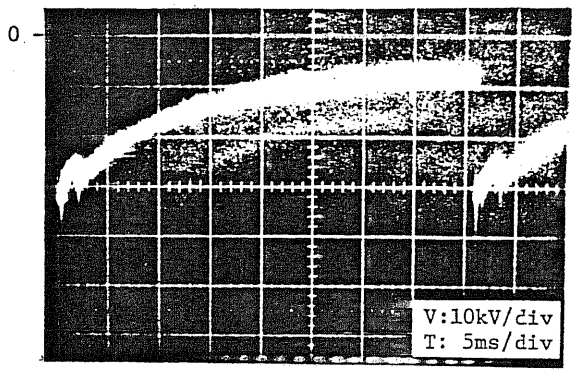

(a) F_p = 25 Hz

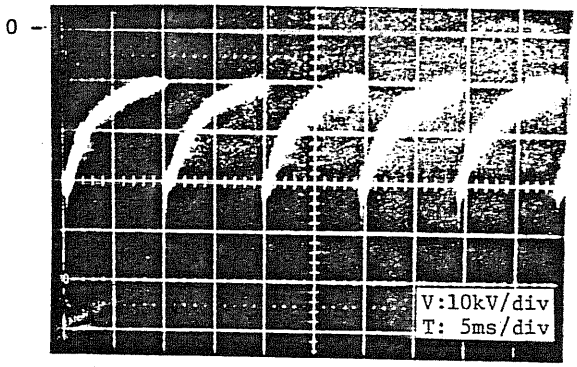

(d) F_p = 100 Hz

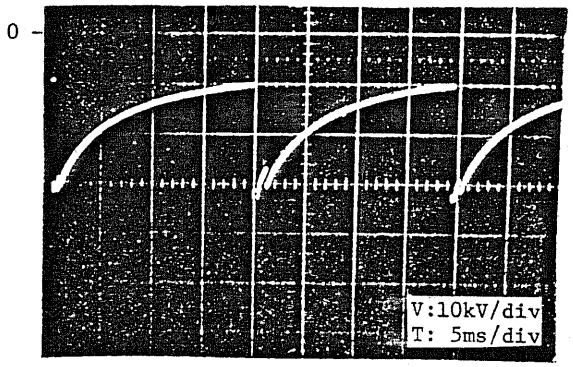

(b) F_p = 50 Hz

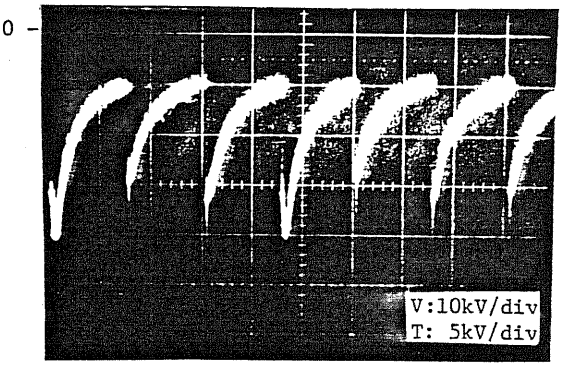

(e) F_p = 125 Hz

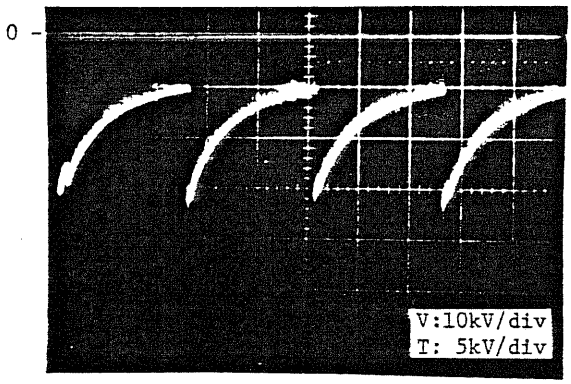

(c) F_p = 75 Hz

Fig. 5.22 Effect of Pulse Repetition Frequency, F_p, on Pulse Voltage Wave Form
(Furnace: Glass Fiber, Lime Conditioning: Off, Water Spray: On, Gas Temperature: T_g = 210 °C, Pulse Conditions: V_M = -50 kV)

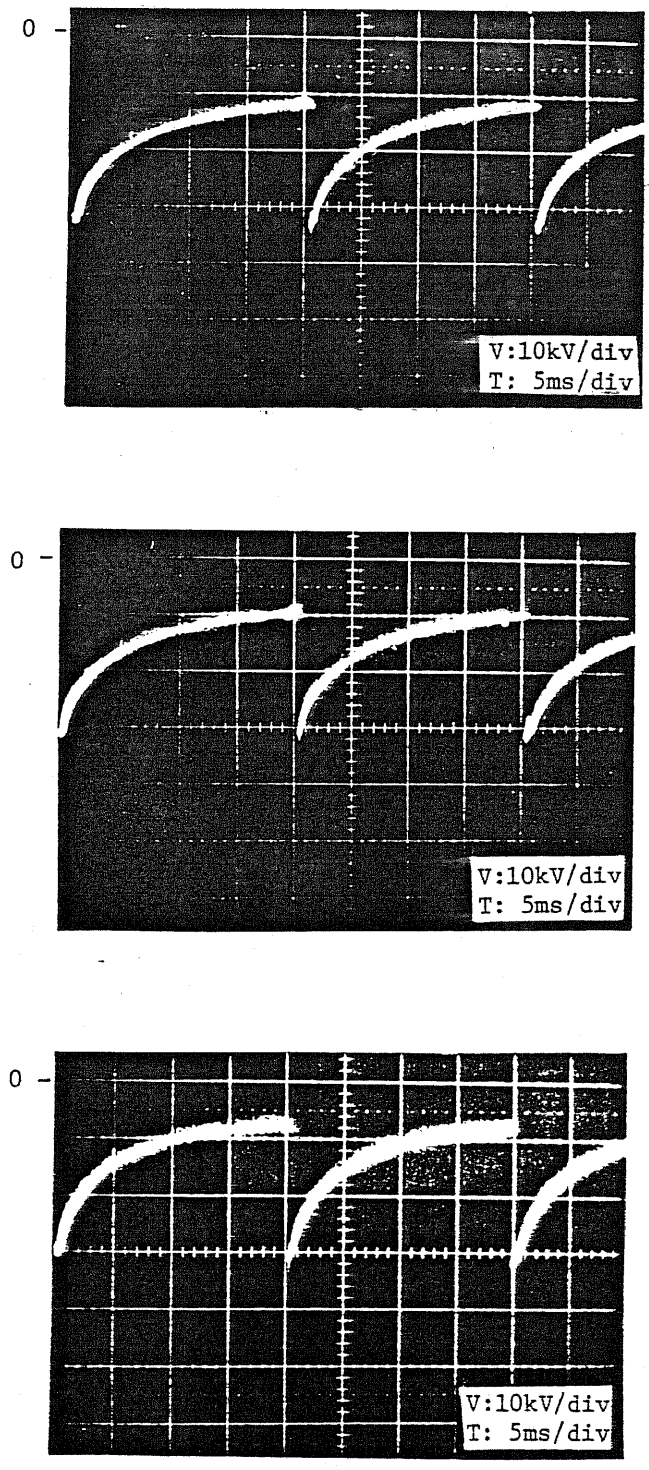

Fig. 5.23 Effect of Time-Dependent Fluctuation of Furnace Conditions on Pulse Voltage Wave Form
(Furnace: Glass Fiber, Lime Conditioning: Off, Water Spray: On, Gas Temperature: T_g = 210 °C, Pulse Conditions: V_M = -50 kV and F_p = 50 Hz)

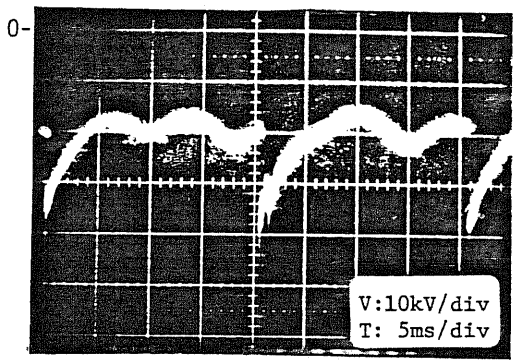

(a-1) Saw-Teeth Voltage Wave Form

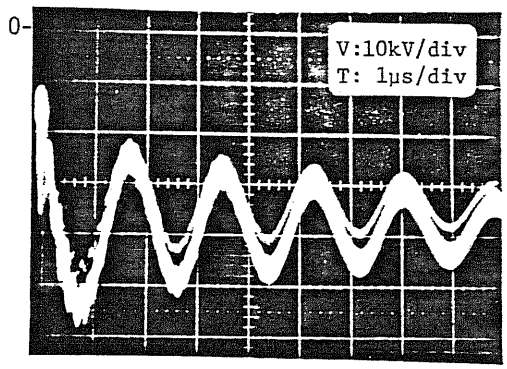

(a-2) Maginified LC Oscillatory Part

(a) F_p = 50 Hz

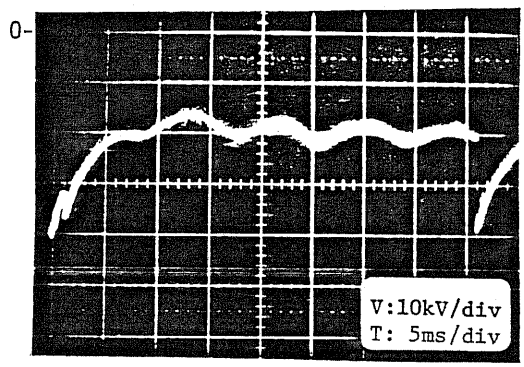

(b-1) Saw-Teeth Voltage Wave Form

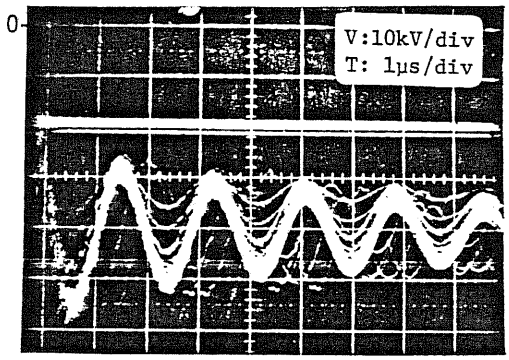

(b-2) Maginified LC Oscillatory Part

(b) F_p = 25 Hz

Fig. 5.24 Pulse Voltage Wave Form in DC-Biased Pulse Energization (Furnace: Glass Fiber, Lime Conditioning: OFF, Water Spray: On, Gas Temperature: T_g = 250 °C, Pulse Conditions: V_M = -55 kV and V_R = -20 kV)

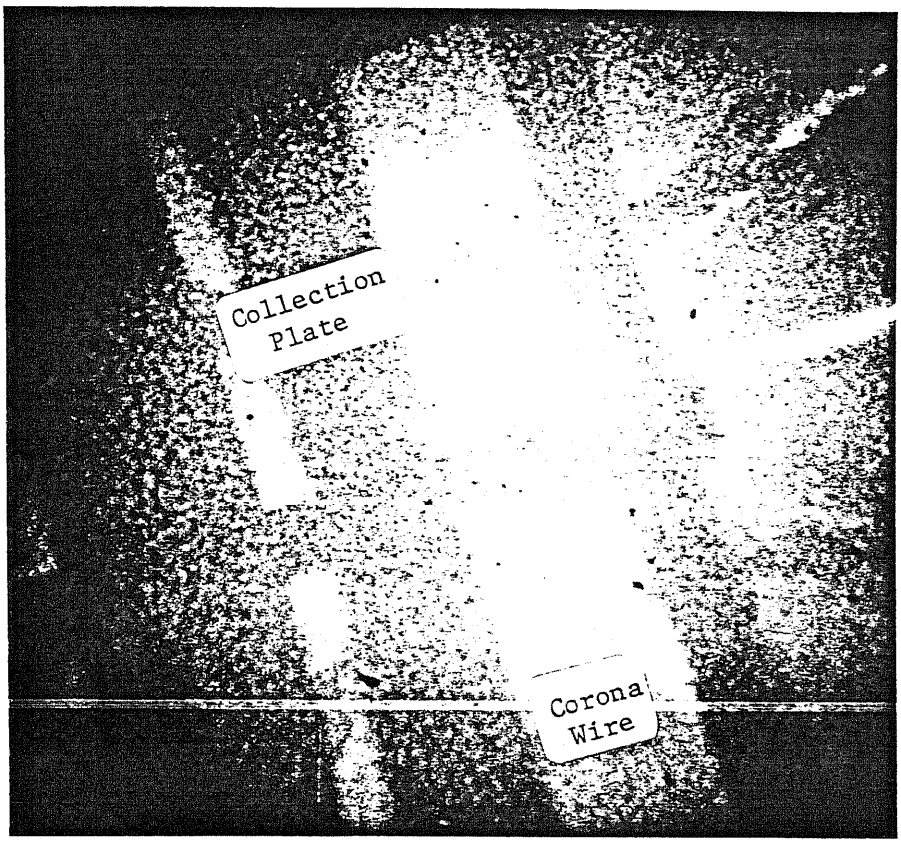

Fig. 5.25 Photograph of Uniform Negative Coronas on Corona Wires of Field 2 under Direct-Coupled Pulse Energization (Furnace: Glass Fiber, Lime Conditioning: Off, Water Spray: On, T_g = 210 °C, Pulse Conditions: V_M = -50 kV and F_p = 50 Hz)
(Note: Light induced by back corona from the collection plate can not be recognized by both naked eyes and the image intensifier.)

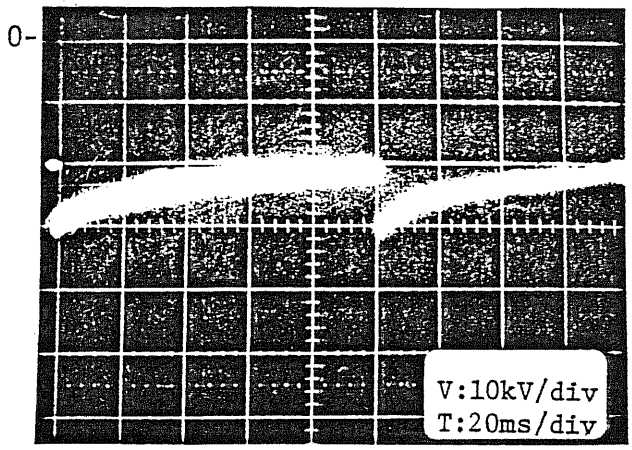

(a) Saw-Teeth Voltage Wave Form

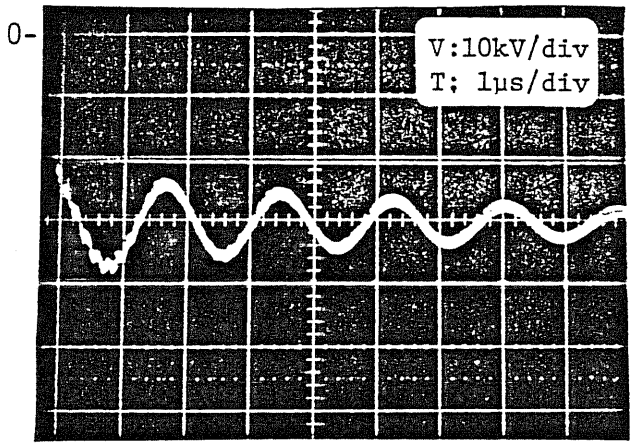

(b) Magnified LC Oscillatory Part

Fig. 5.26 Voltage Wave Form of Direct-Coupled Pulse Energization under Extremely Low Current Operation (Furnace: Glass Fiber, Lime Conditioning: Off, Water Spray: On, Gas Temperature: T_g = 250 °C, Pulse Conditions: V_M = 38 kV and F_p = 10 Hz)

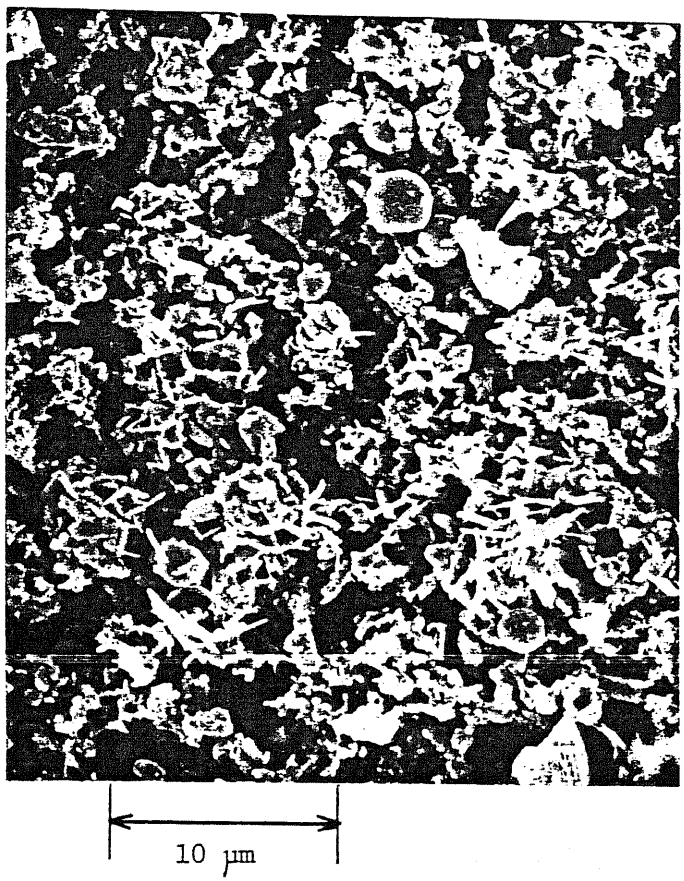

Fig. 5.27 Photograph of Dust Sampled at EP Outlet by Electron Microscope
(Furnace: Glass Fiber, Lime Conditionig: Off, Water Spray: Off, DC Energization)

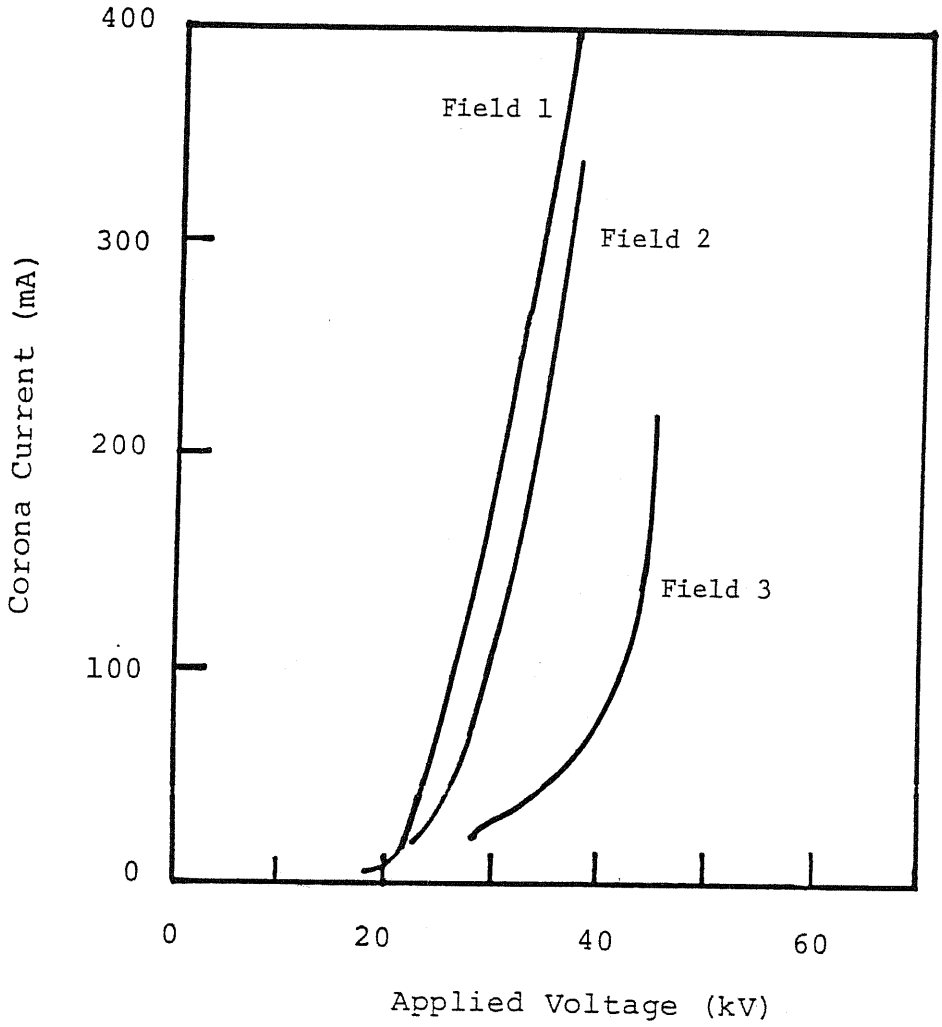

Fig. 5.28 V-I Characteristics of Fields 1, 2, and 3 under DC Energization
(Furnace: Cathode-Ray Tube, Lime Conditioning: On, Water Spray: On, Gas Temperature: T_g = 340 °C)

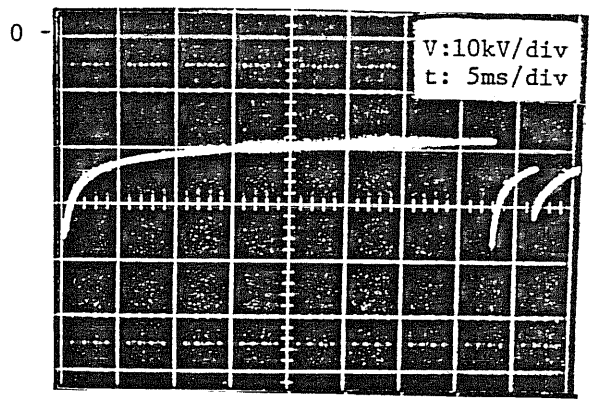

(a) Saw-Teeth Voltage Wave Form

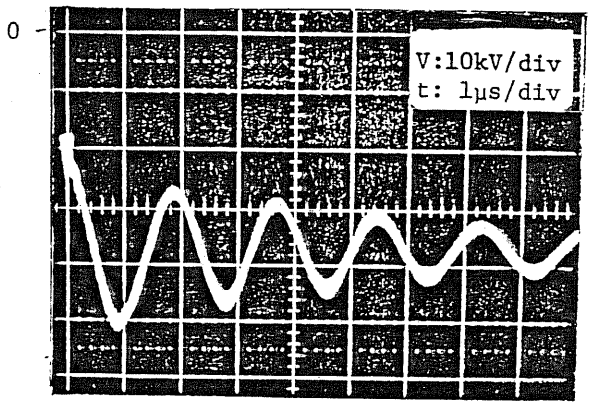

(b) Magnified LC Oscillating Part

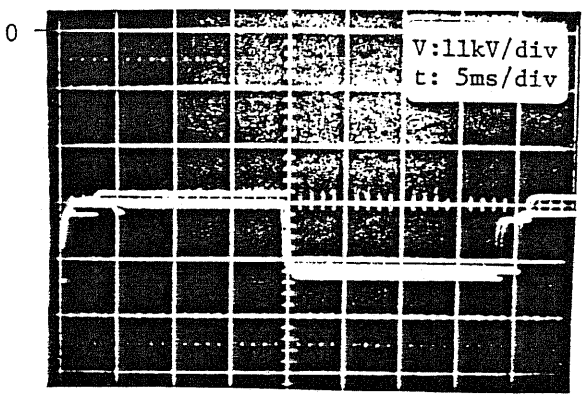

(c) Condenser Voltage Wave Form

Fig. 5.29 Pulse Voltage Wave Form and Voltage Wave Form of Pulse Forming Condenser
(Furnace: Cathode-Ray Tube, Lime Conditioning: On, Water Spray: On, Gas Temperature: T_g = 340 °C, Pulse Conditions: V_M = -50 kV, V_R = -18 kV, F_p = 25 Hz)

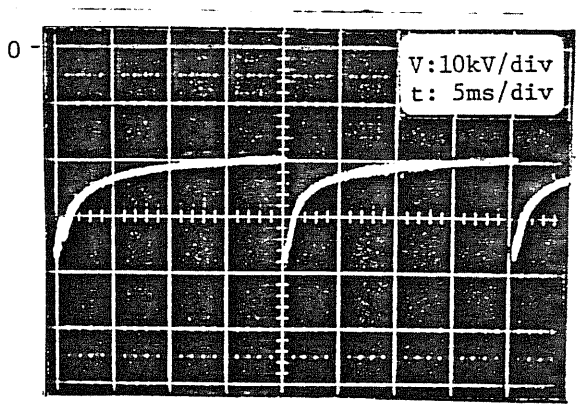

(a) Saw-Teeth Voltage Wave Form

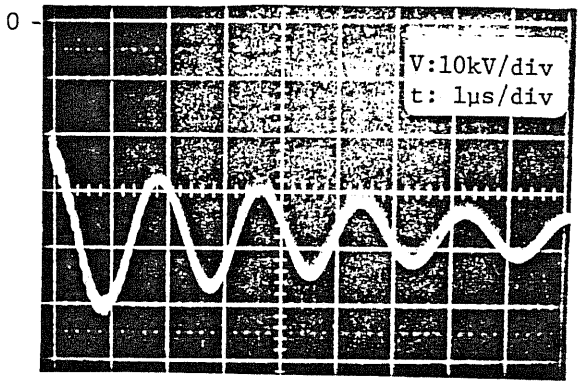

(b) Magnified LC Oscillating Part

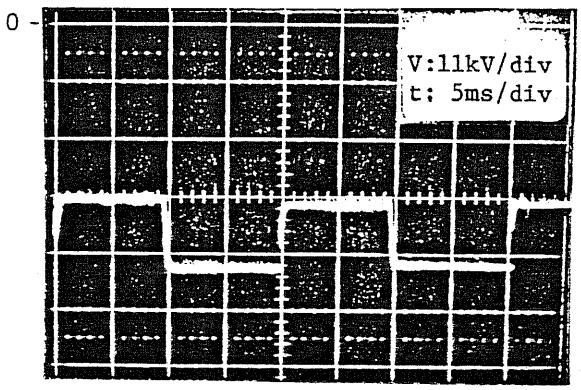

(c) Condenser Voltage Wave Form.

Fig. 5.30 Pulse Voltage Wave Form and Voltage Wave Form of Pulse Forming Condenser
(Furnace: Cathode-Ray Tube, Lime Conditioning: On, Water Spray: On, Gas Temperature: T_g = 340 °C, Pulse Conditions: V_M = -50 kV, V_R = -20 kV, F_p = 50 Hz)

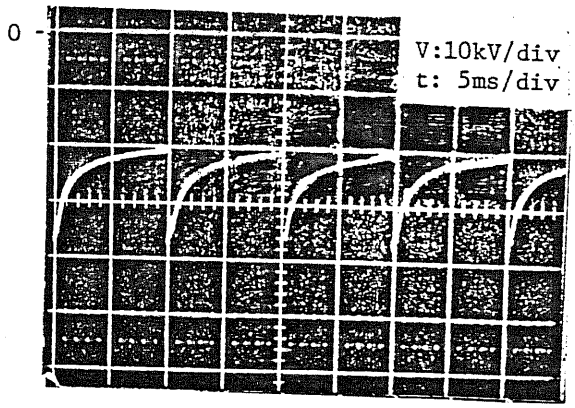

(a) Saw-Teeth Voltage Wave Form

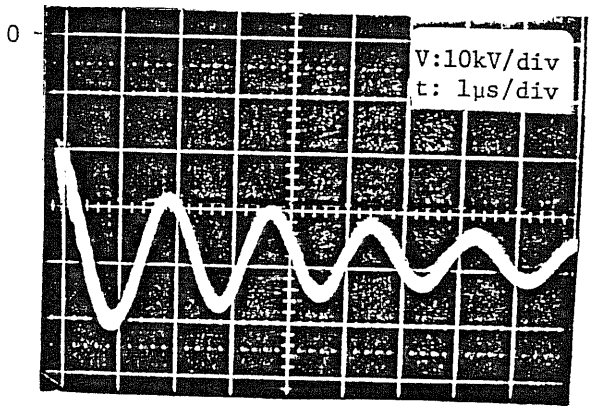

(b) Magnified LC Oscillating Part

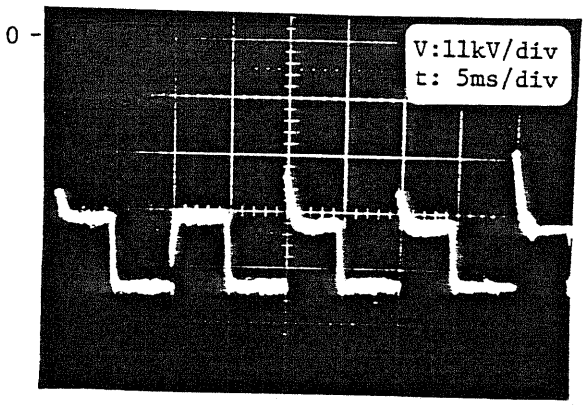

(c) Condener Voltage Wave Form

Fig. 5.31 Pulse Voltage Wave Form and Voltage Wave Form of Pulse Forming Condenser
(Furnace: Cathode-Ray Tube, Lime Conditioning: On, Water Spray: On, Gas Temperature: T_g = 340 °C, Pulse Conditions: V_M = -50 kV, V_R = -21 kV, F_p = 100 Hz)

CHAPTER 6. CONCLUSION

In this series of the research program, the pulse energization in an electrostatic precipitator has been developed in order to solve the back corona problems. There are several systems of pulse energization, including the condenser-coupled traveling pulse energization, the condenser-coupled LC-oscillatory pulse energization, the condenser-coupled feeder-formed pulse energization, and the direct-coupled pulse energization, suggested and their basic natures of corona characteristics are experimentally obtained. The application to the practical plants is possible by any of these systems. However, the direct-coupled pulse energization system possesses the inherent possibility of the smallest initial cost, and of retrofitting application in the existing electrostatic precipitators.

It is confirmed in the laboratory precipitators that the direct-coupled pulse energization system corrects back corona and enhances the collection performance drastically in most cases. However, there may exist the limit of the dust resistivity range, say $r_d > 10^{14}$ ohm-cm where even the direct-coupled pulse energization causes severe back corona and the collection performance can not be enhanced.

The cassette type pulser module is designed and constructed by the direct-coupled pulse energization concept obtained in the laboratory test of corona characteristics using a full scale duct. It is designed to be inserted between the existing dc power supply and the precipitator of a medium size precipitator of a 1200 - 1800 m^2 collection area. Its electrical performance is confirmed to be the one designed in the laboratory using the simulated load.

The field tests of the direct-coupled pulse energization are also

performed. In the case of the precharger for the granular bed filter in the wooden-chips burning boiler, the flyash treated has a dust resistivity of 10^{11} -10^{12} ohm-cm and causes back corona by the dc energization. By application of the direct-coupled pulse energization to this precharger, back corona is completely disappears. However the space charge effect hidden behind of back corona appears to cause corona quenching in the downstream region of the corona wires. The dust surface loading in this case is assumed to be very large and the amount of the negative current is not enough to provide sufficient charge to the dust particles, although the time constant based on the Pauthenier's theory is small enough compared to the residence time of the dust in the charging field. As a result, the output dust mass loading measured at the outlet of the granular bet filter can not be reduced.

In the case of the electrostatic precipitator in the glass furnace producing fiber glass, the size of the precipitator is as a good size as to apply the cassette type pulser module constructed ant it is installed to perform the direct-coupled pulse energization. However, the dust resistivity is very high in the level of $r_d = 10^{14}$ ohm-cm due to boron compounds and even in the direct-coupled pulse energization, back corona can not be corrected and its voltage wave form indicates severe back corona taking place. This test indicates that there is a limit of dust resistivity where back corona problem is solved only by the pulse energization. The continuous condensation of boron compounds in the precipitator causes another problem of high dust surface loading.

Using the same precipitator, the furnace is change to the one producing cathode-ray tube glass and the energy saving effect of the direct-coupled pulse energization is tested. In this case, both dc energization and pulse energization shows the very high collection performance (dust emission less than 10 mg/Nm^3). 22.2 kW of energy is used by dc energization to operate the precipitator of 1500 m^2. By the pulse energization,

the energy used to energize the same field becomes 1.4 kW when operated in F_p = 25 Hz. The drastical reduction in energy consumption is obtained.

From these field tests, the capablity and the limit of the direct-coupled pulse energization in collecting difficult dusts are recognized.

In conclusion, the novel pulse energization system of an electrostatic precipitator is developed from its basic consept to the practical application level.

ACKNOWLEDGEMENTS

The author wishes to ackowledge,

with his deepest gratitude the guidance not only at every stage of the research, but also as the teacher of the life given by Prof. Dr. Senich Masuda

Ass. Prof. Dr. T. Oda, Mr. T. Itagaki, and Dr. H. Nakatani for their kind comments on the reseach and lavished help

Mr. A. Iijima of Origin Co., Ltd, for his various help during the reseach especially in construction of the pulser module

All the people in the Prof. Masuda's Laboratory for their pertinent help

Mistubishi Heavy Industries Co., Ltd. for the oppotunity of using the test facility, in particular Mr. N. Tachibana, Mr. T. Ando, Dr. Y. Matsumoto and Mr. Y. Nakayama

Takuma Co., Ltd, for the kind offer of the tests shown in the paragraph 5-2, in particular Mr. M. Inazumi, Mr. K. Uno, and Mr. I. Nakagawa

Nippon Electric Glass Co., Ltd, for the kind offer of the tests shown in the paragraph 5-3, in particular Mr. I. Nagata and K. Nishimura.

REFERENCE

(1) S.Masuda; Performance of Modern Precipitators -Position Paper-, Proc. of Int. Conf. on Electrostatic Precipitation, (1981).

(2) S.Masuda and A.Mizuno; Initiation Condition and Mode of Back Discharge for Extremely High Resistivity Powders, Record of IEEE IAS 1977 Annual Conference, pp867-874, (1977).

(3) S.Masuda and A.Mizuno; Initiation Conditon and Mode of Back Discharge, J. of Electrostatics, 4, pp35-52, (1977/1978).

(4) G.Nichols; Time Dependent Performance Degradation in Hot Side Electrostatic Precipitators Collecting Fly Ash from Coal Combustion, Doctoral Dissertation, University of Tokyo, (1981).

(5) EPRI PROJECT 724-2; Flue Gas Conditioning For Enhanced Precipitation of Difficult Ashes, (1983).

(6) J.Gooch, E.Dismukes, R.Bickelhaupt and R.Altman; Flue Gas Conditioning Studies, Proc. of 2nd Int. Conf. on Electrostatic Precipitation, pp200-209, (1984).

(7) E.Coe; SO_3 Conditioning for High Resistivity Fly Ash, ibid, pp275-282, (1984).

(8) H.Gomoll; SO_3 Gas Conditioning, a Proven Method to Increase the Efficiency of Existing Electrostatic Precipitataors, ibid, pp319-327, (1984).

(9) H.White; A Pulse Method for Supplying High-Voltage Power for Electrostatic Precipitation, Trans. AIEE, Nov. pp326-330, (1952).

(10) J.Lutti; Grundlagen zur Elektrostatischen Abscheidung von Hochohmigen Stauben, Dissertation. No. 3924, ETHZ, Zurich (1967).

(11) S.Masuda, E.Doi, M.Aoyama, and A.Shibuya; Bias-Controlled Pulse Charging System for Electrostatic Precipitator, Staub-Reinhalf. Luft 36, pp19-26, (1976).

(12) S.Masuda; Novel Electrode Construction for Pulse Charging, Proc. 1st EPA-Symposium on Transfer and Utilization of Particulate Control Technology, Vol. 1 (EPA-600/7-79-004a, Feb. 1979), p241, (1978).

(13) S.Masuda, S.Obata, and J.Hirai; A Pulse Voltage Source for Electrostatic precipitators, Record of IEEE IAS 1978 Annual Conference, pp23-30, (1978).

(14) H.Milde and P.Feldman; Pulse Energization of Electrostatic Precipitators, ibid, pp66-70, (1978).

(15) H.Milde and H.van Hossen; Application of Fast Rising Pulses to Electrostic Precipitators, Record of IEEE IAS 1979 Annual Conference, pp158-162. (1979).

(16) P.Lausen, H.Henriksen, and H.Petersen; Energy Conserving Pulse Energization of Precaipitators, ibid, pp163-171. (1979).

(17) H.Petersen; Application of Energy Conserving Pulse Energization for Electrostatic Precipitators - Practical and Economic Aspects, Proc. of 3rd EPA-Symposium of Transfer and Utilization of Particulate Control Technology (1981).

(18) P.Lausen and H.Joergensen; Theory and Application of Pulse Energization, Proc. of Int. Conf. on Electrostatic Precipitation (1981).

(19) T.Ando, N.Tachibana, and Y.Matsumoto; A New Energization Method for Electrostatic Precipitators, Mitsubishi Intermittent Energization Systems, 4th EPA-Symposium of Transfer and Utilization of Particulate Control Technoloty (1982).

(20) S.Masuda, H.Nakatani, and S.Hosokawa; Modification in Wave Form of Traveling Pulse Voltage Due to Corona Production Along Transmission Line, Record of IEEE IAS 1983 Annual Conference, pp959-965, (1983).

(21) S.Masuda, S.Hosokawa, and H.Nakatani; Pulse Energization System of Electrostatic Precaipitators, ibid, pp966-973, (1983).

(22) G.Dinelli, F.Mattachini, and M. Rea; Pulsed Power Supply Exaperiments in Industrial ESP, ibid, pp982-985, (1983).

(23) S.Olesen; A New Way of Dedusting Dry Process Kilns, World Cement, April, PP84-86, (1983).

(24) S.Masuda and S.Hosokawa; Pulse Energization System of Electrostatic Precipitator for Retrofitting Application, Record of IEEE IAS 1984 Annual Conference, ppl177-1184, (1984).

(25) T.Ando, Y.Nakayama, and Y.Matsumoto; Reduction of Power Consumption in Precipitators, Proc. of 2nd Int. Conf. on Electrostatic Precipitation, (1984).

(26) O.Sinhuber; Improvement of Electrostatic Precipitator Performance with Pulse Energization, ibid, pp557-574, (1984).

(27) K.Darbay; Pulse Energization - an Altearnative to Conditioning for highly Resistive Dusts, ibid, pp575-584, (1984).

(28) K.Porle and Y.Matsui; Practical Equipment Now Available for Pulse Energization Will Save Energy and Improve Performancae, ibid, pp585-594, (1984).

(29) H.Joergensen, E.Jacobsen and P.Lausen; Influence of Process Parameters on Pulse Enhancement Factors, ibid, pp600-607, (1984).

(30) S.Masuda and S.Hosokawa; Submicrosecond Pulse Energization for Retrofitting Applications, ibid, pp613-622, (1984).

(31) S.Masuda and S.Hosokawa; Pulse Energization of Precipitators Using Lonag Corona Transmission Lines, ibid, pp756-763, (1984).

(32) G.Dinelli and M.Rea; Inpulse Energization of Industrial ESP, ibid, pp896-904, (1984).

(33) J.DuBard, W.Piulle and L.Sparks; Effects of Pulse Energization on Electrical Mechanisms in a Fly Ash, ibid, pp920-928, (1984).

(34) S.Masuda; Novel Particulate Control Technology, Plenum Talk at 4th EPA-Symposium on Transfer and Utilization of Particulate Control Technology, (1982).

(35) S.Masuda and Y.Shishikui; Production of Monopolar Ions from Streamer Coronas Induced by Very Short Pulse Voltage, IEEE Trans. on IAS, Vol. IA-20, pp1212-1218, (1984).

(36) S.Masuda and Y.Nonogaki; Sensing of Back Discharge and Bipolar Ionic Current, J. of Electrostatics, 10, pp73-80, (1981).

(37) S.Masuda and Y.Nonogaki; Bi-Ioninzed Structure of Back Discharge Field in an Electrostatic Precipitator, Rec. of IEEE IAS 1982 Annual Conference, (1982).

(38) S.Masuda, T.Itagaki, S.Nohso, O.Tanaka, K.Hironaga, and N.Fukushima; Bipolar Current Probe for Diagnosing Full-Scale Precaipitators, Proc. of EPA-EPRI 5th Symp. on Transfer and Utilization of Particulate Control Technology, (1984).

(39) S.Masuda, T.Itagaki, S.Nohso, O.Tanaka, K.Hironaga, and N.Fukushima; Bipolar Current Probe for Measuring Space Potential and Back Corona Severity, Proc. of 2nd Int. Conf. on Electrostatic Precipitation, pp210-218, (1984).

(40) S.Masuda, A.Mizuno, H.Nakatani, and H.Kawahara; Application of Boxer-Charger in Pulsed Electrostatic Precipitator, Record of IEEE IAS 1980 Annual Conference, pp904-911, (1980).

(41) S.Masuda, S.Hosokawa, and S.Kaneko; Ceramic-Made Boxer-Charger for Precharging Application, Proc. of EPA-EPRI 5th Symp. on Transfer and Utilization of Particulate Control Technology, (1984).

(42) S.Masuda; State of the Art of Precharging, Proc. of 2nd Int. Conf. on Electrostatic Precipitation, pp177-193, (1984).

(43) H.Nakatani; Doctral Dissertation, University of Tokyo, (1982).

(44) A.Donaldson, M.Hagler, M.Kristiansen, G.Jackson, and L.Hatfield; Electrode Elosion Phenomena in a High-Energy Pulsed Discharge, IEEE Trans. on Plasma Science, Vol. PS-12, pp28-38, (1984).

(45) S.Masuda and J.Moon; Electrostatiac Precipitation of Carbon Soot from Diesel Engine Exhaust, Record of IEEE IAS 1982 Annual Conference, pp1086-1094, (1982).

(46) S.Masuda and S.Hosokawa; Performance of Two-Stage Type Electrostatic Precipitators, ibid, pp1094-1101, (1982).